Implications of Flavour Data on Dark Matter Phenomenology

Lopamudra Mukherjee

A thesis
submitted for the degree of

Doctor of Philosophy

Supervisor

Dr. Soumitra Nandi

Department of Physics
Indian Institute of Technology Guwahati
Guwahati - 781039, Assam, India

Implications of Flavour Data on Dark Matter Phenomenology

A thesis submitted by

Lopamudra Mukherjee

to

Indian Institute of Technology Guwahati
in partial fulfillment of the requirements
for the award of the degree of
Doctor of Philosophy in Physics

Supervisor

Dr. Soumitra Nandi

Department of Physics
Indian Institute of Technology Guwahati
Guwahati - 781039, Assam, India

To Ma and Momma...

"We shall not cease from exploration
And the end of all our exploring
Will be to arrive where we started
And know the place for the first time."

-T. S. Eliot

Declaration

Lopamudra Mukherjee
Roll No. 166121012
Department of Physics,
IIT Guwahati,
Assam - 781039, India.

I hereby declare that works presented in the thesis entitled "**Implications of Flavour Data on Dark Matter Phenomenology**" has been carried out by me under the supervision of Dr. Soumitra Nandi at the Department of Physics, Indian Institute of Technology Guwahati, India. The content of this thesis, in full or in parts, have not been submitted to any other University or Institute for the award of any degree or diploma. Works presented in the thesis are all my own unless referenced to the contrary in the text.

Signed: Lopamudra Mukherjee

Lopamudra Mukherjee
Date: 30/09/2021

Certificate

Dr. Soumitra Nandi
Associate Professor
Department of Physics
Indian Institute of Technology Guwahati
Guwahati, India
email:soumitra.nandi@iitg.ac.in

This is to certify that the thesis entitled "**Implications of Flavour Data on Dark Matter Phenomenology**", submitted by Lopamudra Mukherjee (Roll No - 166121012), a research scholar in the Department of Physics, Indian Institute of Technology Guwahati, for the award of the degree of Doctor of Philosophy, is a record of an original research work carried out by him under my supervision and guidance. The thesis has fulfilled all requirements as per the regulations of the institute and in my opinion has reached the standard needed for submission. The results embodied in this thesis have not been submitted to any other University or Institute for the award of any degree or diploma.

Signed: 

Dr. Soumitra Nandi
Date: 30/09/2021

Acknowledgement

The journey of the five years of the doctoral program has been really exciting and fulfilling. I have received support, assistance and encouragement from many people throughout. First and foremost, I would like to convey my deepest gratitude towards my supervisor, Dr. Soumitra Nandi, whose knowledge, guidance and support has been extremely beneficial. Your insightful and critical feedbacks always helped me to polish up my thinking and brought my work to a better level. His dedication, hard work and immense knowledge always inspires me to learn new things. It was indeed a great learning experience for me throughout.

I am also grateful to my doctoral committee members Dr. Arunansu Sil, Dr. Subhaditya Bhattacharya and Dr. M.C.Kumar for their comments on my progress and research and suggestions whenever needed. I must acknowledge Hemanta Da, Basab Da and other physics office staff for their cooperation with computational and administrative issues. I would also like to thank all the members of the HEP journal club for providing a platform for active discussions on recent topics of HEP. I also congratulate them for keeping the journal club active even during the COVID times by quickly adapting to the online mode yet keeping it as stimulating as before.

I thank all my collaborators and co-authors: Dr. Debasish Borah, Dr. Basabendu Barman, Dr. Aritra Biswas and Dr. Sunando Kumar Patra. Our discussions and exchange of ideas helped me learn a lot from them. I am grateful to Prof. Paolo Gambino, Prof. Ulrich Nierste and Prof Manuel Drees for giving me the opportunity to visit INFN Trieste, Karlsruhe Institute of Technology and University of Bonn and the fruitful discussions. I am also thankful to them for their hospitality and support during my visit. The list of acknowledgement would be incomplete without mentioning all my teachers, Mrs. R. Dutt, Mrs. A. Chatterjee, Prasanta Sir, Dr. Ruma Basu and Dr. Malabika Sengupta who pushed me hard and always encouraged me to give my best under any situation.

The journey of my PhD would not have been as exciting and enjoyable without the company of my close friends Kajal, Suman, Sayandeep, Dibyendu and Abhisek. They kept my spirits high even during the most gloomy days. The hostel life was made dramatic and exciting by my friends and partners-in-crime, Senjuti and Nandita. The close bonds that I made with them during these five years would be cherished lifelong. I was also extremely lucky to have seniors like Srimoy da, Bishu da, Abhijit da, Asmita di, Amit da, Manoj da, Tapo da, Purusottam da and Rishav da with whom I have had long and exciting discussions related to both academic and non-academic stuffs.

The working environment was made enjoyable by my friends and juniors with whom I shared my working space - Ipsita, Madhurima, Arghyajit, Surojit, Devabrat, Suruj, Prantik, Sumit, Esha, Sahabub, Danny, Shafeeque, Rony. I feel lucky to have met Sovan da, Kumar and Charu who have treated me with so much love and care.

Since this thesis is being completed amidst a global pandemic, I must acknowledge every individual who is fighting COVID-19. Together we will come through this. Also, I send my prayers to all those who lost their loved ones.

I want to express my special gratitude to Sayan who has spent long sleepless nights with me while I wrote my thesis. He has always encouraged me and supported me in ways beyond words. Last, but not the least, I would like to convey a very special thanks to my parents and brother for their unconditional love as well as their invaluable support and understanding throughout my academic career. Momma did not live to see me achieve this, but I am sure she would have been very proud to see me here.

Abstract

The Standard Model of particle physics, with all its elegance, has survived most experimental tests at particle accelerators, but not all. This thesis arises in the context of dark matter phenomenology, whose ubiquitous existence cannot be explained within the Standard Model framework. The nature and particle content of dark matter is still a mystery, and proposing suitable models that can explain its properties would be of great value. In this thesis, we perform systematic studies of the phenomenology of dark matter models, focusing on the rich consequences the lepton and quark flavour physics can have for the dark sector. In this regard, we highlight the important observables that play a crucial role in identifying and quantifying possible new physics along with their present experimental status. This sets the essential background of the studies included in the thesis. We then move on to investigate two popular new physics models, the Inert Higgs Doublet model and the $U(1)_X$ extension of SM, that not only gives rise to a suitable DM candidate, but are also motivated by other general issues of the SM, such as light neutrino masses and lepton flavour violation etc. We quantify the contributions from new degrees of freedom to various flavour physics observables such as branching fractions of meson decays, meson-mixings etc. We have displayed the outcome of precise flavour data on the dark matter parameter space while simultaneously explaining some anomalous results in low energy observables. We also highlight some interesting features of these models that allow us to probe our model parameters both in DM and high energy collider experiments using simple cut-based analysis. Further, we have shown how the mediators in WIMP-nucleon scattering can modify elementary quark vertices with the W-boson, which impacts the extraction of the CKM elements. Using the most up-to-date measurements, we successfully constrain the masses and couplings of mediators having scalar or pseudoscalar interactions with the dark matter and SM quarks. In summary, this thesis provides a comprehensive outlook towards the implications of flavour phenomenology on new physics models, with a particular focus on the dark sector.

List of Publications

1. "Correlating the anomalous results in $b \to s$ decays with inert Higgs doublet dark matter and muon $(g-2)$",
   Basabendu Barman, Debasish Borah, **Lopamudra Mukherjee**, Soumitra Nandi,
   $e$print: arXiv: 1808.06639 (hep-ph)
   Published in **Phys.Rev.D 100 (2019) 11, 115010**

2. "Low Scale $U(1)_X$ Gauge Symmetry as an Origin of Dark Matter, Neutrino Mass and Flavour Anomalies",
   Debasish Borah, **Lopamudra Mukherjee** and Soumitra Nandi,
   $e$print: arXiv: 2007.13778 (hep-ph)
   Published in **JHEP 12 (2020) 052**

1. "Constraining New Physics with Possible Dark Matter Signatures from a Global CKM Fit",
   Aritra Biswas, **Lopamudra Mukherjee**, Soumitra Nandi and Sunando Kumar Patra.

List of Conference Proceedings

1. "Flavourful Inert Doublet Dark Matter",
   Lopamudra Mukherjee,
   doi:10.22323/1.390.0404
   Published in **PoS ICHEP2020 (2021), 404**

Contents

List of Figures

List of Tables

Chapter 1

Introduction

Our current understanding of elementary particle physics and its dynamics is best described by the Standard Model (SM) which was formulated way back in 1970. It is a field theoretic description of three of the fundamental forces of nature i.e the strong, weak and electromagnetic forces. Inspite of several efforts, the fourth force of nature, gravity, could not be included in the SM. At the energy scale of sub-atomic particles, the effect of gravity is so negligible that the SM prescription decently works. In this introductory chapter of the thesis, we would like to briefly discuss the basic theoretical framework of the model and reasons to go beyond it.

1.1 The Standard Model of Particle Physics

The SM is a gauge quantum field theory in which all elementary particles are manifestations of quantum fields and the underlying gauge symmetry is $SU(3)_C \times SU(2)_L \times U(1)_Y$. $SU(3)_C$ describes the theory of the strong interaction, also known as the quantum chromodynamics (QCD). The conserved charge corresponding to this gauge group is the 'color' charge and the interactions are mediated by 8 massless gauge bosons called the 'gluons'. The electroweak interactions are described by the unified $SU(2)_L \times U(1)_Y$ gauge group and was first studied by Glashow, Salam and Weinberg [19–22] (which is why it is also referred to as the GSW model). The weak isospin interactions acting only between the left-handed (LH) fermions are described by the $SU(2)_L$ symmetry while the $U(1)_Y$ or the weak hypercharge symmetry distinguishes between the left and right chiral particles. Quantum electrodynamics (QED) or the electromagnetic interactions can be extracted as a sub-group of the larger $SU(2)_L \times U(1)_Y$ group when it is spontaneously broken at low energies to $U(1)_{\text{em}}$. The gauge fields corresponding to the non-Abelian $SU(2)_L$ and the Abelian $U(1)_Y$ symmetries are denoted by W^i_μ ($i = 1, 2, 3$) and B_μ respectively. In addition to the spin-1 mediators, there are 3 generations or families each of spin-$\frac{1}{2}$ fermions which make up all the matter content of the Universe. They are the up & down type quarks and charged & neutral leptons. The particle content is summarized in Table. 1.1. Since parity is maximally violated, the left and right-chiral fields transform differently under the $SU(2)_L \times U(1)_Y$ symmetry. The LH fermions transform as $SU(2)_L$ doublets while the right-handed (RH) ones are singlets under the

Fields			Spin	$SU(3)_C \times SU(2)_L \times U(1)_Y$
Quarks	Q_L	$\begin{pmatrix} u^i_L \\ d^i_L \end{pmatrix}, \begin{pmatrix} c^i_L \\ s^i_L \end{pmatrix}, \begin{pmatrix} t^i_L \\ b^i_L \end{pmatrix}$	$\frac{1}{2}$	$(3,\ 2,\ 1/3)$
	q^u_R	$u^i_R,\ c^i_R,\ t^i_R$		$(3,\ 1,\ 4/3)$
	q^d_R	$d^i_R,\ s^i_R,\ b^i_R$		$(3,\ 1, -2/3)$
Leptons	L_L	$\begin{pmatrix} \nu_{eL} \\ e_L \end{pmatrix}, \begin{pmatrix} \nu_{\mu L} \\ \mu_L \end{pmatrix}, \begin{pmatrix} \nu_{\tau L} \\ \tau_L \end{pmatrix}$	$\frac{1}{2}$	$(1,\ 2, -1)$
	ν_R	Absent		$(1,\ 1,\ 0)$
	ℓ_R	$e_R,\ \mu_R,\ \tau_R$		$(1,\ 1, -2)$
Gauge bosons	Gluons	G^a_μ	1	$(8,\ 1,\ 0)$
	W-bosons	$W^{1,2,3}_\mu$		$(1,\ 3,\ 0)$
	B-Boson	B_μ		$(1,\ 1,\ 0)$
Scalar	Higgs Boson (H)	$\begin{pmatrix} \phi^+ \\ \phi_0 \end{pmatrix}$	0	$(1,\ 2,\ 1)$

Table 1.1: Charge assignment of SM fields under the SM gauge group $SU(3)_C \times SU(2)_L \times U(1)_Y$. Electromagnetic charge is obtained by: $Q = I_3 + \frac{Y}{2}$, where I_3 is the third component of isospin and Y is the $U(1)_Y$ hypercharge quantum number. Here i denote the $SU(3)$ color charges red (r), green (g) and blue (b) and $a = 1, 2, .., 8$ represent the colour charges of gluons.

same gauge group and hence their interactions with the gauge sector also differs. The particle list is rounded off with the massive spin-0 scalar, the Higgs boson which is responsible for generating the mass of all fermions and vector bosons.

The most general form of the SM Lagrangian can be written as

$$\mathcal{L}_{\text{SM}} \;=\; i\bar{\psi}_i \not{D}\psi_i - \frac{1}{4}F^{a\mu\nu}F^a_{\mu\nu} - y_{ij}\bar{\psi}_i\psi_j H + |D_\mu H|^2 - V(H), \tag{1.1}$$

where, D_μ denotes the gauge covariant derivative, $F^a_{\mu\nu}$ is the gauge field strength tensor and $V(H)$ is the scalar potential. The above equation is written using the Feynman slash notation where $\not{A} \stackrel{\text{def}}{=} \gamma^\mu A_\mu$ for a covariant vector A and γ_μ are the Dirac gamma matrices.

The first term of the SM Lagrangian written above illustrate the kinetic interaction of a fermion field (represented by a Dirac spinor ψ) with the gauge bosons. Under the full $SU(3)_C \times SU(2)_L \times U(1)_Y$ symmetry, the covariant derivative is given by

$$D_\mu = \partial_\mu - ig'YB_\mu - i\frac{g}{2}\sigma^a W^a_\mu - i\frac{g_s}{2}\lambda_a G^a_\mu, \tag{1.2}$$

where g', g and g_s are the $U(1)$, $SU(2)$ and $SU(3)$ coupling strengths respectively. Y is the weak hypercharge whch is related to the electromagnetic charge (Q) and the third component of isospin (T_3) as $Q = T_3 + \frac{Y}{2}$. The generators of $SU(2)$ are the three Pauli matrices σ^a ($a = 1, .., 3$) while that of $SU(3)$ are the Gell-Mann matrices λ^a ($a = 1, .., 8$). As is evident from Eqn. (1.2), the kinetic Lagrangian is dependent on the quantum charge assignment of the spinors under the different gauge groups. For example, only the LH weak isodoublets couple to W^a_μ and so the $\sigma^a W^a_\mu$ part of

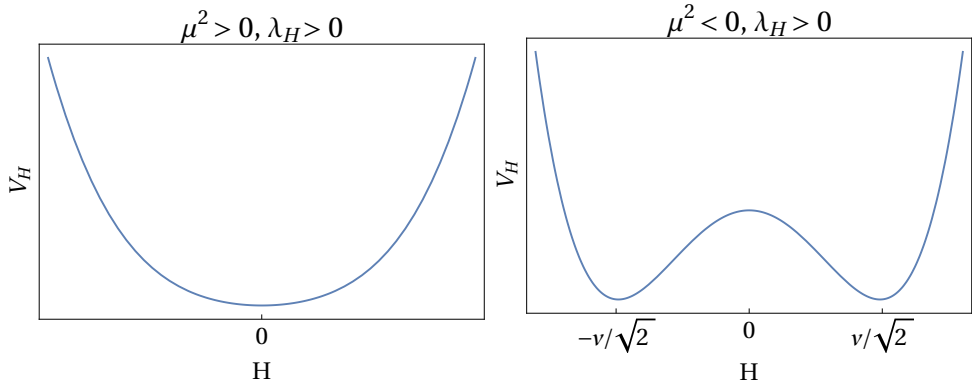

Figure 1.1: The Higgs potential plotted for $\mu^2 > 0$ and $\mu^2 < 0$ showing the spontaneous symmetry breaking of the vacuum.

the covariant derivative will be absent for RH $SU(2)_L$ singlet fields. Also, the coupling with the gluon fields G^a_μ is applicable only for a fermion with $SU(3)$ color i.e for the quarks.

The second term of $\mathcal{L}_{SM}$ is the gauge field Lagrangian and the field stress tensor is given by $F^a_{\mu\nu} = \partial_\mu F^a_\nu - \partial_\nu F^a_\mu + g f_{abc} F^b_\mu F^c_\nu$ for a general gauge field $F(= B, W, G)$ with g being the corresponding coupling strength and f_{abc} are the structure constants. For the Abelian $U(1)_Y$ group, $f_{abc} = 0$; hence, there are no self-interaction terms for the B_μ fields. In presence of f_{abc}, the Lagrangian is also known as the Yang-Mills Lagrangian.

The next part of the Lagrangian is characteristic of the Yukawa interaction of the SM fermions with the Higgs boson where y_{ij} are complex 3×3 matrices. The Yukawa term can be split into different pieces for the quarks and leptons forming the basis of the flavour sector. Further, since H is an $SU(2)_L$ doublet, gauge invariance of the Lagrangian demands that H must couple to one $SU(2)_L$ doublet fermion along with one $SU(2)_L$ singlet field. Following this prescription, the Yukawa Lagrangian was constructed as

$$\mathcal{L}_{\text{Yukawa}} = -\sum_{i,j} \left(y^u_{ij} \overline{Q}_{Li} \widetilde{H} u_{Rj} + y^d_{ij} \overline{Q}_{Li} H d_{Rj} + y^\ell_{ij} \overline{L}_{Li} H \ell_{Rj} + \text{h.c} \right), \tag{1.3}$$

where i, j denote the generation index of the quarks and leptons, $y^{u,d,\ell}_{ij}$ are dimensionless matrices and $\widetilde{H} = i\sigma^2 H^*$. The subscripts L, R stand for left- and right-handed helicities respectively. Note that, due to the absence of right handed neutrinos in the SM, the Higgs does not couple to the neutrinos.

Finally, the last two terms of $\mathcal{L}_{SM}$ make up the scalar Lagrangian of the SM where the first part is the kinetic term and $V(H)$ denotes the Higgs potential which is given by

$$V(H) = \mu^2 \left(H^\dagger H \right) + \lambda_H \left(H^\dagger H \right)^2. \tag{1.4}$$

Here, H is a complex scalar field whose $SU(2)_L$ representation is shown in Tab. 1.1 and λ_H is the strength of the quartic self-interactions among the scalar fields. In order to ensure the stability

of the minimum or the absolute vacuum, λ_H needs to be greater than zero. The SM gauge symmetry do not allow us to write the mass terms of fermions and gauge bosons since such terms are not gauge invariant. So fermions and gauge bosons are massless under the unbroken $SU(2)_L \times U(1)_Y$ symmetry which contradict our observation.

The mass of the SM particles can be generated through spontaneous symmetry breaking (SSB) or the Higgs mechanism [23–25]. In layman's language, symmetry breaking is a phenomenon by which the ground state (or the equillibrium state) of a stable system no longer remains symmetric under the symmetry of its Hamiltonian or Lagrangian. The μ^2 term of the potential plays a crucial role here. If $\mu^2 > 0$, the potential energy has a minimum at $|H| = 0$ as shown in the left plot in Fig. 1.1 which preserves the symmetry of the potential. However, if $\mu^2 < 0$, then $|H| = 0$ no longer remains a stable minimum and is shifted to

$$\langle H \rangle = \sqrt{\frac{-\mu^2}{2\lambda}} \equiv \frac{v}{\sqrt{2}}, \tag{1.5}$$

as shown in the RHS of Fig. 1.1. Due to the symmetry of $V(H)$, there exists an infinite number of degenerate minimum energy states or vacua which satisfies $H^\dagger H = \frac{v^2}{2}$ and the moment we choose a particular vacuum out of the infinite solutions, the symmetry gets "spontaneously broken". In other words the scalar is said to acquire a vacuum expectation value (vev) 'v'. Note that, one is free to choose the direction of the minimum which, for convenience, is chosen along the real axis of H-field. It is convenient to express the Higgs field in the unitary gauge as

$$H = \frac{1}{\sqrt{2}} \begin{pmatrix} 0 \\ h + v \end{pmatrix}, \tag{1.6}$$

where h is the real physical scalar of the Higgs field, discovered as the 125 GeV Higgs particle at the LHC. It can be easily seen that the electromagnetic charge of H using the relation $Q = T_3 + Y/2$ is zero. Hence, as mentioned before, as a result of the spontaneous symmetry breaking (SSB), the $SU(2)_L \times U(1)_Y$ gauge symmetry breaks down to a remnant electromagnetic symmetry $U(1)_{em}$ which is preserved by the vacuum state.

Let us recall the Goldstone theorem, which states that for a physical system with a global symmetry group $\mathcal{G}_1$ which is spontaneously broken down to a subgroup $\mathcal{G}_2$, there is a massless mode corresponding to each broken generator. In the SM, there are 3 Goldstone bosons corresponding to the 3 broken generators which are eaten up to give mass to the 3 physical heavy gauge bosons from the kinetic term as follows :

$$\begin{aligned} (D^\mu H)^\dagger (D_\mu H) &= \left| (\partial_\mu - i\frac{g'}{2} B_\mu - i\frac{g}{2}\sigma^a W_\mu^a) \frac{1}{\sqrt{2}} \begin{pmatrix} 0 \\ h + v \end{pmatrix} \right|^2 \\ &= \frac{v^2}{8} \left(g^2 \left| W_\mu^1 - i W_\mu^2 \right|^2 + (g W_\mu^3 - g' B_\mu)^2 \right). \end{aligned} \tag{1.7}$$

From the above equation, the mass of the W-boson is obtained from the first term as

$$M_W = \frac{1}{2}gv \tag{1.8}$$

where the charged W-boson is defined as $W_\mu^\pm \equiv \frac{1}{\sqrt{2}}(W_\mu^1 \mp iW_\mu^2)$. While it is straightforward to derive the mass of the W-boson from Eqn. (1.8), the mass matrix of the neutral bosons are not diagonal in the (W_μ^3, B_μ) basis as they undergo mixing. In order to obtain their masses, we need to carry out the electroweak rotation as

$$\begin{pmatrix} Z_\mu \\ A_\mu \end{pmatrix} = \begin{pmatrix} c_W & -s_W \\ s_W & c_W \end{pmatrix} \begin{pmatrix} W_\mu^3 \\ B_\mu \end{pmatrix}, \tag{1.9}$$

where $c_W \equiv \cos\theta_W$ and $s_W \equiv \sin\theta_W$, and the weak mixing angle θ_W (also known as the Weinberg angle) is given by:

$$\tan\theta_W = \frac{g'}{g}. \tag{1.10}$$

The physical neutral gauge bosons are therefore defined as

$$Z_\mu \equiv \frac{1}{\sqrt{g^2+g'^2}}(gW_\mu^3 - g'B_\mu), \tag{1.11}$$

$$A_\mu \equiv \frac{1}{\sqrt{g^2+g'^2}}(g'W_\mu^3 + gB_\mu), \tag{1.12}$$

where A_μ is the photon field and their masses are given by

$$M_Z = \frac{1}{2}v\sqrt{g^2+g'^2}, \tag{1.13}$$

$$M_\gamma = 0. \tag{1.14}$$

As expected, the photon remains massless (Eqn. (1.14)) after spontaneous symmetry breaking owing to the unbroken $U(1)_{em}$. Similarly, the eight gluons corresponding to the $SU(3)_c$ gauge symmetry also remain massless due to the unbroken color symmetry.

In addition to the gauge boson masses, the Higgs boson is also responsible for generating the fermion masses. This can be achieved by replacing Eqn. (1.6) into the Yukawa Lagrangian Eqn. (1.3). Considering only the first generation of leptons, the Lagrangian terms featuring its interaction with the Higgs is given by

$$\mathcal{L}_{\text{Yukawa}} \supset -\left[y_e \bar{e}_R H^\dagger L_L + y_e^* \bar{L}_L H e_R\right] \tag{1.15}$$

$$\supset -\left[y_e \bar{e}_R \begin{pmatrix} 0 & \frac{h+v}{\sqrt{2}} \end{pmatrix} \begin{pmatrix} \nu_e \\ e \end{pmatrix}_L + y_e^* \begin{pmatrix} \bar{\nu}_e & e \end{pmatrix}_L \begin{pmatrix} 0 \\ \frac{h+v}{\sqrt{2}} \end{pmatrix} e_R\right] \tag{1.16}$$

$$\supset \quad -\left(\frac{y_e v}{\sqrt{2}}\right)(\bar{e}_R e_L + \bar{e}_L e_R) - \frac{y_e}{\sqrt{2}} h(\bar{e}_R e_L + \bar{e}_L e_R) \tag{1.17}$$

$$\supset \quad -m_e \bar{e} e - \frac{y_e}{\sqrt{2}} h \bar{e} e, \tag{1.18}$$

where $m_e = \left(\frac{y_e v}{\sqrt{2}}\right)$ is the mass of the electron and $\frac{y_e}{\sqrt{2}} \equiv \frac{m_e}{v}$ denotes the strength of the interaction of Higgs with the electron. Hence, in general, one can write the charged lepton masses as

$$m_\ell = \frac{y_\ell v}{\sqrt{2}}. \tag{1.19}$$

Proceeding in a similar fashion as above, one can obtain the mass matrices for the three generations of up and down-type quarks as

$$\mathcal{M}^u_{ij} = \frac{y^u_{ij} v}{\sqrt{2}}, \quad \mathcal{M}^d_{ij} = \frac{y^d_{ij} v}{\sqrt{2}}. \tag{1.20}$$

These matrices are, however, in the generation space (also known as the weak basis). In order to obtain the mass eigenstates i.e. the physical states, we need to diagonalize $\mathcal{M}^{u,d}$ with suitable unitary transformation matrices. Let us consider four different unitary matrices $\mathcal{U}_L, \mathcal{U}_R, \mathcal{D}_L, \mathcal{D}_R$ according to

$$\begin{pmatrix} u_1 \\ u_2 \\ u_3 \end{pmatrix} = \mathcal{U}_{L,R} \begin{pmatrix} u \\ c \\ t \end{pmatrix}_{L,R} \quad \text{and} \quad \begin{pmatrix} d_1 \\ d_2 \\ d_3 \end{pmatrix} = \mathcal{D}_{L,R} \begin{pmatrix} d \\ s \\ b \end{pmatrix}_{L,R}, \tag{1.21}$$

such that it leads to the diagonal quark mass matrices as

$$\mathcal{U}_R^{-1} \mathcal{M}^u \mathcal{U}_L = \text{diag}\,(m_u, m_c, m_t) \;\; \text{and} \;\; \mathcal{D}_R^{-1} \mathcal{M}^d \mathcal{D}_L = \text{diag}\,(m_d, m_s, m_b) \tag{1.22}$$

where u, c, t, d, s, b are the quark mass eigenstates while u_i, d_i are the weak states. The diagonalizing matrices also diagonalize the quark Yukawa matrices $y^{u,d}_{ij}$ which generates the $h\bar{q}q$ couplings as $y_q = \frac{m_q}{v}$ in the quark mass basis.

Since we have rotated the up-type quarks of the quark doublet by $\mathcal{U}_L$ and the down-type quarks by a different matrix $\mathcal{D}_L$, the mass eigenstates of the down-type quarks no longer match that of the up-type quarks. Also, the left-chiral and right-chiral fields are rotated by different amounts. The effect of such mismatch shows up in the charged-current (CC) interaction Lagrangian given by

$$\mathcal{L}_{cc} \supset -\frac{g}{\sqrt{2}} \sum_{i=1}^{3} (\bar{u}_{Li} \gamma^\mu W^+_\mu d_{Li} + \bar{d}_{Li} \gamma^\mu W^-_\mu u_{Li}). \tag{1.23}$$

We have already seen that the u_i, d_i fields belong to the weak basis and are not the physical mass eigenstates. Therefore, using Eqn. (1.22), it is more convenient to write the charged-current inter-

action in terms of the mass eigenstates as

$$\mathcal{L}_{cc} \supset -\frac{g}{\sqrt{2}}\begin{pmatrix}\bar{u} & \bar{c} & \bar{t}\end{pmatrix}_L \mathcal{U}_L^\dagger \gamma^\mu W_\mu^+ \mathcal{D}_L \begin{pmatrix} d \\ s \\ b \end{pmatrix}_L + h.c. \tag{1.24}$$

$$= -\frac{g}{\sqrt{2}}\begin{pmatrix}\bar{u} & \bar{c} & \bar{t}\end{pmatrix}_L \gamma^\mu W_\mu^+ \mathbf{V_{CKM}} \begin{pmatrix} d \\ s \\ b \end{pmatrix}_L + h.c. \tag{1.25}$$

where $V_{\text{CKM}} = \mathcal{U}_L^\dagger \mathcal{D}_L$ is a general 3×3 complex matrix. This shows that due to the bi-unitary transformations of the quark mass matrices, any up-type quark couples to any other down type quark resulting in quark mixing or "*flavour*" mixing which is an essential ingredient of this thesis. This phenomenon was first studied by Cabibbo [26] for two generations of quarks and later extended by Kobayashi and Maskawa [27] for 3 quark generations resulting in the name "CKM matrix" for V_{CKM} after their initials. The CKM matrix is unitary

$$V_{CKM}^\dagger V_{CKM} = (\mathcal{U}_L^\dagger \mathcal{D}_L)^\dagger (\mathcal{U}_L^\dagger \mathcal{D}_L) = \mathcal{D}_L^\dagger \mathcal{U}_L \mathcal{U}_L^\dagger \mathcal{D}_L = \mathbb{1}, \tag{1.26}$$

and can be parametrized by four independent parameters : three mixing angles and one phase. It is interesting to note that all the CP violation in the quark sector arise from this unremovable phase of the quark-mixing matrix which was pointed out by Kobayashi and Maskawa in 1973. The general form of the matrix parametrization is given by

$$V_{CKM} \equiv \begin{pmatrix} V_{ud} & V_{us} & V_{ub} \\ V_{cd} & V_{cs} & V_{cb} \\ V_{td} & V_{ts} & V_{tb} \end{pmatrix} = \begin{pmatrix} c_{12}c_{13} & s_{12}c_{13} & s_{13}e^{-i\delta} \\ -s_{12}c_{23} - c_{12}s_{23}s_{13}e^{-i\delta} & -c_{12}c_{23} - s_{12}s_{23}s_{13}e^{-i\delta} & s_{23}c_{13} \\ s_{12}s_{23} - c_{12}c_{23}s_{13}e^{-i\delta} & -c_{12}s_{23} - s_{12}c_{23}s_{13}e^{-i\delta} & c_{23}c_{13} \end{pmatrix} \tag{1.27}$$

where $s_{ij} \equiv \sin\theta_{ij}$, $c_{ij} \equiv \cos\theta_{ij}$ and δ is the CP violating phase. In 1983, Wolfenstein proposed a more convenient parametrisation [28] of the CKM matrix which took into account the fact that there is a certain hierarchy in the mixing angles, viz. $s_{13} << s_{23} << s_{12} << 1$. This hierarchy is expressed by orders of λ ($= \sin\theta_{12}$ where θ_{12} is the Cabibbo angle) and is given by

$$V_{CKM} = \begin{pmatrix} 1-\frac{\lambda^2}{2} & \lambda & A\lambda^3(\rho - i\eta) \\ -\lambda & 1-\frac{\lambda^2}{2} & A\lambda^2 \\ A\lambda^3(1-\rho-i\eta) & -A\lambda^2 & 1 \end{pmatrix} + \mathcal{O}(\lambda^4). \tag{1.28}$$

The diagonal elements are close to unity and the magnitude of the off-diagonal ones decrease with increasing distance from the diagonal. The hierarchy is expresed in terms of the quantities :

$$\lambda^2 = \frac{|V_{us}|^2}{|V_{ud}|^2 + |V_{us}|^2}, \quad A^2\lambda^4 = \frac{|V_{cb}|^2}{|V_{ud}|^2 + |V_{us}|^2}, \quad \bar{\rho} + i\bar{\eta} = -\frac{V_{ud}V_{ub}^*}{V_{cd}V_{cb}^*} \tag{1.29}$$

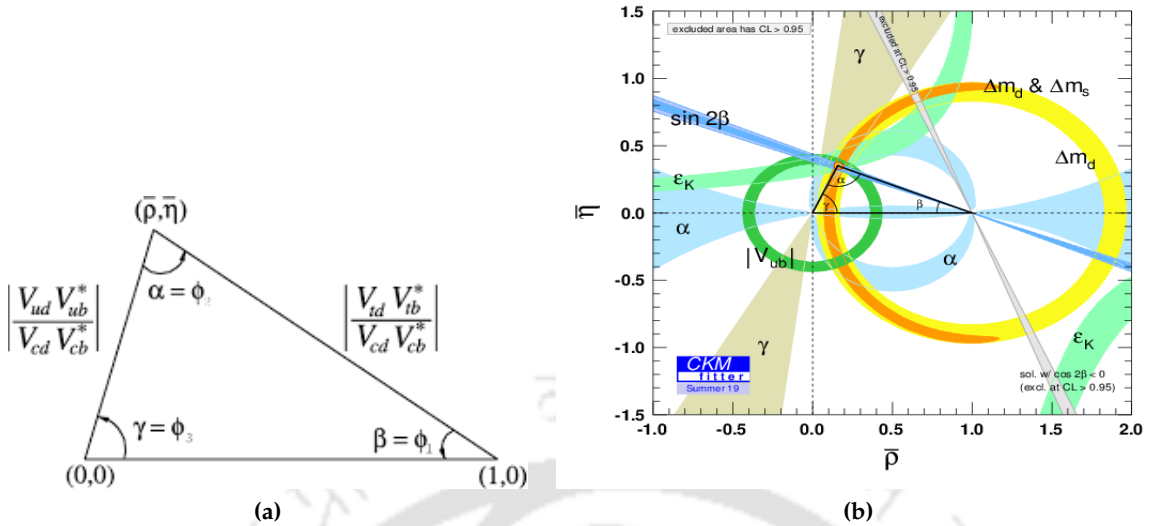

(a) (b)

Figure 1.2: (a) A schematic sketch of the Unitarity Triangle. Figure taken from [1]. (b) Constraints in the $(\bar{\rho}, \bar{\eta})$ plane of the UT. The red hashed region of the latest global combination by the CKMFitter group corresponds to 68% CL. Figure taken from [2].

where $\bar{\rho}, \bar{\eta}$ are related to ρ, η as

$$\rho + i\eta = \frac{\sqrt{1 - A^2\lambda^4}(\bar{\rho} + i\bar{\eta})}{\sqrt{1 - \lambda^2}\,[1 - A^2\lambda^4(\bar{\rho} + i\bar{\eta})]}. \tag{1.30}$$

The allowed region of the Wolfenstein parameters can be magnificently represented in the $(\bar{\rho}, \bar{\eta})$ plane in terms of a rescaled Unitarity Triangle (UT) using the unitarity conditions (1.26) as shown in Fig. 1.2a. There can be six such triangles having the same area $J/2$, where, J is the Jarlskog invariant defined as

$$J \equiv |\mathfrak{Im}(V_{i\alpha}V_{j\beta}V^*_{i\beta}V^*_{j\alpha})| = \lambda^6 A^2 \bar{\eta}, \quad (i \neq j, \alpha \neq \beta). \tag{1.31}$$

The Jarlskog invariant is directly proportional to the CP violating phase η and hence is a measure of the CP violation in the SM. The sides of the UT are given by

$$R_u = \left|\frac{V_{ud}V^*_{ub}}{V_{cd}V^*_{cb}}\right| = \sqrt{\bar{\rho}^2 + \bar{\eta}^2} \;\text{ and }\; \mathrm{R_t} = \left|\frac{\mathrm{V_{td}V^*_{tb}}}{\mathrm{V_{cd}V^*_{cb}}}\right| = \sqrt{(1-\bar{\rho}^2) + \bar{\eta}^2} \tag{1.32}$$

with the third side scaled to unity. The three angles of the triangle are given by

$$\alpha \equiv \phi_2 = \arg\left(-\frac{\mathrm{V_{td}V^*_{tb}}}{\mathrm{V_{ud}V^*_{ub}}}\right), \;\; \beta \equiv \phi_1 = \arg\left(-\frac{\mathrm{V_{cd}V^*_{cb}}}{\mathrm{V_{td}V^*_{tb}}}\right), \;\; \gamma \equiv \phi_3 = \arg\left(-\frac{\mathrm{V_{ud}V^*_{ub}}}{\mathrm{V_{cd}V^*_{cb}}}\right) \tag{1.33}$$

with

$$\begin{aligned} &\cos\gamma = \bar{\rho}/R_u, \quad \sin\gamma = \bar{\eta}/R_u \\ &\cos\beta = (1-\bar{\rho})/R_t, \quad \sin\beta = \bar{\eta}/R_t \end{aligned} \tag{1.34}$$

$$\alpha = \pi - \beta - \gamma.$$

Fig. 1.2b depicts the constraints in the complex $(\bar{\rho}, \bar{\eta})$ plane of the UT. We will discuss more about the CKM matrix and constraints on the parameters from different sources in the coming sections as this is one of the relevant topic of discussion of this thesis.

In passing we would like to mention that it is often convenient to rotate only the down-type quark flavours to their mass eigenstates while keeping the basis of the up-type intact because it is not possible to extract both $\mathcal{U}$ and $\mathcal{D}$ matrices simultaneously from experiments. One can only find out their combination represented by the CKM matrix. Hence one can choose $\mathcal{U} = \mathbb{1}$ without loss of generality.

Let us now take a look at the neutral current (NC) interactions in the SM. The interaction Lagrangian involving the fermion and the neutral gauge boson Z can be written in the general form as

$$\mathcal{L}_{nc} = -\frac{g}{c_W} \sum_{i=1}^{3} \bar{\psi}_{iL(R)} \gamma^\mu (T_3 - Q s_W^2) \psi_{iL(R)} Z_\mu \tag{1.35}$$

where $\psi_i (= u_i, d_i, \ell_i, \nu_i)$ is a general quark or lepton spinor. In the SM, the Z-boson couplings are universal i.e they are same for each of the three generations of fermions since it is only a function of the third component of isospin T_3 and the electromagnetic charge Q. Therefore, for the LH down-type quarks, one can write

$$\mathcal{L}_{nc} \supset -\frac{g}{c_W} \begin{pmatrix} \bar{d}_1 & \bar{d}_2 & \bar{d}_3 \end{pmatrix}_L \gamma^\mu \left(-\frac{1}{2} + \frac{1}{3} s_W^2 \right) \begin{pmatrix} d_1 \\ d_2 \\ d_3 \end{pmatrix}_L Z_\mu \tag{1.36}$$

$$\supset -\frac{g}{c_W} \left(-\frac{1}{2} + \frac{1}{3} s_W^2 \right) \begin{pmatrix} \bar{d} & \bar{s} & \bar{b} \end{pmatrix}_L \mathcal{D}_L^\dagger \gamma^\mu \mathcal{D}_L \begin{pmatrix} d \\ s \\ b \end{pmatrix}_L Z_\mu \tag{1.37}$$

$$= -\frac{g}{c_W} \left(-\frac{1}{2} + \frac{1}{3} s_W^2 \right) \bar{q}_d \gamma^\mu P_L q_d Z_\mu \tag{1.38}$$

where $q_d = (d, s, b)$ and $P_{L,R} = \frac{1 \mp \gamma^5}{2}$ are the chirality projection operators. Therefore, it is clear that the neutral current interaction is flavour diagonal when the couplings are generation-independent. One can follow the same method to work out the neutral current interactions of the up-quarks as well as the leptons. A similar logic also follows in case of the electromagnetic interactions whose strength of interaction with the fermions are also universal (proportional to the electromagnetic coupling $e = g s_W = g' c_W$). Hence, "*flavour changing neutral currents*" (FCNCs) are naturally forbidden in the SM which is one of the many successes of this theory. It is quite intriguing to note that in the SM with just the three light quarks u, d and s, both neutral and charged current interactions would allow flavour changing and strangeness changing ($\Delta S = 1$) processes to take place. However, the non-observation of such decays (e.g $K_L \to \mu^+ \mu^-$) in experiments made Glashow, Iliopoulos and Maiani (GIM) propose the existence of a fourth flavour of quark, the "charm" quark, as a solution to this problem [29, 30]. The GIM mechanism, conceived in 1968, later became an

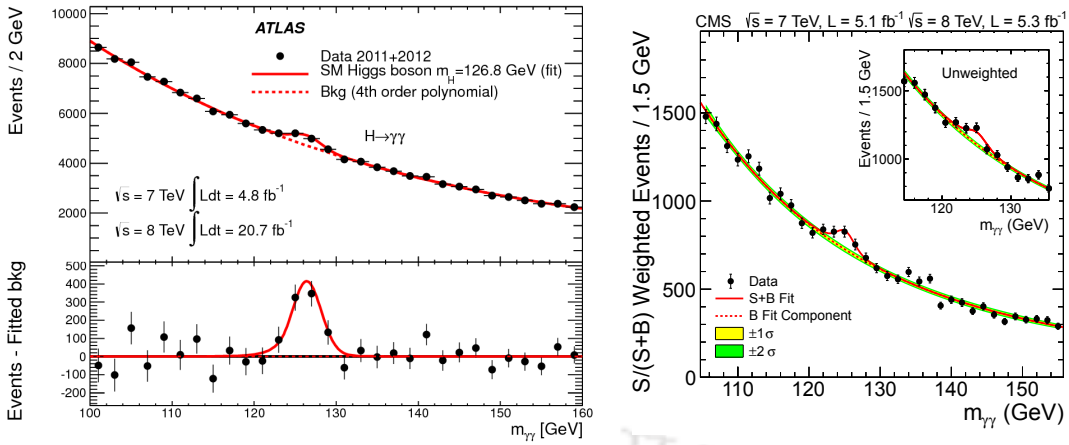

Figure 1.3: The number of diphoton signal events as a function of the invariant diphoton mass distribution as obtained by ATLAS [3] and CMS [4] experiments at CERN. The bump in the signal seen at $m_{\gamma\gamma} \sim 126$ GeV shows that this comes from the Higgs boson and is considered to be the greatest discovery of the last decade.

essential tool in the developement of the electroweak theory by Glashow, Weinberg and Salam in order to naturally suppress FCNC and $\Delta S = 2$ transitions at the tree level. In the SM, such processes occur only at the one-loop level and are therefore very important probes of physics beyond the SM. The success of the CKM and GIM mechanisms can be attributed to the observation of CP violation in Kaon decays in 1964 [31] and subsequent discovery of charm quark in 1974 [32, 33].

The mixing phenomenology in the leptonic sector is much less complicated than the quark sector since the charged current interactions are diagonal both in the weak basis as well as in the mass eigenstate basis of the leptons. For example, one can, in general, diagonalize the lepton mass matrices using 3×3 matrices in a similar fashion as Eqn. (1.21)

$$e_{L\alpha} = \mathcal{V}_L e_{Li} \quad \text{and} \quad e_{R\alpha} = \mathcal{V}_R e_{Ri} \tag{1.39}$$

where $\alpha = e, \mu, \tau$ are the flavour indices while $i = 1, 2, 3$ are the generation indices in the mass basis. The leptonic charged current interaction can be written as

$$\mathcal{L}_{cc} \supset \frac{g}{\sqrt{2}} \bar{\nu}_{L\alpha} \gamma^\mu \ell^-_{L\alpha} W^+_\mu + h.c. \tag{1.40}$$

$$= \frac{g}{\sqrt{2}} \bar{\nu}_{L\alpha} \gamma^\mu \mathcal{V}_L \ell^-_{Li} W^+_\mu + h.c. \tag{1.41}$$

Now since neutrinos are massless, one can always rotate the neutrino fields and define them as

$$\nu_{L\alpha} = \mathcal{V}_L \nu_{Li} \tag{1.42}$$

such that the charged current interaction Eqn. (1.40) would still remain diagonal. The leptons also participate in neutral current interaction similar to the quarks.

The hunt for elementary particles of nature began with the discovery of electron in the late 19th century and the SM was deemed to be complete with the detection of the Higgs boson in 2012 at the Large Hadron Collider (LHC) at CERN [3, 4]; see Fig. 1.3. However, there are many inconsis-

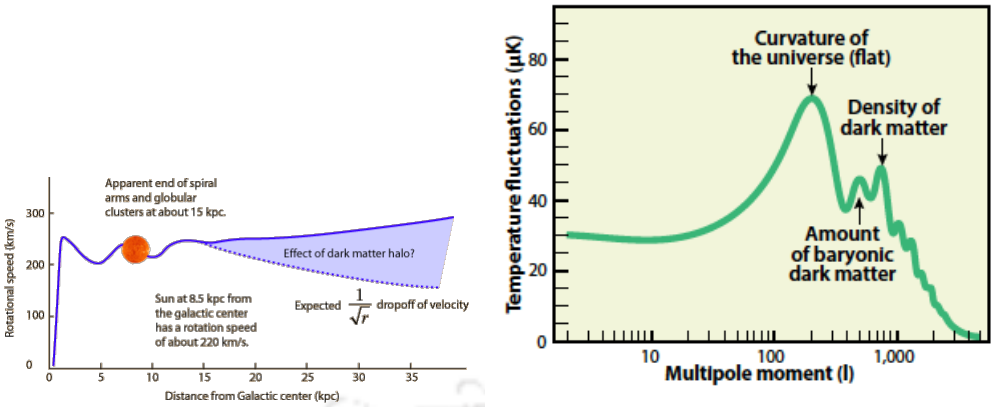

(a) (b)

Figure 1.4: (a) : A schematic diagram of the rotational velocity of stars in the Milky Way galaxy. The dotted line is the expected Newtonian nature of the velocity distribution while data (solid line) suggests a flat curve even at large distances from the galactic centre signifying the role of the DM halo. Fig taken from [5]. (b) : The first three peaks of the CMB anisotropy spectrum explained. Courtesy : Astronomy: Roen Kelly, after Wayne Hu.

tencies in the theory and there are many experimental facts that cannot be addressed within the framework of the SM. Inspite of being so far the best theoretical foundation to explain the interactions of nature, there is a need to go beyond it. In the subsequent sections we will elaborate on the shortcomings of the SM and motivate the need to formulate theories beyond the SM (BSM).

1.2 Need For Beyond the Standard Model

In this section, we are going to briefly summarize some of the pressing issues of the SM theory which would also be relevant for the thesis.

It is now a well established fact that about 27% of the total energy density of the Universe is comprised of a non-luminous and non-baryonic form of matter known as the "*dark matter*" (DM). The first conjecture regarding its existence was made by Fritz Zwicky in 1930's while estimating the mass of the Coma cluster [34]. He reported a mismatch of ~ 100 times between the gravitional mass of the cluster calculated using virial theorem and the total luminous mass. He referred to the missing mass as "*Dunkle materie*" or dark matter. However, his observations were greatly ignored until the 1970s when Vera Rubin [35] reported similar observations within the galaxies themselves. She observed that the velocities of visible objects, like stars and gas, does not follow the usual Newtonian mechanics, according to which, the velocity should decrease as $v \propto r^{1/2}$ (where r is the distance from the center of the galaxy). As a matter of fact, the rotational velocity curve flattens out at distances much larger than the galactic radius as depicted in Fig. 1.4a. This has been observed in all galaxies including our own Milky Way. Although there are ample evidences of the presence of DM coming from astrophysical and cosmological observations, no particle candidate for it has been found yet. Hence, it remains one of the most exciting open questions in physics till date.

The Cosmic Microwave Background (CMB) plays a very important role in quantifying the abundance of the dark matter in the present Universe. The CMB radiation is characterized by

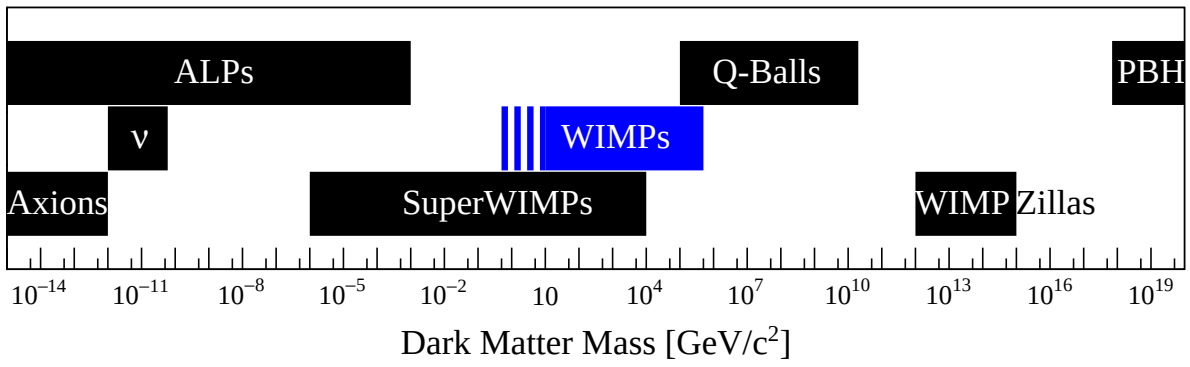

Figure 1.5: A schematic diagram showing the different classes of dark matter candidates depending upon the mass of DM. Fig. taken from [6]

a uniform black body spectrum at a temperature of 2.73 K with the anisotropy being at the level of 10^{-5}. COBE [36], WMAP [37], Planck [17] satellites have been imaging the fluctuations in the CMB temperature over the entire sky over different angular scales which is represented by the power spectrum shown in Fig. 1.4b. Using the ΛCDM cosmological model, it is possible to fit the CMB power spectrum with parameters such as the energy density of different matter components and radiation. The most recent data by Planck suggests that the present day abundance of dark matter in the Universe is [17]

$$\Omega_{DM}h^2 = \frac{\rho_{DM}}{\rho_c} = 0.120 \pm 0.001 \tag{1.43}$$

where $h = H_0/(100\ \text{kms}^{-1}\text{Mpc}^{-1})$, is the present day normalized Hubble expansion rate (H_0) of the Universe, while ρ_{DM} and $\rho_c = \frac{3H_0^2}{8\pi G}$ are the DM density and the critical density of the Universe respectively.

The mere fact that dark matter needs to be massive matter particles which experience gravitational force and weakly interact with other particles makes our lives complicated since the SM does not account for any such particle in its list. This has led to several beyond the Standard Model (BSM) proposals which can successfully explain DM in the Universe. Fig. 1.5 is a schematic diagram showing the different possible DM candidates along with their typical mass ranges. Among different BSM prescriptions, the paradigm with a generic weakly interacting massive particle (WIMP) is well motivated. In such scenarios, the DM particle has mass and interactions typically around the electroweak ballpark and can give rise to the correct dark matter relic abundance, a remarkable coincidence often referred to as the "*WIMP Miracle*". For some comprehensive reviews/articles on particle dark matter and WIMPs, see [6, 38–43].

Another reason for much dispute in the scientific community was due to the fact that neutrinos are the only fermions which are massless in the SM. Ever since the first hint that neutrinos might have mass came from the Homestake experiment [44] by Raymon Davis Jr. and collaborators during 1970, there has been significant evolution of neutrino phenomenology beyond the SM. The scientists observed a reduction in the solar neutrino flux compared to the theoretically calculated one. However, the results were not compelling enough at that moment. Later, in June 1998, the Super-Kamiokande collaboration reported the observation of a deficit in the detected atmospheric

neutrino flux compared to the expected flux providing strong evidence for neutrino oscillations [45]. This paved the way for a whole new area of research and was enough for scientists to believe that the SM needs to be extended. We now know that neutrinos not only have non-zero mass but different flavours of neutrinos mix with each other and over time change from one flavour to another. At present the best estimate of the neutrino oscillation parameters from a fit to the global data is summarized in Fig. 1.6. There are quite a few theoretical models which succesfully generate tiny neutrino masses at or beyond tree level. The most popular one is the tree-level seesaw mechanism [46–53] and its variants [54–58] as well as some mechanisms to generate neutrino mass at the one loop level [59–63]. However, many other questions related to neutrino physics still remain a mystery. For example, there is no concrete answer as to why the neutrino masses are so small or why there is a hierarchy in the masses and mixing angles; we do not know whether neutrinos are Dirac or Majorana fermions or whether there is CP violation in the lepton sector similar to the quark sector. Therefore it is not only important to ramp up experimental efforts in order to find answers to these questions but to also develop unique theoretical description of the non-trivial lepton Yukawa structure.

Amusingly, SM neutrinos were once considered to be the solution to the dark matter problem since they are massive, electrically neutral and are weakly interacting with other particles. However, the formation of the observed large scale structures depends a lot on the velocity of the dark matter particles at the time of the beginning of structure formation. The rest mass of neutrinos are so small that it would have been extremely relativistic ("hot") at the onset of structure formation that would wash out the anisotropies and prevent the growth of small-scale structures. This is contrary to what is observed in the Universe and hence the dark matter needs to be non-relativistic ("cold"). There is a possibility of the existence of exotic new types of neutrinos, such as sterile neutrinos or heavy Majorana neutrinos, which are also motivated from the point of view of small active neutrino masses inferred from neutrino oscillation. For a nice and comprehensive review on neutrino physics, see [64].

Another important issue that the SM cannot provide an answer for is the fact that there is a huge abundance of matter over antimatter in the present Universe also known as the baryogenesis problem. The baryon-to-photon ratio, defined as

$$\eta_B \equiv \frac{n_B - n_{\bar{B}}}{n_\gamma}, \tag{1.44}$$

is measured to be $\sim 6 \times 10^{-10}$ in the present Universe from Big-Bang Nucleosynthesis (BBN) [65] and CMB data [66]. Here, $n_B, n_{\bar{B}}$ and n_γ denote the number densities of baryons, antibaryons and photons, respectively. However, it is expected that when the Universe started with a Big Bang, equal amounts of matter (baryons) and antimatter (antibaryons) were produced. Hence there must be some dynamical evolution due to which we are left only with matter particles at present times. This was first realized by Sakharov in 1967 [67] and he suggested that in order to succesfully explain the baryon asymmetry of the Universe, the following conditions need to be satisfied : (i) baryon number violation, (ii) C and CP violation and (iii) loss of thermal equillibrium. The SM has

NuFIT 5.0 (2020)

		Normal Ordering (best fit)		Inverted Ordering ($\Delta\chi^2 = 2.7$)	
		bfp $\pm 1\sigma$	3σ range	bfp $\pm 1\sigma$	3σ range
without SK atmospheric data	$\sin^2\theta_{12}$	$0.304^{+0.013}_{-0.012}$	$0.269 \to 0.343$	$0.304^{+0.013}_{-0.012}$	$0.269 \to 0.343$
	$\theta_{12}/^\circ$	$33.44^{+0.78}_{-0.75}$	$31.27 \to 35.86$	$33.45^{+0.78}_{-0.75}$	$31.27 \to 35.87$
	$\sin^2\theta_{23}$	$0.570^{+0.018}_{-0.024}$	$0.407 \to 0.618$	$0.575^{+0.017}_{-0.021}$	$0.411 \to 0.621$
	$\theta_{23}/^\circ$	$49.0^{+1.1}_{-1.4}$	$39.6 \to 51.8$	$49.3^{+1.0}_{-1.2}$	$39.9 \to 52.0$
	$\sin^2\theta_{13}$	$0.02221^{+0.00068}_{-0.00062}$	$0.02034 \to 0.02430$	$0.02240^{+0.00062}_{-0.00062}$	$0.02053 \to 0.02436$
	$\theta_{13}/^\circ$	$8.57^{+0.13}_{-0.12}$	$8.20 \to 8.97$	$8.61^{+0.12}_{-0.12}$	$8.24 \to 8.98$
	$\delta_{\rm CP}/^\circ$	195^{+51}_{-25}	$107 \to 403$	286^{+27}_{-32}	$192 \to 360$
	$\frac{\Delta m^2_{21}}{10^{-5}\ \text{eV}^2}$	$7.42^{+0.21}_{-0.20}$	$6.82 \to 8.04$	$7.42^{+0.21}_{-0.20}$	$6.82 \to 8.04$
	$\frac{\Delta m^2_{3\ell}}{10^{-3}\ \text{eV}^2}$	$+2.514^{+0.028}_{-0.027}$	$+2.431 \to +2.598$	$-2.497^{+0.028}_{-0.028}$	$-2.583 \to -2.412$
		Normal Ordering (best fit)		Inverted Ordering ($\Delta\chi^2 = 7.1$)	
		bfp $\pm 1\sigma$	3σ range	bfp $\pm 1\sigma$	3σ range
with SK atmospheric data	$\sin^2\theta_{12}$	$0.304^{+0.012}_{-0.012}$	$0.269 \to 0.343$	$0.304^{+0.013}_{-0.012}$	$0.269 \to 0.343$
	$\theta_{12}/^\circ$	$33.44^{+0.77}_{-0.74}$	$31.27 \to 35.86$	$33.45^{+0.78}_{-0.75}$	$31.27 \to 35.87$
	$\sin^2\theta_{23}$	$0.573^{+0.016}_{-0.020}$	$0.415 \to 0.616$	$0.575^{+0.016}_{-0.019}$	$0.419 \to 0.617$
	$\theta_{23}/^\circ$	$49.2^{+0.9}_{-1.2}$	$40.1 \to 51.7$	$49.3^{+0.9}_{-1.1}$	$40.3 \to 51.8$
	$\sin^2\theta_{13}$	$0.02219^{+0.00062}_{-0.00063}$	$0.02032 \to 0.02410$	$0.02238^{+0.00063}_{-0.00062}$	$0.02052 \to 0.02428$
	$\theta_{13}/^\circ$	$8.57^{+0.12}_{-0.12}$	$8.20 \to 8.93$	$8.60^{+0.12}_{-0.12}$	$8.24 \to 8.96$
	$\delta_{\rm CP}/^\circ$	197^{+27}_{-24}	$120 \to 369$	282^{+26}_{-30}	$193 \to 352$
	$\frac{\Delta m^2_{21}}{10^{-5}\ \text{eV}^2}$	$7.42^{+0.21}_{-0.20}$	$6.82 \to 8.04$	$7.42^{+0.21}_{-0.20}$	$6.82 \to 8.04$
	$\frac{\Delta m^2_{3\ell}}{10^{-3}\ \text{eV}^2}$	$+2.517^{+0.026}_{-0.028}$	$+2.435 \to +2.598$	$-2.498^{+0.028}_{-0.028}$	$-2.581 \to -2.414$

Figure 1.6: The figure summarizes the present status of the light neutrino masses and mixings for normal and inverted hierarchy scenarios from a global analysis of neutrino oscillation measurements by the νFIT Collaboration [7, 8]

all the ingredients of successfull generation of the above conditions. Baryon number is violated through triangle anomalies, CP violation occurs during quark mixing and out-of-equillibrium condition is achieved during electroweak phase transition [68]. However, the amount of CP violation is many orders of magtinude smaller than what is required in order to explain the observed asymmetry. Therefore, it fails to provide a solution to this problem and we need to go beyond it.

There are individual solutions to each of these issues and many BSM scenarios also solve more than one problem at a time. There are many other drawbacks such as the Higgs vacuum stability problem [69–71], the hierarchy problem, gauge coupling unification issue [72] etc. which are complications related to the theoretical formulation of the SM and require modifications to the theory. The general proposals include extension of either the SM gauge symmetry or addition of new particles to the spectrum within the SM gauge group. However, the need of the hour is not only to extend the theoretical framework of the SM but to also validate it in experiments. Unfortunately, there has been no other direct detection of new particles at LHC or other colliders in the last decade barring that of the Higgs boson. Direct detection experiments of dark matter particles have also produced null results, thereby producing more and more stringent upper bounds on the WIMP-nucleon scattering cross-sections. The much sought-after heavy neutrinos, required in order to explain the tiny neutrino masses, have also not been found. Under such circumstances, it is highly motivating to adopt an alternate avenue through which one can look for new physics (NP) via tiny deviations from SM expections in low energy experiments. In recent times, this approach has been further facilitated by the precisions of the theoretical predictions and experimental measurements. This is precisely where "flavour physics" plays a crucial role and has been pivotal in the discovery of physics beyond the Standard Model.

1.3 Relevance of Flavour Physics

The foundations of flavour physics is embedded in the Yukawa structure of the SM as discussed in sec. 1.1. It is interesting to see that in absence of the Yukawa terms, there exists a global $U(3)^5$ symmetry or "*flavour symmetry*" for a total of 5 fermion families (Q_L, u_R, d_R, L_L, e_R) with 3 copies (generations) of each field. The Yukawa Lagrangian in Eqn. (1.3) explicitly breaks the flavour symmetry in the SM by introducing a hierarchy in the fermion masses, a separation between up and down type quarks and mixing between different generations of quarks. The residual symmetry allow us to rotate the quark fields in a way such that only one of the two quark-mass matrices is diagonal (CKM mechanism discussed earlier).

The SM has emerged through both theoretical and experimental discoveries spanning the last couple of decades. Also, it has been extensively tested and reaches a point of highest development after the discovery of Higgs. In this development, flavour physics has played a central role. As discussed earlier, the CKM mixing matrix in charged weak interactions represents the single source of CP violation in the quark sector. The FCNCs have also played an essential role in indicating the key pieces of evidence of the existence of charm quark, weak gauge bosons and top quark even before their discovery. The CKM mechanism's success was that it could predict a large set

of physical phenomena spread over a massive energy scale from nuclear decays to the top quark mass with an economical set of only four independent parameters. Despite these successes, the SM fails in some key aspects, which has been discussed in the last subsection. The extensions of the SM are expected to address these issues by introducing new degrees of freedom beyond the SM. New particles or interactions introduced at a high scale could have a related shorter-distance interaction. Therefore, apart from the direct searches at the colliders, low energy observables will play an essential role in the indirect detection of the new particles through deviations from the respective SM predictions.

In the SM, the tree-level processes are mediated by charged current interactions, and the decay rates are directly sensitive to the square of the CKM elements. On the other hand, the FCNC processes are loop suppressed in the SM, and the corresponding amplitudes are sensitive to the product of CKM elements. Due to its simple and constrained structure in the SM, the weak processes are potentially sensitive to new interactions beyond the SM and therefore, can be a potent probe of models beyond the SM. It is necessary to measure the CKM parameters very precisely, and during the last few decades extensive research has been performed at the BaBar, Belle and LHCb experiments. High-luminosity experiments like Belle-II has also become operational and within a few years we will expect a wealth of precise data which could be useful to put constraints on new physics model parameters. Siginificant development has been made on the theory side as well. As for example, precise predictions on the non-perturbative parameters like form-factors, decay constants, bag-factors etc. are available from lattice QCD. In the following, we breifly review the main experimental constraints on the relevant parameters of the CKM unitarity triangle which will be later relevant for discussions present in the thesis.

Both the $\Delta F = 1$ decays as well as $\Delta F = 2$ meson mixing processes provide important constraints on the Wolfenstein parameters. Here F denotes the flavour quantum number which is changing during the process. The $\Delta F = 1$ processes may involve both tree or loop level leptonic, semileptonic decays as well as hadronic decays. Direct measurements of the elements of the first two rows of the CKM matrix are available. The precise determination of the Fermi constant G_F from muon decay [73] has been quite instrumental in facilitating the absolute determination of the magnitude of the CKM elements. The first element of the matrix, V_{ud} is most precisely determined from the super-allowed $0^+ \to 0^+$ nuclear beta decays [74, 75]

$$|V_{ud}| = 0.97420(21). \tag{1.45}$$

Although the semileptonic electroweak process $\pi^+ \to \pi^0 e^+ \nu_e$, is by far the most theoretically clean probe of $|V_{ud}|$, the tiny branching fraction $\mathcal{O}(10^{-8})$ makes it difficult to achieve the precise determination of $|V_{ud}|$ unless statistically large amount of data are collected. The knowledge of $|V_{ud}|$ from neutron beta-decay experiments are not very reliable since the mean-life of the neutron measured from two different methods yield different results and hence cannot be meaningfully averaged. The leptonic and semileptonic Kaon decays are known as the "*golden modes*" of extraction of CKM elements. The K_{ℓ_3} processes $K_L^0 \to \pi^\pm \ell \nu_\ell$ and $K^+ \to \pi^0 \ell \nu_\ell$ are traditionaly used in

the determination of the quantity [76]

$$|V_{us}|f_+(0) = 0.2165(4). \tag{1.46}$$

The leptonic modes $K \to \mu\nu(\gamma)$ and $\pi \to \mu\nu(\gamma)$ (known as the K_{ℓ_2} and π_{ℓ_2} decays respectively), on the other hand, help us to obtain the ratio $\frac{|V_{us}|}{|V_{ud}|}\frac{f_{K^+}}{f_{\pi^+}}$. The only source of uncertainty in leptonic decays come from the decay constant measurements. Hence, the precise extraction of V_{us} requires the accurate determination of the hadronic quantities like the Kaon and pion decay constants f_K, f_π and the semileptonic form factor at zero momentum transfer $f_+(0)$, all of which, can be obtained using lattice QCD techniques [77]. Recently there has been an emerging tension between the absolute values V_{us} coming from different sources [78]. They are : (i) V_{us} from $K_{\ell 3}$ decays using the knowledge of $f_+(0)$, (ii) V_{us} from the ratio $(V_{us}/V_{ud})^{K_{\ell 2}}$ using CKM unitarity, (iii) V_{us} from CKM unitarity using the input of V_{ud} from superallowed nuclear beta-decays and (iv) from the ratio of (V_{us}/V_{ud}) from the ratio of tau decays $\tau \to K\nu/\tau \to \pi\nu$. The violation is at the level of $\sim 4\sigma$. This is known as the Cabibbo Angle Anomaly (CAA). There are many new physics explanations to this discrepancy [79–86]. $|V_{cd}|$ and $|V_{cs}|$ can be extracted from the leptonic and semileptonic decays of D, D^+ and D_s^+ mesons. Various experimental collaborations like Belle [87], BABAR[88], BES III[89–91] etc have provided measurements on $f_+^\pi(0)|V_{cd}|$ and $f_+^K(0)|V_{cs}|$. The errors are dominated by the theoretical uncertainties of the form factors. Generally, the flavour-tagged $W^+ \to c\bar{s}$ decays help to probe V_{cs} directly and is found to be [1]

$$|V_{cs}| = 0.94^{+0.32}_{-0.26} \pm 0.13. \tag{1.47}$$

On the other hand, from the neutrino scattering data, one can obtain V_{cd} with sufficient precision as [1]

$$|V_{cd}| = 0.230 \pm 0.011. \tag{1.48}$$

Both V_{ub} and V_{cb} are best determined from the semileptonic $b \to (u, c)\ell\nu$ decays, $(\ell = e, \mu)$. However, there exists a tension between the determinations from the inclusive and exclusive modes in both cases. On the basis of unitarity, $|V_{ub}|$ is expected to be very small. The total inclusive semileptonic decay rate to charmless final states, $\Gamma(B \to X_u\ell\nu_\ell)$ $(X_u = \pi, \rho, \omega, \eta, \eta')$ can be reliably calculated using an operator product expansion known as the Heavy Quark Expansion (HQE). However, there is an overwhelming background from the abundant semileptonic decays to charmed final states, $B \to X_c\ell\nu_\ell$. Limited theoretical knowledge of the form factors also make the precise determination of $|V_{ub}|$, a challenging task. There are different techniques to model the QCD shape functions for the extraction of inclusive V_{ub}. However, the result from the different approaches do not agree well with each other. Belle has recently analyzed the inclusive spectra with hadronic-tagging and extracted the values of $|V_{ub}|$ by four different methods (BLNP, DGE, GGOU, ADFR) and the average of all these result in [92]

$$|V_{ub}|^{incl} = (4.10 \pm 0.09 \pm 0.22 \pm 0.15) \times 10^{-3}. \tag{1.49}$$

Currently the best estimate of $|V_{ub}|$ is from $B \to \pi\ell\nu$ since the branching ratio is now known to $\sim 5\%$ accuracy and precise calculations of the $B \to \pi$ form factors from Lattice QCD and Light-cone sum rules (LCSR) are also available. The PDG average of the exclusive determination is [93]

$$|V_{ub}|^{excl} = (3.70 \pm 0.10 \pm 0.12) \times 10^{-3}. \tag{1.50}$$

Using some updated inputs of the form-factors from LCSR for non-zero values of q^2, the exclusive determination of V_{ub} from $B \to \pi\ell\nu$ decay is found to be [94, 95]

$$|V_{ub}|^{excl} = (3.91 \pm 0.13) \times 10^{-3} \tag{1.51}$$

which is closer to the inclusive determination. The measurement of the branching fraction of the leptonic decay $B \to \tau\nu$ is consistent with the SM prediction and also useful for extracting $|V_{ub}|$.

The determination of V_{cb} is crucial in measuring the length of the side of the UT opposite the angle β which is proportional to the quantity $|V_{ub}|/|V_{cb}|$. The extraction of V_{cb} requires the knowledge of form factors which are calculated using the HQET. Preliminary results on the form-factors at non-zero recoil by the lattice groups like Fermilab-MILC and JLQCD are also available. PDG summarizes the values obtained from the inclusive and exclusive determinations as [93, 96]

$$\begin{aligned} &V_{cb}^{incl} = (42.2 \pm 0.8) \times 10^{-3}, \\ &V_{cb}^{excl}\Big|_{B\to D^*\ell\nu} = (39.56^{+1.04}_{-1.06}) \times 10^{-3}, \;\; V_{cb}^{excl}\Big|_{B\to D\ell\nu} = (40.84 \pm 1.15) \times 10^{-3} \end{aligned} \tag{1.52}$$

Additionally, the ratio of $|V_{ub}|/|V_{cb}|$ can also be constrained from the baryonic Λ_b^0 decays [97].

The elements of the third row of the CKM cannot be directly measured from tree level processes involving the top quark. One needs to resort to the loop mediated B or K meson decays and oscillations which are dominated by hadronic uncertainties. The products $(V_{tb}V_{td}^*)$, $(V_{tb}V_{ts}^*)$ can be probed directly from B^0, B_s^0 oscillation frequencies respectively, which are measured to be [98]

$$\Delta m_d = (0.5065 \pm 0.0019)\text{ps}^{-1}, \;\; \Delta\text{m}_\text{s} = (17.757 \pm 0.021)\text{ps}^{-1}. \tag{1.53}$$

The accuracy of these results depend on the determination of the bag factors for which we need to rely on lattice simulations. The mixing phase, ϕ_s, corresponding to the $B_s^0 - \overline{B}_s^0$ mixing, is also known to a pretty good accuracy and its current best estimate is $\phi_s = -0.055(21)$ [98].

The amplitude of the rare $B_s^0 \to \mu^+\mu^-$ decay is directly proportional to the factor $(V_{ts}V_{tb}^*)$ and hence the measurement of the branching fraction provides a complementary measure of the 3^{rd} row CKM elements. LHCb presented an update on this decay channel using full Run 1 and Run 2 dataset [99]

$$\mathcal{B}(B_s^0 \to \mu^+\mu^-) = (3.09^{+0.46+0.15}_{-0.43-0.11}) \times 10^{-9} \tag{1.54}$$

while the most recent measurement by the CMS Collaboration quotes [100]

$$\mathcal{B}(B_s^0 \to \mu^+\mu^-) = (2.9 \pm 0.7 \pm 0.2) \times 10^{-9} \tag{1.55}$$

which is the most precise measurement on this mode till date. This leaves almost no room for NP with the corresponding SM prediction being [101, 102]

$$\mathcal{B}(B_s^0 \to \mu^+\mu^-)_{SM} = (3.66 \pm 0.14) \times 10^{-9}. \tag{1.56}$$

The measure of indirect CP violation in Kaon oscillations, ε_K, also puts important constraints on UT by directly affcecting the imaginary parts of the products $(V_{cs}V_{cd}^*)$ and $(V_{ts}V_{td}^*)$. The present estimate of this CP violating parameter is [1]

$$|\varepsilon_K| = (2.228 \pm 0.011) \times 10^{-3} \tag{1.57}$$

The bag factor parameter, B_K, which enters the dynamics of the Kaon oscillations, has also been precisely estimated from Lattice simulations. $|V_{tb}|$ can also be determined directly from the cross section for single top quark production, ratio of branching ratios $\mathcal{B}(t \to Wb)/\mathcal{B}(t \to Wq)$ as well as from LEP electroweak precision measurements. However, the results are not very competetive.

The angles of the CKM matrix are all determined from hadronic decays of heavy mesons. α is extracted from a Dalitz plot analysis of time-dependent CP asymmetries in $B \to \pi\pi, \rho\rho$ and $\rho\pi$ decays. The angle β is a measure of CP violation arising in the interference between mixing and decay of $b \to c\bar{c}s$ transitions such as $B_d \to J/\psi K_s, J/\psi K^*, D^{*+}D^{*-}$ etc. CP asymmetries in $B^\pm \to D^{(*)}K^{(*)\pm}$, $B^\pm \to D^{(*)}\pi^\pm$, $B^0 \to DK^{*0}$ and $B_s \to D_sK$ decays are sensitive to angle γ. The latest world averages of these angles are [103]

$$\alpha = (85.2^{+4.8}_{-4.3})^\circ, \;\; \beta = (22.2 \pm 0.7)^\circ, \;\; \gamma = (66.2^{+3.4}_{-3.6})^\circ \tag{1.58}$$

The LHCb Collaboration also does an independent global combination of angle γ based on their own measurements of the angle from various decay modes. The results of their most latest combination gives $\gamma = (67 \pm 4)^\circ$ [104].

The CKMFitter group uses a combination of the above flavour physics data and applies a frequentist χ^2 fitting approach to obtain a viable parameter space of the CKM parameters in the SM framework and is considered to be a good consistency test of the CKM paradigm. Their most recent results are summarized in Fig. 1.2b where the different constraints are highlighted and the apex of the UT is denoted by the red hashed region. Although the fit to the SM scenario is consistent with most constraints, there might still be a scope for tiny NP contributions in the data that may resolve the discrepancies related to the unitarity condition violation or the inclusive and exclusive measurements etc. However, the potential sensitivity to new physics is not the same for all processes. Hence it might be an interesting prospect to investigate the allowed region of certain new physics scenarios through these flavour tests.

Charged lepton flavour violating (cLFV) decays such as $\tau \to \mu\gamma, \mu \to e\gamma, \tau \to 3\mu$ are also being rigorously studied by experimentalists because they are highly sensitive to physics beyond the SM. Amongst the above LFV decays the muonic modes are especially interesting since they occur in a clean environment and therefore provide the most stringent bounds on NP parameters. So far, no evidence of LFV decays have been found, thereby resulting in the following upper limits [1]

$$\mathcal{B}(\tau \to \mu\gamma) < 4.4 \times 10^{-8}, \tag{1.59}$$
$$\mathcal{B}(\tau \to e\gamma) < 3.3 \times 10^{-8}, \tag{1.60}$$
$$\mathcal{B}(\tau \to 3\mu) < 2.1 \times 10^{-8}, \tag{1.61}$$
$$\mathcal{B}(\tau \to 3e) < 2.7 \times 10^{-8}, \tag{1.62}$$
$$\mathcal{B}(\mu \to e\gamma) < 4.2 \times 10^{-13}. \tag{1.63}$$

These upper bounds severely constrain NP models where charged lepton flavour violation is significant such as SUSY. These limits are especially relevant for the neutrino mass generating models since different mechanisms predict different rates for cLFV [105]. LHCb has extended their database by also collecting data on lepton flavour violating B-decays such as $B^+ \to K^+\mu^\pm e^\mp$ [106], $B_s^0 \to e^\pm\mu^\mp, B^0 \to e^\pm\mu^\mp$ [107, 108], $B_s^0 \to \tau^\pm\mu^\mp, B^0 \to \tau^\pm\mu^\mp$ [109] etc. Again, only upper limits have been reported.

1.4 Some Anomalous Results

Certain low energy observables in the rare semileptonic FCNC decays of the B meson have hinted towards the presence of new physics beyond the SM. The FCNC decays such as the $b \to s\ell^+\ell^-$ are extremely useful to indirectly probe new physics at high scales since they are suppressed at the tree level in the SM as the Z boson does not couple to quarks of different flavour. Hence, tiny contributions to such decay observables beyond leading order from virtual new particles that are too massive to be produced at colliders may lead to measurable deviations from the expected SM prediction. The excitement in B-physics is high due to the fact that over the past few years, huge amount of data has been collected by the B-factories such as Babar, Belle and LHCb and the current precision and statistics enable us to disentangle the NP from the SM. The study of the rare decays involving the b-quark is therefore one of the primary focus of this thesis.

The exclusive $B \to K^{(*)}\ell^+\ell^-$ $(\ell = e, \mu)$ decays with underlying $b \to s\ell^+\ell^-$ transitions occur at one loop level via box and penguin diagrams. Since the branching fractions of these decays suffer from hadronic uncertainties, it is convenient to consider ratios of the form

$$R_M \equiv \frac{\int_{q^2_{min}}^{q^2_{max}} \frac{\Gamma(B\to M\mu^+\mu^-)}{dq^2} dq^2}{\int_{q^2_{min}}^{q^2_{max}} \frac{\Gamma(B\to Me^+e^-)}{dq^2} dq^2} \tag{1.64}$$

where the hadronic uncertainties cancel out, making them clean probes of NP. Here, M denotes a meson (K, K^* etc.), $q^2_{min} = 4m^2_\ell$ $(\ell = \mu, e)$ and $q^2_{max} = (m_B - m_M)^2$. These observables also

help us to study an important property of the SM, the *lepton-universality*, which predicts that the different flavours of leptons have similar electroweak interactions. Hence, these ratios are also known as Lepton Flavor Universality (LFU) ratios and both their SM expectations are unity [110–112]. However, the most precise experimental measurements from LHCb [113, 114]

$$R_K = 0.846^{+0.042+0.013}_{-0.039-0.012} \text{ for } \mathrm{q}^2 \in [1.1, 6.0] \text{ GeV}^2, \tag{1.65}$$

$$R_{K^*} = \begin{cases} 0.66^{+0.11}_{-0.07} \pm 0.03 \text{ for } \mathrm{q}^2 \in [0.045, 1.1] \text{ GeV}^2, \\ 0.69^{+0.11}_{-0.07} \pm 0.05 \text{ for } \mathrm{q}^2 \in [1.1, 6.0] \text{ GeV}^2 \end{cases} \tag{1.66}$$

are in tension with respect to unity by 3.1 and 2.4σ respectively. The Belle collaboration has also tested the lepton flavor universality in $B \to K^* \ell^+ \ell^-$ decays and obtained a value of R_{K^*} which has huge uncertainty and is hence consistent with SM.[115]. Disregarding the Belle data with large error bars, the precise data from LHCb hints towards lepton flavour universality violation (LFUV) between electrons and muons. One would therefore naively expect it to be present with respect to tau as well. This has been examined in the charged current $B \to D^{(*)}$ decays through similar LFU ratios as described in Eqn. (1.64)

$$R_{D^{(*)}} \equiv \frac{\mathcal{B}(B \to D^{(*)} \tau \bar{\nu}_\tau)}{\mathcal{B}(B \to D^{(*)} \ell \bar{\nu}_\ell)} \quad (\ell = e, \mu). \tag{1.67}$$

The experimental world averages of these ratios are [98]

$$R_D = 0.340 \pm 0.027 \pm 0.013, \quad R_{D^*} = 0.295 \pm 0.011 \pm 0.008, \tag{1.68}$$

while the SM predictions are [96, 98]

$$R_D^{SM} = 0.299 \pm 0.003, \quad R_{D^*}^{SM} = 0.252 \pm 0.007, \tag{1.69}$$

which have a combined 3σ discrepancy amongst each other.

Interestingly, although there exists hints of LFUV, there exist no sign of presence of lepton flavour violating decays such as $\tau \to \mu\gamma, \mu \to e\gamma, \tau \to 3\mu$ etc. as discussed previously. There are a plethora of model-independent studies present in the literature based on the available binned data on branching fractions as well as angular observables that highlight the important features that need to be present in NP models [116–124]. Interestingly, the origin of such discrepancies could be the presence of one or more new interactions (like vector, scalar etc.) beyond the SM which can also have a close connection to the dark sector. Such possibilities are extensively studied in the thesis.

The muon has attracted a lot of attention, not only due to discrepancies in the LFUV observables, but also due to the long standing anomaly between the measured and predicted values of its magnetic dipole moment. The Landé g-factor of a charged elementary particle with half-integer instrinsic spin is equal to 2 at the tree level, first predicted by Dirac in 1928 for electrons [125]. Any

departure from this value due to higher order corrections is known as the "*anomalous magnetic moment*" and is defined as

$$a_\ell \equiv \frac{g_\ell - 2}{2}, \tag{1.70}$$

which includes the quantum loop effects and parametrizes the small calculable deviation from $g_\ell = 2$ for charged leptons ($\ell = e, \mu, \tau$).

The anomalous magnetic moment of muon has been measured very precisely while it has also been predicted in the SM to a great accuracy. The SM contributions to a_μ come from QED, electroweak and hadronic loop corrections respectively. For a recent review on the theoretical and experimental status of muon g-2 read [126]. During the early days of my PhD, the most precise measurement of muon anomalous magnetic moment was given by the Brookhaven National Laboratory (BNL) as

$$\Delta a_\mu = a_\mu^{exp} - a_\mu^{SM} = 26.8(7.6) \times 10^{-10}, \tag{1.71}$$

which deviated from the SM prediction by 3.7σ [127]. However, the most recent result from the run 1 of the Muon $g-2$ experiment at Fermilab [128],

$$\Delta a_\mu = a_\mu^{exp} - a_\mu^{SM} = 25.1(5.9) \times 10^{-10}, \tag{1.72}$$

is an improvement over the previous Brookhaven result and indicates a strengthened anomaly at $\sim 4.2\sigma$. More data are expected to be analyzed by Fermilab in the coming years aiming to reduce the uncertainty by a factor of 4 compared to the Brookhaven result. If the experimental result persists then we expect to observe a $\sim 7\sigma$ inconsistency with the SM prediction.

There has also been an improvement in the measurement of the fine-structure constant which points towards a deviation in the electron anomalous magnetic moment from its theoretical estimate by a negative 2.4σ. Although both the above results have significant room for NP, the opposite sign disparity between the two anomalous magnetic moments makes it quite difficult to simultaneously explain them from a common BSM framework.

1.5 Objective of the Thesis

The source of the discrepancies in these low energy experiments may be attributed to some heavy scale physics belonging to a dark sector. The main purpose of this thesis is to explore some BSM models that can simultaneously accomodate the low energy observables, like data from B-factories, muon anomalous magnetic moment and the LFV data as well as give rise to a stable DM candidate whose relic abundance is generated by the correct amount. To achieve this we have extended the particle content in the minimal possible way such that FCNCs can be generated at the one loop level. We have also investigated the possibility of neutrino mass generation in some of our works. The predictability of our models can be attributed to the different and unique observable collider signals at present and future high luminosity LHC runs which have been investigated. The direct impact of precisely determined flavour observables, such as the CKM elements, on simple

dark matter models have also been studied. DM interactions with SM quarks is important for its direct detection through nuclear recoil in scattering experiments. But, such interactions would also be subject to stringent constraints from flavour changing charged current decays. Such constraints on the DM parameter space have never been considered before and therefore, it is important to re-examine the parameter space of such models.

Chapter 2

Methodology

In this chapter we would look into some of the concepts, tools and methods which will be widely used throughout the rest of the thesis. In particular we would explore the weak effective Hamiltonian for the semileptonic B-decays and mixing, the use of statistical methods for constraining SM and BSM parameters in a model-independent way and study the boltzmann equation useful for the thermal freeze-out of dark matter.

2.1 Theoretical Framework

2.1.1 Effective Field Theory for B-decays and Mixing

Effective field theory (EFT) is an extremely useful tool to incorporate physics at high energy scales (short distances) into the lower energy scale (long distance) by integrating out the heavy degrees of freedom, leaving an effective lagrangian that can be expressed as a dimensional expansion

$$\mathcal{L} = \mathcal{L}_0 + \frac{\mathcal{L}_1}{\Lambda} + \frac{\mathcal{L}_2}{\Lambda^2} + ... + \frac{\mathcal{L}_n}{\Lambda^n} \tag{2.1}$$

where $\mathcal{L}_0$ contains all renormalizable interactions while $\mathcal{L}_n, n \geq 1$, is a combination of non - renormalizable operators of dimension $n+4$ suppressed by n-th power of the new physics energy scale Λ. The separation of scales makes the theory simpler by removing irrelavant degrees of freedom and extracting useful information of physical processes that are relevant at that low scale. The Fermi theory of beta decay is by far the best example of an EFT where the W-boson mass is integrated out in order to express the decay as a four-point interaction. Other examples include the effective theory of low energy QCD or the chiral perturbation theory (CPT), the theory of hadrons described by the heavy quark effective theory (HQET) etc. A very useful lecture note on EFT can be found in [129].

The EFT approach has been extensively used in studying the B-meson decays at the scale of the bottom quark mass since it is much smaller than the top mass and weak interaction scale. However, since QCD is inherently involved in the meson decays, the theoretical formulation of the interplay of QCD with weak interactions become complicated. Two tools that come to our

rescue in this endeavour are the operator product expansion (OPE) [130] and renormalization group [131]. Using OPE one can write the amplitude of any weak meson decay process as

$$\mathcal{A} = \sum_i C_i(\mu) \langle \mathcal{O}_i(\mu) \rangle \tag{2.2}$$

where C_i's are the Wilson coefficients (WCs) containing the information about the short-distance effects, $\langle \mathcal{O}_i(\mu) \rangle$ are the matrix elements of the local operators consisting of long distance contributions and μ is the factorization scale. Fields which are heavier than the factorization scale (for example, W, Z bosons, top, exotic heavy particles etc.) are integrated out and their information get embedded in the Wilson coefficients. Therefore, using OPE, one can separate the problem into two parts such that we can interpret $\sum_i C_i \mathcal{O}_i$ as the effective Hamiltonian of the process under consideration with $\mathcal{O}_i$ as the effective vertices and C_i the corresponding coupling strengths. Since quarks are confined [132], it is only possible to probe weak interactions in a hadronic environment. So the matrix elements are sensitive to long-distance QCD effects which are not perturbative and calculable [133–138]. Alternative techniques are used to estimate the hadronic parameters such as Lattice QCD, light-cone sum rules (LCSR), 1/N expansion, HQET etc which are beyond the scope of this thesis. For more details refer to the following books/reviews [139–150]. The WCs in the effective theory are calculated using perturbations theory. However, the scale of the hadronic matrix elements are much lower (in case of B-meson decays it is the b-quark mass m_b) than the weak scale at which the Wilson coefficients are calculated. Due to the presence of such vastly different scales, large logarithms appear in the calculation which destroy the validity of the perturbation theory. This issue is tackled by summing up large logarithmic terms upto all orders in perturbation theory using renormalization group (RG). So the matching of an effective theory onto a full theory is first done at the high energy scales (corresponding to the scale of each particle that is integrated out) and then the C_i's are evolved down to lower energy scales using renormalization group equations for application to low-energy processes such as B meson decays. In the following sections we are going to elaborate on the effective Hamiltonians of the $b \to s\ell\ell$ and $b \to c\ell\bar{\nu}_\ell$ transitions.

***b → sℓℓ* Transitions :** The effective Hamiltonian for the $b \to s$ transitions at low energy can be written as [151–153]

$$\mathcal{H}_{\text{eff}}^{b\to s} = -\frac{4G_F}{\sqrt{2}} V_{tb}V_{ts}^* \left(\sum_{i=1\ldots6} C_i\mathcal{O}_i + \sum_{i=7,8,9,10,S,P} (C_i\mathcal{O}_i + C_i'\mathcal{O}_i') \right) + h.c. \tag{2.3}$$

Here, the twice Cabibbo-suppressed contributions ($\propto V_{ub}V_{us}^*$) have been safely neglected compared to the ones mentioned above. $\mathcal{O}_i$ and $\mathcal{O}_i'$s are the dimension six effective operators which are given as below,

$$\begin{aligned} \mathcal{O}_1 &= (\bar{s}_\alpha c_\beta)_{V-A}(\bar{c}_\beta b_\alpha)_{V-A}, \;\; \mathcal{O}_2 = (\bar{s}c)_{V-A}(\bar{c}b)_{V-A}, \\ \mathcal{O}_3 &= (\bar{s}b)_{V-A}\sum_q(\bar{q}q)_{V-A}, \;\; \mathcal{O}_4 = (\bar{s}_\alpha b_\beta)_{V-A}\sum_q(\bar{q}_\beta q_\alpha)_{V-A}, \end{aligned}$$

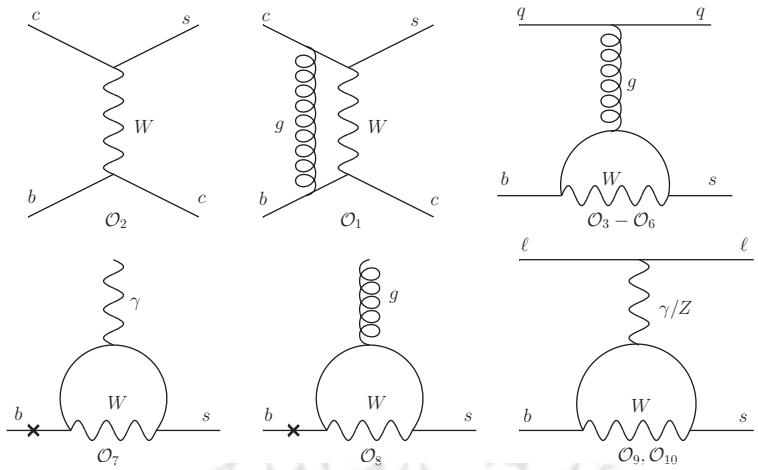

Figure 2.1: Quark level Feynman diagrams for the SM effective operators corresponding to the $b \to s$ transition.

$$
\begin{aligned}
\mathcal{O}_5 &= (\bar{s}b)_{V-A}\sum_q(\bar{q}q)_{V+A}, \;\; \mathcal{O}_6 = (\bar{s}_\alpha b_\beta)_{V-A}\sum_q(\bar{q}_\beta q_\alpha)_{V+A}, \\
\mathcal{O}_7 &= \frac{e}{g^2}m_b(\bar{s}\sigma_{\mu\nu}P_R b)F^{\mu\nu}, \;\; \mathcal{O}_7' = \frac{e}{g^2}m_b(\bar{s}\sigma_{\mu\nu}P_L b)F^{\mu\nu}, \\
\mathcal{O}_8 &= \frac{1}{g}m_b(\bar{s}\sigma_{\mu\nu}T^a P_R b)G^{\mu\nu}, \;\; \mathcal{O}_8' = \frac{1}{g}m_b(\bar{s}\sigma_{\mu\nu}T^a P_L b)G^{\mu\nu}, \\
\mathcal{O}_9 &= \frac{e^2}{g^2}(\bar{s}\gamma_\mu P_L b)(\bar{l}\gamma^\mu l), \;\; \mathcal{O}_9' = \frac{e^2}{g^2}(\bar{s}\gamma_\mu P_R b)(\bar{l}\gamma^\mu l), \\
\mathcal{O}_{10} &= \frac{e^2}{g^2}(\bar{s}\gamma_\mu P_L b)(\bar{l}\gamma^\mu\gamma_5 l), \;\; \mathcal{O}_{10}' = \frac{e^2}{g^2}(\bar{s}\gamma_\mu P_R b)(\bar{l}\gamma^\mu\gamma_5 l), \\
\mathcal{O}_S &= \frac{e^2}{16\pi^2}(\bar{s}P_L b)(\bar{l}l), \;\; \mathcal{O}_S' = \frac{e^2}{16\pi^2}(\bar{s}P_R b)(\bar{l}l), \\
\mathcal{O}_P &= \frac{e^2}{16\pi^2}(\bar{s}P_L b)(\bar{l}\gamma_5 l), \;\; \mathcal{O}_P' = \frac{e^2}{16\pi^2}(\bar{s}P_R b)(\bar{l}\gamma_5 l),
\end{aligned}
\tag{2.4}
$$

where α and β denote the color indices and the labels $(V \pm A)$ refer to $\gamma_\mu(1 \pm \gamma_5)$. The operators $\mathcal{O}_{1,2}$, $\mathcal{O}_{3,..,6}$, $\mathcal{O}_7$, $\mathcal{O}_8$ and $\mathcal{O}_{9,10}$ are the current-current, QCD penguin, electromagnetic penguin, chromo-magnetic penguin and semileptonic operators respectively. The Feynman diagrams leading to these operators are shown in Fig. 2.1. They appear in the SM effective theory, as well as in specific BSM scenarios, while the rest (scalar operator $\mathcal{O}_S$, pseudoscalar operator $\mathcal{O}_P$ and all primed ones) will appear only in NP models. The Wilson coefficients corresponding to the SM effective operators can be found in [151]. In this case the Wilson coefficients are calculated at a matching scale $\mu = m_W$ in a perturbative series expansion of the strong coupling constant α_s and then evolved down to the scale $\mu \approx m_b$.

Another important rare decay mode that plays a crucial role in constraining new physics signals is $B_s \to \mu^+\mu^-$. In the operator basis of Eqn. (2.4), the expression for the branching fraction,

in presence of BSM contributions, is given by

$$\mathcal{B}(B_s \to \mu^+\mu^-) = \tau_{B_s} f_{B_s}^2 m_{B_s}^3 \frac{G_F^2\alpha^2}{64\pi^3}|V_{tb}V_{ts}^*|\sqrt{1-\frac{4m_\mu^2}{m_{B_s}^2}}\left[\frac{m_{B_s}^2}{m_b^2}\left(1-\frac{4m_\mu^2}{m_{B_s}^2}\right)\left|C_S-C_S^{'}\right|^2 + \left|\frac{m_{B_s}}{m_b}(C_P-C_P^{'})+2\frac{m_\mu}{m_{B_s}}(C_{10}-C_{10}^{'})\right|^2\right]. \tag{2.5}$$

We have already mentioned in the previous chapter, cf. equations (1.54) and (1.56), that the experimental observation and theoretical prediction of the above branching fraction are highly consistent with each other within the error bars. Hence, the operators, $C_S^{(')}$ and $C_P^{(')}$, are tightly constrained by the data on $\mathcal{B}(B_s \to \mu^+\mu^-)$. Therefore, the contributions from the scalar and pseudoscalar operators can not explain the observed anomalous results in $R_{K^{(*)}}$ [154, 155]. The operators relevant for the decay $b \to s\ell^+\ell^-$ are given by $\mathcal{O}_{9,10}^{(\prime)}$. Model-independent analysis with $b \to s$ global data suggests that $\mathcal{O}_9$ is the only one operator scenario that can simultaneously explain all the data in $b \to s$ decays [116–120, 156, 157] and there is almost no room left for NP in $\mathcal{O}_{10}$. However, there are a few two or three operator scenarios which can best explain the data at the moment, and that includes the combination $\mathcal{O}_9$ and $\mathcal{O}_{10}$. The expression for the decay rate in the operator basis of Eqn. (2.4) can be found in [152].

***b* → *c* Transitions :** The most general effective Hamiltonian governing the $b \to c\ell\bar{\nu}_\ell$ transitions is given by

$$\mathcal{H}_{\text{eff}}^{b\to c} = \frac{4G_F}{\sqrt{2}}V_{cb}\left[(\delta_{\ell\ell}+C_{V_1}^\ell)\mathcal{O}_{V_1}^\ell + C_{V_2}^\ell\mathcal{O}_{V_2}^\ell + C_{S_1}^\ell\mathcal{O}_{S_1}^\ell + C_{S_2}^\ell\mathcal{O}_{S_2}^\ell + C_T^\ell\mathcal{O}_T^\ell\right] \tag{2.6}$$

where C_X^ℓ ($X = V_1, V_2, S_1, S_2, T$) are the Wilson coefficients corresponding to the operator basis

$$\begin{aligned}
\mathcal{O}_{V_1}^\ell &= (\bar{c}_L\gamma^\mu b_L)(\bar{\ell}_L\gamma_\mu\nu_L),\\
\mathcal{O}_{V_2}^\ell &= (\bar{c}_R\gamma^\mu b_R)(\bar{\ell}_L\gamma_\mu\nu_L),\\
\mathcal{O}_{S_1}^\ell &= (\bar{c}_L b_R)(\bar{\ell}_R\nu_L),\\
\mathcal{O}_{S_2}^\ell &= (\bar{c}_R b_L)(\bar{\ell}_R\nu_L),\\
\mathcal{O}_T^\ell &= (\bar{c}_R\sigma^{\mu\nu}b_L)(\bar{\ell}_R\sigma_{\mu\nu}\nu_L).
\end{aligned} \tag{2.7}$$

The flavour of the neutrino is not determined experimentally in B decays and so all neutrino flavours ($\nu = \nu_e, \nu_\mu, \nu_\tau$) are considered. Also the operator basis is constructed by assuming that neutrinos are left-handed. There is only one dimension six effective operator that appears in the SM i.e $\mathcal{O}_{V_1}^\ell$. The SM contribution comes from the term $\delta_{\ell\ell}$ and all other Wilson coefficients (C_X^ℓ) are zero.

Babar, Belle and LHCb collaborations have collected sufficient data on $B \to D^{(*)}\ell\bar{\nu}_\ell$ decay mode which includes $R_{D^{(*)}}$, tau polarization P_τ, D^* polarization $F_L(D^*)$ and forward-backward asymmetry A_{FB}. The decay distributions in presence of NP can be found in [158, 159].

2.2 Numerical Framework

2.2.1 Boltzmann Equation for Dark Matter Freeze-Out

A WIMP dark matter which was in thermal and chemical equillibrium with the hot SM bath in the early Universe is known to achieve its relic density through thermal freeze-out mechanism. During thermal equillibrium the production and annihilation rate of the DM particles are same. As the temperature of the Universe drops due to its adiabatic expansion, the interaction rate, Γ, of DM starts to reduce due to increased dilution in the number density of DM and at a certain epoch, it falls below the expansion rate of the Universe H (the Hubble rate) i.e $\Gamma \lesssim H$. When this happens, the DM particles decouple or freeze out of the thermal bath and their number density asymptotically reaches a constant value which is called the relic density. The present day relic density of the DM in our Universe is found to be Eqn. (1.43). The accurate description of decoupling can be found out by solving the Boltzmann equation which governs the microscopic evolution of the phase space distribution function.

The evolution of the number density of DM, n_χ, in the expanding Universe is described by the following Boltzmann equation

$$\frac{dn_\chi}{dt} = -\langle\sigma v\rangle_{\text{ann}}(n_\chi^2 - n_{\chi,eq}^2) - 3Hn_\chi \tag{2.8}$$

where H is the Hubble constant, $\langle\sigma v\rangle_{\text{ann}}$ is the thermally averaged annihilation cross-section and $n_{\chi,eq}$ is the equillibrium number density of the DM which is given by

$$n_{\chi,eq} = \begin{cases} g\left(\frac{m_\chi T}{2\pi}\right)^{3/2} e^{-\frac{m_\chi}{T}} & m_\chi >> T \\ g\left(\frac{T^3}{\pi^2}\right) & m_\chi << T \end{cases} \tag{2.9}$$

when the temperature of the thermal bath is T. Here g denotes the number of internal degrees of freedom of the DM and m_χ is its mass. The thermally averaged cross-section $\langle\sigma v\rangle$ is usually expressed in terms of partial waves

$$\langle\sigma v\rangle = a + b\langle v^2\rangle + d\langle v^4\rangle.... \tag{2.10}$$

where a,b,d are the leading s-wave, p-wave and d-wave contributions to the cross section respectively. The first term on the RHS of Eqn. (2.8) is the collision term that accounts for the DM reaction rate while the second term accounts for the dilution due to the expansion of the Universe. It is more convenient to express the Boltzmann equation in terms of the DM yield $Y = n_\chi/s$ where n_χ is the comoving number density and s is the total entropy density per comoving volume given by

$$s = \frac{2\pi^2}{45} g_{\star s}(T) T^3 \tag{2.11}$$

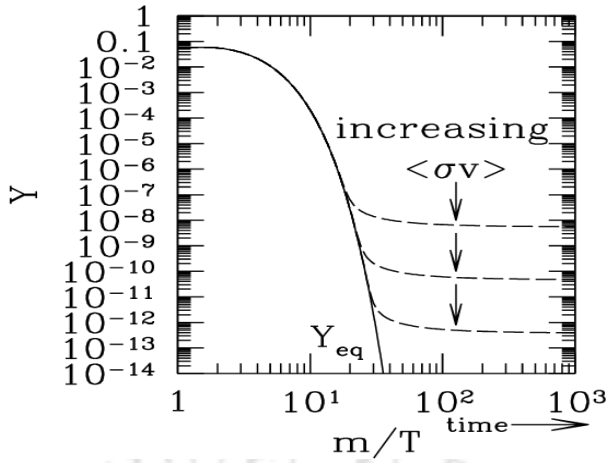

Figure 2.2: The evolution of the number density of dark matter per unit comoving volume as a function of x or time. Figure taken from [9].

with

$$g_{\star s}(T) = \sum_{i=bosons} g_i \left(\frac{T_i}{T}\right)^3 + \sum_{i=fermions} \frac{7}{8} g_i \left(\frac{T_i}{T}\right)^3 . \tag{2.12}$$

It is also convenient to rewrite Eqn. (2.8) in terms of a new time variable $x = \frac{m_\chi}{T}$ which sets the scale for DM freeze-out. The Boltzmann equation as a function of x is given by

$$\frac{dY}{dx} = -\frac{xs\langle\sigma v\rangle_{\text{ann}}}{H(m_\chi)}(Y^2 - Y_{eq}^2) \tag{2.13}$$

where the Hubble parameter is given by $H(x) = H(m_\chi)/x^2$ with $H(m_\chi) = 1.66\sqrt{g_{\star\rho}}\frac{m_\chi^2}{M_{Pl}}$, $g_{\star\rho} = \sum_{i=bosons} g_i \left(\frac{T_i}{T}\right)^4 + \sum_{i=fermions} \frac{7}{8} g_i \left(\frac{T_i}{T}\right)^4$ and $M_{Pl} \approx 2.4 \times 10^{18}$ GeV is the reduced Planck mass. The equillibrium distribution can be expressed as

$$Y_{eq} = 0.145 \frac{g}{g_{\star s}} x^{3/2} e^{-x} \tag{2.14}$$

Finally, we need to solve Eqn. (2.13) numerically in order to obtain the freeze-out of DM. Fig. 2.2 shows the evolution of a WIMP comoving number density over time. Let us understand the different features of this Boltzmann equation. At very high temperatures $x << 1$, the particles are relativistic and the DM interactions are much larger than the expanion rate of the Universe. Therefore the DM yield follows the equillibrium distribution until the time when the temperature of the Universe $\simeq$ DM mass i.e $x \simeq 1$. For $x > 1$, the equilibrium yield is exponentially suppressed and annihilations become so scarce that the DM particles will not be able to maintain the equillibrium abundance. This is the onset of freeze-out. When the temperature falls much below the DM mass, the DM freezes out at $x = x_f = m_\chi/T_f$ where T_f denotes the freeze-out temperature. Once the asymptotic yield $Y(x_\infty)$ is obtained, we can use it to calculate the relic abundance of dark matter as [42, 160]

$$\Omega h^2 = \frac{\rho}{\rho_c} = \frac{m_\chi s_0 \sqrt{g_\star}}{3H_0^2 M_{Pl}^3 0.26 g_{\star s}} Y(x_\infty) \tag{2.15}$$

Here, x_∞ denotes a large enough value of x after decoupling and s_0 is the present entropy density of the Universe which is ≈ 3000 cm^{-3}. For all practical purposes, one can obtain the approximate analytical solution for relic density as [161] :

$$\Omega h^2 = \frac{m_\chi n_\chi}{\rho_c} \approx \frac{10^{-27} cm^3 s^{-1}}{\langle \sigma v \rangle}. \tag{2.16}$$

WIMPs generally freeze out at $x_f \approx \{20 - 30\}$ which can be obtained from the relation:

$$x_f = \ln \frac{0.038 g M_{\rm Pl} m_\chi < \sigma v >}{g_\star^{1/2} x_f^{1/2}} \,, \tag{2.17}$$

that is derived from the equality condition of DM interaction rate $\Gamma = n_\chi \langle \sigma v \rangle$ with the rate of expansion of the Universe $H \approx g_\star^{1/2} \frac{T^2}{M_{Pl}}$ (i.e, the freeze-out condition).

The thermally averaged annihilation cross section $\langle \sigma v \rangle$ is given by [162]

$$\langle \sigma v \rangle = \frac{1}{8 m_\chi^4 T K_2^2(m_\chi/T)} \int_{4m_\chi^2}^{\infty} \sigma \sqrt{s} (s - 4m_\chi^2) K_1(\sqrt{s}/T) ds \,, \tag{2.18}$$

where K_i's are modified Bessel functions of order i. Eqn. (2.16) denotes the relic abundance for a single component dark matter particle. But in general, there may be more than one dark matter particle in a model. In that case we have to solve coupled Boltmann equations for the dark matter evolution and depending upon the mass splitting between the different SM particles, co-annihilation processes may play an important role in the dynamics of the evolution. In presence of co-annihilation, the effective cross section can be expressed as [163]:

$$\begin{aligned} \sigma_{eff} &= \sum_{i,j}^{N} \langle \sigma_{ij} v \rangle r_i r_j \\ &= \sum_{i,j}^{N} \langle \sigma_{ij} v \rangle \frac{g_i g_j}{g_{eff}^2} (1 + \Delta_i)^{3/2} (1 + \Delta_j)^{3/2} e^{\left(-x_f (\Delta_i + \Delta_j)\right)}, \end{aligned} \tag{2.19}$$

where $\Delta_i = \frac{m_i - m_\chi}{m_\chi}$ for $i = 2, 3...., N$ number of DM components with masses m_i. Total number of effective DOF is given by:

$$g_{eff} = \sum_{i=1}^{N} g_i (1 + \Delta_i)^{3/2} e^{-x_f \Delta_i}. \tag{2.20}$$

The thermally averaged cross section then reads:

$$\begin{aligned} \langle \sigma_{ij} v \rangle = & \frac{x_f}{8 m_i^2 m_j^2 m_\chi K_2((m_i/m_\chi) x_f) K_2((m_j/m_\chi) x_f)} \times \\ & \int_{(m_i + m_j)^2}^{\infty} ds \sigma_{ij} (s - 2(m_i^2 + m_j^2)) \sqrt{s} K_1(\sqrt{s} x_f / m_\chi). \end{aligned} \tag{2.21}$$

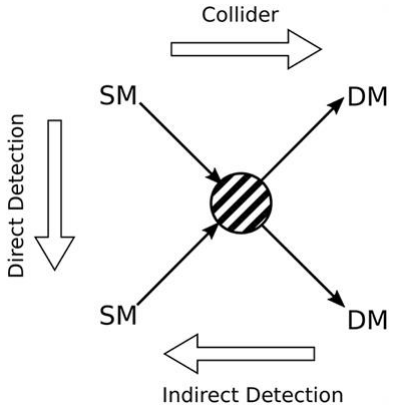

Figure 2.3: A schematic diagram showing the different methods od dark matter detection. Figure taken from [10].

Hence, the relic density boils down to the approximate analytical solution:

$$\Omega h^2 = \frac{2.4 \times 10^{-10}}{\sigma_{eff}} \text{GeV}^{-2}. \tag{2.22}$$

2.2.2 Direct Detection of Dark Matter

There are three ways of detecting dark matter particles in complementary experimental setups when they interact with the visible sector as depicted in Fig. 2.3. In this thesis we mostly concentrate on the direct detection (DD) possibilities of different DM models and hence we briefly review the subject here.

We know that DM particles are electrically neutral and hence cannot be seen directly. But their presence can be felt when they scatter off a target and produce a detectable recoil of the atomic nucleus. Such a possibility of detecting WIMP DM was first pointed out by Goodman and Witten [164]. Therefore direct detection experiments were setup underground to protect the detector from noise. The differential recoil rate per unit recoil energy for a DM of mass m_χ scattering with a target nucleus of mass m_T is given by

$$\frac{dR}{dE_R} = N_T n_\chi \int \frac{d\sigma}{dE_R} v f(v) d^3v \tag{2.23}$$

where, N_T is the number of nuclei per unit target mass, $n_\chi = \rho_\chi / m_\chi$ is the local DM number density, σ is the scattering cross-section of the DM with SM particle and $f(v)$ is the DM velocity distribution in the detector frame. The typical velocity of DM in our local DM halo $\sim 10^{-3}$.

The maximum recoil energy is given by

$$E_R^{max} = \frac{|\vec{q}|^2_{max}}{2m_T} = \frac{2\mu_R^2 v^2}{m_T} \tag{2.24}$$

where, $\vec{q}$ is the momentum transferred to the recoiling nucleus and μ_R is the reduced mass of the DM-nucleus system

$$\mu_R = \frac{m_\chi m_T}{m_\chi + m_T}. \tag{2.25}$$

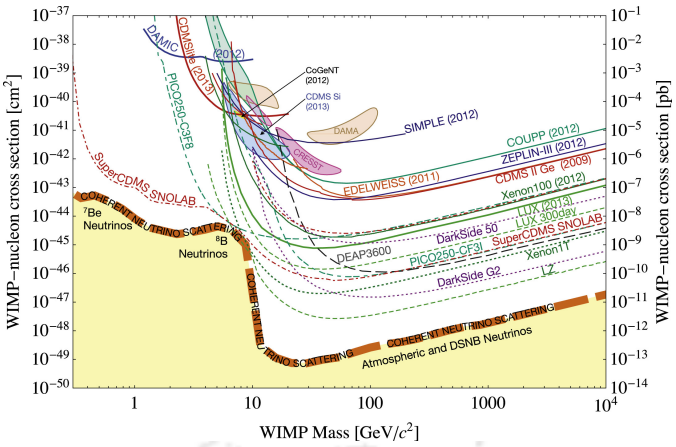

Figure 2.4: Summary of the WIMP–nucleon spin-independent cross section limits from some current and proposed direct detection experiments. The orange thick dashed line shows the background limit from solar, atmospheric and diffuse supernovae neutrino scattering. Figure credit [11].

Typically, for a WIMP DM in the mass range $\sim (10 - 10^3)$ GeV scattering off a Xenon nucleus ($m_T \sim 131$ GeV), say for example, the maximum recoil energy would range from $\approx (1 - 200)$ keV.

The scattering cross-section may vary depending upon whether the DM-SM interaction is spin-dependent or independent. In general, the largest scattering rate can be achieved in case of the spin-independent scenario. The spin independent scattering cross-section is given by [165]

$$\sigma^{SI} = \frac{4\mu_R^2}{\pi} \left(Z f_p + (A - Z) f_n\right)^2 \tag{2.26}$$

where (Z, A) denotes the atomic and mass numbers of the target nuclei and f_p, f_n are the effective couplings of DM to protons and neutrons respectively. The spin-dependent cross-section, for scattering against a target nuclei of spin J, is given by [165]

$$\sigma^{SD} = \frac{32\mu_R^2 G_F^2}{\pi} \frac{J+1}{J} \left(a_p \langle S_p \rangle + a_n \langle S_n \rangle\right)^2 \tag{2.27}$$

where G_F is Fermi's constant, a_p, a_n are the effective couplings of DM to protons and neutrons respectively and $\langle S_{p,n} \rangle = \langle N | S_{p,n} | N \rangle$ are the expectation values of the proton/neutron spin operator.

At present, the best limits on the spin-independent cross-section is put by XENON 1T [18] which rules out spin independent WIMP-nucleon interaction cross section above 7.7×10^{-47} cm^2 for DM mass of $\sim$ 35 GeV, but the bounds are more relaxed for higher DM masses. This limit improves upon the earlier upper bounds from LUX [166]. The XENON nT [167] and DARWIN [168] are some of the proposed future direct detection experiments. The limits on the spin-dependent cross sections are weaker compared to the spin-independent ones. The most recent upper bound on the cross-section is 4.1×10^{-41} cm^2 at 90% confidence level for $m_\chi = 40$ GeV/c^2 reported by the PANDA-II collaboration [169] while other similar bounds are also reported by LUX [170].

2.2.3 χ^2 Analysis

One of the most useful method of parameter estimation of a model based on experimental data is the χ^2-analysis. The *chi-square* (χ^2) is a statistical quantity which is a function of the parameters of a model and is used to test whether any given data are well described by the model hypothesis. Such a method is known as the chi-square test for goodness of fit. In this section we will briefly describe the basics of this technique. For a comprehensive book/review on the introduction to statistical data analysis read [171, 172].

Let us suppose that N independent variables x_i are normally distributed with a mean $\mu_i(x_i;\boldsymbol{\theta})$ and variance σ_i^2. Then the chi-square of the unknown fit parameters $\boldsymbol{\theta}$ is defined as

$$\chi^2(\theta) \equiv \frac{(x_1-\mu_1(x_1;\boldsymbol{\theta}))^2}{\sigma_1^2} + \frac{(x_2-\mu_2(x_2;\boldsymbol{\theta}))^2}{\sigma_2^2} + ... + \frac{(x_N-\mu_N(x_N;\boldsymbol{\theta}))^2}{\sigma_N^2} = \sum_{i=1}^{N}\frac{(x_i-\mu_i(x_i;\boldsymbol{\theta}))^2}{\sigma_i^2}. \tag{2.28}$$

Considering the fact that the values of x_i randomly fluctuate about the mean μ_i, each term is close to unity. Therefore, the value of the chi-square would be approximately equal to N when the data are well described by our hypothized function which, in this case, is the mean x_i. If the chi-square is much larger than N, then one can conclude that the data are not well described by our hypothesized set of μ_i. This is the very general idea of the chi-square test. It is conventional in the literature to quote the reduced chi-square which is defined as χ^2/n_d where n_d is the number of degrees of freedom (dof). Hence for a model with only one free parameter, the reduced chi-square is approximately equal to 1 for a good fit and greater than 1 otherwise.

The chi-square, in a sense, gives the probability of an observed outcome given a set of parameter values and therefore is regarded as the "*likelihood*" of the set of parameter values given the observed outcome. Hence, the chi-square is related to the log-likelihood function as

$$\chi^2(\boldsymbol{\theta}) = -2ln\mathrm{L}(\boldsymbol{\theta}) + \text{constant} \tag{2.29}$$

where the constant represents terms that do not depend on the parameters. The set of parameter values ($\hat{\theta}$) which minimize the chi-square is considered to be the best fit to the data. It is interesting to note that the values of the parameters which minimize the chi-square are also those that maximize the likelihood L. The value of the χ^2 at its minimum (χ^2_{min}) is a measure of the level of agreement between the data and fitted curve and can therefore be employed as a goodness-of-fit statistic to test the hypothesis. It can be shown that if the hypothesis is correct then the χ^2_{min} follows a probability distribution function given by

$$f(z;n_d) = \begin{cases} \frac{z^{\frac{n_d}{2}-1}e^{-\frac{z}{2}}}{2^{\frac{n_d}{2}}\Gamma(\frac{n_d}{2})}, & z>0 \\ 0, \quad \text{otherwise.} \end{cases} \tag{2.30}$$

The goodness of fit can also be determined by the *p-value* of a hypothesis. The p-value is used to determine whether there is evidence to reject the null hypothesis or our initial claim and is

defined as

$$p = \int_{\chi^2}^{\infty} f(z; n_d) dz \tag{2.31}$$

where $\Gamma(x)$ denotes the Euler gamma function. This gives the probability of obtaining a χ^2_{min} as high as the one we obtain using $\hat{\theta}$, or higher, if the hypothesis is correct. The term significance level is used to refer to a pre-chosen probability and if the p-value is less than the chosen significance level then we reject the null hypothesis. In most cases the pre-specified probability is taken to be 5%. Hence, if $p < 0.05$, we reject our initial claim and go for an alternative hypothesis.

Chapter 3

Correlating the anomalous results in $b \to s$ decays with inert Higgs doublet dark matter and muon $(g-2)$

3.1 Introduction

We have already argued that the low energy observables in B decays and $B_q - \bar{B}_q$ (q = d,s) mixings play an important role in the indirect detection of new physics. In this regard, the FCNC processes, such as $b \to s$, are unique in a sense that in the SM they contribute at the loop level thereby keeping their contributions suppressed, in general. For the last couple of years, the semileptonic decays $b \to s\ell^+\ell^-$ ($\ell = \mu, e$) have gained a lot of attention. The measurements of the lepton universality ratios $R_{K^{(*)}}$ by the different experimental collaborations have opened up an alternate avenue for the search for new physics since the observed data indicate a possible violation of lepton universality. Although there is a clear hint of physics beyond the SM, the new physics does not manifest itself as a large effect. In order to explain the observed discrepancies, one needs to develop a new mechanism that will generate lepton universality violation (LUV) either at the tree level or via loops. There have been plenty of analysis on the NP explanations of the observed discrepancies, which we are not going to elaborate here. On the other hand, the fact that we do not have a suitable DM candidate in the SM which satisfies the requirements as given in [39], has led to several BSM proposals which can successfully explain DM in the Universe. Since the WIMP dark matter scenarios involve additional physics around the electroweak scale, it is tempting to speculate if the same new physics can have plausible explanations for the observed flavour anomalies like $R_{K^{(*)}}$, Δa_μ mentioned earlier. Within such unified framework, one needs to find out the allowed NP parameter space consistent with flavour data as well as the requirements for a DM candidate. Also, it is necessary to check that the required NP parameter spaces are consistent with all the other relevant measurements which are not anomalous. In this chapter, we will look for a NP model which is capable of addressing simultaneously both the above mentioned excesses [173]. There have been several attempts along this direction, some of which can be found in [174–178] and

references therein. Apart from being consistent with all these observations, it is also important for such a scenario to be predictive at different experiments like direct detection of dark matter, collider searches and so on.

Here, we consider the inert Higgs doublet model (IDM), which is a simple extension of the SM by an additional scalar field Φ_2 transforming as doublet under $SU(2)_L$ gauge symmetry and has hypercharge $Y = 1$. The model has been introduced in [179], and later studied extensively by several groups in the context of DM phenomenology [61, 180–188]. In this model, an additional discrete $\mathcal{Z}_2$ symmetry is introduced in order to prevent the coupling of this scalar field to the SM fermions. Under this $\mathcal{Z}_2$ symmetry, the additional scalar field transforms as $\Phi_2 \to -\Phi_2$ whereas all SM fields are even. If the lightest component of Φ_2 is electromagnetically neutral, it can be stable and hence a good DM candidate. Being inert in nature, IDM will not contribute to the decay $b \to s\ell\ell$. Hence, we have extended this model by considering three generations of vector like $SU(2)_L$ singlet down type quarks and charged leptons, odd under the same $\mathcal{Z}_2$ symmetry so that they can couple to the SM quarks and leptons only through the inert scalar doublet. The lightest component of Φ_2 remains the lightest $\mathcal{Z}_2$ odd particle of the model and hence the DM candidate. We have shown that apart from explaining the DM abundance of the Universe, the model can also explain the observed pattern in $R_{K^{(*)}}$. This model has family non-universal Yukawa couplings between Φ_2, vector like fermions and the SM fermions. Hence, it will contribute to $b \to s\ell\ell$ at one loop level. Now, if we consider a hierarchical structure between the Yukawa couplings of electron and muon with the new vector like fermions, then we can expect to get $R_{K^{(*)}} \neq 1$. The additional vector like fermions can also contribute to the relic abundance, as well as direct detection scattering rates of DM in this model, giving us a complementary probe of the model parameters in both DM and flavour experiments.

In the pure IDM there exists two mass ranges where DM relic abundance can be satisfied: one in the low mass regime below the W boson mass threshold ($M_{\rm DM} < M_W$) and the other around 550 GeV or above. In our extended IDM, there will be additional annihilation channels of DM. Therefore, it is important to rescan the parameter space for both the pure and the extended IDM. The direct detection scattering in pure IDM is primarily mediated by the SM Higgs and faces the strongest constraints from the direct detection experiments in the low mass regime. For example, the latest data from the LUX experiment rules out DM-nucleon spin independent cross section above around 2.2×10^{-46} cm^2 for DM mass of around 50 GeV [166]. On the other hand, the results from the XENON-1T experiment rules out spin independent WIMP-nucleon interaction cross section above 7.7×10^{-47} cm^2 for DM mass of 35 GeV [18, 189]. These strong bounds reduce the allowed DM masses in the low mass regime to a very narrow region near the SM like Higgs resonance $M_{\rm DM} \approx m_h/2$. Although the direct detection limits can be somewhat relaxed in the high mass regime ($M_{\rm DM} \gtrapprox 550$ GeV), the production of DM at colliders will be suppressed compared to the low mass regime. In the presence of additional vector like quarks, there are additional diagrams which will contribute to the spin independent direct detection cross section. We in fact find that, compared to the pure IDM, the presence of new vector like fermions can keep the dark matter

direct detection rates closer to the experimental upper bound for some choices of parameters.

The mediators of our model couples to SM quarks and leptons, therefore interesting collider signature are expected with leptons and/or jets in the final state with missing energy. We study the final states containing $(\ell^+\ell^- + \not{E}_T)$, $(jj + \not{E}_T)$ and $(\ell^+\ell^- + jj + \not{E}_T)$ to unravel the model in the large hadron collider (LHC). These final states are already explored in supersymmetry (SUSY) searches, and important constraints have been obtained on the parameter space [190, 191]. There have also been some studies on collider signatures of pure IDM, for example see [192–194]. In our model, we prepare few benchmark scenarios by choosing points from the new parameter spaces which are allowed by flavour data and overcome bounds from the DM searches. We have predicted the kinematical distributions of our signal events and compared them with the respective SM backgrounds. We find that at the high luminosity LHC the model may be observed for a few benchmark scenarios at more than 5σ significance. We also check the perturbative unitarity of the model for the chosen benchmark points.

The chapter is organised as follows: in Sec. 3.2 we discuss the particle content and possible interactions, followed by the dark matter phenomenology of the model in Sec. 3.3; constraints from muon $(g-2)$ and lepton flavour violating decays are discussed in Sec. 3.4; contributions in $b \to s$ transitions are studied in Sec. 3.5; results from DM and flavour analysis are discussed Sec. 3.6 and some benchmark points are also chosen for further collider study; we then discuss the fate of this model at the LHC in Sec. 3.7, pointing out the possibility of probing it in future higher luminosity; the RGE runnings are discussed in Sec. 3.8 and finally we summarize in Sec. 3.9.

3.2 IDM with Vector Like Fermions

As mentioned earlier, the IDM is an extension of the SM by an additional global discrete $\mathcal{Z}_2$ symmetry under which a newly incorporated scalar doublet Φ_2 transforms as $\Phi_2 \to -\Phi_2$, while the usual SM fields are even under $\mathcal{Z}_2$. The requirement of keeping the $\mathcal{Z}_2$ symmetry unbroken prevents the neutral component of the second Higgs doublet from acquiring a non-zero vacuum expectation value (vev). Since the same discrete symmetry prevents any coupling of Φ_2 with the SM fermions, it automatically makes the lightest component of Φ_2 stable and hence a good DM candidate. The scalar potential of the model involving the SM Higgs doublet Φ_1 and the inert doublet Φ_2 can be written as

$$\begin{aligned} V(\Phi_1,\Phi_2) = \mu_1^2|\Phi_1|^2 + \mu_2^2|\Phi_2|^2 + \frac{\lambda_1}{2}|\Phi_1|^4 + \frac{\lambda_2}{2}|\Phi_2|^4 + \lambda_3|\Phi_1|^2|\Phi_2|^2 \\ + \lambda_4|\Phi_1^\dagger\Phi_2|^2 + \left\{\frac{\lambda_5}{2}(\Phi_1^\dagger\Phi_2)^2 + \text{h.c.}\right\}. \end{aligned}$$

As the electroweak symmetry has to be broken by the vev of Φ_1, we assume $\mu_1^2 < 0$. Also, $\mu_2^2 > 0$ is assumed so that Φ_2 does not acquire a vev. Writing the scalar fields in terms of components and

Particles	$SU(3)_c \times SU(2)_L \times U(1)_Y$	$\mathcal{Z}_2$
$Q_L = \begin{pmatrix} u_L \\ d_L \end{pmatrix}$	$(3, 2, \frac{1}{6})$	+
u_R	$(3, 1, \frac{2}{3})$	+
d_R	$(3, 1, -\frac{1}{3})$	+
$L_L = \begin{pmatrix} \nu_L \\ e_L \end{pmatrix}$	$(1, 2, -\frac{1}{2})$	+
e_R	$(1, 1, -1)$	+
Φ_1	$(1, 2, \frac{1}{2})$	+
Φ_2	$(1, 2, \frac{1}{2})$	-
$D_{L,R}$	$(3, 1, -\frac{1}{3})$	-
$E_{L,R}$	$(1, 1, -1)$	-

Table 3.1: Particle content of the extension of IDM by vector like fermions.

expanding the field Φ_1 about the non-zero vev, we have

$$\Phi_1 = \begin{pmatrix} 0 \\ \frac{v+h}{\sqrt{2}} \end{pmatrix}, \Phi_2 = \begin{pmatrix} H^{\pm} \\ \frac{H^0+iA^0}{\sqrt{2}} \end{pmatrix} \tag{3.1}$$

in unitary gauge. Here v is the vev of the neutral component of Φ_1. After electroweak symmetry breaking (EWSB), the masses of the physical scalars, at tree level, can be written as

$$\begin{aligned} m_h^2 &= \lambda_1 v^2, \\ M_{H^\pm}^2 &= \mu_2^2 + \frac{1}{2}\lambda_3 v^2, \\ M_{H^0}^2 &= \mu_2^2 + \frac{1}{2}(\lambda_3+\lambda_4+\lambda_5)v^2 = M_{H^\pm}^2 + \frac{1}{2}(\lambda_4+\lambda_5)\,v^2, \\ M_{A^0}^2 &= \mu_2^2 + \frac{1}{2}(\lambda_3+\lambda_4-\lambda_5)v^2 = M_{H^\pm}^2 + \frac{1}{2}(\lambda_4-\lambda_5)\,v^2. \end{aligned} \tag{3.2}$$

Here $m_h \approx 125$ GeV is the mass of the SM Higgs, M_{H^0}, M_{A^0} are the masses of the CP even and CP odd scalars of the inert doublet while $M_{H^\pm}$ being the mass of the charged scalar. Without any loss of generality, we consider $\lambda_5 < 0, \lambda_4 + \lambda_5 < 0$ so that the CP even scalar is the lightest $\mathcal{Z}_2$ odd particle and hence a stable dark matter candidate.

Apart from the $\mathcal{Z}_2$ odd scalar doublet Φ_2, we consider additional vector like charged fermions too, which are odd under the same $\mathcal{Z}_2$ symmetry. The particle content of the model is shown in Table 3.1. Here D is the down-type vector like quark and E is the vector like lepton. This allows the coupling of the inert doublet scalar with the SM fermions through the vector like fermion portal. The relevant Yukawa Lagrangian can be written as

$$\mathcal{L} = (y_u)_{ij}\bar{Q}_i\tilde{\Phi}_1 u_{Rj} + (y_d)_{ij}\bar{Q}_i\Phi_1 d_{Rj} + (y_e)_{ij}\bar{L}_i\Phi_1 e_{Rj} + (\lambda^D)_{ij}\bar{Q}_i\Phi_2 D_{Rj} + (\lambda^E)_{ij}\bar{L}_i\Phi_2 E_{Rj} + M_{D_i}\bar{D}_{Li}D_{Ri} + M_{E_i}\bar{E}_{Li}E_{Ri} + \text{h.c.} \quad (3.3)$$

where $\tilde{\Phi}_{1,2} = i\tau_2\Phi^*_{1,2}$ and $\lambda^{E,D}$ are the Yukawa couplings associated with the vector fermion interactions. Also, i and j are the generation indices. [1]

3.3 Dark Matter Phenomenology

3.3.1 Relic abundance of DM

In the present model, discussed in the previous section, we consider one of the neutral component of the scalar doublet Φ_2 namely H^0, as the DM candidate for our analysis. This is similar to the inert doublet model of dark matter discussed extensively in the literature [61, 180–186]. We have already discussed the methodology of calculating the relic abundance of a single component WIMP dark matter is section 2.2.1. In the low mass regime ($M_{H^0} \equiv M_{\text{DM}} \leq M_W$), the annihilation of DM to the SM fermions (through s-channel Higgs mediation) dominates over other channels. As pointed out in [183], the annihilation $H^0H^0 \to WW^* \to Wf\bar{f}'$ also plays a role in the $M_{\text{DM}} \leq M_W$ region. Depending on the mass differences $M_{H^\pm} - M_{H^0}\,(\equiv \Delta M_{H^\pm}), M_{A^0} - M_{H^0}\,(\equiv \Delta M_{A^0})$, co-annihilation of $H^0, H^\pm$ and H^0, A^0 become important in determining the relic abundance of the DM. Typically, when the heavier components of the inert scalar doublet have masses close to the DM mass, they can be thermally accessible at the epoch of DM freeze-out. Therefore, the annihilation cross section of DM in such a case gets additional contributions from co-annihilations between the DM and the heavier components of the scalar doublet Φ_2.

3.3.2 Dark matter direct search

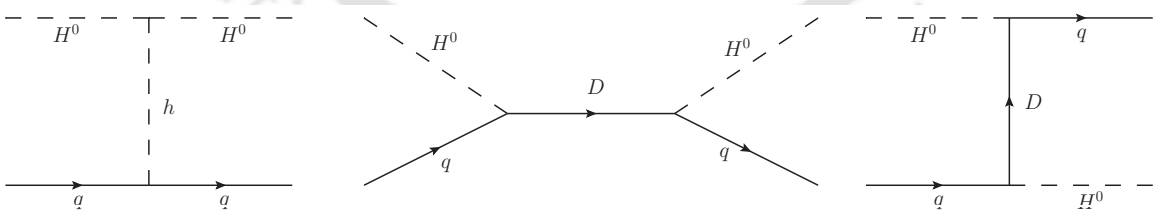

Figure 3.1: The Feynman diagrams contributing to the direct search of H^0. Here, D indicates the contributions from down type vector like quarks (all the three generations).

As mentioned earlier, there are severe constraints on spin independent DM-nucleon scattering rates from ongoing experiments [18, 166, 189]. In the pure IDM, the tree level DM-nucleon elastic scattering can arise through the SM Higgs mediation and the current bounds on direct detection

[1] Note that even if we consider CKM-like flavour mixing of the down-type vector-like quarks, then the new couplings (say ${\lambda^D}'_{ij}$) would just be $(\lambda^D)_{ij}$ multiplied by the mixing parameter V'_{CKM} and thus just a re-definition of the old couplings. This will not change the phenomenology discussed in this work.

cross section can rule out some portion of the parameter space satisfying relic specially in the low mass regime $M_{\rm DM} \approx m_h/2$ where bounds are stronger. The elastic DM nucleon scattering in the present model gets additional contributions from exotic quark D, as depicted in Fig. 3.1 where the first diagram corresponds to the usual SM Higgs mediated one. The additional contributions will come from the rest of the two diagrams. There is another possible diagram mediated by Z-boson, even in the pure IDM, but that has already been excluded by recent direct search data. Therefore, in order to forbid the Z-mediated channel, the mass of A^0 has to be kept higher than that of H^0 by a non-zero value, higher than typical kinetic energy ($\mathcal{O}(100$ keV$)$) of a DM particle so that H^0 can not scatter inelastically into A^0. The chosen mass splitting in our analysis satisfy this bound as well as the ones from LEP II data [195]. Hence, in this model we have three direct search graphs corresponding to t-channel Higgs and exotic quark mediation and another s-channel diagram mediated by the vector like quark. Due to these additional diagrams, the direct detection rates of the extended IDM can be more promising compare to the pure IDM, as we will discuss later. In the limit of very large exotic quark masses or very small couplings of exotic quarks to DM, the direct detection rates will converge towards the ones known for pure IDM.

3.4 Muon $(g-2)$ and the lepton flavour violation (LFV) decays

The effective vertex of photon with any charged particle is given by:

$$\bar{u}(p')e\Gamma_\mu u(p) = \bar{u}(p')\left[e\gamma_\mu F_1(q^2) + \frac{ie\sigma_{\mu\nu}q^\nu}{2m_f}F_2(q^2) + ...\right]u(p). \tag{3.4}$$

The factor $g_\mu \equiv 2(F_1(0)+F_2(0))$, and the anomalous magnetic moment is given as $a_\mu \equiv F_2(0) \neq 0$ (since $F_1(0) = 1$ at all order). Similarly, the amplitude for the LFV decays $\ell_i \to \ell_j\gamma$ can be written as:

$$M_\gamma = \bar{u}_{\ell_j}(p')\left[A_L q^2 \gamma_\mu P_L + iA_R m_{\ell_i}\sigma_{\mu\nu}q^\nu P_R\right]u_{\ell_i}(p). \tag{3.5}$$

The associated branching fraction can be expressed as:

$$\mathcal{B}(\ell_i \to \ell_j\gamma) = \frac{\alpha\tau_{\ell_i}}{4}m_{\ell_i}^5 A_R^2, \tag{3.6}$$

where τ_{ℓ_i} is the life time of the lepton ℓ_i and $\alpha = 1/137$ is the fine structure constant.

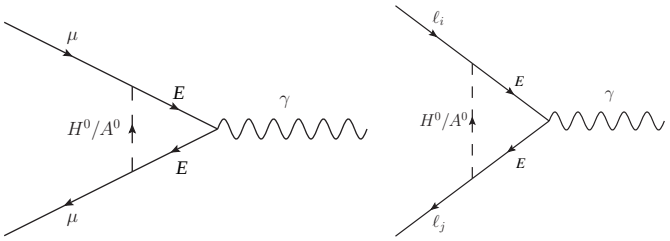

Figure 3.2: Feynman diagrams contributing to muon anomalous magnetic moment a_μ (left) and lepton flavour violating decays (right). Here, E $(= E_1/E_2/E_3)$ is the vector like lepton.

In our model, the leading contributions in a_μ and the LFV decays like $\tau \to \mu\gamma$, $\mu \to e\gamma$ and $\tau \to e\gamma$ are obtained from the diagrams in Fig. 3.2. In the loop, we have either H^0 or A^0 and the vector like lepton E (which could be either of E_1, E_2 or E_3). The diagram on the left hand side will contribute to a_μ, which is given by [196–198]

$$a_\mu = \sum_i \frac{\lambda^E_{2i}\lambda^{E\,*}_{2i} m_\mu^2}{16\pi^2}\left[\frac{1}{M^2_{H^0}}\left(\xi_1(r^{H^0}_{E_i}) - \xi_2(r^{H^0}_{E_i})\right) + \frac{1}{M^2_{A^0}}\left(\xi_1(r^{A^0}_{E_i} - \xi_2(r^{A^0}_{E_i})\right)\right], \tag{3.7}$$

with $r^X_{E_i} = m^2_{E_i}/M^2_X$ ($X = H^0$ or A^0). Here, m_{E_i} is the mass of i-th generation vector like lepton and λ^E_{2i} is the corresponding coupling to muon as expressed in Eqn. (3.3). Note that in the Yukawas of the vector like fermions, the first index corresponds to the SM fermion generation while the second index represents that for vector like fermions. The functions ξ_1 and ξ_2 are given by:

$$\begin{aligned}\xi_1(r) &= \frac{-3+4r-r^2}{2(1-r)^3} - \frac{\ln r}{(1-r)^3}\\ \xi_2(r) &= \frac{1}{6(1-r)^4}[-11+18r-9r^2+2r^3-6\ln r].\end{aligned} \tag{3.8}$$

The contributions to the decay $\ell_i \to \ell_j\gamma$ will be obtained from the RHS diagram of Fig. 3.2, which is given as [197, 198] :

$$A_R = \sum_k \frac{\lambda^E_{ik}\lambda^{E\,*}_{jk} m_{\ell_i}}{16\pi^2}\left[\frac{1}{M^2_{H^0}}\left(\xi_1(r^{H^0}_{E_k}) - \xi_2(r^{H^0}_{E_k})\right) + \frac{1}{M^2_{A^0}}\left(\xi_1(r^{A^0}_{E_k}) - \xi_2(r^{A^0}_{E_k})\right)\right]. \tag{3.9}$$

In this section we have only shown the analytical expressions of various contributions in a_μ and $\mathcal{B}(\ell_i \to \ell_j\gamma)$, the numerical results are presented in section 3.6.

3.5 NP contributions in $b \to s$ decays

3.5.1 $b \to s\ell^+\ell^-$ decays ($\ell = \mu, e$)

In our model, the diagrams that will contribute to the process $b \to s\ell\ell$ are shown in Fig. 3.3, where X/X' can be either of H^0 or A^0. As one can see from Eqn. (3.3), the new couplings ($\lambda^{E,D}_{ij}$) carry the generation indices of the SM fields (first index) as well as that of the vector like fermions (second index). Therefore, depending on the type of vector like fermion in the loop, there will be several contributions to the decay amplitude. This will be function of the new Yukawa couplings and the masses of the new particles. However, for the simplicity of the analysis, we have followed the hierarchy: $\lambda^{E,D}_{ij} << \lambda^{E,D}_{ii}$ (i, j = 1, 2 and 3), i.e, the off diagonal Yukawas are suppressed with respect to the diagonal terms. Also, since one of our goals is to explain the $R_{K^{(*)}}$ anomaly, which requires lepton universality violation, we have further assumed $\lambda^{E,D}_{33} >> \lambda^{E,D}_{22} >> \lambda^{E,D}_{11}$. In this simplified picture, the box diagram with D_3 and E_2 (in the loop) will have the dominant contribu-

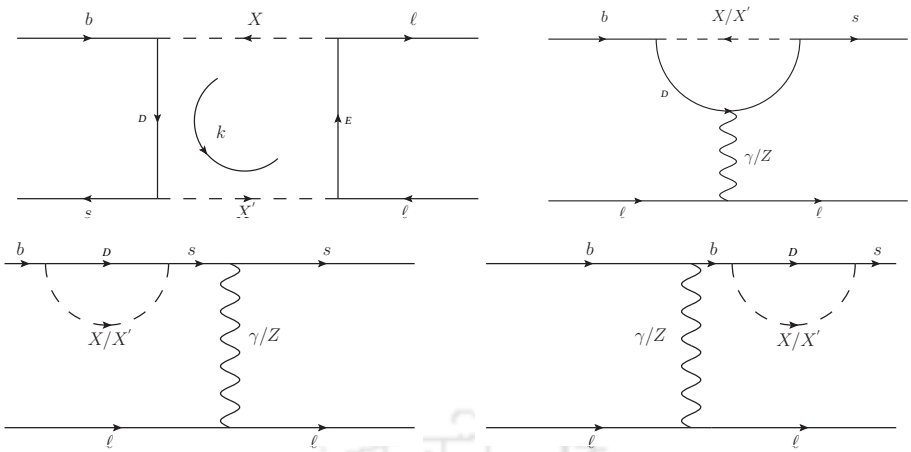

Figure 3.3: Feynman diagrams contributing to $b \to s\ell\ell$ process. Here X and $X^{'}$ can be either of H^0 or A^0. The box diagrams with $X = X' = H^0/A^0$ will also contribute to $b \to s\ell\ell$ processes.

tion to the process $b \to s\mu^+\mu^-$. Since the dominant contribution to all the observables mentioned above occur via the third generation of down-type vector like fermion D_3 (due the to hierarchy in the couplings), we will from now on talk only about the mass of D_3. In general, the contributions from the penguin diagrams are dominant over that of the box diagrams. However, the penguin diagrams alone can not explain $R(K^{(*)})$ anomaly, as they contribute equally to the decay rates of $B \to K^{(*)}\mu\mu$ and $B \to K^{(*)}ee$. Perhaps it is possible to explain the observed data by considering contributions from the new box diagrams alone. In such cases, the interference of the SM Wilson coefficient with that obtained from the box diagrams will play the leading role in explaining the observed pattern in $R_{K^{(*)}}$ data. If we add the contributions from the penguin diagrams, then there will be interference of the WC obtained from the box and the penguin diagrams. Hence, depending on the size of the individual contributions, the interference of the new box and penguin diagrams could also play an important role in the explanation of the observed data. For completeness, in our analysis we have considered the contributions from all types of diagrams which are shown in Fig. 3.3.

The most general expression for the box diagram with two different scalars X and $X^{'}$ in the loop is given by :

$$i\mathcal{M}_{Box} = \frac{i\pi^2 \lambda_{3i}^{D*} \lambda_{2i}^{D} \lambda_{2j}^{E*} \lambda_{2j}^{E}}{(2\pi)^4}\, \mathcal{A}\, \mathcal{O}_{eff}, \tag{3.10}$$

where the loop factor is given by [197]

$$\begin{aligned}\mathcal{A} = \Bigg[& \frac{M_{X'}^4}{(M_X^2 - M_{X'}^2)(M_{D_i}^2 - M_{X'}^2)(M_{E_j}^2 - M_{X'}^2)} \ln\left(\frac{M_X^2}{M_{X'}^2}\right) \\ & + \frac{M_{D_i}^4}{(M_{D_i}^2 - M_{E_j}^2)(M_{D_i}^2 - M_{X'}^2)(M_{D_i}^2 - M_X^2)} \ln\left(\frac{M_{D_i}^2}{M_X^2}\right) \\ & + \frac{M_{E_j}^4}{(M_{E_j}^2 - M_{D_i}^2)(M_{E_j}^2 - M_{X'}^2)(M_{E_j}^2 - M_X^2)} \ln\left(\frac{M_{E_j}^2}{M_X^2}\right) \Bigg].\end{aligned} \tag{3.11}$$

We have also added the contributions of the box diagrams with only one type of scalar (H^0, A^0) in the loop. The expression for this can be found from Eqn. (3.11) by taking the limiting case $X \to X'$.

The effective operator is given by

$$\begin{aligned} \mathcal{O}_{eff} &= [\bar{b}\gamma_\mu(1-\gamma_5)s][\bar{l}\gamma^\mu(1-\gamma_5)l] \\ &= [\bar{b}\gamma_\mu(1-\gamma_5)s][\bar{l}\gamma^\mu l] - [\bar{b}\gamma_\mu(1-\gamma_5)s][\bar{l}\gamma^\mu\gamma_5 l] \\ &= \mathcal{O}_9 - \mathcal{O}_{10} \end{aligned} \tag{3.12}$$

where $\mathcal{O}_{9,10}$ are the semileptonic operators introduced in Eqn. (2.4). For simplicity, from now on we will rewrite the couplings $\lambda^D_{33} \equiv \lambda_b$, $\lambda^D_{23} \equiv \lambda_s$ and $\lambda^D_{13} \equiv \lambda_d$. On the other hand, we write $\lambda^E_{11} \equiv \lambda_e$, $\lambda^E_{22} \equiv \lambda_\mu$ and $\lambda^E_{33} \equiv \lambda_\tau$ to simplify our notations. Thus Eqn. (3.10) can be written as

$$i\mathcal{M}_{Box} \sim i[C_9^{\rm NP}\mathcal{O}_9 + C_{10}^{\rm NP}\mathcal{O}_{10}], \tag{3.13}$$

where,

$$\boxed{C_9^{\rm NP} = -C_{10}^{\rm NP} = -\left(\frac{\lambda_b\lambda_s\lambda_\mu^2\mathcal{A}}{32\pi^2}\right)}, \tag{3.14}$$

which has to be normalized with a factor $\mathcal{N} = -\left(\frac{\sqrt{2}}{4G_F V_{tb}^* V_{ts}} \times \frac{4\pi}{\alpha}\right)$ so that the operators are at par with those given in Eqn. (2.4).

The amplitude of the photon exchanged penguin diagrams can be written as

$$\mathcal{M}_\gamma = [\bar{b}(A_L q^2\gamma_\mu P_L + iA_R m_\tau \sigma_{\mu\nu}q^\nu P_R)s]\frac{e^2}{q^2}[\bar{\ell}\gamma^\mu\ell], \tag{3.15}$$

where q is the photon momentum. The dominant contribution will come from D_3, therefore, the form-factors A_L and A_R are induced by the product $\lambda_s\lambda_b$ coupling. The contribution to C_9 will come only from A_L, whose approximate form is given by:

$$A_L = \frac{\lambda_s\lambda_b^*}{32\pi^2 M^2_{X^{(\prime)}}}\frac{\xi(r_{D_3})}{3}, \tag{3.16}$$

with

$$\xi(r_{D_3}) = \frac{1}{6(1-r_{D_3})^4}[-11 + 18r_{D_3} - 9r_{D_3}^2 + 2r_{D_3}^3 - 6\ln r_{D_3}]. \tag{3.17}$$

and $r_{D_3} = M^2_{D_3}/M^2_{X^{(\prime)}}$.

The Z-mediated penguin amplitude for the process $b \to s\ell\ell$ can be written as

$$\mathcal{M}_Z = [\bar{b}F_L\gamma_\mu P_L s]\frac{1}{M_Z^2}[\bar{\ell}\gamma^\mu(a_L^\ell P_L + a_R^\ell P_R)\ell], \tag{3.18}$$

where

$$a_L^f = \frac{g}{\cos\theta_W}(t_3^f - Q_f\sin^2\theta_W), \quad a_R^f = \frac{g}{\cos\theta_W}(-Q_f\sin^2\theta_W). \tag{3.19}$$

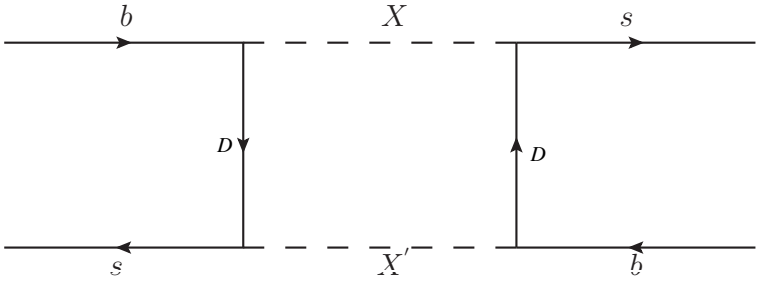

Figure 3.4: The Feynman Diagram contributing to the B_s-meson mixing in our model with X, X' denoting either H^0 or A^0. All other possible symmetric diagrams have also been considered during computation. The dominant contributions will come from D_3.

From the diagrams of Fig. 3.3 we obtain

$$F_L = \frac{g}{\cos\theta_W}\frac{\lambda_s\lambda_b^*}{32\pi^2}\left[a_R^{D_3}\left(\frac{1}{2}-2C\right)+a_L^{D_3}r_{D_3}\xi_0(r_{D_3})+a_L^s B\right]. \tag{3.20}$$

The finite parts of C, ξ_0 and B are given by

$$\begin{aligned} C &= \frac{1}{2}\int_0^1 dx(1-x)\ln[xM_{X^{(\prime)}}^2+(1-x)M_{D_3}^2], \\ \xi_0(r_D) &= \int_0^1 dx\frac{1-x}{x+(1-x)r_{D_3}} \\ B &= \frac{1}{2}\int_0^1 dx x\ln[xM_{X^{(\prime)}}^2+(1-x)M_{D_3}^2]. \end{aligned} \tag{3.21}$$

The details of the above calculations can be seen from [197]. The Z-mediated penguin diagrams will contribute to both C_9 and C_{10}. Therefore, the total contributions to C_9 and C_{10} can be extracted from

$$\mathcal{M} = \mathcal{M}_{Box} + \mathcal{M}_Z + \mathcal{M}_\gamma. \tag{3.22}$$

The numerical analysis is done in the next section (3.6).

3.5.2 $B_s - \overline{B}_s$ Mixing

The $\Delta F = 2$ process $B_s - \overline{B}_s$ mixing may play a crucial role in constraining the parameters of our model relevant for $b \to s$ transitions. In this case the important observable is the mass difference ΔM_{B_s}, which is defined as

$$\Delta M_{B_s} = 2|M_{12}^{B_s}|. \tag{3.23}$$

In the SM, the dominating contributions to $M_{12}^{B_s}$ will come from the dispersive part of the box diagram amplitude with W boson and the top quark in the loop. The mathematical expression for it is given by

$$M_{12}^{B_s}\Big|_{SM} = \frac{G_F^2}{12\pi^2}f_{B_s}^2\hat{B}_{B_s}M_{B_s}M_W^2(V_{tb}^*V_{ts})^2\eta_B S_0\left(\frac{\overline{m}_t^2}{M_W^2}\right), \tag{3.24}$$

S_0 is the Inami-Lim function:

$$S_0(x) = \frac{4x - 11x^2 + x^3}{4(1-x)^2} - \frac{3x^3 \log x}{2(1-x)^3}. \tag{3.25}$$

The detail of the SM calculations can be seen from [199].

In the presence of NP there will be additional contributions to $M_{12}^{B_s}$. In our model the dominant contributions will come from the box diagram as shown in Fig. 3.4, which is given by

$$M_{12}^{B_s}\Big|_{NP} = \left(\frac{4\lambda_b^2\lambda_s^2}{32\pi^2}\right) f_{B_s}^2 \hat{B}_{B_s} M_{B_s} S_{NP} \tag{3.26}$$

where,

$$S_{NP} = \Bigg[\frac{M_{D_3}^2}{(M_{X'}^2 - M_{D_3}^2)(M_{D_3}^2 - M_X^2)} + \frac{M_{D_3}^4(M_X^2 + M_{X'}^2) - 2M_{D_3}^2 M_X^2 M_{X'}^2}{(M_{X'}^2 - M_{D_3}^2)^2(M_{D_3}^2 - M_X^2)^2} \ln\left(\frac{M_{D_3}^2}{M_X^2}\right) - \frac{M_{X'}^4}{(M_{X'}^2 - M_{D_3}^2)^2(M_{X'}^2 - M_X^2)} \ln\left(\frac{M_{X'}^2}{M_X^2}\right)\Bigg] \tag{3.27}$$

There will be several such diagrams with H^0 and/or A^0 in the loop. Our loop factor can be compared with that given in [200].

In the SM, the B_s mixing phase is negligibly small, also in our analysis we are assuming real Yukawa couplings. Hence, we can express the mixing amplitude as

$$\Delta M_{B_s} = (\Delta M_{B_s})_{\text{SM}} + (\Delta M_{B_s})_{\text{NP}} = (\Delta M_{B_s})_{\text{SM}} \ \big(1 + \Delta_{\text{Mix}}\big), \tag{3.28}$$

with $\Delta_{\text{Mix}} = \frac{\left(\Delta M_{B_s}\right)_{\text{NP}}}{\left(\Delta M_{B_s}\right)_{\text{SM}}}$. In this ratio, the bag factor and the decay constant will cancel which are the major sources of uncertainties in the SM predictions of the oscillation frequency. Δ_{Mix} is sensitive to the NP parameters and using Eqn. (3.28) we can find out the maximum allowed ranges of this observable. Using the latest data on ΔM_{B_s} [12] and the following inputs for decay constant and the bag factor [77, 201]

$$f_{B_s} = 0.2284 \pm 0.0037 \text{ GeV}, \text{and } \ \text{B}_{\text{B}_\text{s}} = 1.327 \pm 0.034, \tag{3.29}$$

we find that Δ_{Mix} could be as big as 15% if we consider the 1σ allowed ranges of all the relevant inputs. This could be even 20% if one uses the projected lattice results as given in ref. [201]. The $B_d - \overline{B}_d$ mixing data allows sizeable NP contributions ($\approx 30\%$)[202]. In our model, the contributions to $B_d - \overline{B}_d$ mixing will come from the diagram in Fig. 3.4, with the strange quarks (s) in the external legs replaced by down (d) quarks. The dominant contribution will thus be proportional to $(\lambda_b\lambda_d)^2$. Therefore, following our assumption of the hierarchical structures of the new Yukawas, the contributions will be highly suppressed. The same argument is also true for K-$\overline{K}$ mixing in which the NP contribution due to our model is proportional to $(\lambda_d\lambda_s)^2$. Actually, for all practical purposes, we can set $\lambda_d \approx 0$. This assumption does not have any impact on our final results since

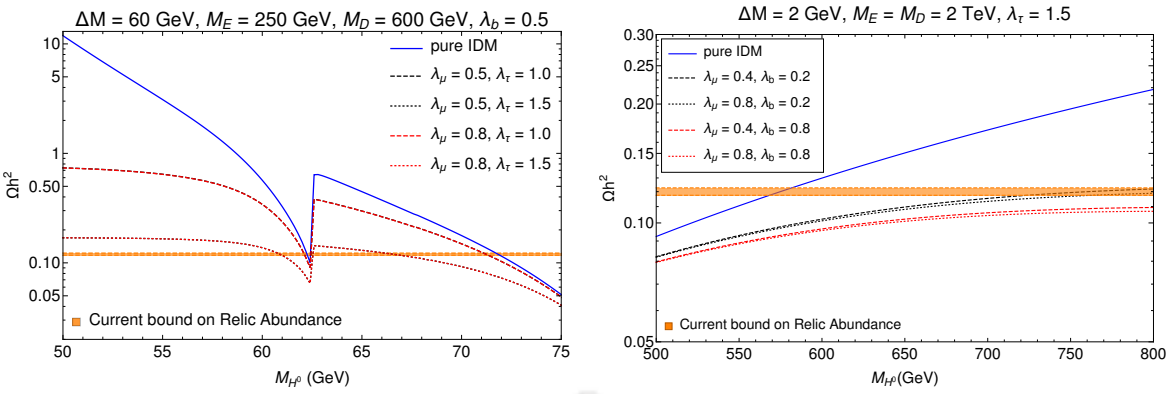

Figure 3.5: Variations of relic abundance with the DM mass M_{H^0} for different values of the couplings in the (a) low mass and (b) high mass regions of the DM. The plots show that as we switch on the leptonic and/or quark portal couplings, new annihilation channels open up, lowering the relic abundance for a fixed DM mass. In Fig.3.5a, the black-dashed and red-dashed lines overlap and hence not visible. This is due to the fact that when λ_τ is large, small variations in λ_μ does not affect the relic abundance. Similarly, the black and red dotted lines are also overlapped. See text for more details.

we are mostly interested in the observables which do not have dominant contributions from λ_d.

3.6 Results: DM and flavour

In this section we discuss the results obtained from the analysis of the DM and flavour sector of our model. We scan the NP parameter space using the constraints from flavour data, relic density and direct detection bounds. In the context of our model, the relevant free parameters are: λ_b, λ_s, λ_μ, λ_τ, M_{H^0}, M_{A^0}, $M_{H^\pm}$, M_{E_3}, M_{E_2}, M_{E_1}, and $M_{D_1} = M_{D_2} = M_{D_3} = M_D$ [2] .

In order to simplify the analysis, amongst them we have fixed few of the couplings, such as $\lambda_s = 0.01$ and $\lambda_e = 0.001$. Also, we choose $\lambda_b < 1$, $\lambda_\mu < 1.5$ and $\lambda_\tau \approx 1.5$. The rest of the free parameters are constrained from the $R_{K^{(*)}}$, $\mathcal{B}(B_s \to \mu\mu)$, Δa_μ and relic data. With these choices of the couplings, we can easily overcome the present constraints on flavour changing $b \to s$ processes, like $B_s - \bar{B}_s$ mixing, $\mathcal{B}(B \to X_s\gamma)$ etc. We will explicitly show this for $B_s - \bar{B}_s$ mixing. We have checked that in our model within the chosen benchmark points given in Table 3.2, the new physics contribution to the branching fraction $\mathcal{B}(B \to X_s\gamma)$ will be of order $\mathcal{O}(10^{-6})$ which is suppressed with respect to the corresponding SM branching fraction by two order of magnitude.

First, we will discuss the effects of different parameters of our model on DM relic abundance. As mentioned earlier, in pure IDM, there exists two distinct regions of DM mass which satisfy the relic abundance criterion. In Fig. 3.5 we have shown the variations of DM relic abundance with M_{H^0} in two different DM mass regions (low and high) for different new couplings and masses of the exotic vector like fermions. In Fig. 3.5a, we have kept $\Delta M = 60$ GeV and varied M_{H^0} between 50 GeV and 75 GeV (low DM mass region). In this region, with the variation of our new

[2]Though in our case the significant contributions will come from $M_{D_3} = M_D$.

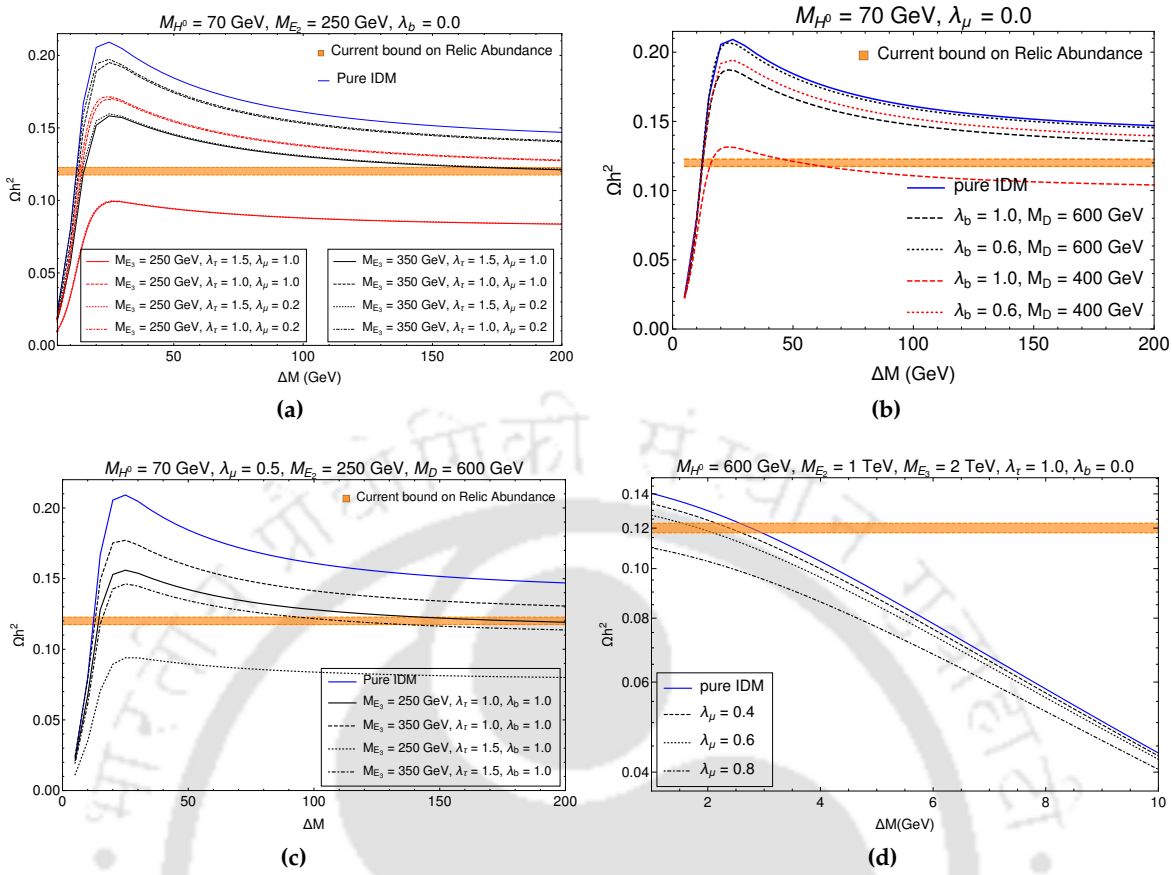

Figure 3.6: The plots in the top panel (3.6a,3.6b) and the bottom left plot (3.6c) shows the variations of relic abundance with the mass splitting $\Delta M = M_{H^\pm} - M_{H^0} = M_{A^0} - M_{H^0}$ for the DM mass $M_{H^0} = 70$ GeV. Here, different benchmark points are chosen for the other new parameters. The similar correlations in the high DM mass region ($M_{H^0} = 600$ GeV) is shown in the bottom right plot (3.6d).

parameters, the allowed values of M_{H^0} do not change significantly from that obtained in pure IDM case. In Fig. 3.5b, we have kept $\Delta M = 2$ GeV and $M_{H^0} > 500$ GeV (high DM mass region). Here, the same mass splitting between different components of the inert scalar doublet namely, $\Delta M = M_{H^\pm} - M_{H^0} = M_{A^0} - M_{H^0}$ are considered. In this region, the deviation from pure IDM scenario is significant.As expected, for the fixed values of the masses of the vector like fermions, the new couplings and the associated allowed values of M_{H^0} are positively correlated. For the pure IDM scenario, in the low mass region, the allowed values of M_{H^0} is not strongly correlated with the choice of ΔM, while in the high mass region the relic abundance is only satisfied when ΔM is very small, or in other words when the inert scalars are nearly degenerate. Also, in Fig. 3.5a, the black-dashed and red-dashed lines overlap with each other. This shows that the DM mostly annihilates to $\tau^+\tau^-$ pairs through vector-like lepton E_3 and the annihilation to muon pair is sub-dominant since the coupling λ_τ is much larger than λ_μ. Hence small changes in λ_μ does not affect the relic abundance when λ_τ is large for universal vector-like lepton masses.

For simplicity, in the low DM mass region, we have fixed M_{H^0} at 70 GeV for the rest of our analysis. In Fig. 3.6, we have shown the variations of the relic abundance with the mass splitting

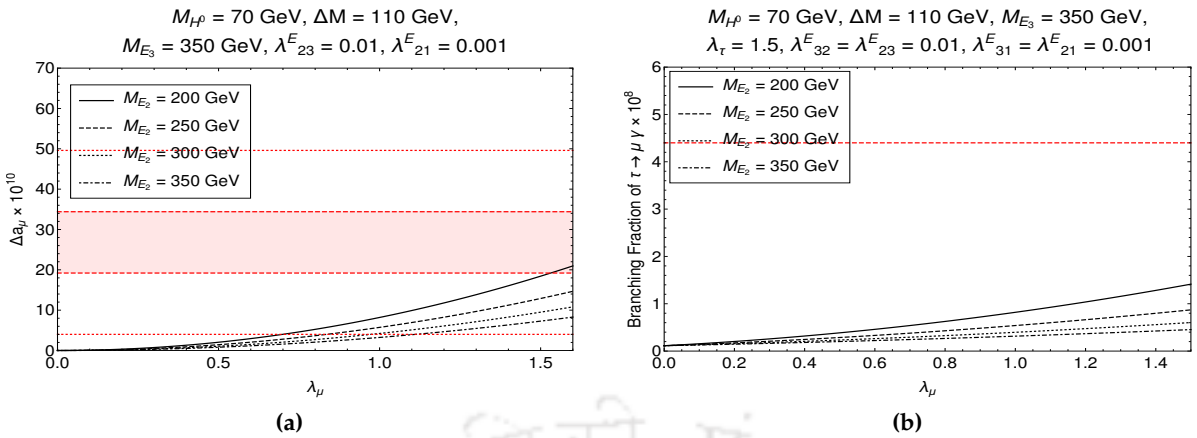

Figure 3.7: The left plot shows the variations of Δa_μ (muon $(g-2)$) with the coupling λ_μ for different values of M_{E_2}. In these plots M_{H^0} has been taken as 70 GeV. The red dashed and dotted lines represent the 1-σ and 3-σ bands of the Δa_μ, respectively. The right plot shows that with the same benchmark values of the NP parameters the decay width for $\tau \to \mu\gamma$ is well below the present experimental limit [12].

ΔM for different benchmark values of the new couplings and masses. From Fig. 3.6a, 3.6b and 3.6c we note that, as the new parameters are switched on, the relic abundance decreases compared to pure IDM scenario due to the increase in annihilation cross section. Also, the required mass splitting ΔM will be less in our model compared to that in pure IDM. Since we have assumed $\lambda_\tau > \lambda_\mu$ the dominant contributions to the relic abundance will come from the annihilation to $\tau^+\tau^-$, which can be seen from Fig. 3.6a where the variations are almost independent of the choices of λ_μ. The sensitivity of the relic abundance to the mass splitting in the high mass region is shown in Fig. 3.6d. With the increase in λ_μ, the mass degeneracies are becoming tighter compared to pure IDM scenario. Similar trend is also expected with the variation of λ_b as well.

In section 3.4, we have discussed various diagrams and their contributions to muon $(g-2)$ and LFV decays $\ell_i \to \ell_j\gamma$. There will be contributions from penguin diagrams with vector like leptons E_3, E_2 or E_1 in the loop. However, since we are assuming hierarchical structure for the couplings: $\lambda^E_{21} < \lambda^E_{23} << \lambda^E_{22}(= \lambda_\mu) \lesssim \lambda^E_{33}(\equiv \lambda_\tau)$, the diagrams with E_3 and E_1 in the loop will not give significant contributions to Δa_μ. However for completeness, we consider all those contributions in our analysis. The dominant contribution will come from the penguin diagram with E_2 in the loop. The variations of Δa_μ with the new coupling λ_μ for different values of M_{E_2} are shown in Fig. 3.7a. We note that if we restrict ourselves to the values of $\lambda_\mu < 1.5$, then it will be difficult to explain the excess in muon $(g-2)$ within its 1-σ range, unless we consider vector like lepton mass $\lesssim 200$ GeV. However, the excess can be succesfully explained within its $3-\sigma$ range for values of $\lambda_\mu \lesssim 1.5$ and we restrict ourselves to this limit only. Especially, higher masses prefer higher values of the coupling λ_μ. In future with more precision measurements, the tension between the predicted and measured values may reduce i.e the data may become more SM-like. In such situations, the data on a_μ will not put strong constraints on our model parameters. In the opposite situations, one may need to consider values of $\lambda_\mu \gtrsim 1.5$. On the other hand, the contribution from all the vector like

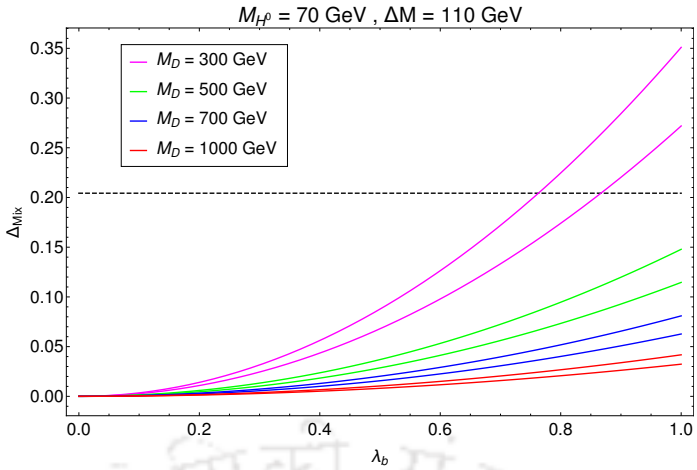

Figure 3.8: Variation of $\Delta_{\rm Mix}$ with λ_b for four different values of the vector-like quark mass $M_D(= M_{D_3})$, since the dominant contribution will come from $D = D_3$. The black dashed line indicates the maximum allowed value of $\Delta_{\rm Mix}$ if we take all the inputs in Eqn. (3.28) within their respective 1σ confidence interval.

fermions will be relevant for the LFV decays. However, since in our framework the off-diagonal elements are small compared to the diagonal elements, the contribution to the branching fraction will not be significantly large. As an example, we have chosen $\lambda^E_{32} = \lambda^E_{23} \approx 0.01$. With this choice, the branching fraction $\tau \to \mu\gamma$ will be much below the current experimental limit, even if we choose λ_μ or λ_τ roughly $\sim \mathcal{O}(1)$ (Fig. 3.7b). Here, we have not discussed the LFV $\tau^- \to \mu^-\mu^+\mu^-$ decay. In our model, the leading diagram for this decay is same as $\tau \to \mu\gamma$, with a virtual photon converting into a muon pair [3]. It is expected that for the same set of NP parameters the branching fraction $\mathcal{B}(\tau \to \mu^-\mu^+\mu^-)$ will be small compared to $\mathcal{B}(\tau \to \mu\gamma)$; as an example see [197]. Therefore, our NP parameters will be safe with respect to present limit $\mathcal{B}(\tau \to \mu\mu\mu)(\approx \mathcal{O}(10^{-8}))$ [12]. The LFV decays and Δa_μ are insensitive to the coupling λ_b. However, observables like $R_{K^{(*)}}$ and DM relic abundance are sensitive to all the relevant couplings and masses of the model.

In the case of $B_s - \bar{B}_s$ mixing, in Fig. 3.8 we have shown the variations of $\Delta_{\rm Mix}$ with λ_b for different values of the masses of M_{D_3}. The black dashed line indicates the 15% allowed range in $\Delta_{\rm Mix}$, the solid lines represent our model predictions for different values of the vector-like quark mass. The other relevant parameters are fixed as before. We note that for $M_{D_3} \geq 500$ GeV, the allowed value of λ_b could be as big as 1. However, for lower values of M_{D_3} higher values of λ_b will be disfavoured, as an example we can see that for $M_{D_3} = 300$ GeV, $\lambda_b \gtrsim 0.7$ will not be allowed. Here, we would like to point out that the major uncertainties in the theory prediction is associated with the decay constant. Therefore, if we consider the errors within their 1σ confidence limit (CL) ranges, then that will give us a conservative estimate of the allowed NP. We would like to stress that data will still allow a NP contribution up to 30-40% at the 3σ CL [202].

As mentioned earlier, the branching fraction for the rare decay $B_s \to \mu^+\mu^-$ is consistent with its SM prediction within 1σ confidence level. Therefore, the data on $\mathcal{B}(B_s \to \mu^+\mu^-)$ is expected to

[3]There will be one additional box diagram, the contribution of which will be suppressed compared to that of the penguin diagram.

put tighter constraints on the parameters of any NP model in the decay $b \to s\mu\mu$. More importantly if we see the current data, the measured value is below that of SM prediction and our model has the potential to accommodate it. Although we are not considering it seriously, we have to wait for more precise data and lattice inputs to conclude it further, but at the moment one can not rule out this possibility. The main source of error in $B_s \to \mu\mu$ is the decay constant f_{B_s} whose different lattice predictions have different errors (for detail see ref. [77]). Therefore, in order to be conservative, the errors in the measured value have been taken in their 2σ confidence level allowed ranges to constrain the NP parameters.

From phenomenology point of view according to the low and high DM mass regions, we divide our analysis into two parts: in one part, we choose $M_{H^0} = 70$ GeV (low DM mass), and in the other we have considered $M_{H^0} = 600$ GeV (high DM mass). These will be discussed in the following sections.

3.6.1 Low mass DM

In this section we show our main results for a light dark matter of mass 70 GeV and mass splitting $\Delta M = 110$ GeV. Keeping in mind all the relevant correlations between the different parameters shown above, we do a multi-parameter scan to find out the common parameter space that satisfies all relevant flavour constraints i.e. $R_{K^{(*)}}$, $\mathcal{B}(B_s \to \mu^+\mu^-)$, muon magnetic moment anomaly in Δa_μ as well as the correct relic abundance and direct detection bounds of dark matter as shown in Fig. 3.9. To generate these plots we assumed, for simplicity, that all generations of the vector-like leptons have the same mass i.e $M_{E_1} = M_{E_2} = M_{E_3} = M_E$. More regions on the parameter spaces of λ_μ and M_{E_2} will be allowed if we relax this mass degeneracy. We allow both M_E and M_D to vary between 200 and 1000 GeV instead of keeping them fixed. In these plots λ_τ has been varied between $1.0 - 1.5$, while we have kept $\lambda_\mu < 1.5$ and $\lambda_b < 1$. As mentioned earlier, the major constraints on the new parameters are mainly coming from the flavour data, in particular from $\mathcal{B}(B_s \to \mu\mu)$. The blue scattered points satisfy the data on R_K, R_{K^*} and $\mathcal{B}(B_s \to \mu\mu)$ in their respective 2σ confidence intervals which shrink to the green points when we also consider Δa_μ as a constraint. Here, we have considered the excess in Δa_μ within its 3-σ range. The red regions represent the bound on the NP parameters from the relic density and direct detection cross section of DM. An interesting feature here is the presence of two distinct regions in the parameter spaces of λ_μ, λ_b and M_D (Fig. 3.9a and 3.9b). These two regions correspond to high and low values of λ_b, respectively. In both the allowed regions, λ_μ can take moderate values > 0.5. However, its magnitude can not be very high ($>> 1$) when $\lambda_b \gtrsim 0.7$. On the other hand when λ_b is small, the common parameter spaces are obtained in regions where $\lambda_\mu \approx 1.5$, which could be relaxed and the values $\lambda_\mu \lesssim 1.5$ will be allowed if we lift the mass degeneracies of the vector like leptons, for example see Fig. 3.10a[4]. Hence, for completeness we have analysed both these regions in the collider searches as will be

[4]If we lift the mass degeneracies in the vector like leptons than for higher masses of M_{E_3} the DM will mostly annihilate to $\tau^+\tau^-$ and this channel will contribute maximally to the relic abundance. Hence, their won't be any strong constraints on the parameter spaces of M_{E_2} and λ_μ from relic abundance which can also be understood from the observations made in Fig. 3.6a and 3.6c.

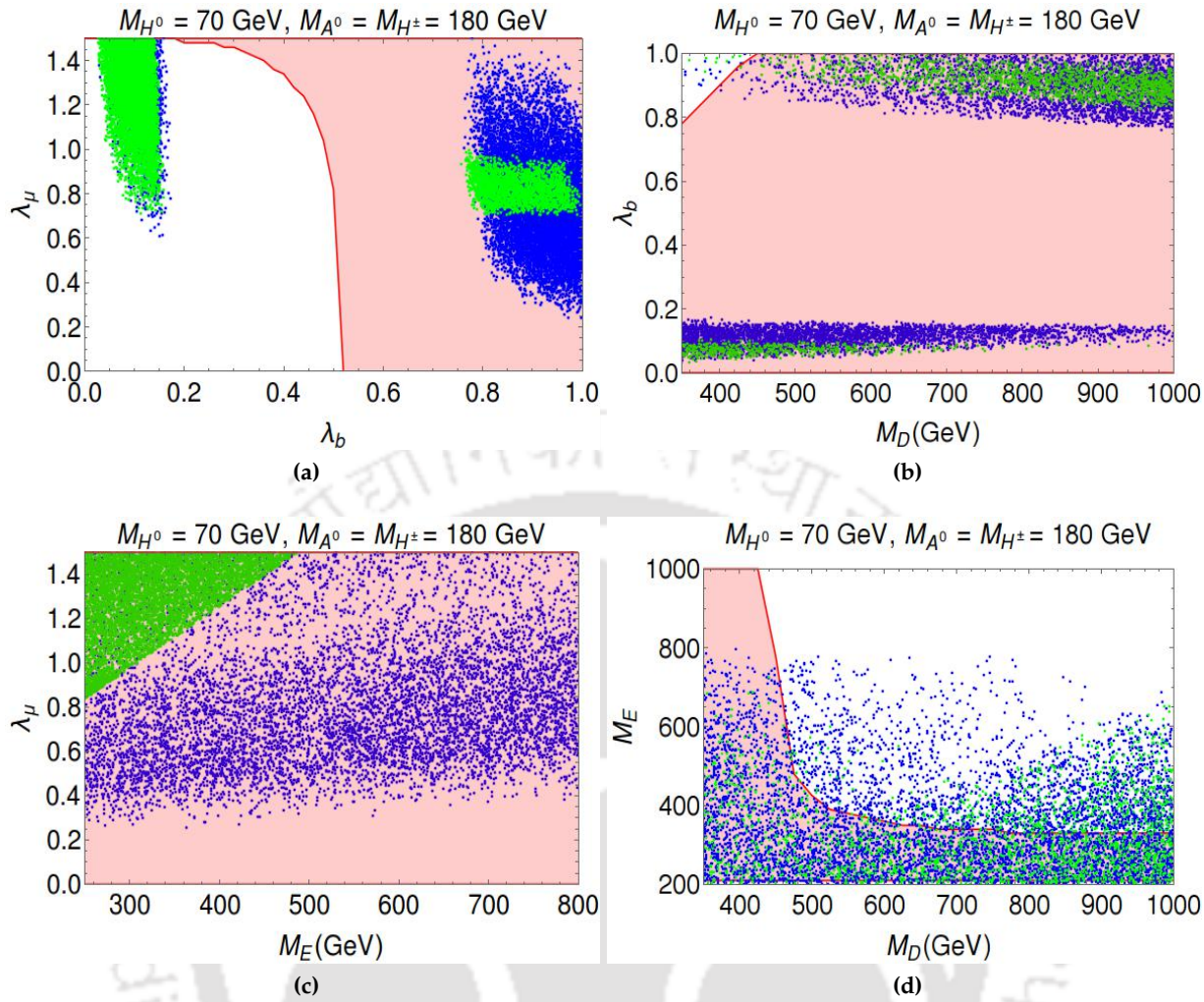

Figure 3.9: Correlation between different NP parameters for a Low Mass DM at $M_{H^0} = 70$ GeV. The blue points satisfy all relevant flavour constraints within their 2σ confidence intervals except muon (g-2) anomaly. When we further apply the muon anomalous magnetic moment bounds then the allowed region shrinks as depicted by the green points(see text). The red region satisfy the relic and direct search constraints when we consider degenerate vector-like fermion masses.

discussed later. Also, we note that $\lambda_\mu > 0.4$ for $M_E \lesssim 800$ GeV and $\lambda_b > 0.7$ in the whole range of M_D are allowed by all data. Note that muon $(g-2)$ is not sensitive to λ_b or M_D. Also, we see a nice correlation between M_E and M_D, for the higher values of M_D (≥ 500 GeV) the relic density prefer $M_E \leq 400$ GeV. We have checked that this constraint can be relaxed if we assume non degenerate vector like fermion masses for all the generations, for example see Fig. 3.10b.

Following the above discussions, from the allowed parameter spaces we have chosen seven benchmark points (BPs), listed in Table. 3.2, for collider analysis elaborated in Sec. 3.7. Also, we have checked that the values of the Wilson coefficients C_9^{NP} and C_{10}^{NP} in all these benchmark scenarios are consistent with those obtained from the global fit [157], in particular the scenario with $C_9^{NP} = -C_{10}^{NP}$. We have focussed on both the allowed regions of couplings as shown in Fig. 3.9a, so that we can phenomenologically distinguish them from each other. BP1 to BP5 have the characteristics of high λ_b and intermediate λ_μ while a low λ_b and high λ_μ characterize BP6 and

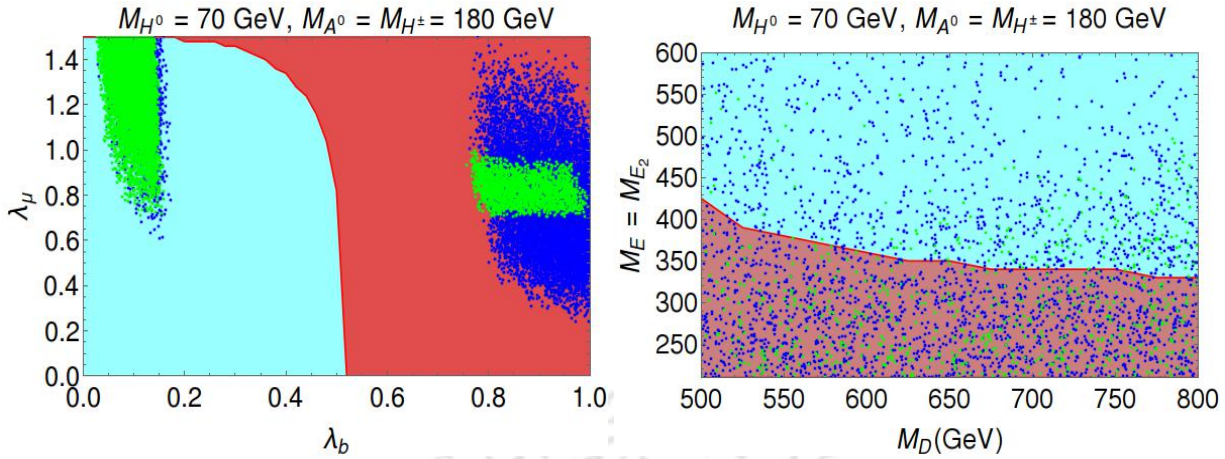

Figure 3.10: Similar plots as given in 3.9a and 3.9d. In addition, we have considered the case $M_{E_2} \neq M_{E_3}$ which is represented by cyan region. This region satisfies the relic and direct detection constraints when we assume the non-degenerate vector-like lepton masses.

BP	M_D (GeV)	λ_b	M_{E_2} (GeV)	λ_μ	M_{E_3} (GeV)	λ_τ	Ωh^2	R_K	R_{K*}	$\Delta a_\mu \times 10^{10}$	$\mathcal{B}(\tau \to \mu\gamma) \times 10^9$	$\mathcal{B}(B_s \to \mu\mu) \times 10^9$
1.	500	0.9	150	0.5	350	1.5	0.120	0.769	0.760	3.15	5.98	1.95
2.	750	0.9	250	0.7	250	1.2	0.117	0.777	0.769	2.8	5.71	2.49
3.	750	0.9	200	0.7	350	1.5	0.122	0.758	0.749	4.01	5.39	2.55
4.	850	0.9	250	0.7	250	1.2	0.118	0.808	0.800	2.81	5.71	2.59
5.	900	0.9	350	0.8	350	1.5	0.119	0.803	0.796	2.07	2.67	2.69
6.	800	0.1	300	1.5	350	1.5	0.121	0.908	0.903	9.5	6.03	1.89
7.	800	0.1	180	1.5	500	1.5	0.121	0.885	0.880	4.62	5.35	1.84

Table 3.2: Model prediction of different relevant observables corresponding to our chosen benchmark points.

BP7. Here we would like to mention that there is an existing lower limit on pair-produced charged heavy vector-like leptons from LEP [203] : $m_{L^\pm} \gtrsim 101.2$ GeV. Our benchmark points satisfy this limit.

In pure IDM, the electroweak precision observables (EWPO) like S and T, play an important role in constraining the mass splitting ΔM between the inert scalars [180]. We have already taken care of this constraint while scanning the new parameter spaces. Our model contains singlet vector fermions which do not mix. Hence, there will not be any additional significant contributions in S, T and U parameters, although there will be diagrams that contribute to $Z \to \mu\bar{\mu}$ and $Z \to b\bar{b}$ decays at one loop level. However, we have checked that within our chosen model parameters those contributions are highly suppressed. Therefore, the EWPO will not put any stringent constraint on our model parameters.

Before moving on to the collider analysis, we show, for illustrative purpose, the variation of spin-independent direct search cross section (per nucleon) with the DM mass in Fig. 3.11 for some

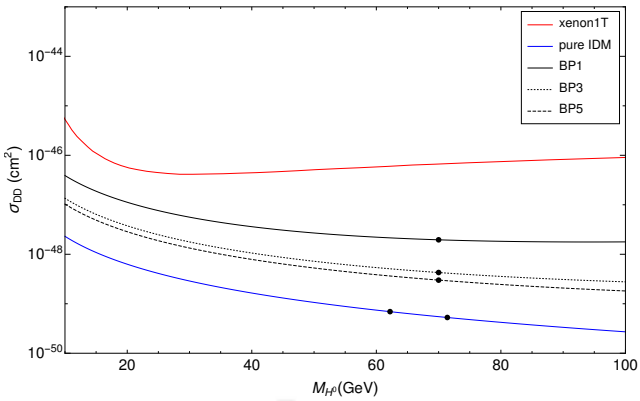

Figure 3.11: The plot shows the variation direct detection cross section with DM mass in direct search plane. The black lines correspond to different BPs, where the DM mass has been varied, while the dots correspond to specific choices of the DM mass (see text for details), the red line is the exclusion limit from recent XENON-1T data and the blue line is the direct search limit from pure IDM case.

of the chosen BPs in Table. 3.2. For a comparison, the similar correlation for pure IDM is presented in the same figure. The solid red line is the exclusion limit from recent XENON-1T data [189]. The black dots on each black line refer to particular point corresponding to a fixed M_{H^0}, satisfying constraints from relic density, direct search (as they lie below the experimental exclusion limit) and flavour bounds (which we have discussed in Sec. 3.4 and Sec. 3.5.1). As pointed out earlier, and can now be seen from these plots, the presence of exotic quarks increases the direct detection rates compared to the pure IDM keeping it more promising for observing at ongoing direct search experiments.

3.6.2 High Mass DM

We analyze the high DM mass region of the IDM in context of our extended framework. As discussed earlier, we need to consider degenerate masses for the IDM scalars (as we need to resort on co-annihilation channels in order to satisfy relic density) and also tune $\lambda_L (= \lambda_3 + \lambda_4 + \lambda_5)$, which involves the DM-Higgs interaction, to an appropriate value. So the masses of vector-like leptons (E_i) and the vector-like bottom partner (D) will have to be greater than the masses of A^0 or $H^\pm$ to maintain the stability of the DM. We consider a mass splitting of 2 GeV between the inert scalars and set λ_L to 0.0001.

The parameter space which are allowed by flavour data are shown in Fig. 3.12a and Fig. 3.12b. We have kept the value of the DM mass fixed at $M_{H^0} = 600$ GeV. It is interesting to note that, in this case, we will be able to explain the $R_{K^{(*)}}$ anomaly only for higher values of λ_μ (≈ 3 or 4). However, for the same masses, such high values of λ_μ will not allow us to achieve right relic abundance (see Fig. 3.12c). Hence, it is not possible to obtain a common parameter space that satisfies both relic abundance and flavour constraints simultaneously. When we add new interactions, new annihilation channels open up and they make the DM under-abundant. So in order to make the effects of NP minimal, we require the couplings to be small but masses to be large (Fig .3.5b). However,

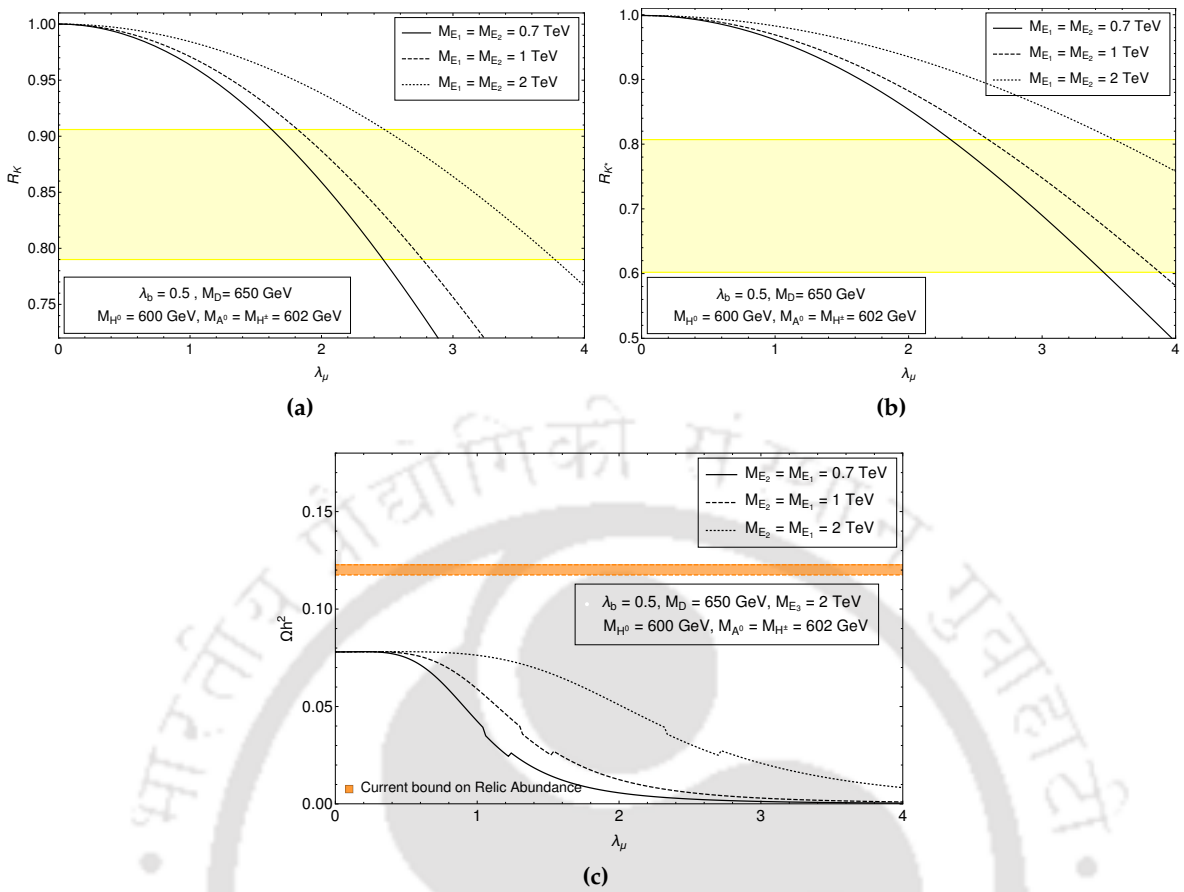

Figure 3.12: Top Left (3.12a): Variation of R_K with λ_μ for fixed values of DM mass and λ_b, for three different values of M_{E_2}. The yellow band shows the 1σ experimental range of R_K. Top Right (3.12b): Same for 1σ experimental range of $R_{K^{(*)}}$. Middle (3.12c): Variation of relic abundance with λ_μ for the same chosen parameters as in 3.12a and 3.12b, the orange band shows the Planck-observed relic density bound.

if we also want to explain the flavour anomalies for such high values of the vector like fermions masses, we need very high values of couplings as well ($\lambda_\mu \gtrsim 3$) . So it is impossible to achieve solution in this region of DM mass and hence we discard further investigations for this case.

3.7 Collider Phenomenology

Our goal is to investigate the implications of our model on collider searches at the LHC. As mentioned earlier, we have expanded the contact interaction of the DM with the SM and included the vector like fermions (mediators) as propagating degrees of freedom of the theory. Also, it is clear from the above discussions that the mediators have decay channels to the SM fermions. In this section, we will analyze the prospects for detecting our model at the LHC through various channels. Due to the presence of the exotic vector like leptons and quarks, the model gives rise to several tantalizing collider signatures. Here, we have discussed a few of them:

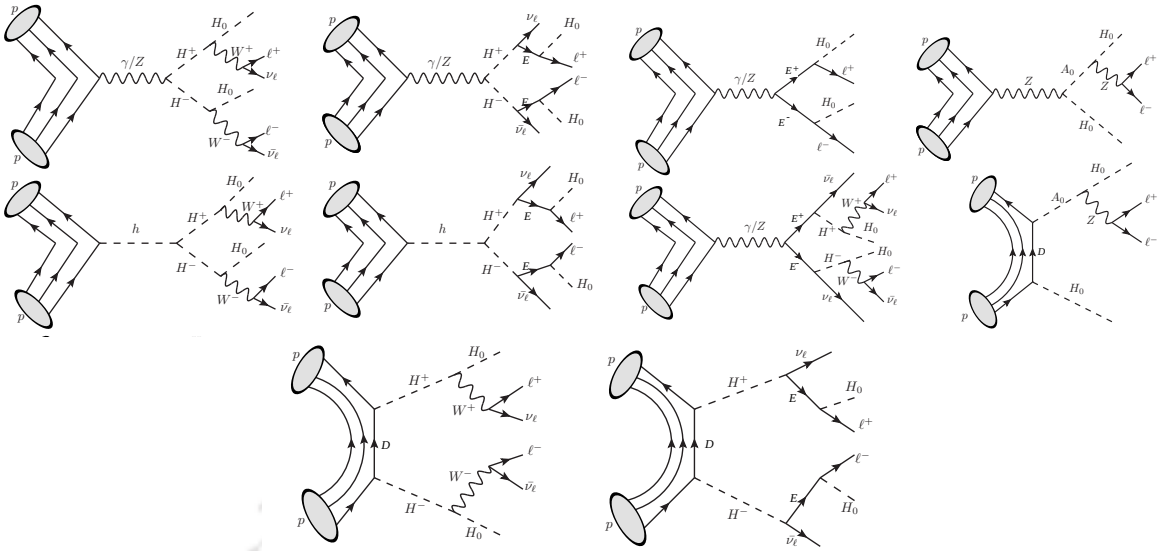

Figure 3.13: Feynman diagrams for the production of $(\ell^+\ell^- + \not{E}_T)$ final state at a hadron collider like LHC

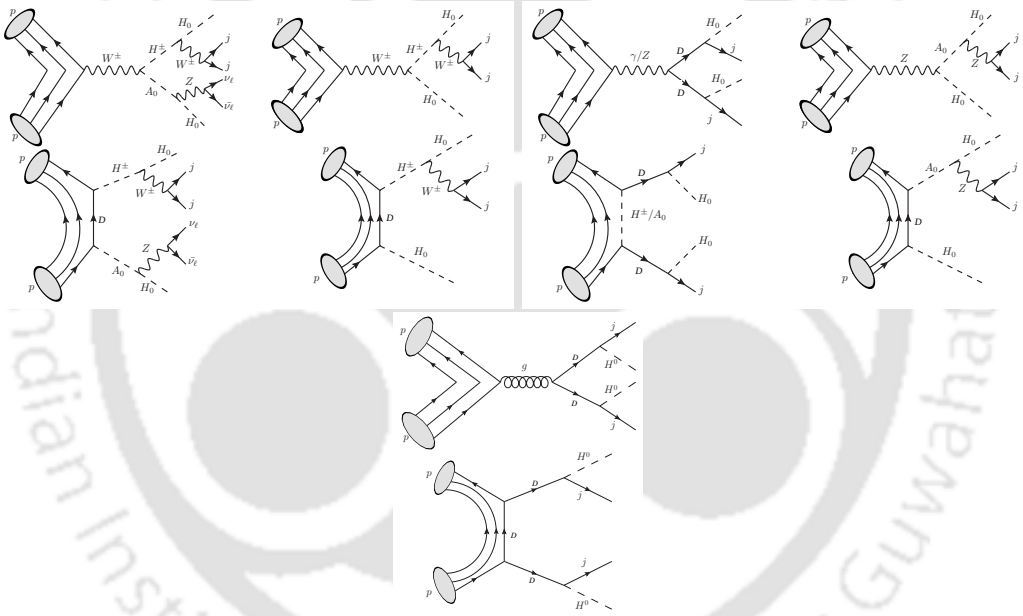

Figure 3.14: Feynman diagrams for channels contributing to $jj + \not{E}_T$ final state. The gluon fusion diagram has also been considered in this case

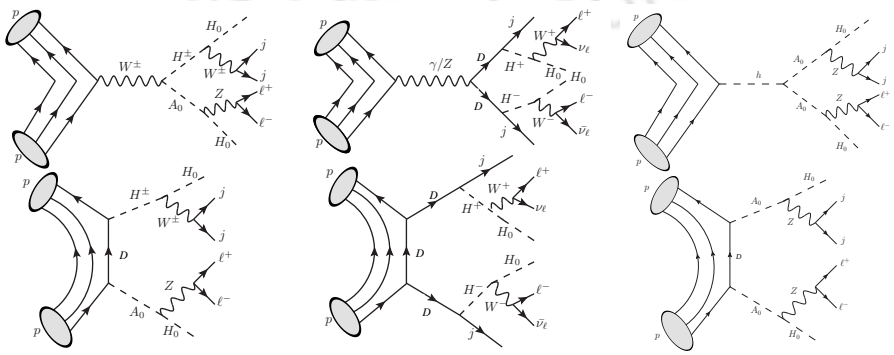

Figure 3.15: Feynman diagrams for channels contributing to $\ell^+\ell^- + jj + \not{E}_T$ final state.

- Opposite sign dilepton (OSD) with missing energy $(\ell^+\ell^- + \not{E}_T)$[5].
- Dijet with missing energy $(jj + \not{E}_T)$, there are cases where the b-jets have been tagged separately.
- Dilepton with dijet and missing energy $(\ell^+\ell^- + jj + \not{E}_T)$.

All these three final states could be tested at the LHC. The corresponding Feynman diagrams for the final states $(\ell^+\ell^- + \not{E}_T)$, $(jj + \not{E}_T)$ and $(\ell^+\ell^- + jj + \not{E}_T)$ are given in figures 3.13, 3.14 and 3.15, respectively. In all these diagrams, the proton (p) is considered a multiparticle composed of both quarks and gluons. Hence, all possible initial states with quarks and gluons have been taken into account. We note that amongst all the diagrams, some will appear only in pure IDM case. Therefore, it is important to test whether it is possible to discriminate the signatures of our model from that of pure IDM at the LHC.

As mentioned earlier, from the common parameter space satisfying flavour constraints, relic density of DM and direct detection bound, we have chosen our benchmark points (BP), which are given in Table 3.2. All other parameters are fixed at the values: $M_{H^0} = 70$ GeV, $\Delta M = 110$ GeV, $m_h = 125$ GeV, $\lambda_L = 0.0001$, $\lambda_2 = 0.1$, $\lambda_{\rm d} = 0.001$, $\lambda_{\rm s} = 0.01$, $\lambda_{\rm e} = 0.001$.

BP	$\sigma_{\ell^+\ell^-+\not{E}_T}$ (fb)	$\sigma_{jj+\not{E}_T}$ (fb)	$\sigma_{\ell^+\ell^-+jj+\not{E}_T}$ (fb)
1.	588	278	0.31
2.	54	181	2.91
3.	173	177	2.73
4.	54	172	2.75
5.	17	173	2.98
6.	20	174	2.88
7.	307	174	1.00

Table 3.3: Production cross-sections for the different signals corresponding to the chosen benchmark points.

3.7.1 Object reconstruction and simulation strategy

We implemented the model in `FeynRule` [204]. The parton level events are generated in `MADGRAPH` [205], which are further showered through `PYTHIA` [206]. All the events are generated at $\sqrt{s} = 14$ TeV using `CTEQ6l` [207] as the parton distribution function. All the leptons and jets are reconstructed in order to mimic the LHC environment using the following criteria:

[5]Hadronically quiet dilepton with missing energy

- *Lepton ($l = e, \mu$):* Leptons are identified with a minimum transverse momentum $p_T > 20$ GeV and pseudorapidity $|\eta| < 2.5$ such that they are in the central part of the detector. Two leptons are distinguished as isolated objects if their mutual distance in the $\eta - \phi$ plane is $\Delta R = \sqrt{(\Delta\eta)^2 + (\Delta\phi)^2} \geq 0.2$, while that separation between an isolated lepton and a jet is given by $\Delta R \geq 0.4$.

- *Jets (j):* The cone jet algorithm `PYCELL` has been used to build jets inside `PYTHIA`. All the partons within $\Delta R = 0.4$ from the jet initiator cell are included to form the jets. We require $p_T > 20$ GeV for a clustered object to be considered as jet. Jets are isolated from unclustered objects for $\Delta R > 0.4$.

- *Unclustered Objects:* All the final state objects which are neither clustered to form jets, nor identified as isolated leptons, belong to this category. All particles with $0.5 < p_T < 20$ GeV and $|\eta| < 5$, are considered as unclustered.

- *Missing Energy ($\not{E}_T$):* The transverse momentum of all the missing particles (those are not registered in the detector) can be estimated from momentum imbalance of the visible particles in the transverse direction. Thus, missing energy (MET) is defined as:

$$\not{E}_T = -\sqrt{(\sum_{\ell,j} p_x)^2 + (\sum_{\ell,j} p_y)^2}, \tag{3.30}$$

  where the sum runs over all visible objects that include the leptons and jets, and the unclustered components.

- H_T: We have used another observable for collider searches which is the scalar sum of all isolated lepton/jet transverse momentum:

$$H_T = \sum_{\ell,j} p_T \tag{3.31}$$

The dominant SM backgrounds have been generated in `MADGRAPH` and then showered through `PYTHIA`. Also appropriate K-factors were used to match them with the Next-to-Leading order (NLO) cross section. We have identified dominant SM backgrounds as: $t\bar{t}$, W^+W^-, $W^\pm Z$, ZZ, Wj, Zj and $Drell - Yan$ for the chosen signal regions. The discovery potential of the the model, in terms of signal significance, are shown for only those cases where the signal can be clearly distinguished from the SM background. In each case, we have also shown the status of pure IDM scenario for comparison purpose. Once again we would like to remind the readers that the purpose of the collider phenomenology in our context is not to search for signals of the VLFs, but to look for the signature of the model itself. In that sense, our choice of observables and cuts are different from that of dedicated experimental searches done at the LHC or LEP.

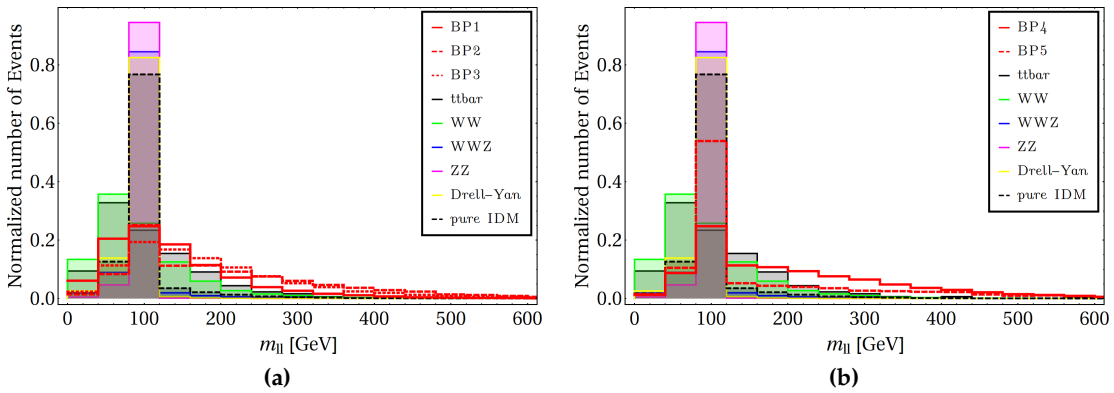

Figure 3.16: Invariant dilepton mass ($M_{\ell\ell}$) distribution for the signals (in red), with SM backgrounds for ($\ell^+\ell^- + \not{E}_T$) channel.

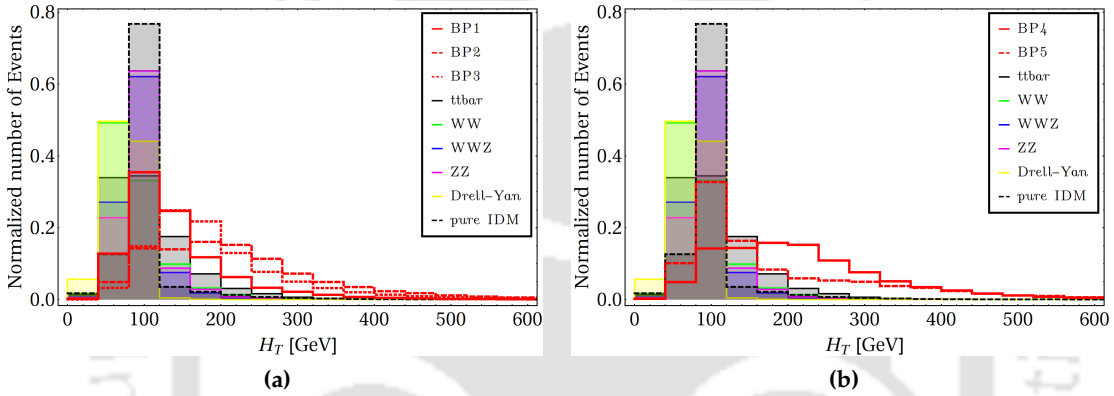

Figure 3.17: H_T distribution for the signals (in red), with SM backgrounds ($\ell^+\ell^- + \not{E}_T$) channel.

3.7.2 Dilepton with missing energy final state

In Fig. 3.16 and 3.17, we have shown respectively the dilepton invariant mass ($M_{\ell\ell}$) and H_T distributions for the signal, in comparison with the relevant SM background for final states containing opposite sign dilepton and MET. As one can see from Fig. 3.16, the primary difference in the $M_{\ell\ell}$ distribution between the signal and the background lies in the fact that we observe a long tail in case of signal, which is not present in the background. The reason being, in case of signal, the source of the leptons in the final state are the heavy new particles apart from the SM gauge bosons. Since these particles are heavier than the SM gauge bosons, hence the leptons in this case are much boosted than those coming only from the SM gauge bosons. As a result, we see a flatter distribution for $M_{\ell\ell}$ for the signal compared to the SM background (Fig. 3.16). As an example in Fig. 3.13, we see that for signal, the leptons in the final state arise not only from SM Z or W but also from the decay of heavy new particles *e.g*, $E^+ \to H^0\ell^+$. The same arguement holds for H_T, where a flatter signal distribution (Fig. 3.17) arises because of the less boosted leptons in the final state.

From $M_{\ell\ell}$ distributions shown in Fig. 3.16 we can see that a cut: $M_{\ell\ell} \gtrsim 300$ GeV can help us to get rid of the SM background completely for all BPs except BP1, retaining the signal intact. For

Benchmark Points	$\sigma^{\text{production}}$ (pb)		σ^{OSD} (fb)
BP1	0.58		11.98
BP2	0.05	$M_{\ell\ell} > 200$ GeV	3.05
BP3	0.16	$H_T > 280$ GeV	8.77
BP4	0.05		3.04
BP5	0.01		0.45
BP6	0.02		0.48
BP7	0.30		0.85
Pure IDM	0.16		0.03

Table 3.4: Final state signal cross-section with $M_{\ell\ell} > 200$ GeV and $H_T > 280$ GeV for $OSD + \not{E}_T$ final state. All simulations are done at $\sqrt{s} = 14$ TeV.

Benchmark Points	$\sigma^{\text{production}}$ (pb)		σ^{OSD} (fb)
$t\bar{t}$	81.64		48.78
WW	99.98	$M_{\ell\ell} > 200$ GeV	36.99
WWZ	0.15	$H_T > 280$ GeV	0.06
ZZ	14.01		0.14
Drell-Yan	2272.80		0.14

Table 3.5: Final state SM background cross-section with $M_{\ell\ell} > 200$ GeV and $H_T > 280$ GeV for $OSD + \not{E}_T$ final state. All simulations are done at $\sqrt{s} = 14$ TeV.

BP1, on the other hand, such a cut kills the background along with the signal as well. Similar kind of trend is also observed in the H_T distribution. In order to determine the signal significance We have used $M_{\ell\ell} > 200$ GeV and $H_T > 280$ GeV cuts for BP1-5.

For all the benchmarks, final state cross-section with all the above mentioned cuts imposed are tabulated in Table 3.4. Corresponding cross-sections for dominant SM backgrounds are also shown in Table 3.5. Inspite of the fact that such a cut kills most of the signals for BP1, due to its high production cross section (as shown in Table 3.3) it shows a very high significance along with BP3. Similarly, $\not{E}_T > 200$ GeV and $H_T > 320$ GeV have been used to compute the significance of BP6 and BP7 and a similar excess is seen in case of BP7 due to its high production cross section. Therefore,the benchmarks BP1, BP3 and BP7 are prone to be eliminated in ongoing LHC runs, if no excess is being found in those channels.

The significance plots for $OSD + \not{E}_T$ channels are shown in Fig. 3.18. From the plot we can

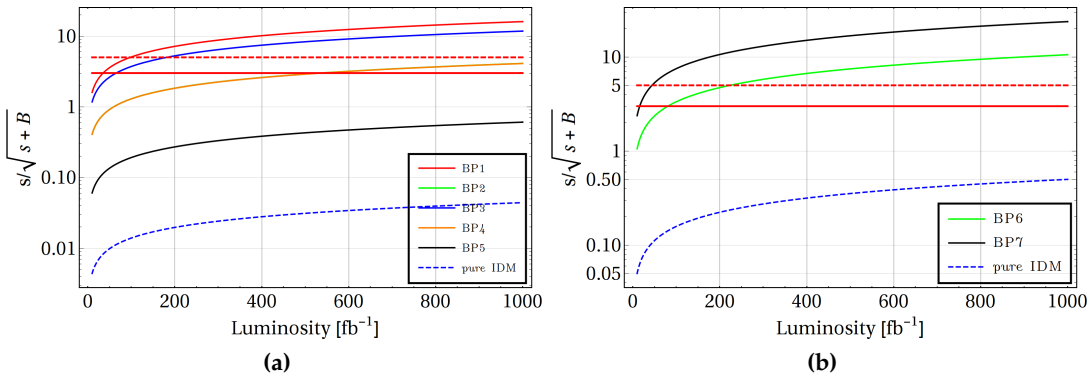

Figure 3.18: Significance plot for dilepton plus $\not{E}_T$ final state for the different BPs. The dashed blue line shows the significance for the pure IDM scenario for comparison. The thick red and the dashed red lines are respectively showing the 3σ and 5σ confidences. Note that we have used $M_{\ell\ell} > 200$ GeV and $H_T > 280$ GeV cuts to compute the significance of BP1 to BP5 (left plot) while $\not{E}_T > 200$ GeV and $H_T > 320$ GeV have been used to compute the significance of BP6 and BP7 (right plot).

infer that:

- So far at LHC, we have not seen any excess in $\ell^+\ell^- + \not{E}_T$ channels, therefore, our model parameters in BP1 and BP7 are most likely to be ruled out by LHC.
- There is still a possibility that BP3 and BP6 might be probed in the future run of LHC at a luminosity $\mathcal{L} \sim 60$ fb^{-1} and 200 fb^{-1} respectively.
- Due to identical masses of the vector like leptons (and hence same production cross section for dilepton final state), the significance of BP2 and BP4 are exactly the same. Both of them reach a discovery potential of 5σ at very high luminosity ($\mathcal{L} \sim 700$ fb^{-1}).
- It will be very hard to distinguish BP5 from pure IDM and seems almost impossible to be probed within the future limit of LHC luminosity.

Therefore, from the collider searches of the $(\ell^+\ell^- + \not{E}_T)$ final state, it is hard to rule out the model parameters entirely for some specific choices of BPs. What we see is that, vector like leptons with masses $\lesssim 200$ GeV are prone to be ruled out by LHC at present luminosity. But vector like leptons with masses of $\gtrsim$ 250 GeV and above are yet to be probed by the future high luminosity runs. In the future runs the non-observance of any excess in the data will help us to rule out higher mass regions of the vector like leptons.

3.7.3 Dijet plus $\not{E}_T$ final state with and without b-tagging

We have used $\not{E}_T$ and H_T as observables in order to distinguish the jet final state signal from that of the SM backgrounds. For the SM, the only source of $\not{E}_T$ are the SM neutrinos, which can be approximately taken to be massless at the colliders. As a result, the peak of the $\not{E}_T$ distribution for the background lies at a very low value of $\not{E}_T$. For signal, on the other hand, we can see from

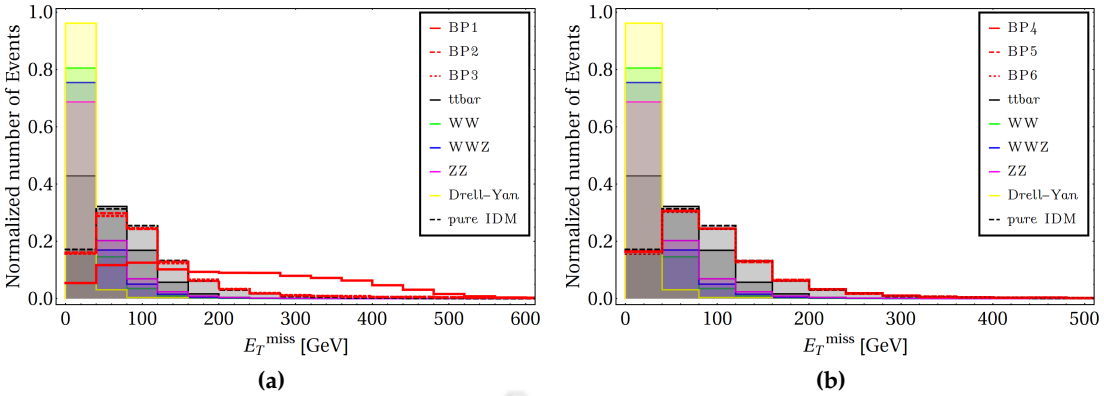

Figure 3.19: Missing energy ($\not{E}_T$) distribution for the signals (in red), with SM backgrounds for dijet+$\not{E}_T$ channel. We note that in the left plot, it is hard to distinguish the distributions of the benchmark scenarios BP2 and BP3 from each other. Similarly in the right plot all the signal distributions almost overlap with each other.

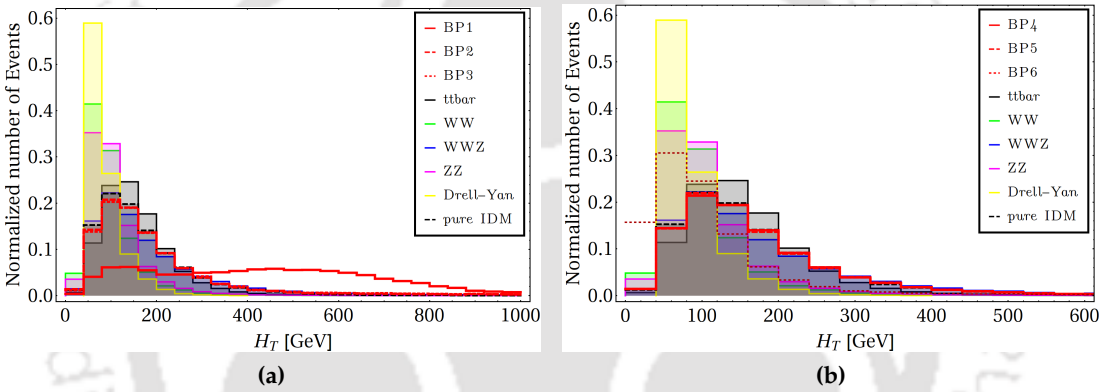

Figure 3.20: H_T distribution for the signals (in red), with SM backgrounds for dijet+$\not{E}_T$ channel. We note that in the left plot, it is hard to distinguish the distributions of the benchmark scenarios BP2 and BP3 from each other. Similarly in the right plot all the signal distributions for BP4 and BP5 almost overlap with each other.

Fig. 3.19 and Fig. 3.20 that except for BP1, in all the other benchmark scenarios it is extremely difficult to separate the signal of our model from the SM background and also from pure IDM signal. This is due to fact that in our model the dominant contributions to missing energy are coming from the diagrams in Fig. 3.14, where final states contain both SM neutrinos and the DM. Hence the shape of the distribution is not just dictated by the massive DM, but the massless neutrinos as well. The final state cross-sections are listed in Table 3.6 for the signal where we can see that the cross-section for BP1 is significantly large, while for other benchmarks they are almost the same. For the SM backgrounds corresponding cross-sections are also tabulated in Table 3.7. Note that, due to hadronic final state, the backgrounds are more vigorous here, making the signal less significant than that of leptonic final state.

In Fig. 3.21, we have shown the significance of different BPs for dijet final state with (left) and without (right) b tagging. For BP1, a significant excess can be seen in all the distributions and it shows a very high significance for present LHC luminosity, which are very likely to be ruled out

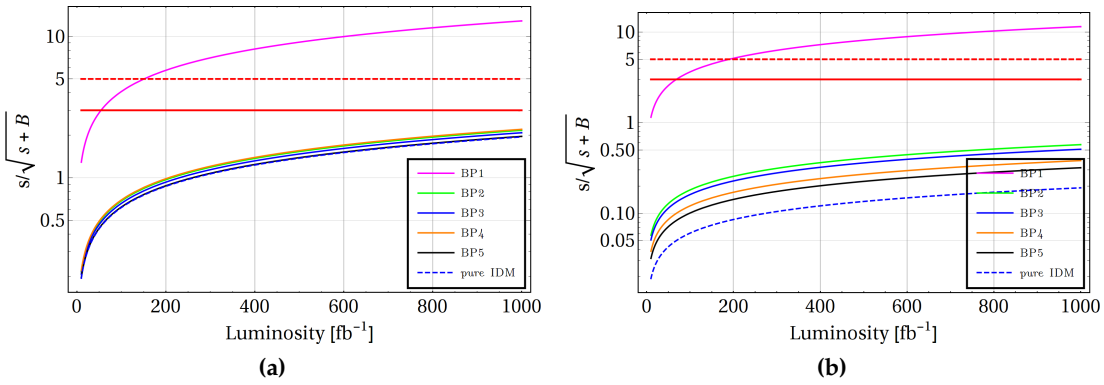

Figure 3.21: Left: Significance plot for dijet+$\not{E}_T$ final state for different BPs. Right: Same when only b-jets are considered. In both the plots, the dashed blue line shows the significance for pure IDM scenario; the thick red and the dashed red lines are respectively showing the 3σ and 5σ confidences. We have refrained from showing the significance plots for BP6 and BP7 because they were similar and very close to BP3-5, making the plot look messy.

Benchmark Points	$\sigma^{\text{production}}$ (pb)		$\sigma^{\text{jj}}(\sigma^{\text{bb}})$ (fb)
BP1	0.27	$\not{E}_T$: 240-280 GeV	7.62 (1.87)
BP2	0.18		1.27 (0.09)
BP3	0.16		1.22 (0.08)
BP4	0.17		1.29 (0.06)
BP5	0.17		1.15 (0.05)
Pure IDM	0.16		1.14 (0.03)

Table 3.6: Final state signal cross-section with $\not{E}_T : 240 - 280$ GeV for $dijet + \not{E}_T$ final state. The numbers in the parenthesis is the corresponding cross-section for exclusive b-jet final state . All simulations are done at $\sqrt{s} = 14$ TeV.

Benchmark Points	$\sigma^{\text{production}}$ (pb)		$\sigma^{\text{jj}}(\sigma^{\text{bb}})$ (fb)
$t\bar{t}$	814.64	$\not{E}_T$: 240-280 GeV	317.71 (24.43)
WW	99.98		12.99 (0.00)
WWZ	0.15		0.14 (0.00)
ZZ	14.01		11.76 (0.28)

Table 3.7: Final state signal cross-section with $\not{E}_T : 240 - 280$ GeV for $dijet + \not{E}_T$ final state. The numbers in the parenthesis is the corresponding cross-section for exclusive b-jet final state . All simulations are done at $\sqrt{s} = 14$ TeV.

by LHC data. So far, no excess has been found in the present LHC run [208]. For inclusive dijet search, all other BPs reach a 5σ significance for a luminosity $\mathcal{L} \sim 600$ fb^{-1}, as shown in the LHS

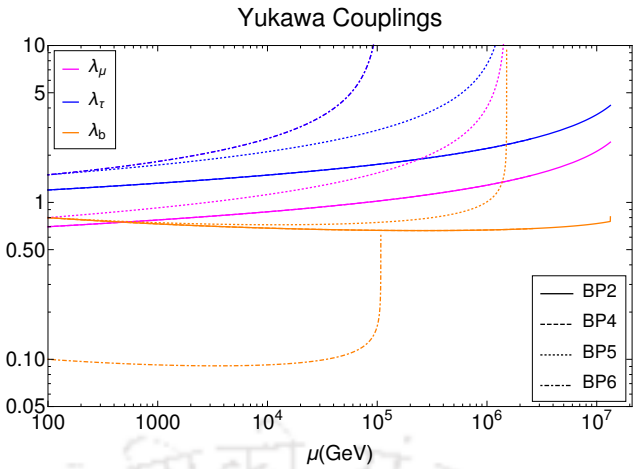

Figure 3.22: Running of the NP Yukawa couplings of our model with energy scale μ (in GeV) is shown here. The magenta lines represent the evolution of λ_μ, the blue ones represent that of λ_τ while the orange ones are for λ_b. The solid, dashed, dotted and dotdashed styles for the legends are used to represent the running for benchmarks points 2, 4, 5 and 6 respectively. Note that the solid and dashed lines overlap (due to similar variation of the couplings) and hence are indistinguishable. Also the magenta and blue dot-dashed lines for BP6 overlap due to similar coupling strengths.

of Fig. 3.21. It is also impossible to distinguish BP5 from pure IDM scenario, while all other BPs (except BP1) lie very close to each other because of comparable production cross sections. On the other hand, for exclusive b-tagged final states, although the BPs can be distinguished from pure IDM case, but none of them reach a discovery limit even at very high luminosity. This makes the model impossible to be probed at the LHC for final states containing b-jets. Thus, we can infer that, at the present LHC luminosity the non-observation of any excess rules out the vector like quark with masses $\leq$ 500 GeV (BP1). However, M_D in between 700 GeV and 900 GeV are still allowed which can further be constrained if we do not see any excess in the dijet plus $\not{E}_T$ signal at high luminosity LHC runs. We have also noted that $M_D \gtrsim 900$ GeV can not be ruled out at the LHC even at very high luminosity run. This makes the model difficult to be probed in dijet plus $\not{E}_T$ final state even at high luminosity LHC runs.

In passing we would like to mention that dilepton plus dijet with missing energy final state has production cross-section lower than that of other final state signatures we discussed so far (as tabulated in Table. 3.3) which will result in very low signal significance over background. Therefore, we refrain from elaborating the fate of such final states at the LHC.

3.8 Renormalization Group Equation (RGE) Running of the Couplings

Any finite coupling is expected to hit a Landau pole at some scale. The Landau pole is the scale where the couplings become infinite. We check the high scale validity of our model by solving the RGEs using PyR@TE 2 [209]. The RG equations for pure IDM has been studied extensively before [210], but the addition of vector-like particles will modify the gauge, quartic and Yukawa couplings. We have considered the running of the SM Yukawas and gauge couplings at two loop

level as furnished in Appendix A.2. The running of all the new couplings are considered at one loop level which can be seen from Appendix A.1.

In Fig. 3.22, we have shown the variation of the Yukawa couplings in our model for the allowed benchmark scenarios. We note that, the Landau pole is reached at $\sim 10^7$ GeV for both BP2 and BP4, for BP5 the Landau pole is reached at $\gtrsim 10^6$ GeV, while for BP6, it is reached at 10^5 GeV. We note that the cut-off scale is dependent on the initial value of our NP couplings. The cut-off scale is higher if any one of the couplings are small as in BP2 (here the smaller one being $\lambda_\mu = 0.7$ while the largest one being $\lambda_\tau = 1.2$) while for BP6 in which both λ_μ and λ_τ equal 1.5 and $\lambda_b = 0.1$, the Landau pole is reached at 10^5 GeV. Thus the Landau pole is mainly driven by the smaller coupling and since we have chosen λ_τ to be high in all the cases, the perturbativity of our theory is mostly determined by the value either λ_μ or λ_b, whichever is smaller.

3.9 Summary

In this chapter we have studied an extension of the inert Higgs doublet model with $SU(2)_L$ singlet vector like fermions. The model offers a DM candidate same as that in pure IDM, while the vector like fermions act as mediators between the dark sector and the visible sector in addition to the usual SM Higgs portal interactions. Due to the presence of the Yukawa interaction and family-dependent couplings, we have interesting FCNC and LFV processes, which can explain anomalies in $R_{K^{(*)}}$ data and also have the potential to incorporate the observed data on muon $(g-2)$. At the moment, satisfying all the other constraints, our model can comfortably explain the lower limit of the observed discrepancy in muon $(g-2)$. We have studied the parameter space of the model in detail considering bounds from DM relic density, direct detection, as well as from flavour data for both low and high mass region of the DM. Apart from change in allowed DM mass values from relic density requirements, due to the existence of new interactions mediated by vector like fermions, we also find more promising direct detection rates compared to pure IDM, for chosen benchmark points.

From the resulting constrained parameter space, we have chosen a set of benchmark points for further collider studies. Because of the presence of the exotic particles, this model gives rise to several interesting signals in collider consisting of: hadronically quiet dilepton channel ($\ell^+\ell^- + \not{E}_T$), dijet channel ($jj + \not{E}_T$) and dilepton plus dijet channel ($\ell^+\ell^- + jj + \not{E}_T$), along with missing energy. Final states containing two leptons with two jets plus missing energy provide a very small production cross-section, and we refrain from analyzing such signals in our work. Of the other two channels, hadronically quiet dilepton final state shows a 5σ significance in few of our chosen benchmark scenarios (BP2 and BP4) with M_{E_2} and $M_{E_3} \gtrsim 200$ GeV for $M_{\ell\ell} > 200$ GeV and $H_T > 280$ GeV, and the required luminosity is ~ 700 fb^{-1}. BP6 is also likely to be probed at the future run of the LHC when the luminosity reaches ~ 200 fb^{-1}. We note that the vector like lepton masses $\lesssim 200$ GeV are very likely ruled out by LHC data since they have not seen any excess in the above mentioned final states at the present luminosity. Similar bounds were also later reported by Bißmann et al. [211] from a more sophisticated analysis of multi-lepton signatures of vector-

like leptons at $\sqrt{s} = 13$ TeV LHC. For inclusive dijet plus $\not{E}_T$ final state, on the other hand, a 5σ discovery can be claimed in couple of benchmark scenarios with $M_D \gtrsim 600$ GeV for luminosity ≥ 600 fb^{-1}.

To summarize, the vector-like fermion extension of IDM is capable of explaining anomalous results like $R_{K^{(*)}}$ and muon $(g-2)$; the required new parameter spaces are allowed by other flavour data like the rare and radiative B_q $(q = d, s)$ decays, $B_q - \bar{B}_q$ mixing and the LFV decays like $\tau \to \mu\gamma$, $\mu \to e\gamma$ etc. The DM of the model satisfies Planck-observed relic density, obeying bounds from recent direct search data. The model can also be probed in the LHC experiment for a higher luminosity for some particular final states satisfying all the constraints mentioned above. We also check the perturbative unitarity of the model and find that for the chosen benchmark points the model can remain perturbative up to an energy scale $10^5 - 10^7$ GeV.

Chapter 4

Phenomenology of a Light Leptophilic Z' in the context of Dark Matter, Neutrino Mass and Flavour Anomalies

4.1 Introduction

Gauged $U(1)_X$ extensions of the SM are quite popular in the phenomenological studies pertaining to dark matter and neutrino mass. In some cases, these models also provide an explanation to the discrepancies in the LFUV observables $R_{K^{(*)}}$ and muon anomalous magnetic moments. Readers may refer to these studies present in the literature [175, 176, 212–218] and the references therein. In this chapter, we consider a $U(1)_X$ gauge extension of the SM whose symmetry is determined from low energy $b \to s$ data and Δa_μ. The resulting gauge group of the model will be $SU(3)_c \times SU(2)_L \times U(1)_Y \times U(1)_X$ which is an extension of SM by an abelian factor. For a review of such Abelian gauge extension of SM, see [219].The advantage of such an extension is that it introduces a minimal set of free parameters. The other most important feature of the new gauge symmetry we adopt here is that it is leptophilic in nature i.e. only the leptons will be charged under $U(1)_X$, not the quarks. For an explanation of the above mentioned anomalous results, the lepton generations must have different charges under $U(1)_X$. The degree of fermion non-universality should explain the observed discrepancies in $R_{K^{(*)}}$ and muon anomalous magnetic moment. In this minimal model with GeV scale mass of $U(1)_X$ gauge boson, we can not explain R_{D^*} and the data on electron anomalous magnetic moment.

However, charging the fermions under this new gauge group in the absence of additional chiral fermions generally leads to triangle anomalies which must be cancelled in order to validate the gauge theory at the quantum level. Hence, in order to cancel the gauge anomalies, we need to introduce additional degrees of freedom into our model, in terms of chiral fermions. Here, following the constraints from gauge anomaly cancellation, we discuss only two different possible scenarios in which we can explain the existing data on DM and neutrino oscillation. In extended version of such minimal model with more particle and interactions, there will be additional Feyn-

Particles	$SU(3)_c \times SU(2)_L \times U(1)_Y$	$U(1)_X$
$Q_L = \begin{pmatrix} u_L \\ d_L \end{pmatrix}$	$(3, 2, \frac{1}{6})$	0
u_R	$(3, 1, \frac{2}{3})$	0
d_R	$(3, 1, -\frac{1}{3})$	0
$\begin{pmatrix} \nu_e \\ e \end{pmatrix}_L$	$(1, 2, -\frac{1}{2})$	n_1
$\begin{pmatrix} \nu_\mu \\ \mu \end{pmatrix}_L$	$(1, 2, -\frac{1}{2})$	n_2
$\begin{pmatrix} \nu_\tau \\ \tau \end{pmatrix}_L$	$(1, 2, -\frac{1}{2})$	n_3
e_R	$(1, 1, -1)$	n_1
μ_R	$(1, 1, -1)$	n_2
τ_R	$(1, 1, -1)$	n_3

Table 4.1: $U(1)_X$ charges of the SM fermions.

man diagrams which will contribute to R_{D^*} and Δa_e that help us to explain the observed data.

While such models with heavy $U(1)_X$ gauge boson have been extensively studied, there have been very few studies on low mass regions [220–224]. However, our working model is very much different compared to the ones discussed in the references mentioned above and we also correlate the flavour anomalies with origin of neutrino mass and dark matter. Both the scenarios we discuss here consider the viability of a leptophilic $U(1)_X$ gauge symmetry in a way that it is anomaly free, predicts lepton flavour non-universality and the origin of light neutrino masses while the stability of DM candidate is ensured by an additional $\mathcal{Z}_2$ symmetry which also plays a non-trivial role in neutrino mass generation for one of the models.

This chapter is organised as follows. In section 4.2 we briefly discuss our overall framework followed by the corresponding analysis of flavour anomalies in section 4.3 by considering only the SM particle spectrum along with a massive leptophilic and family non-universal $U(1)_X$ gauge boson. We then move onto the discussions of the complete models in sections 4.4, 4.5 covering the details of flavour anomalies, dark matter and neutrino mass. In section 4.6 we discuss about different Higgs invisible and charged lepton flavour violating decays and also comment on other possible ways to probe our model at the LHC and finally summarise our findings in section 4.7.

4.2 Our Framework

As mentioned before, our goal is to extend the SM by an Abelian $U(1)_X$ symmetry with a corresponding massive gauge boson X. We restrict our study to only low mass regime (GeV scale) of this additional gauge boson and allow only the leptons to couple to it. The charge assignments of the different SM particles under the different gauge groups are listed in Table. 4.1 and the NP interaction Lagrangian is given by

$$\mathcal{L}_{\text{int}}^{\text{NP}} = i \sum_{i=1}^{3} n_i g_X (\bar{\ell}_i^L \gamma^\mu \ell_i^L + \bar{e}_i^R \gamma^\mu e_i^R) X_\mu - \frac{1}{4} X_{\mu\nu} X^{\mu\nu} + \frac{\epsilon}{4} B_{\mu\nu} X^{\mu\nu}, \tag{4.1}$$

where g_X is the gauge coupling of the $U(1)_X$ group, i represents the lepton generation and n_i are the charges of the lepton families under $U(1)_X$ which we want to constrain from anomaly cancellation requirements as well as flavour phenomenology. Here, in the above Lagrangian, ℓ_i^L is the left-handed lepton doublet while e_i^R is the right-handed singlet with same gauge charge n_i. While writing the above Lagrangian, we have assumed that the $U(1)_X$ charges for the right and left-handed leptons are same, leading to a vector type interaction. In Eqn. (4.1), $B_{\mu\nu}$ and $X_{\mu\nu}$ are the standard $U(1)_Y$ and $U(1)_X$ field stress tensors, respectively, and the factor ϵ represents the kinetic mixing between them. We assume that the leptophilic X mixes kinetically with the SM Z boson with a strength ϵ. This mixing will be helpful to get contributions in various low energy observables like R_K, R_{K^*} through penguin diagrams with the lepton vertex dominated by the above interaction and the one-loop quark vertex modified by the mixing parameter ϵ. In muon or electron anomalous magnetic moments or in other lepton flavour violating (LFV) decays, at leading order, this mixing parameter does not have any specific role.

As mentioned before, assigning charges to the SM fermions under a generic $U(1)_X$ symmetry leads to non-zero contributions to the one-loop triangle diagrams and makes the model anomalous. Therefore in order to realise a anomaly-free renormalisable model, one needs to put additional chiral fermions into the model which may also provide a natural candidate for DM. At the same time the additional chiral fermions required for anomaly cancelation could be made useful for neutrino mass generation as well. For similar construction of Abelian gauge extended models in the context of DM and neutrino mass generation, see [225–233] and references therein.

The equations that govern the anomaly cancellation requirements in our setup are given by :

(A) $[\mathbf{SU(2)}]^{\mathbf{2}}[\mathbf{U(1)_X}]$:

$$\left(\frac{1}{2}\right)\times 2\times n_1+\left(\frac{1}{2}\right)\times 2\times n_2+\left(\frac{1}{2}\right)\times 2\times n_3-\left(\frac{1}{2}\right)\times 1\times n_1-\left(\frac{1}{2}\right)\times 1\times n_2 - \left(\frac{1}{2}\right)\times 1\times n_3=\mathbf{\frac{1}{2}(n_1+n_2+n_3)} \tag{4.2}$$

(B) $[\mathbf{U(1)_Y}]^{\mathbf{2}}[\mathbf{U(1)_X}]$:

$$\left(-\frac{1}{2}\right)^2\times 2\times n_1+\left(-\frac{1}{2}\right)^2\times 2\times n_2+\left(-\frac{1}{2}\right)^2\times 2\times n_3-(-1)^2\times n_1-(-1)^2\times n_2 - (-1)^2\times n_3=\mathbf{-\frac{1}{2}(n_1+n_2+n_3)} \tag{4.3}$$

(C) $[\mathbf{U(1)_Y}][\mathbf{U(1)_X}]^{\mathbf{2}}$:

$$\left(-\frac{1}{2}\right)\times 2\times n_1^2+\left(-\frac{1}{2}\right)\times 2\times n_2^2+\left(-\frac{1}{2}\right)\times 2\times n_3^2-(-1)\times n_1^2-(-1)\times n_2^2-(-1)\times n_3^2=\mathbf{0} \tag{4.4}$$

(D) $[\mathbf{U(1)_X}]^{\mathbf{3}}$:

$$n_1^3\times 2+n_2^3\times 2+n_3^3\times 2-n_1^3-n_2^3-n_3^3=\mathbf{n_1^3+n_2^3+n_3^3} \tag{4.5}$$

(E) $[\mathbf{U(1)_X}]$:

$$\mathbf{n_1+n_2+n_3} \tag{4.6}$$

From the above set of conditions (A-E) one can infer that :

- $n_1 + n_2 + n_3 = 0$ ensures anomaly cancellation of all the anomalies except Eqn. (4.5).
- In order to ensure Eqn. (4.5) is also zero, we can add N extra fermions with $U(1)_X$ charges ($m_1, m_2, ...$ etc.) such that $\sum_{\mathbf{i=1}}^{\mathbf{N}} \mathbf{m_i} = \mathbf{0}$ and $\sum_{\mathbf{i=1}}^{\mathbf{N}} \mathbf{m_i^3} = -\left(\sum_{\mathbf{i=1}}^{\mathbf{3}} \mathbf{n_i^3}\right)$.

The one way of cancelling the anomaly without adding more fermions is to consider equal and opposite charges for any two generations of leptons and let the charge of the third generation be zero. These are the symmetries like $U(1)_{L_e - L_\mu}$, $U(1)_{L_\mu - L_\tau}$ which has been discussed earlier in the references [176, 215, 218, 234]. However, if we want to consider non-zero charges for all the three lepton generations, then we need to have additional chiral fermions in our model for anomaly cancellation. So without choosing random charges and adding fermions in an ad-hoc manner, we can try to constrain the possible values of n_1, n_2 and n_3 from the available low-energy data. Note that n_1 and n_2 will be sensitive to the observables like $R_{K^{(*)}}$ as well as electron and muon anomalous magnetic moments. There will not be any contributions to the lepton flavour violating decays and the rare decays like $B_s \to \mu\mu$ or $B_s \to ee$. Also, depending on the lepton in the final state, the $b \to c\ell\nu_\ell$ decays (with $\ell = e, \mu, \tau$) will be sensitive to the charges as mentioned above. However, due to the low mass of X, the new contributions in $B \to D^{(*)}\ell\nu_\ell$ decays are much smaller as compared to the corresponding SM counterpart. Therefore, effectively we can get constraints on n_1 and n_2 using the available data on $b \to s\ell\ell$ decays (for $\ell = \mu, e$) and anomalous magnetic moments; however, due to unavailability of sufficient data, n_3 can not be constrained. We then look for possible solutions for the charges (n_1, n_2, n_3) such that $n_1 + n_2 + n_3 = 0$. Such a prescription also allows us to constrain the mass of X and the kinetic mixing parameter effectively. The detailed analysis is described in the next section.

Note that for general $U(1)_X$ charges of leptons, one can have a general structure of charged lepton mass matrices. One can have non-diagonal terms in charged lepton mass matrix even with vector-like couplings of leptons to X (equal charge of left-handed doublet and right-handed singlets). This is because of the equality of $U(1)_X$ charges across multiple fermion generations or in case we extend our model with additional Higgs doublets with appropriate $U(1)_X$ charges. In such a case, the charged lepton mass matrix has to be diagonalised using a bi-unitary transformation as follows

$$M_l = V_L M_l^{\text{diag}} V_R^\dagger$$

where $M_l^{\text{diag}} = \text{diag}(m_e, m_\mu, m_\tau)$. As will be discussed later, the PMNS mixing matrix will get additional contribution from charged lepton sector via $U_{\text{PMNS}} = V_L^\dagger U_\nu$ where U_ν diagonalises the complex symmetric Majorana light neutrino mass matrix $M_\nu = U_\nu M_\nu^{\text{diag}} U_\nu^T$ with $M_\nu^{\text{diag}} = \text{diag}(m_1, m_2, m_3)$.

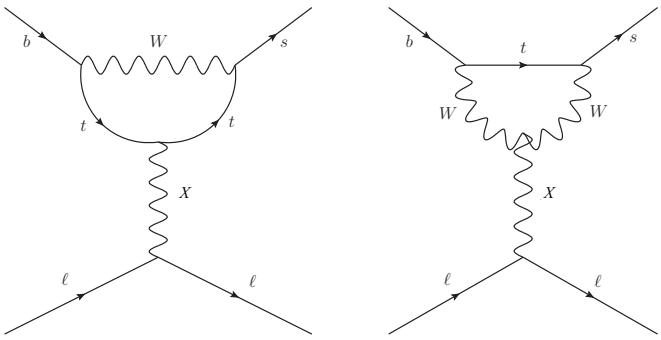

Figure 4.1: Dominant diagrams contributing to $b \to s\ell^+\ell^-$ decay.

4.3 Analysis

In the following subsection, we will discuss different observables which will be useful to constrain various model parameters like $U(1)_X$ charges of leptons n_i, new gauge coupling g_X, new gauge boson mass M_X, and the kinetic mixing parameter ϵ.

4.3.1 Exclusive $b \to s\ell\ell$ (with $\ell = e, \mu$) decays

The measured value of $R_{K^{(*)}}$ by LHCb can be found in eqs. (1.65),(1.66). In our model, the leading contributions to the Wilson coefficients will come from the diagrams shown in Fig. 4.1, and we will have contributions only in C_9 due to the vectorial coupling of the X to the leptons. There will be contributions in both $b \to s\mu^+\mu^-$ and $b \to se^+e^-$ decays. As can be seen from Eqn. (4.1), due to the absence of axial-vector coupling of X to the leptons, we do not have contributions to C_{10}. Therefore, at the leading order, the new WC is given by

$$C_9^{\ell,\mathrm{NP}} = \left(\frac{M_W^2 n_\ell g_X \epsilon}{C_W S_W}\right)\left(1 - \frac{4}{3}S_W^2\right)\left(\frac{1}{q^2 - M_X^2 + i\Gamma_X M_X}\right) \times C(x_t) \tag{4.7}$$

with

$$C(x_t) = \frac{x_t}{8}\left[\frac{6 - x_t}{1 - x_t} + \frac{3x_t + 2}{(1 - x_t)^2} ln(x_t)\right], \quad x_t = \frac{m_t^2}{M_W^2}. \tag{4.8}$$

Here, m_t and M_W are the top quark and W-boson masses, respectively. The sine of the Weinberg angle is defined as $S_W = \sin\theta_W$ and $C_W = \sqrt{1 - S_W^2}$. Also, $n_\ell \equiv (n_1, n_2)$ depending upon the lepton flavour it contributes to.

As mentioned earlier, to build a UV complete theory, gauge anomalies should cancel, for which we need to introduce new heavy fermions in our theory in addition to the X boson. It is important to note that there can be an additional contribution to C_9 due to the anomalous coupling of the longitudinal mode of X boson with SM gauge bosons [235, 236]. Depending on the masses of the heavy fermions, the contributions can be significant. However, such contributions from the Wess-Zumino terms will only occur if the new fermions have vectorial coupling with the SM gauge bosons and chiral coupling with the $U(1)_X$ gauge boson. As we will see later, in our construction of the toy models, we have added only three right-handed neutrinos which do not couple to the SM gauge bosons. We do not have any other exotic fermions in our models. Hence, we will not

have any such contributions as mentioned above from the longitudinal mode of X boson.

Note that we are working in a model with the mass of X in the GeV or sub-GeV range, in particular, we are focusing in the region $M_X > 2m_\mu$. On the other hand for $B \to K^{(*)}\ell\ell$ decays, the allowed values of q^2 lie in the range $4m_\ell^2 < q^2 < (M_B - M_{K^{(*)}})^2$. In such a situation, one cannot Taylor expand the X propagator in powers of q^2/M_X^2. Therefore, the new WC, as shown in Eqn. (4.7) will have explicit q^2 dependence and in general, could be complex. Note that for the X-boson, we have introduced the Breit Wigner (BW) propagator. In this form of the propagator, we will get a finite analytic expression for the amplitude at the resonance region. This is because, around the mass of X, the zeroth-order propagator vanishes and the higher-order effects are leading, which is given by the imaginary part proportional to the X decay width. The imaginary part will receive contributions from every particle into which X can decay. In general, without a priori knowledge of all the decay channels of X, it is hard to predict its total decay width. However, we have considered a leptophilic X, and its primary decay channels are the dilepton final states, like $\ell^+\ell^-$ and $\nu\bar{\nu}$ with $\ell = e, \mu$. Hence, one needs to estimate the decay width $\Gamma_X \approx \Gamma(X \to \ell\ell) + \Gamma(X \to \nu\bar{\nu})$.

In this model, there are free parameters which need to be constrained using the existing data. In particular, the constraints from low energy experiments, like neutrino trident production (NTP) bound, rare kaon decay $K^+ \to \nu_\mu \mu^+ X(\to \nu\bar{\nu})$, BaBar 4μ channel search etc. along with cosmological observations of BBN are important. As can be seen from [237–239], the current data allow a gauge coupling $n_\ell g_X \sim 0.0018$ for $M_X \sim 0.5$ GeV and it could be $\gtrsim 0.003$ for $M_X \gtrsim 1.0$ GeV[1]. Depending on the values of the lepton charges the upper limits on g_X would scale accordingly. For example, for $n_\ell = 2$, g_X as large as 0.001 is allowed for $M_X = 0.5$ GeV, and it will be ≈ 0.0015 for $M_X = 1$ GeV[2]. On the other hand, the kinetic mixing parameter ϵ is constrained from neutrino-electron scattering experiments like CHARM-II, GEMMA and TEXONO, for details see [241]. Mixing strength $\gtrsim 10^{-3}$ is ruled out for gauge bosons of mass around the electroweak (EW) scale. For keV scale bosons, the bound is even tighter $\mathcal{O}(10^{-6})$. LEP II has put a lower bound on the ratio of new gauge boson mass to the new gauge coupling to be $M_X/g_X \geq 7$ TeV [242]. However, since we are interested in the low mass of the gauge boson, bounds from hadron colliders like ATLAS and CMS will not be very relevant. Similarly, LEP bound is also not applicable in such low mass regime[3]. With all these inputs, the X decay width as mentioned above, will be of order $\mathcal{O}(10^{-9}\text{-}10^{-7})$ GeV for $g_X \in (10^{-4}, 10^{-3})$, which is much smaller than M_X. In the limit $\frac{\Gamma_X}{M_X} \to 0$ (narrow-width approximation (NWA)), the BW becomes a delta distribution: $\delta(q^2 - M_X^2)$.

LHCb has done a dedicated search for light hidden-sector bosons by measuring the branching fraction $\mathcal{B}(B^0 \to K^{*0}\chi(\mu^+\mu^-)) = \mathcal{B}(B^0 \to K^{*0}\chi) \times \mathcal{B}(\chi \to \mu^+\mu^-)$. Here, χ is the light boson in the hidden sector similar to X in our case. Depending on the lifetime $\tau(\chi)$, LHCb has put bounds on the above mentioned branching fraction for a given mass range of χ [244]. One can refer to Fig.7

[1] Note that the experimental bounds exist on the combined quantity $(n_\ell \times g_X)$ and therefore a proper rescaling with the lepton charge is required in order to correctly infer the bound on g_X.

[2] Note that depending on the mass M_X, the bound obtained on the coupling g_X in the refs. [237–239] and from BaBar 4μ channel search [240] will be little more relaxed in our case. The obtained bound depends on the assumption that the Z' couples with all the charged leptons and neutrinos with the same strength, while in our case coupling strengths are not the same.

[3] As an example, one could see at the ref. [243] for a detail of the direct search bounds on such a light gauge boson.

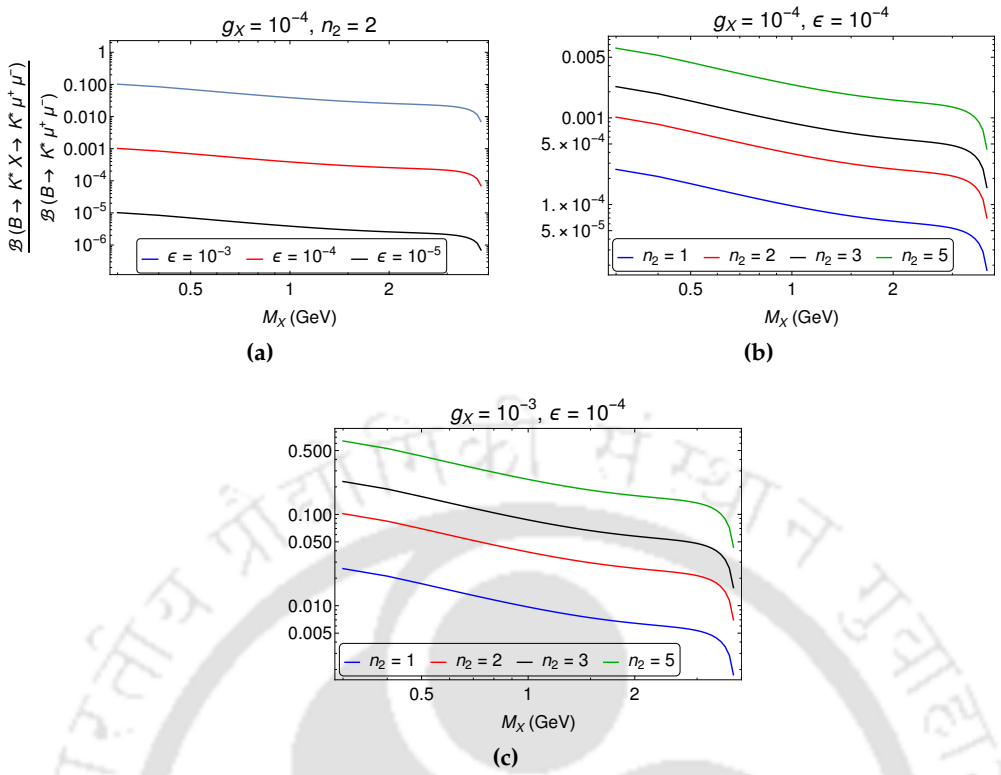

Figure 4.2: Variation of $\mathcal{B}(B^0 \to K^{*0}\chi(\mu^+\mu^-))/\mathcal{B}(B^0 \to K^{*0}\mu^+\mu^-)$ as a function of the mass M_X for different values of (a) the mixing parameter 'ϵ' and (b) the $U(1)_X$ charge n_i. From Figs. (b) and (c), we can check the dependence of the above ratio on the coupling g_X.

of the supplemental material of reference [244] in which the ratio $\mathcal{B}(B^0 \to K^{*0}\chi(\mu^+\mu^-))/\mathcal{B}(B^0 \to K^{*0}\mu^+\mu^-)$ has been plotted as a function of $m(\chi)$ (with $214 \leq m(\chi) \leq 4350$ MeV) for different values of $\tau(\chi)$ including $\tau(\chi) = 0$. Here, the branching fraction $\mathcal{B}(B^0 \to K^{*0}\mu^+\mu^-)$ is defined for $1.1 < m^2(\mu^+\mu^-) < 6.0$ GeV^2. Note that if we choose the lifetime $\tau(\chi) = 1000$ ps, which corresponds to a very small decay width of X, the ratio as mentioned above could be of order one. However, the bounds on the same ratio will be $\leq \mathcal{O}(10^{-2})$ (at 95% CL) for $\tau(\chi) = 10$ ps, which is even the case in the limit $\tau(\chi) \to 0$. The width $\Gamma_X \approx 10^{-9}$ GeV corresponds to a lifetime $\approx 10^{-4}$ ps which is close to zero.

In our model, we have estimated $\mathcal{B}(B^0 \to K^{*0}X(\mu^+\mu^-))/\mathcal{B}(B^0 \to K^{*0}\mu^+\mu^-)$ within the accessible ranges of M_X. The normalisation $\mathcal{B}(B^0 \to K^{*0}\mu^+\mu^-)$ has been measured by LHCb for $1.1 < q^2 < 6.0$ GeV^2 [245], which is given by $(1.6 \pm 0.3) \times 10^{-7}$. The dependences of this ratio on different model parameters like ϵ, the charge n_2 and the coupling g_X are shown in Fig. 4.2. A close inspection of Figs. 4.2b and 4.2a suggests that if we choose $\epsilon \lesssim 10^{-4}$, for values of n_2 as large as 5, the constraints from LHCb will be satisfied within the accessible ranges of M_X. However, even though for $g_X = 10^{-3}$, $n_2 \sim 5$ is allowed by the LHCb constraints as shown in Fig. 4.2c, it will not be able to satisfy other low energy experimental bounds mentioned previously. To satisfy the low energy bounds for $n_2 = 5$, we need $g_X \lesssim 0.5 \times 10^{-4}$. In the rest of our analysis, we will consider $\epsilon \approx 10^{-4}$. Note that even for a relatively large gauge coupling ($\sim 10^{-3}$) we can still be able to

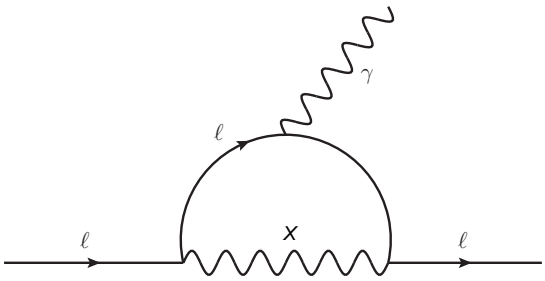

Figure 4.3: Diagram contributing to the anomalous magnetic moment of charged leptons.

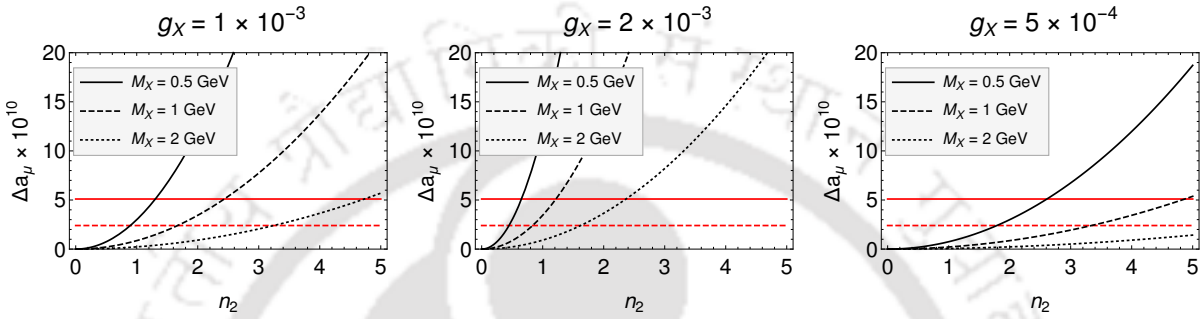

Figure 4.4: The dependencies of the muon anomalous magnetic moment (Δa_μ) on the different new physics model parameters. The red-dashed and solid lines represent the 3σ lower limit of the measured values of Δa_μ given in eqs.(1.71) and (1.72) respectively.

satisfy the upper bound provided by LHCb.

4.3.2 Anomalous Magnetic Moments

Another important observable which could be useful to put tight constraints on the model parameters is the anomalous magnetic moments of muon or electron. As one can see from Eqn. (4.1), since we do not have lepton-flavour violating couplings of X, the gauge boson mediated diagram will not contribute to decays like $\tau \to \mu\gamma, \mu \to e\gamma$ etc.

The effective vertex of photon with any charged particle is given by:

$$\bar{u}(p')e\Gamma_\mu u(p) = \bar{u}(p')\left[e\gamma_\mu F_1(q^2) + \frac{ie\sigma_{\mu\nu}q^\nu}{2m_f}F_2(q^2) + ...\right]u(p). \tag{4.9}$$

The factor $g_\mu \equiv 2(F_1(0) + F_2(0))$, and the anomalous magnetic moment is given as $a_\mu \equiv F_2(0) \neq 0$ (since $F_1(0) = 1$ at all order). In our model, the diagram that will contribute to muon and electron anomalous magnetic moments is given in Fig. 4.3. In our model, the contribution to Δa_ℓ is given by

$$\Delta a_\ell^{(X)} = \frac{n_\ell^2 g_X^2}{8\pi^2}\frac{m_\ell^2}{M_X^2}\int_0^1 dx \frac{2x^2(1-x)}{(1-x) + x^2 r_\ell(x)} \tag{4.10}$$

where $r_\ell(x) = \left(\frac{m_\ell^2}{M_X^2}\right)$, $\ell \equiv e, \mu$ and $n_\ell (= n_i)$ denotes the $U(1)_X$ charge of the lepton. Our analytical expression can be compared with the one obtained in [198]. Note that the contributions in Δa_ℓ for

both $\ell = \mu$ and e are positive; however, in the case of electron magnetic moment, the expectation is negative. Also, as compared to the requirement, the contribution in electron anomalous magnetic moment is negligibly small. The dependences of Δa_μ on various model parameters are shown in Fig. 4.4. We can easily explain the excess in Δa_μ for values of g_X of order $\mathcal{O}(10^{-3})$, and the data prefers a value of $M_X \lesssim 1$ GeV. In such situation, the value of n_2 need not be $>> 1$. However, if we choose $g_X \approx 10^{-4}$ then in order to explain the excess in muon $(g-2)$, we need relatively larger values of $n_2 (>> 1)$.

We have already pointed out in the introduction that the current measurement of the fine structure constant poses a negative $\sim 2.4\sigma$ deviation in anomalous magnetic moment of electron from its theory prediction [246]:

$$\Delta a_e = -8.8(3.6) \times 10^{-13}. \tag{4.11}$$

In electron anomalous magnetic moment, the contribution from the diagram in Fig. 4.3 will be positive and is given by

$$\Delta a_e^{(X)} = 2.11 \times 10^{-15} \tag{4.12}$$

for $M_X = 1$ GeV, $g_X = 0.001$ and $n_1 = 1$. Hence, we can not explain the current trend of data in Δa_e with only an additional $U(1)_X$ gauge boson.

4.3.3 Combined parameter spaces

In this subsection, we discuss the constraints obtained on the model parameters from a simultaneous analysis of the observables in $b \to s\ell\ell$ decays and Δa_μ. As we can see from eqs. (1.66), data are available in two different q^2 regions, one for $q^2 \in [0.045, 1.1]$ GeV^2 (low-q^2) and the other for $q^2 \in [1.1, 6]$ GeV^2 (high-q^2). In our analysis, we have considered the inputs from $R_{K^{(*)}}$, $\mathcal{B}(B \to K^{(*)}\mu^+\mu^-)$ (in both the q^2 regions) and Δa_μ. For $R_{K^{(*)}}$, we have considered the LHCb data in their 2σ CL and Δa_μ has been considered in its 3σ CL interval.

As mentioned earlier, the mixing parameter ϵ plays a crucial role in constraining the other relevant new parameters. We have noted that when $\epsilon \approx 10^{-4}$ the allowed regions of the other parameters are more relaxed than the one obtained for $\epsilon \approx 5 \times 10^{-4}$. We scan the parameters over the following intervals: $0.5 \leq M_X \leq 1.5$ (in GeV), $-5 \leq n_1 \leq 5$, $-5 \leq n_2 \leq 5$, $0.1 \leq g_X(\times 10^3) \leq 3$. Here, we would like to mention that the low mass regions $0.22 < M_X < 0.5$ (GeV) are also allowed by the data as discussed above; in the next section, we will show it in a specific scenario. The allowed parameter spaces for $\epsilon = 1 \times 10^{-4}$ are shown in Fig. 4.5. Note that n_2 and n_1 have a nice correlation, higher positive values of n_2 prefers higher negative values of n_1. Also, within our chosen parameter values, only negative values of n_1 are allowed. For a fixed value of n_2, a wide range of values of n_1 is allowed. However, as expected, the scenario $n_1 = n_2$ is excluded. Here, we have shown only the positive values of n_2, which are allowed by the data. The allowed values of n_2 are symmetrically distributed about the origin along the n_2-axis. In addition, we see that for $\epsilon \approx 1 \times 10^{-4}$, within the given range of M_X, the allowed values of the coupling g_X lies in between

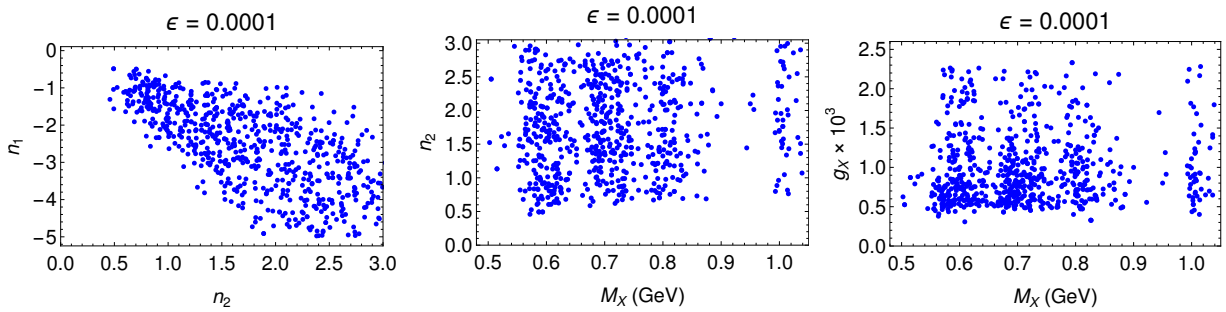

Figure 4.5: The allowed parameter spaces for n_1, n_2, g_X and M_X which passes the constraints from $R_{K^{(*)}}$, the anomalous magnetic moment of the muon and $\mathcal{B}(B \to K^{(*)}\mu\mu)$. Note that the observables in $b \to s\ell\ell$ decays are defined in high ($1.1 < q^2 < 6.0$ (GeV^2)) as well as in the low-q^2 ($0.045 < q^2 < 1.1$ (GeV^2)) regions.

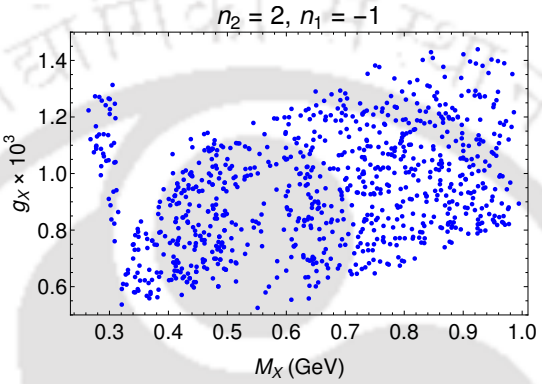

Figure 4.6: Correlation between M_X and g_X constrained from all low energy flavour data and muon anomalous magnetic moment for n_2 and n_1 fixed at 2 and -1 respectively.

0.5×10^{-3} and 2×10^{-3}. To be conservative, we have not considered values of g_X larger than 2×10^{-3} since other low energy observables constrain higher values, for details see [237–240].

4.4 The extension of $U(1)_X$ with additional degrees of freedom

A certain combination of n_1, n_2 would lead to a particular extension of the SM with chiral fermions. While such an extension is not unique, we stick to minimal possible extensions in order to address the problems discussed earlier. Therefore we can now proceed towards making a specific choice for these parameters in order to complete our model in a way that the extension is minimal. We have already been able to constrain n_1 and n_2 from low energy data while n_3 remains unconstrained. One can easily see that the minimal way to cancel the anomalies would be to add three chiral singlet fermions with $U(1)_X$ charges $n_1' = -n_1, n_2' = -n_2$ and $n_3' = -n_3$. This will make the sum of the charges as well as sum of the cubes of the charges equal to zero. The three fermions can be considered to be 3 right-handed neutrinos (RHNs). As a benchmark scenario we choose $(n_1, n_2, n_3) = (-1, 2, -1)$ which is in good agreement with the flavour data as shown in Fig. 4.5. For $n_2 = 2$,$n_1 = -1$, the correlation between M_X and g_X is shown in Fig. 4.6, here we have shown the region $0.25 \lesssim M_X \lesssim 1.0$ (GeV). For these values of $[n_2, n_1]$ and for $g_X = 0.001$, within the allowed ranges of q^2 and M_X the numerical values of the WCs ΔC_9^μ and ΔC_9^e will lie in between $[-0.827, -1.83]$ and $[0.413, 0.91]$, respectively. These values of the WCs are consistent with the re-

sult (within 2σ CI) obtained from a global fit to all the available data in $b \to s\ell\ell$ decays considering NP effects in both the muon and electron final states [247].

Since the light gauge boson also couples to SM neutrinos, our model will have contributions to both exclusive and inclusive rare B-meson FCNC decay to invisible final states. The present upper limits on such modes are [12]

$$\begin{aligned} \mathcal{B}(B^+ \to K^+ \nu\bar{\nu}) &< 1.6 \times 10^{-5}, \\ \mathcal{B}(B^0 \to K^{0*} \nu\bar{\nu}) &< 1.8 \times 10^{-5}. \end{aligned} \tag{4.13}$$

In Table. 4.2, we have specified the SM and NP contributions to the branching fractions of these rare decay modes considering only central values of form factors and other decay parameters [248, 249]. Our choice of the light gauge boson mass and mixing modifies the SM prediction of the branching fraction of the exclusive decay channels by $\sim (1-3)\%$ only while the inclusive $B \to X_s \nu\bar{\nu}$ branching is enhanced by upto $\sim 20\%$. At present, the predicted branching fractions are well within the current experimental limit. Note that no experimental bounds are available on $\mathcal{B}(B \to X_s \nu\bar{\nu})$.

	$\mathcal{B}(B^+ \to K^+ \nu\bar{\nu}) \times 10^6$	$\mathcal{B}(B^0 \to K^{0*} \nu\bar{\nu}) \times 10^6$	$\mathcal{B}(B \to X_s \nu\bar{\nu}) \times 10^6$
SM	**3.90**	**9.12**	**28.11**
$M_X = 0.3$ GeV	4.02	9.39	34.07
$M_X = 0.6$ GeV	3.94	9.15	28.51
$M_X = 0.9$ GeV	3.95	9.49	35.23

Table 4.2: Predictions for the SM and NP branching fractions for the rare B-meson decay to a pair of neutrinos. The NP branching fractions are mentioned for three different light gauge boson masses considering $g_X = 10^{-3}$, $\epsilon = 10^{-4}$ and $U(1)_X$ charges as mentioned above.

One can make the fermion content richer by adding more chiral fermions with appropriate charges that satisfy the anomaly cancellation requirements. However, we would like to have a plausible explanation for the neutrino masses, and at the same time, we want to keep our model minimal. Therefore, we extend our model with only three RHNs. All these fermions couple directly to SM leptons via SM Higgs (due to equal and opposite $U(1)_X$ charges of right and left handed leptons while SM Higgs remains chargeless under it), and therefore we cannot consider one of them to be our DM candidate. One can, of course, add a Dirac fermion on top of this which will not contribute to any anomaly and assign this to be the DM. But such a scenario will be ad-hoc and less motivating since the DM does not arise naturally from the anomaly cancellation requirements. Also, its mass remains a free parameter without being connected to the scale of $U(1)_X$ symmetry breaking. Thus we need to look beyond this minimal solution by extending the particle content further[4]. On the other hand, imposing a discrete $\mathcal{Z}_2$ symmetry on the new chiral fermions (at least in one of them) will help us in forbidding their direct coupling to SM fermions and SM

[4]One can consider one of the RHNs to have very tiny Yukawa couplings with leptons and become a candidate for sterile neutrino DM. We do not consider this possibility here, for details of such scenarios please refer to the review article [250].

Particles	$SU(3)_c \times SU(2)_L \times U(1)_Y$	$U(1)_X$	$\mathcal{Z}_2$
$Q_L = \begin{pmatrix} u_L \\ d_L \end{pmatrix}$	$(3, 2, \frac{1}{6})$	0	+
u_R	$(3, 1, \frac{2}{3})$	0	+
d_R	$(3, 1, -\frac{1}{3})$	0	+
$L_1 = \begin{pmatrix} \nu_e \\ e \end{pmatrix}_L$	$(1, 2, -\frac{1}{2})$	-1	+
$L_2 = \begin{pmatrix} \nu_\mu \\ \mu \end{pmatrix}_L$	$(1, 2, -\frac{1}{2})$	2	+
$L_3 = \begin{pmatrix} \nu_\tau \\ \tau \end{pmatrix}_L$	$(1, 2, -\frac{1}{2})$	-1	+
e_R	$(1, 1, -1)$	-1	+
μ_R	$(1, 1, -1)$	2	+
τ_R	$(1, 1, -1)$	-1	+
H_1	$(1, 2, \frac{1}{2})$	0	+
N_{1R}	$(1, 1, 0)$	-1	-
N_{2R}	$(1, 1, 0)$	2	-
N_{3R}	$(1, 1, 0)$	-1	-
H_2	$(1, 2, \frac{1}{2})$	0	-
φ_1	$(1, 1, 0)$	2	+
φ_2	$(1, 1, 0)$	4	+

Table 4.3: Particle content for Toy model I.

Higgs. In non-minimal or UV complete version of such minimal scenarios, it is possible to realise such $\mathcal{Z}_2$ symmetry as a remnant after spontaneous symmetry breaking of $U(1)_X$ [227–229, 231–233]. Our minimal setup here will enable us to have a DM candidate without adding new fermions apart from the RHNs. Under such a scenario, there are two possibilities with the different origin of light neutrino masses but with almost the same DM phenomenology, which we discuss in the following section.

4.5 Toy Models

In the following subsections, we discuss the toy models which have been built considering the $U(1)_X$ charge assignments of the SM leptons and new chiral fermions as described in the previous section i.e. $(n_1, n_2, n_3) = (-1, 2, -1)$ and $(n'_1, n'_2, n'_3) = (1, -2, 1)$. We consider the additional fermions (namely, N_1, N_2 and N_3) to be right-handed, hence, their $U(1)_X$ charges will be the sign-flipped version of (n'_1, n'_2, n'_3) i.e. $(-1, 2, -1)$. Based on how we are imposing the $\mathcal{Z}_2$ symmetry on the new chiral fermions, one can come up with different models, and here we will discuss two such toy models.

4.5.1 Toy Model I

Particle Content

In this scenario, we consider that all generations of the RHNs, N_i ($i = 1, 2, 3$), to be odd under a discrete $\mathcal{Z}_2$ symmetry while all the SM particles are even. Thus to write a Yukawa term for the RHNs with the SM leptons, we would require an additional Higgs doublet (H_2) which is also odd under this discrete symmetry. The unbroken $\mathcal{Z}_2$ symmetry prevents H_2 from acquiring a non-zero vacuum expectation value (vev), and it remains inert. However, it plays a crucial role in neutrino mass generation by the radiative seesaw mechanism [61], which has been described later. To give Majorana masses to right handed neutrinos, we require at least two singlet neutral scalars with non-zero $U(1)_X$ charges. The particular choice of the $U(1)_X$ charge of the RHNs mentioned above, automatically necessitates that the singlet scalars carry charge 2 and 4 respectively, allowing us to right the Majorana mass terms for N_i . The lightest singlet neutral fermion can be a suitable DM candidate since the $\mathcal{Z}_2$ symmetry protects its decay into other lighter particles. However, since N_2 is unique from the other singlet fermions in terms of its $U(1)_X$ charge, so we consider this to be our DM candidate and ensure that it is the lightest among all the $\mathcal{Z}_2$ odd fermions. In Table 4.3, we have shown the entire particle content alongside with their respective charges with respect to different symmetries of the model.

Lagrangian and Scalar Mass Spectrum

In the set up given above, the total Lagrangian can be written as

$$\mathcal{L}_{\rm Tot} = \mathcal{L}_{\rm SM} + \mathcal{L}_S - \mathcal{L}_Y + \frac{i}{2}\sum_{i=1}^{3}\bar{N}_i \not{\partial} N_i + i g_X \sum_{i=1}^{3}\left[n_i\,(\bar{\ell}_i^L\gamma^\mu\ell_i^L + \bar{e}_i^R\gamma^\mu e_i^R) + n_i'\,\bar{N}_{iR}\gamma^\mu N_{iR}\right]X_\mu - \frac{1}{4}X_{\mu\nu}X^{\mu\nu} + \frac{\epsilon}{4}B_{\mu\nu}X^{\mu\nu} \tag{4.14}$$

where n_i, n_i' are the $U(1)_X$ charges of the SM lepton generations and RHN generations, respectively. The relevant Yukawa interactions are given by :

$$-\mathcal{L}_Y \supset \sum_{i,j} Y_{ij}^{\ell}\bar{L}_i H_1 e_{jR} + \sum_{i,j} Y_{ij}\bar{L}_i\tilde{H}_2 N_j + Y_{kk}\bar{L}_k\tilde{H}_2 N_k + \sum_{i,j} Y_{ij}^{\varphi}\bar{N}_i^c N_j\varphi_1 + Y_{kk}^{\varphi}\bar{N}_k^c N_k\varphi_2^\dagger \tag{4.15}$$

where i, j, k are the generation indices with $i, j = (1, 3)$, while $k = 2$ and $\tilde{H}_2 = i\sigma_2 H_2^*$. The scalar Lagrangian $\mathcal{L}_S$ can be written as:

$$\mathcal{L}_S = (D_\mu H_1)^\dagger(D^\mu H_1) + (D_\mu H_2)^\dagger(D^\mu H_2) + (D_\mu\varphi_1)^\dagger(D^\mu\varphi_1) + (D_\mu\varphi_2)^\dagger(D^\mu\varphi_2) - V(H_1, H_2, \varphi_1, \varphi_2), \tag{4.16}$$

where the covariant derivative is given by

$$D_\mu = \left(\partial_\mu + ig\frac{\tau^a}{2}W^a_\mu + ig'YB_\mu - iG_X X_\mu\right). \tag{4.17}$$

Here, $G_X = (g_X X + g'\epsilon Y)$ and (Y, X) are the hypercharges related to $U(1)_Y$ and $U(1)_X$ gauge groups respectively. In the above mentioned scenario, $X = 4$ and 2 for φ_2 and φ_1, respectively, while $X = 0$ for H_1 and H_2. As defined earlier, ϵ is the kinetic mixing parameter. The scalar potential $V(H_1, H_2, \varphi_1, \varphi_2)$ is defined as

$$\begin{aligned} V(H_1, H_2, \varphi_1, \varphi_2) &= \mu_1^2|H_1|^2 + \mu_2^2|H_2|^2 + \frac{\lambda_1}{2}|H_1|^4 + \frac{\lambda_2}{2}|H_2|^4 + \lambda_3|H_1|^2|H_2|^2 + \lambda_4|H_1^\dagger H_2|^2 \\ &+ \left\{\frac{\lambda_5}{2}(H_1^\dagger H_2)^2 + \text{h.c.}\right\} + \mu_3^2|\varphi_1|^2 + \mu_4^2|\varphi_2|^2 + \frac{\lambda_6}{2}|\varphi_1|^4 + \frac{\lambda_7}{2}|\varphi_2|^4 \\ &+ \lambda_8(\varphi_1^\dagger\varphi_1)(\varphi_2^\dagger\varphi_2) + \lambda_9|H_2|^2|\varphi_1|^2 + \lambda_{10}|H_2|^2|\varphi_2|^2 + \lambda_{\varphi_1}|H_1|^2|\varphi_1|^2 \\ &+ \lambda_{\varphi_2}|H_1|^2|\varphi_2|^2 + \left\{\delta\ \varphi_1\varphi_1\varphi_2^\dagger + \text{h.c.}\right\}, \end{aligned} \tag{4.18}$$

with the doublet and singlet scalars after the electroweak symmetry breaking (EWSB) defined as

$$H_1 = \begin{pmatrix} w^\pm \\ \frac{v+h'+iz}{\sqrt{2}} \end{pmatrix}, H_2 = \begin{pmatrix} H^\pm \\ \frac{H^0+iA^0}{\sqrt{2}} \end{pmatrix}, \varphi_1 = \left(\frac{v_1 + s_1' + iA_1'}{\sqrt{2}}\right), \varphi_2 = \left(\frac{v_2 + s_2' + iA_2'}{\sqrt{2}}\right). \tag{4.19}$$

After spontaneous symmetry breaking, all the scalars apart from H_2 acquires a vev and is responsible for giving mass to other particles. In order to spontaneously break the electroweak symmetry as well as $U(1)_X$, we must have $\mu_1^2 < 0$, $\mu_3^2 < 0$ and $\mu_4^2 < 0$. Also since the inert doublet does not acquire a vev, $\mu_2^2 > 0$. Here, the term proportional to δ in the scalar potential (4.18) will play an important role in determining the mass of pseudo-scalars like A_2'. The potential minimization conditions are given by

$$\begin{aligned} \mu_1^2 &= -\frac{1}{2}\left(\lambda_1 v^2 + \lambda_{\varphi_1} v_1^2 + \lambda_{\varphi_2} v_2^2\right), \\ \mu_3^2 &= -\frac{1}{2}\left(\sqrt{2}v_2\delta + \lambda_6 v_1^2 + \lambda_8 v_2^2 + \lambda_{\varphi_1} v^2\right), \\ \mu_4^2 &= -\frac{1}{2}\left(\lambda_7 v_2^2 + \lambda_8 v_1^2 + \lambda_{\varphi_2} v^2\right) + \left(\frac{\sqrt{2}v_1^2\delta}{2v_2}\right). \end{aligned} \tag{4.20}$$

The gauge boson mass term can be obtained from the kinetic terms in Eqn. (4.16) which is given by

$$\mathcal{L}_{mass} = M_W^2 W_\mu^+ W^{-\mu} + \frac{1}{2}M_{Z^0}^2 Z_\mu^0 Z^{0\mu} - \Delta^2 Z_\mu^0 X^\mu + \frac{1}{2}M_X^2 X_\mu X^\mu, \tag{4.21}$$

with

$$\begin{aligned} M_W^2 &= \frac{1}{4}g^2v^2, \\ M_\gamma^2 &= 0, \\ M_{Z^0}^2 &= \frac{1}{4}(g^2+g'^2)v^2, \\ \Delta^2 &= \frac{1}{4}v^2g'\epsilon\sqrt{g^2+g'^2}, \\ M_X^2 &= \frac{1}{4}g'^2v^2\epsilon^2 + 4g_X^2(v_1^2+4v_2^2). \end{aligned} \tag{4.22}$$

Note that H_2 does not acquire a vev; hence, it does not play any role in the mass generation of the gauge bosons or fermions. We obtain the masses of W-boson, Z-boson and photon as in case of SM. The X boson mass has been obtained as a combination of the vevs of the singlet scalars and the vev of H_1; the contributions from H_1 is suppressed by the factor ϵ^2.

In Eqn. (4.21), to obtain the masses of the neutral gauge bosons, we need to carry out the standard electroweak rotation as given below

$$W_\mu^3 = S_W A_\mu + C_W Z_\mu^0 \tag{4.23}$$

$$B_\mu = C_W A_\mu - S_W Z_\mu^0, \tag{4.24}$$

where A_μ is the photon field. Note that after the symmetry breaking there will be a remaining mixing between Z_μ^0 and X_μ, which can be written as:

$$M_{GB}^2 = \begin{pmatrix} M_{Z^0}^2 & -\Delta^2 \\ -\Delta^2 & M_X^2 \end{pmatrix}. \tag{4.25}$$

Here, we have neglected the mixing between the photon and the new gauge boson. The masses of the physical heavy gauge bosons (Z, Z') can be obtained after diagonalising the above matrix by a rotation, and the masses are given by

$$M_Z^2 = \frac{1}{2}\left(M_{Z^0}^2 + M_X^2 + \sqrt{(M_{Z^0}^2 - M_X^2)^2 + 4\Delta^4}\right), \tag{4.26}$$

$$M_{Z'}^2 = \frac{1}{2}\left(M_{Z^0}^2 + M_X^2 - \sqrt{(M_{Z^0}^2 - M_X^2)^2 + 4\Delta^4}\right). \tag{4.27}$$

In the limit that $M_X << M_{Z^0}$ and mixing parameter $\epsilon << 1$, we obtain the masses as

$$M_Z^2 \simeq M_{Z^0}^2, \tag{4.28}$$

$$M_{Z'}^2 = M_X^2 - \left(\frac{\Delta^4}{M_{Z^0}^2}\right) \approx M_X^2, \quad \text{since } \Delta^4 \propto \epsilon^2 \text{ (in our case, } \epsilon^2 \approx 10^{-8}) \tag{4.29}$$

and the mixing angle is given by :

$$\tan 2\zeta = \left(\frac{2\Delta^2}{M_{Z^0}^2 - M_X^2}\right). \tag{4.30}$$

On the other hand, the mass mixing matrix for the CP even and $\mathcal{Z}_2$ even neutral scalars $(h^{'}, s_1^{'}, s_2^{'})$ is given by :

$$M_{hs}^2 = \begin{pmatrix} \lambda_1 v^2 & \lambda_{\varphi_1} v v_1 & \lambda_{\varphi_2} v v_2 \\ \lambda_{\varphi_1} v v_1 & \lambda_6 v_1^2 + \frac{v_2 \delta}{\sqrt{2}} & v_1(\sqrt{2}\delta + \lambda_8 v_2) \\ \lambda_{\varphi_2} v v_2 & v_1(\sqrt{2}\delta + \lambda_8 v_2) & -\left(\frac{\sqrt{2} v_1^2 \delta - 2\lambda_7 v_2^3}{2 v_2^3}\right) \end{pmatrix} \tag{4.31}$$

The physical scalars (h, s_1, s_2) are obtained after diagonalising the above mass mixing matrix and they are related to the unphysical ones by an orthogonal transformation. We consider a general real orthogonal 3×3 rotation matrix $\mathcal{O}$ as given in Appendix. B.1 with three mixing angles α_{ij}, $(i, j = (1, 2, 3); i \neq j)$ and no phase, for diagonalising the above mentioned mass mixing matrix as

$$\begin{pmatrix} h \\ s_1 \\ s_2 \end{pmatrix} = \mathcal{O}^T \begin{pmatrix} h^{'} \\ s_1^{'} \\ s_2^{'} \end{pmatrix} \tag{4.32}$$

In order to make the notation simpler, we redefine the angles as $\alpha_{12} \equiv \alpha_1$, $\alpha_{13} \equiv \alpha_2$ and $\alpha_{23} \equiv \alpha_3$. Another important variable is the ratio between the vevs v and v_1 which we have defined as $\tan\beta = \frac{v_1}{v}$. In general, to keep the analysis simple, we can assume that the mixing of s_2 with s_1 and h are negligibly small. In such situation, we need to focus only on the mixing between s_1 and h, i.e s_{α_1} or c_{α_1}. There are studies on the singlet scalar extension of the SM, and bounds are available on the respective model parameters like $\tan\beta$ and s_{α_1}; for example, see [251–253]. These studies took into account the bounds from various experimental measurements like the precision observables S, T and U parameters, W-mass, LEP and LHC bounds. Alongside, they have considered various theory inputs, like perturbative unitary constraints on scalar self-interactions, vacuum stability, etc. All these studies suggest that for $300 \leq M_{s_1} \leq 800$ (in GeV), one can safely assume $|\sin\alpha_1| \leq 0.3$ and $\tan\beta > 1$. Note that in our model, we have two singlet scalars, and as discussed above we have more free parameters. In general, we can expect that the bounds as mentioned above will be little more relaxed in case of our model parameters. However, to be on the safe side, we have used these bounds in our analysis. This will help us to constrain a few of the other model parameters. In our analysis, we have considered $|\sin\alpha_1| \lesssim 0.2$ and $\tan\beta = 2.0$ and $M_{s_1} = 500$ GeV [252, 253] which is even more conservative. The corresponding values of M_{s_2} can be obtained after the evaluation of v_2 from Eqn. (4.22).

The mass mixing matrix for the CP odd and $\mathcal{Z}_2$ even neutral scalars $(A_1^{'}, A_2^{'})$ is given by

$$M_{AA}^2 = \begin{pmatrix} -2\sqrt{2}v_2\delta & \sqrt{2}v_1\delta \\ \sqrt{2}v_1\delta & -\left(\frac{v_1^2\delta}{\sqrt{2}v_2}\right) \end{pmatrix}. \tag{4.33}$$

After diagonalizing this matrix with an orthogonal transformation we will obtain one massless goldstone (A_1) corresponding to the gauge boson of $U(1)_X$ and another massive physical CP odd scalar (A_2) of mass $\left(-\frac{2\sqrt{2}v_1\delta}{s_\gamma^2}\right)^{1/2}$. Here, $s_\gamma \equiv \sin\gamma$, where γ is the mixing angle between the physical and unphysical CP odd scalars. It is evident from this expression that the dimensionful coupling δ has to be negative. Also here, for simplicity, we can limit our discussion to the value $s_\gamma << 1$.

The masses of the neutral and charged inert scalars are given by :

$$\begin{aligned} M_{H^0}^2 &= \frac{1}{2}\left(2\mu_2^2 + \lambda_L v^2 + \lambda_9 v_1^2 + \lambda_{10} v_2^2\right) \\ M_{A^0}^2 &= \frac{1}{2}\left(2\mu_2^2 + \lambda_A v^2 + \lambda_9 v_1^2 + \lambda_{10} v_2^2\right) \\ M_{H^\pm}^2 &= \mu_2^2 + \frac{1}{2}\left(\lambda_3 v^2 + \lambda_9 v_1^2 + \lambda_{10} v_2^2\right) \end{aligned} \tag{4.34}$$

where $\lambda_L = (\lambda_3 + \lambda_4 + \lambda_5)$ and $\lambda_A = (\lambda_3 + \lambda_4 - \lambda_5)$. To summarise, in Appendix C.1, we have presented various couplings in terms of the relevant physical masses, vevs and the mixing angles. These are the most general relations from which one can obtain the approximate relations for small mixing angle. The coupling strength of the interaction between H_1 and H_2 is defined by $\lambda_L = \lambda_3 + \lambda_4 + \lambda_5$. In an inert two Higgs doublet model (2HDM) where H^0 is considered as a suitable DM candidate, the bound on this type of coupling is given by $\lambda_L \lesssim 6 \times 10^{-3}$ [254]. We have not explored this possibility. In our study, the doublet H_2 is relevant for the neutrino mass generation and the required coupling is λ_5 which we have treated as free parameter.

DM Phenomenology

We adopt the thermal DM paradigm where DM gets produced in the early Universe thermally followed by its freeze-out from the thermal bath which decides its present day abundance. The relic abundance of DM can be computed by solving the appropriate Boltzmann equation and the model parameters can be constrained by comparing the calculated relic with observed abundance which, in terms of density parameter Ω and h = Hubble Parameter/(100 km s^{-1}Mpc^{-1}), is conventionally reported as [66]: $\Omega h^2 = 0.120 \pm 0.001$ at 68% C.L. We solve the Boltzmann equation numerically using `micrOMEGAs` [255] where the model information has been supplied to `micrOMEGAs` using `FeynRules` [204].

In our model, we choose N_2 as the DM candidate which is supposed to be the lightest RHN. Note that its $U(1)_X$ charge is different from the other two RHNs. The dominant contributions to

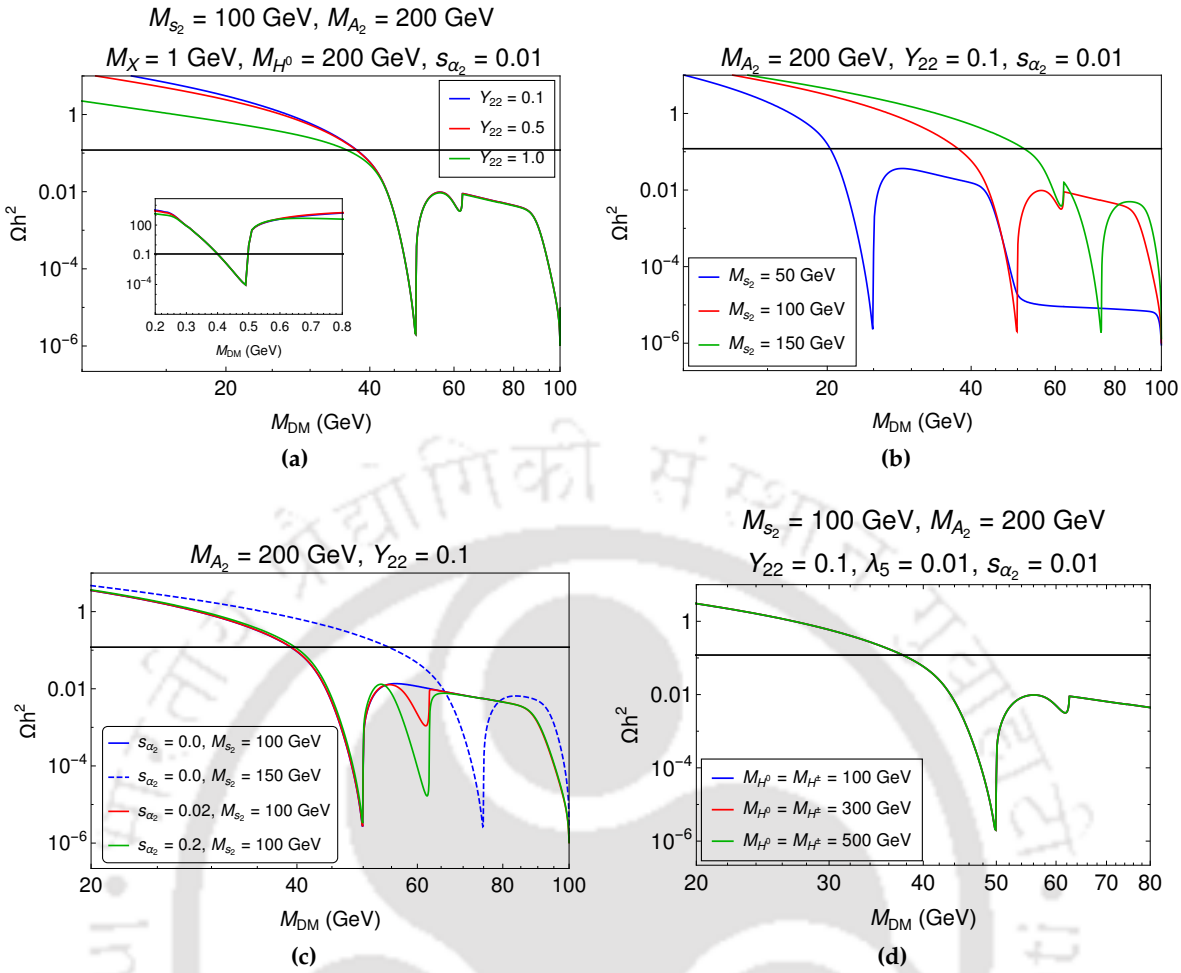

Figure 4.7: Relic density vs dark matter mass (in GeV) for different values of Yukawa coupling Y_{22} (4.7a), M_{s_2} (4.7b), mixing angle s_{α_2} (4.7c) and masses of inert scalars (4.7d). The solid black line in each figure denotes the Planck observed relic abundance of DM. In Fig. 4.7a we have also shown the variation of the relic for sub-GeV masses of the DM in the inset.

the relic abundance of DM will come from the annihilation diagrams shown in Fig. D.1. There are a few other diagrams which are shown in Fig. D.3 in Appendix D.2 whose contributions in the DM relic abundance will be sub-leading[5]

In this model, apart from $M_X(\equiv M_{Z'})$ and $g_X(\equiv g_{Z'})$ the other parameters that are relevant for DM phenomenology are M_{N_2}, M_{H^0}, $M_{H^\pm}$, M_{A^0}, Y_{22}, and $Y_{22}^{\varphi} \approx \frac{\sqrt{2}M_{N_2}}{v_2}$, respectively. The co-annihilation diagrams in Fig. D.4 are sensitive to Y_{ij} (with $i, j = 1$ or 3). Therefore, the relic density is almost insensitive to these parameters since the contributions from these diagrams are suppressed. Considering the bounds from the low energy data in the rest of our analysis, we have fixed the mass $M_{Z'}$ at 1 GeV; also, we have set $g_{Z'} \approx 10^{-3}$. As mentioned earlier, with a

[5]See [230, 256] for scenarios where such contributions can be important. As we can see, the mediators of the DM interactions are the following: $X \equiv Z'$, s_2, H_0, $H^\pm$ and A_2. The scalar s_2 does not interact directly with the SM fermions, and it decays into them via mixing with the SM Higgs (h). In general, s_2 can mix with s_1 as well. However, those diagrams will be highly (doubly) suppressed because s_1 will decay to SM fermions or gauge bosons via its mixing with h. Also, when the mass of the neutral inert scalars or the other RHNs are close to the mass of N_2, there would be several other co-annihilation channels that may contribute to the relic abundance as shown in Fig. D.4. However, we have checked that those contributions are negligible compared to the one given by annihilation diagrams in Fig. D.1. Note that in the low DM mass range of our interest, the efficient coannihilation processes will require the scalars from inert Higgs doublet to be also in the low mass regime which is in tight constraints with LEP data.

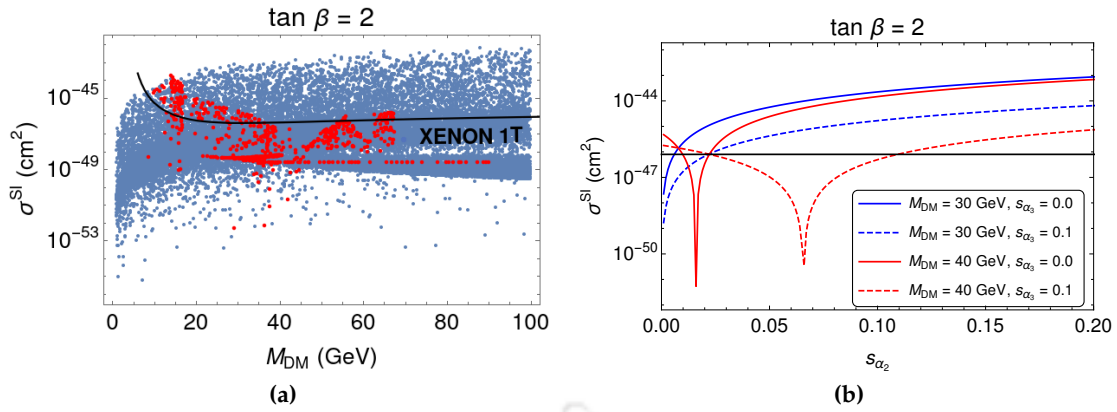

Figure 4.8: (a) The allowed regions of the DM mass satisfying the bounds on relic density and the spin-independent direct detection cross section (σ^{SI}) of DM from XENON 1T, please see the text for other details. The allowed DM masses near $M_{Z'}/2$ are not shown in this plot. (b) Dependencies of σ^{SI} on s_{α_2} and s_{α_3} within the allowed ranges of M_{DM}.

particular choice of $\tan\beta$ one can fix the value of M_{s_1} since M_h is known. Once this is done the allowed values M_{s_2} can be fixed from Eqn. (4.22). In this regard, the perturbativity of the scalar couplings will also play an important role. Since we have chosen $\tan\beta \approx 2$ and $M_{s_1} \approx 500$ GeV, the corresponding values of M_{s_2} and M_{A_2} will be limited to $\lesssim 200$ GeV. Accordingly, the mass of DM will be restricted because s-channel annihilations are the dominant annihilation process for the DM.

In Fig. 4.7, we have shown the variation of the relic abundance with $M_{DM} = M_{N_2}$ for different choices of the other model parameters as mentioned above. The sensitivities of the relic abundance to Y_{22}, M_{s_2}, $M_{H^0}(M_{H^\pm})$ and s_{α_2} are shown in Figs. 4.7a, 4.7b, 4.7d and 4.7c, respectively. Note that with the increasing values of M_{DM}, the relic density decreases to a minimum value at the resonances, and it starts increasing again as the DM mass moves away from the respective resonances. In this model, we have a couple of such resonances; the first one is at $M_{DM} \sim M_{Z'}/2$ (Fig. 4.7a) which is the annihilation via the gauge boson Z'. Notice that for values of M_{DM} close to this resonance (on both sides) the relic density satisfy its measured value. The other resonance peaks are at $M_{DM} \sim M_{s_2}/2$ and $\sim M_h/2$, respectively. Fig. 4.7b shows the pattern of the changes in variations of relic density with M_{DM} for different values of M_{s_2}. Note that for $M_{s_2} < M_h$ the bound on relic density is satisfied for DM masses close to, but less than $M_{s_2}/2$. In such scenario, the relic density is under-abundant at or near $M_{DM} \sim M_h/2$. On the contrary, when $M_{s_2} > M_h$ the relic density is satisfied at a DM mass close to $M_h/2$, provided we assume that there is a mixing between h and s_2, i.e $s_{\alpha_2} \neq 0$.

As discussed earlier, we have restricted our analysis to the small values of $s_{\alpha_2}(\approx 0.01)$. Later we will see that such a restriction will be useful to evade stringent bounds on the direct detection of Higgs portal DM from XENON-1T experiment [257]. However, we have shown the dependences of the relic density on s_{α_2} in Fig. 4.7c. As expected, in the no-mixing scenario, the resonance peak due to the Higgs mass vanishes. In such situation, when $M_{s_2} > M_h$, the relic density will be satisfied for values of DM mass close to $M_{s_2}/2$ instead at $M_h/2$, which is the case for non-zero s_{α_2}.

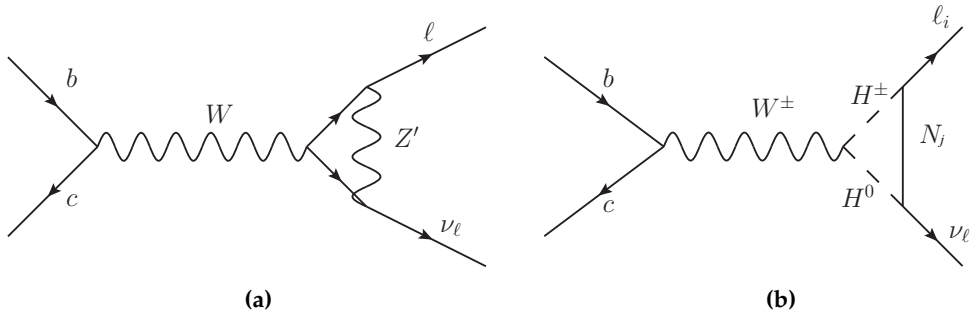

Figure 4.9: Diagrams contributing to flavour changing charge current process $b \to c\ell\bar{\nu}_\ell$.

Note that there will be another resonance peak at $M_{DM} \sim M_{A_2}/2$, at or around which the relic density will be much lower than the existing bound. One can also see from the Figs. 4.7a and 4.7d that the co-annihilations with inert scalars do not play much role since the relic abundance do not change with change in the value of coupling Y_{22} and the masses M_{H_0} or $M_{H^\pm}$. This is precisely due to the fact that the scalar masses are much larger than DM mass making the coannihilation processes inefficient.

In Fig. 4.8a, we have shown the allowed ranges of the DM mass obtained from a scan with the constraints from relic density projected against the upper limit on direct detection cross-section σ^{SI} (spin-independent) of DM from XENON 1T experiment [257]. To generate this plot we consider $\tan\beta = 2$, and the values of the other relevant parameters are the following: $s_{\alpha_1} \sim 0.01, 0 < s_{\alpha_3} < 0.01$, $0 < s_{\alpha_2} < 0.01$, $20 \leq M_{s_2} \leq 200$ GeV and $M_{s_1} \sim 500$ GeV. In this model, the spin-dependent direct detection cross-section is highly suppressed; hence we have not considered it for a numerical study. Note that the allowed values of the DM mass lies in between 5 and 90 GeV. It is evident that there will be an allowed region near $M_{Z'}/2$ which is not shown in this plot. The dependencies of σ^{SI} on s_{α_2} and s_{α_3} are shown in Fig. 4.8b. As expected, the large values of s_{α_3} allows the relatively larger values of s_{α_2}, however, we will stick to the low values of both like $s_{\alpha_2} \approx s_{\alpha_3} = 0.01$.

Additional contribution to $b \to c\ell\bar{\nu}_\ell$

We have already argued that the observables $R_{D^{(*)}}$ are useful for the test of lepton universality. For the last couple of years special attention has been given to these modes, both theoretically and experimentally. Recall that the measured values of both R_D and R_{D^*} are higher than the respective predictions (Eqn. (1.68),(1.69)). Also, in both R_D and R_{D^*}, the measured values are higher than the respective predictions. At the moment the measurements of R_D and R_{D^*} exceeds the respective SM predictions by 1.4σ and 3σ, respectively. It could be little more if we consider the experimental correlation between them which is -0.38. Therefore, in principle, we don't need a large new physics contribution to explain the current excesses.

We have noticed that due to the coupling of the $Z^{'}$ to the lepton families, there would be a vertex correction diagram contribution to the channel $b \to c\tau\bar{\nu_\tau}$ as shown in Fig. 4.9a. However,

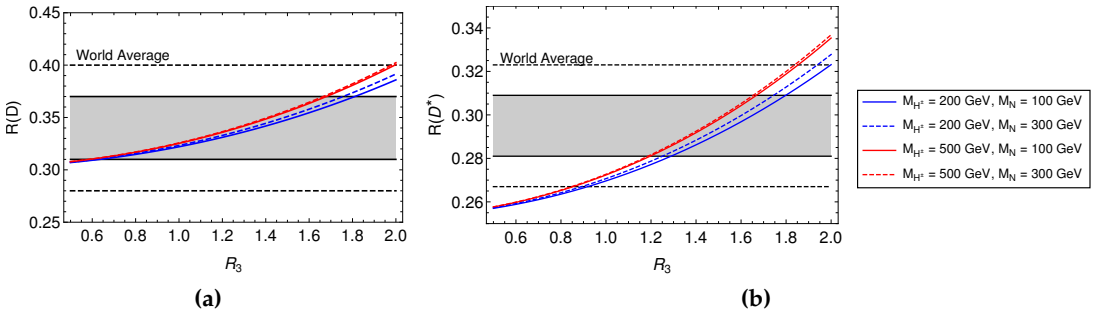

Figure 4.10: Variation of R_D and $R - D^*$ with coupling R_3 for two different values of $M_{H^\pm}$ and M_N as shown by the legends. The grey bands are the respective 1σ ranges of the world averages of these observables [13]. The dashed lines are the similar 2σ ranges of the data. We have plotted these for $M_{H^0} = M_{H^\pm}$ and $R_1 = 0.2$.

that contribution is not sufficient to explain the anomalies in $R_{D^{(*)}}$. With the addition of the inert scalar doublet and RHNs, we will have additional diagrams as shown in Fig. 4.9b. The lepton vertex is modified due to the loop corrections coming from the scalars $H^\pm$, H^0 and N_i, $(i = 1, 2, 3)$. Hence one can obtain a bound on the Yukawa couplings Y_{ij} of Eqn. (4.14) and masses of $H^\pm$, H^0 and RHN from the semi-leptonic $b \to c$ decays.

The diagram given in Fig. 4.9b will contribute to $\mathcal{C}_{V_1}$ of Eqn. (2.6) which is the WC of the four-fermion operator $\mathcal{O}_{V_1}$ in Eqn. (2.8). The following is the corresponding mathematical expression :

$$\mathcal{C}^i_{V_1} = \frac{Y^2_{ij}}{32\pi^2} \int_0^1 dx \int_0^{1-x} \ln \Delta^j_{WHH}, \tag{4.35}$$

and

$$\Delta^j_{WHH} = xM^2_{N_j} + (1 - x - z)M^2_H + zM^2_{H^\pm}. \tag{4.36}$$

Here (i, j) denote the generation index of the lepton and RHN respectively and M_H denotes the mass of H^0 or A^0 running in the loop. Hence depending on the generation of RHN running in the loop, we would have different contributions to $\mathcal{C}_{V_1}$ corresponding to each lepton flavour.

As shown earlier, N_2 is our DM candidate, hence, the corresponding diagram will contribute only to $\bar{B} \to D^{(*)}\mu\bar{\nu}_\mu$ decays and will be proportional to Y^2_{22}. There will be other diagrams with N_1 and N_3 which can contribute simultaneously to both $\bar{B} \to D^{(*)}\tau\bar{\nu}_\tau$ and $\bar{B} \to D^{(*)}e\bar{\nu}_e$ decays. Since the loop factor as mentioned above is sensitive to M_{N_i}, if we consider the masses of N_1 and N_3 equal, for simplicity, then the total NP WC for the tau mode would be proportional to $R^2_3 \equiv (Y^2_{31} + Y^2_{33})$ while that for the electron mode would be proportional to $R^2_1 \equiv (Y^2_{11} + Y^2_{13})$. If we assume that $Y_{13} << Y_{11}$ or $Y_{31} << Y_{33}$ then we can write down the following approximate relations: $R^2_3 \approx Y^2_{33}$ and $R^2_1 \approx Y^2_{11}$. Since the semi-leptonic branching fractions of the B meson into the light lepton channels are precisely measured [258, 259] and SM consistent, global fits of the NP Wilson coefficients to R_D, R_{D^*} data [96] is done by considering NP only in the τ decay modes. However, since we have contributions to all semi-leptonic decay channels, we consider NP in both the numerator and denominator of R_D, R_{D^*} while also ensuring that the contribution to the light lepton modes does not overshoot the experimental limits on their branching fractions.

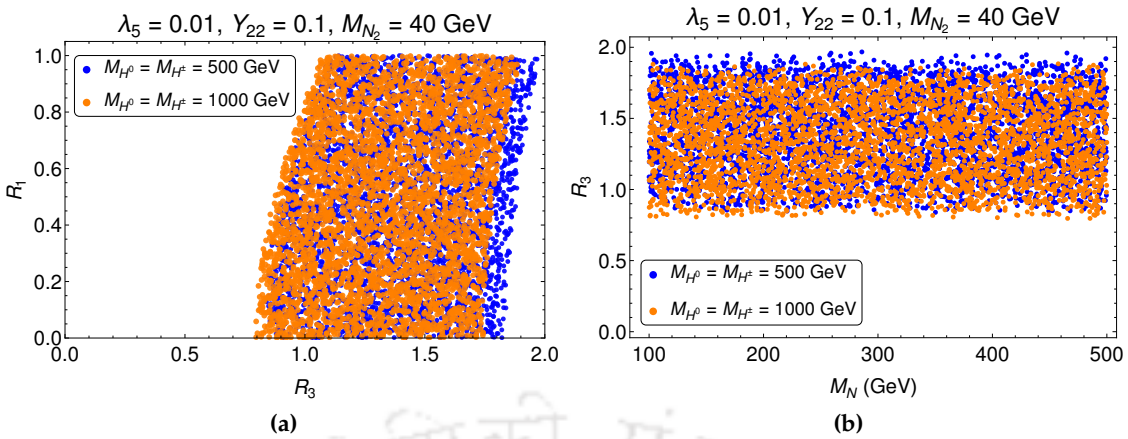

Figure 4.11: In the left plot, the region bounded by the points is the parameter space of R_1 and R_3 that satisfies R_D, R_{D^*} and $\mathcal{B}(\bar{B} \to D^{(*)}\ell\bar{\nu}_\ell)$ constraints in their 2σ CL and $\mathcal{B}(B_c \to \tau\nu) < 30\%$ for $M_{H^\pm} = 500$ GeV (blue) and $M_{H^\pm} = 1000$ GeV (orange). The other relevant parameters have been fixed as shown in the plot label. The correlation between R_3 and M_N is shown in the right plot.

In Fig. 4.10 we have shown the variation of R_D and R_{D^*} with the coupling R_3 for two different values of $M_{H^\pm} = M_{H^0}$ and M_N as shown by the blue and red legends. Since the measured value of R_D has a large error, a value of $R_3 \gtrsim 0.6$ can easily explain the observed data in its 1σ interval. On the other hand, to explain R_{D^*} within its 1σ range we need a value of $R_3 \gtrsim 1.2$; however, to explain the data at its 2σ range we need $R_3 \gtrsim 1.0$. Note that in these plots, we have not included the errors in the respective SM predictions.

We perform a parameter space scan of R_1, R_3 and $M_N (\equiv M_{N_1} = M_{N_3})$ by fixing $Y_{22} = 0.1$ and the masses of the inert scalars as shown in Fig. 4.11. The blue and the orange points are the allowed regions for $M_{H^\pm} = 500$ GeV and 1000 GeV respectively, when the RHN masses are varied between $100 - 500$ GeV. All these allowed points satisfy the experimental constraints on R_D, R_{D^*} and the branching fraction of $\bar{B} \to D^{(*)}\ell\bar{\nu}_\ell$ at their respective 2σ confidence interval (CI). These parameter spaces also satisfy the bound $\mathcal{B}(B_c \to \tau\nu) < 30\%$ and the corresponding expression in terms of $\mathcal{C}_{V_1}$ can be seen in [260]. From Fig. 4.11a it is evident that the data prefers $R_3 > R_1$. Also, as expected, athough it is allowed, we don't necessarily need large values for R_1 and the data allows a solution like $R_1 \approx 0$ while $R_3 \gtrsim 1$. In our model, $\mathcal{C}_{V_1}$ is positive; hence, the new contribution will interfere constructively with the SM and increase the relevant branching fractions from their SM predictions. Notice that there are minimal dependencies of $R_{D^{(*)}}$ on $M_{H^\pm}$ and M_{H^0}. However, as can be seen from Fig. 4.11b, it is almost independent of M_N.

Similar type of diagrams as given in Figure 4.23 with the replacement $c \to u$ will contribute to $b \to u\tau\bar{\nu}_\tau$ processes like $B^\pm \to \tau^\pm\nu_\tau$, $\bar{B}^0 \to \pi^+\tau^-\bar{\nu}_\tau$ decays. We have checked that the required values of the parameters for an explanation of the data in $b \to c\tau\bar{\nu}_\tau$ decays can accommodate the current observation $\mathcal{B}(B^\pm \to \tau^\pm\nu_\tau) = (1.09 \pm 0.24) \times 10^{-4}$ [12]. Similarly, our model will contribute to $s \to u\tau\bar{\nu}_\tau$, $c \to s\tau\bar{\nu}_\tau$ decays which will lead to semileptonic and purely leptonic decays of K and D/D_s-mesons, respectively.

The readers may note that in our model the contributions to the semileptonic decays mentioned

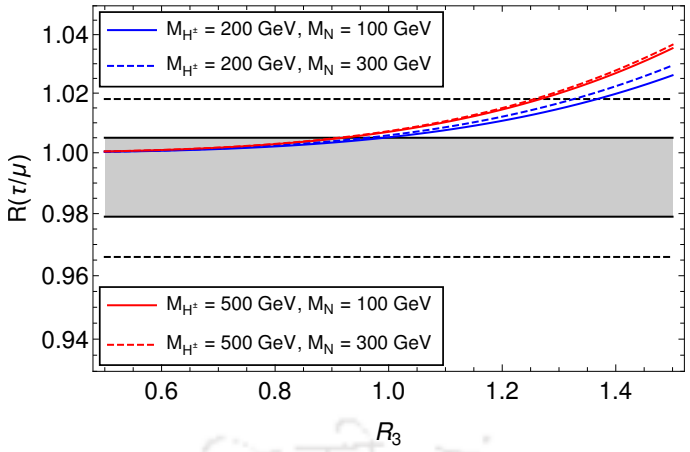

Figure 4.12: Dependence of lepton flavour universality test ratio $R(\tau/\mu)$ on parameter R_3 for different values of scalar and heavy neutrino masses as shown in the legends keeping Y_{22} fixed at 0.1.

above will modify the W-ℓ-ν_ℓ vertex. Therefore, in this respect, the ratio $R(\tau/\mu) = \frac{\mathcal{B}(W\to\tau\nu_\tau)}{\mathcal{B}(W\to\mu\nu_\mu)}$ will be a good probe for such kind of NP effects. The most recent measurement of this ratio by ATLAS Collaboration [261]

$$R(\tau/\mu) = 0.992 \pm 0.013, \tag{4.37}$$

is by far most precise and is in well agreement with the SM expectation. Therefore, it is important to ensure that our modification of the W-vertex does not overshoot this result. In Fig. 4.12, we have shown the variation of this ratio with R_3 for some fixed values of the inert Higgs and RHN masses and $Y_{22} = 0.1$. If we consider the data withing its 1-σ CI then $R_3 > 1$ is not allowed, however within the 2-σ range of $R(\tau/\mu)$ the values like $R_3 \approx 1.4$ is allowed. Therefore, we still have some part of the parameter space shown in Fig. 4.11 which is not excluded by this lepton flavour universality test; to conclude it further we have to wait for more precise data.

Anomalous Magnetic Moment and LFV

Magnetic moments :- In toy model-I, the additional contributions to anomalous magnetic moments will come from the type of diagram given in Fig. 4.13 (for $i = j$) with charged Higgs and RHNs in the loop. The contribution is given by

$$\Delta a_\ell^{(H^\pm, N_R)} = -\frac{|Y_{ij}|^2}{8\pi^2}\frac{m_\ell^2}{M_{H^\pm}^2}\int_0^1 dx \frac{2x^2(1-x)}{x + (1-x)(1-\lambda_j^{-2}x)\lambda_j^2 r_\ell(\mathrm{H}^\pm)} \tag{4.38}$$

where (i, j) denotes the generation of the lepton and RHN respectively, $\lambda_j = \frac{M_{N_j}}{m_\ell}$ and $r_\ell(\mathrm{H}^\pm) = (\frac{m_\ell}{M_{H^\pm}})^2$. In case of muon anomalous magnetic moment, for $M_{N_2} = 40$ GeV and $Y_{22} = 0.1$, we will obtain the following from Eqn. (4.38)

$$\Delta a_\mu(H^\pm) = \begin{cases} -1.10\times10^{-11}, & \text{For } M_{H^\pm} = 200 \text{ GeV}, \\ -1.86\times10^{-12}, & \text{For } M_{H^\pm} = 500 \text{ GeV}, \\ -4.70\times10^{-13}, & \text{For } M_{H^\pm} = 1000 \text{ GeV}, \end{cases} \tag{4.39}$$

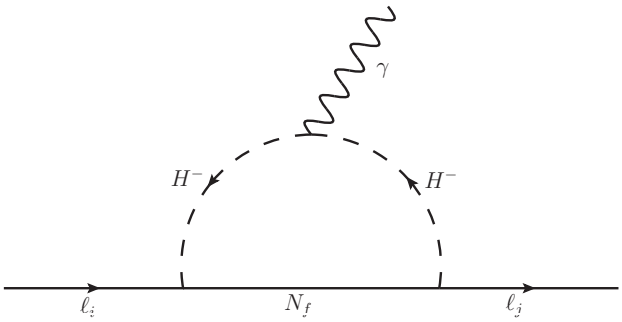

Figure 4.13: One loop charged Higgs contribution to lepton anomalous magnetic moment and $\tau \to e\gamma$.

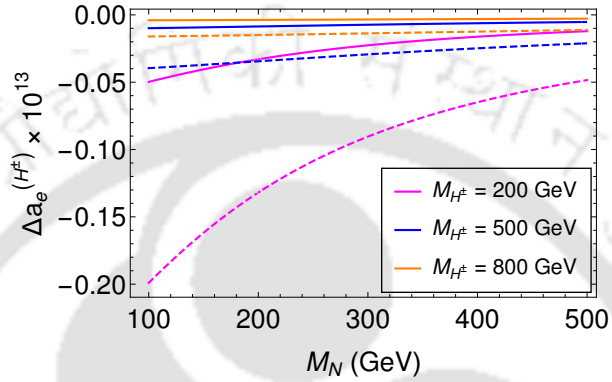

Figure 4.14: Plot shows the variation of the electron magnetic moment with the mass of RHNs for three different values of charged scalar mass $M_{H^\pm}$ as denoted by the legends. We have plotted each curve for two different values of R_1 : $R_1 = 0.5$ (solid) and $R_1 = 1.0$ (dashed).

which are suppressed compared to the gauge boson mediated diagram for it, which is shown in Fig. 4.3 (with X in the loop), by two or three orders in magnitude. On the contrary, as shown in Eqn. (4.12), the contribution to electron anomalous moment from the same diagram is negligibly small. Therefore, by extending the symmetry of the SM by an abelian $U(1)_X$ gauge group without additional degrees of freedom, we cannot explain the observed discrepancy in the electron magnetic moment.

Note that Δa_e (Eqn. (4.11)) has a significant error, and at 3-σ CI it is consistent with zero. Therefore, it would be too early to prejudge the potential impact of new physics on this observable. Here, we will show that our model has the potential to predict negative values Δa_e although it is difficult to explain the data in one or two-σ CI. From Eqn. (4.38) it is clear that Δa_e is sensitive to our predefined variable $R_1 \equiv \sqrt{Y_{11}^2 + Y_{13}^2}$. In Fig. 4.14, we show the variation of Δa_e with M_N for two different values of R_1 and three values of $M_{H^\pm}$. The chosen values of R_1, M_N and $M_{H^\pm}$ explain the data on R_D, R_{D^*} as previously shown in Fig. 4.11. From the plot we see that the contribution is negative and small and we can not reach the present experimental limit within its 1 or 2-σ CI. To get a large negative contribution we need small values of $M_{H^\pm}$ and M_N, and a large value of R_1 ($R_1 > 1$). However, $R_1 >> 1$ is not allowed by $\mathcal{B}(B \to D^{(*)}\ell\nu)$ data. Therefore, within the allowed parameter space of R_1 and M_N, we have a contribution to the electron anomalous magnetic moment which is negative and of order $\mathcal{O}(10^{-14})$ and within the 3σ range of the experimental data.

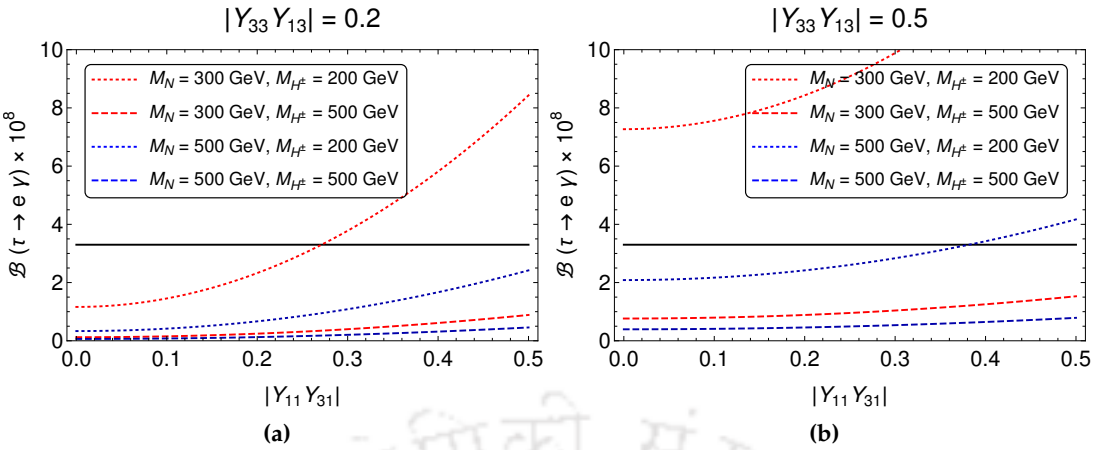

Figure 4.15: Variation of $\mathcal{B}(\tau \to e\gamma)$ with the coupling combination $|Y_{11}Y_{31}|$ for two different values of RHN mass $M_N \equiv M_{N_1} = M_{N_3}$ (red and blue). For a fixed M_N, we have also shown the variation with respect to the charged Higgs mass $M_{H^\pm}$ by dotted and dashed legends. The black solid line is the experimental upper limit on the branching fraction.

Lepton flavour violation:- The same one loop diagram given in Fig. 4.13 will also contribute to the LFV process $\tau \to e\gamma$. Therefore, one must ensure that the contribution is within the current experimental limit $\mathcal{B}(\tau \to e\gamma) < 3.3 \times 10^{-8}$[12]. However, in our model there will not be any contribution to $\tau \to \mu\gamma$ or $\mu \to e\gamma$. The expression for the partial decay width $\Gamma(\ell_i \to \ell_j\gamma)$ for the diagram in Fig. 4.13 is given by [262] :

$$\Gamma(\ell_i \to \ell_j\gamma) = \frac{\alpha}{4}\frac{|Y^*_{if}Y_{jf}|^2}{(16\pi^2)^2}\frac{m_i^5}{M^2_{H^\pm}}\mathcal{A}(r)^2 \tag{4.40}$$

where,

$$\mathcal{A}(r) = \frac{2r^2 - 5r - 1}{12(r-1)^3} - \frac{r^2 \log r}{2(r-1)^4} \tag{4.41}$$

and $r \equiv \left(\frac{M^2_{N_f}}{M^2_{H^\pm}}\right)$.

In the above expression for the decay width we have a combination $|Y_{11}Y_{31}|$ or $|Y_{33}Y_{13}|$ depending on whether N_1 or N_3 runs in the loop. So we can constrain the allowed values of these product couplings from the experimental upper limit on the branching fraction of $\tau \to e\gamma$. As we have seen earlier, if we assume that the off-diagonal Yukawas are much smaller in value than the diagonal ones, the data on $B \to D^{(*)}\ell\nu_\ell$ allow $R_3 \equiv Y_{33} \sim 1$ and $R_1 \equiv Y_{11} \sim 1$ for M_N in the range $(100 - 500)$ GeV or more. Therefore, in general, the magnitude of the product couplings as mentioned above could be small even if we assume $Y_{33} \sim Y_{11} \approx 1$.

In Figs. 4.15a and 4.15b, we have shown the variation of $\mathcal{B}(\tau \to e\gamma)$ with the product coupling $|Y_{33}Y_{13}|$ for different values of $M_{H^\pm}$ and M_N. Also, these two figures are generated for two discrete values of $|Y_{11}Y_{31}|$, which will be helpful to understand the dependence of $\mathcal{B}(\tau \to e\gamma)$ on this coupling. Notice that for low values of the masses, both the product couplings are tightly constrained. Masses like $M_{H^\pm} \sim 200$ GeV and $M_N \sim 200$ GeV are allowed for values of the product couplings about 0.2 or less which are perfectly consistent with all the other observations as men-

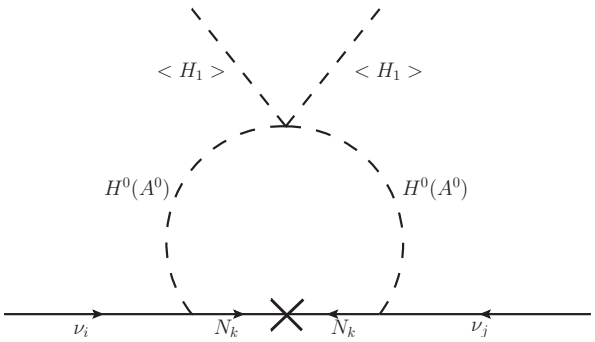

Figure 4.16: One loop neutrino mass generation mechanism.

tioned earlier. For higher values of the masses more higher values of the the product couplings are allowed.

Neutrino Mass Generation

The neutrino mass will be generated by radiative scotogenic mechanism in a way similar to the original proposal of [61] as depicted in Fig. 4.16 and will be mainly moderated by the mass splitting between H^0 and A^0. The one-loop contribution is given by :

$$(M_\nu)_{ij} = \sum_k \frac{Y_{ik} Y_{jk} M_k}{32\pi^2} \left(\frac{M^2_{H^0}}{M^2_{H^0} - M^2_k} \ln \frac{M^2_{H^0}}{M^2_k} - \frac{M^2_{A^0}}{M^2_{A^0} - M^2_k} \ln \frac{M^2_{A^0}}{M^2_k} \right) \tag{4.42}$$

where, M_k is the mass of the RHN N_k running in the loop. The Majorana mass matrix, however, has the following texture :

$$M_R = \begin{pmatrix} \frac{v_1}{\sqrt{2}} Y^\varphi_{11} & 0 & \frac{v_1}{\sqrt{2}} Y^\varphi_{13} \\ 0 & \frac{v_2}{\sqrt{2}} Y^\varphi_{22} & 0 \\ \frac{v_1}{\sqrt{2}} Y^\varphi_{31} & 0 & \frac{v_1}{\sqrt{2}} Y^\varphi_{33} \end{pmatrix}. \tag{4.43}$$

From the expression of the inert scalar masses in Eqn. (4.35), one can immediately see that $(M^2_{H^0} - M^2_{A^0}) = \lambda_5\, v^2$. Thus by tuning the parameter λ_5, one can obtain the correct light neutrino masses. However, it is important to ensure that the Yukawa couplings involved in the expression of light neutrino mass are consistent with the upper bound on the sum of the light neutrino masses, $\sum_i m_i \leq 0.12$ eV [66], as well as oscillation data on the neutrino mass squared differences and mixing angles [263, 264]. Hence it is convenient to rewrite the Yukawa couplings in terms of the light neutrino parameters in order to automatically incorporate the above constraints on the couplings. One useful way of achieving this is through the Casas-Ibarra (CI) parametrisation [265] extended to the radiative seesaw model [266] which enables us to express the Yukawa coupling matrix as

$$Y = U D_\nu^{1/2} R^\dagger \Lambda^{1/2} \tag{4.44}$$

where, U is the usual Pontecorvo-Maki-Nakagawa-Sakata (PMNS) mixing matrix, D_ν is the diagonal light neutrino mass matrix, R is an arbitrary complex orthogonal matrix satisfying $RR^T = 1$

and Λ is a diagonal matrix with elements

$$\Lambda_i = \frac{2\pi^2}{\lambda_5}\zeta_i \frac{2M_i}{v^2} \tag{4.45}$$

$$\text{and } \zeta_i = \left(\frac{M_i^2}{8(M_{H^0}^2 - M_{A^0}^2)}\left[L_i(M_{H^0}^2) - L_i(M_{A^0}^2)\right]\right)^{-1}, \tag{4.46}$$

where $L_i(m^2)$ is the mass function defined as

$$L_i(m^2) = \frac{m^2}{m^2 - M_i^2}\ln\frac{m^2}{M_i^2}. \tag{4.47}$$

Note that we are working in a basis where the charged lepton mass matrix is not diagonal. The PMNS mixing matrix can be parametrised as

$$U = U_{\text{PMNS}} = \begin{bmatrix} c_{12}c_{13} & s_{12}c_{13} & s_{13}e^{-i\delta} \\ -c_{23}s_{12} - s_{23}s_{13}c_{12}e^{i\delta} & c_{23}c_{12} - s_{23}s_{13}s_{12}e^{i\delta} & s_{23}c_{13} \\ s_{23}s_{12} - c_{23}s_{13}c_{12}e^{i\delta} & -s_{23}c_{12} - c_{23}s_{13}s_{12}e^{i\delta} & c_{23}c_{13} \end{bmatrix} P, \tag{4.48}$$

where $c_{ij} = \cos\theta_{ij}$, $s_{ij} = \sin\theta_{ij}$ and δ is the leptonic Dirac CP phase. The diagonal matrix $P = \text{diag}(1, e^{i\alpha}, e^{i(\beta+\delta)})$ contains the Majorana CP phases α, β that appears when ν is Majorana and are not constrained by neutrino oscillation data but has to be probed by alternative experiments. This leptonic mixing matrix is related to the diagonalising matrices of charged lepton and neutrino mass matrices as $U = V_L^\dagger U_\nu$ and as mentioned above, V_L is not a unit matrix in our model. It consists of a rotation in $(1-3)$ plane which can be parametrised as

$$V_L = \begin{pmatrix} c_{13}^l & 0 & s_{13}^l e^{-i\delta_l} \\ 0 & 1 & 0 \\ -s_{13}^l e^{i\delta_l} & 0 & c_{13}^l \end{pmatrix}, \tag{4.49}$$

where $c_{13}^l = \cos\theta_{13}^l$, $s_{13}^l = \sin\theta_{13}^l$ and δ_l is an arbitrary phase which we assume to be zero for simplicity. Using this and the above parametric form of PMNS mixing matrix U, one can parametrise U_ν which can then be used to parametrise the light neutrino mass matrix as

$$M_\nu = U_\nu M_\nu^{(\text{diag})} U_\nu^T. \tag{4.50}$$

In the above expression for M_ν, the diagonal light neutrino mass matrix is denoted by $M_\nu^{(\text{diag})} = \text{diag}(m_1, m_2, m_3)$ where the light neutrino masses can follow either normal ordering (NO) or in-

verted ordering (IO). For NO, the three neutrino mass eigenvalues can be written as

$$M_\nu^{\rm diag} = {\rm diag}(m_1, \sqrt{m_1^2 + \Delta m_{21}^2}, \sqrt{m_1^2 + \Delta m_{31}^2})$$

while for IO, they can be written as

$$M_\nu^{\rm diag} = {\rm diag}(\sqrt{m_3^2 + \Delta m_{23}^2 - \Delta m_{21}^2}, \sqrt{m_3^2 + \Delta m_{23}^2}, m_3)$$

Structure of this parametric form of light neutrino mass matrix can now be compared with the structure of light neutrino mass matrix predicted by the model. Note that the model not only predicts a specific structure of right handed neutrino mass matrix given by Eqn. (4.43), but also predicts the Dirac Yukawa coupling matrix to have a similar structure

$$Y = \begin{pmatrix} Y_{11} & 0 & Y_{13} \\ 0 & Y_{22} & 0 \\ Y_{31} & 0 & Y_{33} \end{pmatrix}. \tag{4.51}$$

Using the formula for light neutrino masses given in Eqn. (4.42), it can be shown that the above mentioned textures of Dirac Yukawa coupling matrix Y and right handed neutrino mass matrix M_R lead to a very specific structure of light neutrino mass matrix with two independent zeros namely, $(M_\nu)_{e\mu} = (M_\nu)_{\mu e} = 0, (M_\nu)_{\mu\tau} = (M_\nu)_{\tau\mu} = 0$ where the equality $(M_\nu)_{\alpha\beta} = (M_\nu)_{\beta\alpha}$ results due to Majorana nature of light neutrinos giving rise to a complex symmetric structure of mass matrix.

We numerically solve these two texture zero complex equations in order to evaluate the unknowns namely, the lightest neutrino mass m_1 (NO), m_3 (IO), leptonic Dirac CP phase δ as well as two Majorana CP phases α, β. The additional rotation angle in charged lepton sector θ_{13}^l is considered as a free parameter which can lie anywhere in $(0, \pi/2)$. The other known parameters namely, three mixing angles, two mass squared differences are varied in 3σ range [264]. We find that these textures in light neutrino mass matrix predict a large value of the lightest neutrino mass, which is in tension with Planck 2018 bound on sum of absolute neutrino masses $\sum_i m_i \leq 0.12$ eV [66] as well as bounds on absolute neutrino mass scale from laboratory based experiments like KATRIN [267]. Even if we consider a non-zero CP phase in charged lepton correction matrix V_L, this conclusion does not change. This is not surprising, given the fact that almost all possible two-zero textures in diagonal charged lepton basis are ruled out by latest experimental data [268].

One possible way to make it consistent with neutrino data without changing the model significantly is to change the $U(1)_X$ charge of the singlet scalar ϕ_2 from 4 to 1. This results in a right handed neutrino mass matrix having only one zero at (22) entry. While the lightest eigenstate of singlet fermion mass matrix can still be a DM candidate, no zeros appear in the light neutrino mass matrix even with the same Dirac Yukawa (4.51). Such a general structure of light neutrino

mass matrix can be fitted with light neutrino data as there are sufficient free parameters, unlike in the previous case with two texture zeros. It is very unlikely that such a setup will change our DM and flavour physics results significantly. In the following subsection, we have added a discussion on this modified scenario.

Modified Setup for Toy Model I

As mentioned in the previous section, the light neutrino mass matrix that we obtain in this scenario violates the Planck 2018 bound on the sum of absolute neutrino masses. We also identified that a possible way out of this issue is by choosing the $U(1)_X$ charge of the singlet scalar ϕ_2 to be 1 instead of 4. In this subsection, we will briefly point out the changes that will occur in our theoretical setup and how it might affect the other observables. First of all, the Yukawa interactions given in Eqn. (4.15) will be modified as given below in Eqn. (4.52).

$$-\mathcal{L}_Y \supset \sum_{i,j} Y_{ij}\bar{L}_i\tilde{H}_2 N_j + Y_{22}\bar{L}_2\tilde{H}_2 N_2 + \sum_{i,j=(1,3)} Y^{\varphi}_{ij}\bar{N}^c_i N_j\varphi_1 + \sum_{i=1,3} Y^{\varphi}_{i2}\bar{N}^c_i N_2\varphi_2. \tag{4.52}$$

Note that the first three terms of the Yukawa Lagrangian remain unchanged, however, the interaction term involving N_2 and ϕ_2 has changed. Also, there will be a little change in the scalar potential, the trilinear term in Eqn. (4.18) now becomes $\left\{\delta\ \varphi_2\varphi_2\varphi_1^{\dagger} + \text{h.c.}\right\}$. Hence, the pseudoscalar mass, which primarily depended on this trilinear term, modifies to $M_{A_2} = \left(-\frac{v_2^2\delta}{\sqrt{2}v_1 s_\gamma^2}\right)^{1/2}$. Recall that the gauge boson mass M_X mass and gauge coupling g_X are related to the singlet vevs (Eqn. (4.22)). With the change in the $U(1)_X$ charge of φ_2, the aboove relation changes to

$$M_X^2 = \frac{1}{4}g'^2 v^2\epsilon^2 + g_X^2(4v_1^2 + v_2^2), \tag{4.53}$$

and for $\epsilon << 1$, we obtain $M_{Z'} \simeq M_X = g_X\sqrt{(4v_1^2 + v_2^2)}$. For simplicity, if we consider $v_1 = v_2$, then from Eqn. (4.53), $v_1 \approx 450$ GeV for $M_X = 1$ GeV and $g_X \simeq 0.001$. Therefore the masses of s_1 and s_2 will be restricted to be $\lesssim 450$ GeV for the Yukawa and quartic couplings to remain perturbative.

The analysis of relic abundance and the direct detection cross section will be in a similar line as discussed in subsection 4.5.1. The annihilation via Z' remains the same. However, we can not consider a pure N_2 state as our DM candidate, since the the Yukawa Lagrangian does not have a Majorana mass term for N_2. Therefore, in principle, the lightest particle of N_1 and N_3 can be our DM candiate, and the dominating contributions will come from the annihilation diagrams shown in Fig. D.2. In such situation, as before, depending on the mass of s_1, the relic abundance will once again be satisfied near the resonances i.e. near $M_{DM} \sim M_{s_1}/2$. In the presence of s-channel annihilation, the role of co-annihilations are expected to be sub-dominant as in the previous setup.

The possibility of mixing of the pure states N_1, N_2 and N_3 can be considered by rotating the

interaction basis N_i to a new basis N_i' by using a general unitary transformation as

$$\begin{pmatrix} N_1 \\ N_2 \\ N_3 \end{pmatrix} = \mathcal{O}_{\nu_R} \begin{pmatrix} N_1' \\ N_2' \\ N_3' \end{pmatrix} \tag{4.54}$$

which will result in a mass matrix of the form

$$\begin{pmatrix} M_1' \\ M_2' \\ M_3' \end{pmatrix} = \mathcal{O}_{\nu_R} M_R \mathcal{O}_{\nu_R}^T. \tag{4.55}$$

In the rotated basis, the lowest mass eigenstate can be considered as the DM candidate which will contribute via the annihilation diagram as given in Fig. D.2.

The Yukawa Lagrangian responsible for the RHN masses also gets modified such that the Majorana mass mixing matrix now becomes

$$M_R = \begin{pmatrix} \frac{v_1}{\sqrt{2}} Y_{11}^{\varphi} & \frac{v_2}{\sqrt{2}} Y_{12}^{\varphi} & \frac{v_1}{\sqrt{2}} Y_{13}^{\varphi} \\ \frac{v_2}{\sqrt{2}} Y_{21}^{\varphi} & 0 & \frac{v_2}{\sqrt{2}} Y_{23}^{\varphi} \\ \frac{v_1}{\sqrt{2}} Y_{31}^{\varphi} & \frac{v_2}{\sqrt{2}} Y_{32}^{\varphi} & \frac{v_1}{\sqrt{2}} Y_{33}^{\varphi} \end{pmatrix}. \tag{4.56}$$

This is in contrast to the mass matrix we obtained before in Eqn. (4.43). Since the mixing angles (s_{ij}^{ν}) of $\mathcal{O}_{\nu_R}$ are completely arbitrary, we have full freedom of choosing them in a way such that $M_2' < M_1', M_3'$ and the Yukawa couplings are also perturbative.

It is important to note that the contributions to the other observables like anomalous magnetic moments, LFV decays and $R_{D^{(*)}}$ remain unaltered. We have already seen that a charged Higgs and RHN mediated diagram contributes to the magnetic moments of the leptons (cf. Fig. 4.13). In the modified set-up, the changes occur in the Majorana- Yukawa interactions, which involves the coupling Y_{ij}^{ϕ}, and they do not contribute to $\Delta a_{\mu,e}$, LFV decays or $R_{D^{(*)}}$.

4.5.2 Toy Model II

Particle Content

In this toy model, we have the same particle content as in the previous case, with the only difference being that all particles except N_2 are even under the discrete $\mathcal{Z}_2$ symmetry. This will once again prevent it from interacting directly with SM leptons. However, in this scenario, the neutrino mass generation mechanism will be different from the previous one. The particle content, along with their respective gauge quantum number and charges, has been described in Table 4.4.

Particles	$SU(3)_c \times SU(2)_L \times U(1)_Y$	$U(1)_X$	$\mathcal{Z}_2$
$Q_L = \begin{pmatrix} u_L \\ d_L \end{pmatrix}$	$(3, 2, \frac{1}{6})$	0	+
u_R	$(3, 1, \frac{2}{3})$	0	+
d_R	$(3, 1, -\frac{1}{3})$	0	+
$L_1 = \begin{pmatrix} \nu_e \\ e \end{pmatrix}_L$	$(1, 2, -\frac{1}{2})$	-1	+
$L_2 = \begin{pmatrix} \nu_\mu \\ \mu \end{pmatrix}_L$	$(1, 2, -\frac{1}{2})$	2	+
$L_3 = \begin{pmatrix} \nu_\tau \\ \tau \end{pmatrix}_L$	$(1, 2, -\frac{1}{2})$	-1	+
e_R	$(1, 1, -1)$	-1	+
μ_R	$(1, 1, -1)$	2	+
τ_R	$(1, 1, -1)$	-1	+
H_1	$(1, 2, \frac{1}{2})$	0	+
N_{1R}	$(1, 1, 0)$	-1	+
N_{2R}	$(1, 1, 0)$	2	-
N_{3R}	$(1, 1, 0)$	-1	+
H_2	$(1, 2, \frac{1}{2})$	-3	+
φ_1	$(1, 1, 0)$	2	+
φ_2	$(1, 1, 0)$	4	+

Table 4.4: Particle content for Toy model II.

Lagrangian and Scalar Mass Spectrum

In this scenario, the successful generation of charged lepton and light neutrino masses require H_2 to be charged under $U(1)_X$. The relevant Yukawa interactions are given by:

$$\begin{aligned} -\mathcal{L}_Y \supset & \sum_{i,j} Y^{\ell}_{ij} \bar{L}_i H_1 e_{jR} + \sum_{j} Y^{\ell}_{jk} \bar{L}_j H_2 e_{kR} + \sum_{i,j} Y^{\nu}_{ij} \bar{L}_i \tilde{H}_1 N_{jR} + \sum_{j} Y^{\nu}_{kj} \bar{L}_k \tilde{H}_2 N_{jR} \\ & + \sum_{i,j} Y^{\varphi}_{ij} \bar{N^c_{iR}} N_{jR} \varphi_1 + Y^{\varphi}_{kk} \bar{N^c_{kR}} N_{kR} \varphi_2^\dagger \end{aligned} \tag{4.57}$$

where both i and j can take values $(1, 3)$ and $k = 2$. Thus only the second generation of lepton doublet couples to $N_{1,3}$ via the second Higgs doublet H_2. The scalar Lagrangian will be similar to the one defined in Eqn. (4.16) with the scalar potential as given below:

$$\begin{aligned} V(H_1, H_2, \varphi_1, \varphi_2) = & \mu_1^2 |H_1|^2 + \mu_2^2 |H_2|^2 + \mu_3^2 |\varphi_1|^2 + \mu_4^2 |\varphi_2|^2 + \frac{\lambda_{H_1}}{2} |H_1|^4 + \frac{\lambda_{H_2}}{2} |H_2|^4 \\ & + \frac{\lambda_{\varphi_1}}{2} |\varphi_1|^4 + \frac{\lambda_{\varphi_2}}{2} |\varphi_2|^4 + \lambda_1 |H_1|^2 |H_2|^2 + \lambda_2 (H_1^\dagger H_2)(H_2^\dagger H_1) \\ & + \lambda_3 (\varphi_1^\dagger \varphi_1)(\varphi_2^\dagger \varphi_2) + \lambda_4 |H_1|^2 |\varphi_1|^2 + \lambda_5 |H_1|^2 |\varphi_2|^2 + \lambda_6 |H_2|^2 |\varphi_1|^2 \\ & + \lambda_7 |H_2|^2 |\varphi_2|^2 + \left\{ \delta \, \varphi_1 \varphi_1 \varphi_2^\dagger + \text{h.c.} \right\} + \frac{c}{\Lambda^2} \left\{ (H_1^\dagger H_2)^2 (\varphi_1 \varphi_2) + \text{h.c.} \right\}. \end{aligned} \tag{4.58}$$

In this case, all the scalars acquire a vev and are given by :

$$H_1 = \begin{pmatrix} w^{\pm} \\ \frac{v+h^{'}+iz^{'}}{\sqrt{2}} \end{pmatrix}, \; H_2 = \begin{pmatrix} h^{\pm} \\ \frac{u+H^{0^{'}}+iA^{0^{'}}}{\sqrt{2}} \end{pmatrix}, \; \varphi_1 = \begin{pmatrix} \frac{v_1+s_1^{'}+iA_1^{'}}{\sqrt{2}} \end{pmatrix}, \; \varphi_2 = \begin{pmatrix} \frac{v_2+s_2^{'}+iA_2^{'}}{\sqrt{2}} \end{pmatrix} \tag{4.59}$$

Under such a scenario, electroweak symmetry breaking of the scalars require $\mu_i^2 < 0$ $(i = 1, 2, 3, 4)$ and the minimization conditions are given by:

$$\begin{aligned}
\mu_1^2 &= -\frac{1}{2}\Big(u^2(\lambda v_1 v_2 + \lambda_1 + \lambda_2) + \lambda_4 v_1^2 + \lambda_5 v_2^2 + \lambda_{H_1} v^2\Big), \\
\mu_2^2 &= -\frac{1}{2}\Big(v^2(\lambda v_1 v_2 + \lambda_1 + \lambda_2) + \lambda_6 v_1^2 + \lambda_7 v_2^2 + \lambda_{H_2} u^2\Big), \\
\mu_3^2 &= -\frac{1}{4v_1}\Big(u^2 v^2 v_2 \lambda + 2v_1(2\sqrt{2}v_2\delta + \lambda_3 v_2^2 + \lambda_4 v^2 + \lambda_6 u^2) + 2\lambda_{\varphi_1} v_1^3\Big), \\
\mu_4^2 &= -\frac{1}{4v_2}\Big(u^2 v^2 v_1 \lambda + 2v_1^2(\sqrt{2}v_2\delta + \lambda_3 v_2) + 2v_2(\lambda_5 v^2 + \lambda_7 u^2 + \lambda_{\varphi_2} v_2^2)\Big),
\end{aligned} \tag{4.60}$$

where $\lambda = \frac{c}{\Lambda^2}$; the usefulness of this term will be discussed later in this subsection. The covariant derivative can be defined in the same way as in the previous case Eqn. (4.17). From the kinetic part of the scalar Lagrangian, we obtain the mass of the W-boson as :

$$M_W^2 = \frac{1}{4} g^2 (u^2 + v^2). \tag{4.61}$$

One can rewrite the mass of W as $M_W^2 = \frac{1}{4} g^2 v_H^2$ where, $v_H^2 = (u^2 + v^2) = (246)^2$ GeV^2. We also express the ratio of the two vevs as $\frac{v}{u} = \tan\beta$. The neutral gauge bosons (W_μ^3, B_μ, X_μ) on the other hand mix and the mixing matrix is given by :

$$M_{GB}^2 = \begin{pmatrix} \frac{1}{4}g^2(u^2+v^2) & -\frac{1}{4}gg'(u^2+v^2) & -\frac{3}{2}gg_X u^2 \\ -\frac{1}{4}gg'(u^2+v^2) & \frac{1}{4}g'^2(u^2+v^2) & \frac{3}{2}g^{'}g_X u^2 \\ -\frac{3}{2}gg_X u^2 & \frac{3}{2}g' g_X u^2 & g_X^2\Big(9u^2 + 4(v_1^2 + 4v_2^2)\Big). \end{pmatrix} \tag{4.62}$$

After the usual Weinberg rotation as given in Eqn. (4.24), we obtain the masses of the physical neutral gauge bosons as :

$$M_\gamma^2 = 0, \tag{4.63}$$

$$M_Z^2 = M_{Z^0}^2 = \frac{1}{4C_W^2} g^2 v_H^2, \tag{4.64}$$

$$M_{Z'}^2 = M_X^2 - \left(\frac{\Delta^4}{M_{Z^0}^2}\right), \tag{4.65}$$

where $M_X^2 = g_X^2(4(v_1^2 + 4v_2^2) + 9u^2) - 3g' g_X u^2 \epsilon + \mathcal{O}(\epsilon^2)$ and $\Delta^2 = \frac{g}{4C_W^2}\left(6g_X u^2 - g' v_H^2 \epsilon\right)$. One can immediately see that in the limit $\epsilon << 1$, $M_{Z'}^2 = M_X^2 \simeq g_X^2(9u^2 + 4(v_1^2 + 4v_2^2) + 9u^2)$.

In this model, none of the scalars are $\mathcal{Z}_2$ odd, therefore, in principle, both the CP even and CP

odd neutral components mix to give two (4×4) mixing mass matrices; one for $(h^{'}, s_1^{'}, s_2^{'}, H^{0^{'}})$ and the other for $(z^{'}, A_1^{'}, A_2^{'}, A^{0^{'}})$ as given below in eqs. (4.66) and (4.67), respectively. We also have a (2×2) mixing matrix for the charged scalars $(w^{\pm}, h^{\pm})$ as given in Eqn. (4.68).

$$M_{sc}^2=\begin{pmatrix} \lambda_{H_1}v^2 & \frac{1}{2}\lambda u^2vv_2+\lambda_4vv_1 & \frac{1}{2}\lambda u^2vv_1+\lambda_5vv_2 & uv(\lambda v_1v_2+\lambda_1+\lambda_2)\\ \frac{1}{2}\lambda u^2vv_2+\lambda_4vv_1 & -\frac{\lambda u^2v^2v_2-4\lambda_{\varphi_1}v_1^3}{4v_1} & \sqrt{2}v_1\delta+\frac{1}{4}\lambda u^2v^2+\lambda_3v_1v_2 & u(\frac{1}{2}\lambda v^2v_2+\lambda_6v_1)\\ \frac{1}{2}\lambda u^2vv_1+\lambda_5vv_2 & \sqrt{2}v_1\delta+\frac{1}{4}\lambda u^2v^2+\lambda_3v_1v_2 & -\frac{2\sqrt{2}v_1^2\delta+\lambda u^2v^2v_1-4\lambda_{\varphi_2}v_2^3}{4v_2} & u(\frac{1}{2}\lambda v^2v_1+\lambda_7v_2)\\ uv(\lambda v_1v_2+\lambda_1+\lambda_2) & u(\frac{1}{2}\lambda v^2v_2+\lambda_6v_1) & u(\frac{1}{2}\lambda v^2v_1+\lambda_7v_2) & \lambda_{H_2}u^2 \end{pmatrix} \tag{4.66}$$

$$M_{pseudo}^2=\begin{pmatrix} -\lambda u^2v_1v_2 & \frac{1}{2}\lambda u^2vv_2 & \frac{1}{2}\lambda u^2vv_1 & \lambda uvv_1v_2\\ \frac{1}{2}\lambda u^2vv_2 & -\frac{v_2(8\sqrt{2}v_1\delta+\lambda u^2v^2)}{4v_1} & \sqrt{2}v_1\delta-\frac{1}{4}\lambda u^2v^2 & -\frac{1}{2}\lambda uv^2v_2\\ \frac{1}{2}\lambda u^2vv_1 & \sqrt{2}v_1\delta-\frac{1}{4}\lambda u^2v^2 & -\frac{v_1(2\sqrt{2}v_1\delta+\lambda u^2v^2)}{4v_2} & -\frac{1}{2}\lambda uv^2v_1\\ \lambda uvv_1v_2 & -\frac{1}{2}\lambda uv^2v_2 & -\frac{1}{2}\lambda uv^2v_1 & -\lambda v^2v_1v_2 \end{pmatrix} \tag{4.67}$$

$$M_{ch}^2=\frac{(v_1v_2\lambda+\lambda_2)}{2}\begin{pmatrix} -u^2 & \frac{1}{2}uv\\ \frac{1}{2}uv & -u^2 \end{pmatrix} \tag{4.68}$$

We therefore require two (4×4) rotation matrices (cf. Appendix B.2) to diagonalize the CP even and CP odd Higgs which we denote by $\mathcal{R}_\alpha$ and $\mathcal{R}_\theta$ respectively (as shown in Eqn. (4.69)) and an orthogonal rotation by angle γ for the charged scalars.

$$\begin{pmatrix} h\\ s_1\\ s_2\\ H^0 \end{pmatrix}=\mathcal{R}_\alpha^T\begin{pmatrix} h^{'}\\ s_1^{'}\\ s_2^{'}\\ H^{0^{'}} \end{pmatrix},\begin{pmatrix} G_z\\ G_{z'}\\ A_2\\ A^0 \end{pmatrix}=\mathcal{R}_\theta^T\begin{pmatrix} z^{'}\\ A_1^{'}\\ A_2^{'}\\ A^{0^{'}} \end{pmatrix}\text{ and, }\begin{pmatrix} G^{\pm}\\ H^{\pm} \end{pmatrix}=\mathcal{R}_\gamma^T\begin{pmatrix} w^{\pm}\\ h^{\pm} \end{pmatrix} \tag{4.69}$$

where $G_z, G_{z'}$ and $G^{\pm}$ are the massless Goldstones corresponding to the physical vector bosons Z, Z' and W respectively. Notice that in the scalar potential in Eqn. (4.58), we have added a higher dimensional symmetry breaking term proportional to $\lambda(=\frac{c}{\Lambda^2})$ apart from the trilinear term. The relevance of this term can be easily understood from the scalar mass matrix given in Eqn. (4.67). In this matrix, the elements of the first and fourth rows and columns are proportional to λ; hence, if we set $\lambda=0$, the resulting mass matrix will be a 2×2 matrix with determinant zero, which results in zero mass pseudo-scalar fields which can give rise to a long range force between the DM and ordinary matter. However, such massless bosons are very tightly constrained by fifth force searches. If the coupling of these pseudoscalars to SM is sizeable, then they can be produced in the early universe giving rise to additional radiation or relativistic degrees of freedom which is tightly constrained by BBN and CMB limits. Also, in absence of this higher dimensional term, the $U(1)_X$ symmetry can be broken by the vev of H_2 alone, and we don't need the additional singlet scalars.

We denote the angles in $\mathcal{R}_{\alpha(\theta)}$ by $\alpha_{ij}(\theta_{ij})$. Thus, we have many unconstrained terms in the rotation matrices $\mathcal{R}_{\alpha,\theta}$ with at least 6 mixing angles in each, and so we make the following assumptions to simplify the analysis:

(i) The mixing angles of h with the singlet scalars are $\alpha_{12} \equiv \alpha_2$ and $\alpha_{13} \equiv \alpha_3$, respectively. Also, we have not considered very large mixing scenarios.

(ii) For simplicity, the mixing angles of H^0 with the singlet scalars are set to zero, i.e $\alpha_{24} = \alpha_{34} \equiv 0$. Also, the possibility of mixing between the two singlet scalars has been neglected, i.e $\alpha_{23} \simeq 0$.

(iii) We denote the mixing of the h and H^0 by $\alpha_{14} \equiv \alpha$.

A similar approximation is also considered for the rotation matrix $\mathcal{R}_\theta$. This helps us to eliminate some of the mixing angles for each of the matrices. Therefore, we are left with the following free parameters:

$$\tan\beta, v_1, M_h, M_{s_1,s_2,H^0}, M_{A^0}, M_{A_2}, M_{H^\pm}, \text{Mixing angles } (\alpha, \alpha_2, \alpha_3, \theta, \theta_2, \theta_3, \gamma). \tag{4.70}$$

The couplings expressed in terms of masses and mixing angles can be found in Appendix C.2. These model parameters are constrained from both theoretical requirements of unitarity, vacuum stability, perturbativity etc. and experimental data on electroweak observables, Higgs decays and so on. We have assumed small values of α_2 and α_3 so that we can utilize the existing bound on the parameters like α and β of a two Higgs doublet model (2HDM) scenario with and without an additional singlet. For recent analyses of extended 2HDM see [269–273]. It has been shown that large singlet doublet admixture is allowed by the LEP and LHC data [271]. However, a large admixture does not allow a large value for $|\cos(\beta-\alpha)|$ [269]. In our analysis, we have considered the scenarios with $\tan\beta \leq 5$ and $|\cos(\beta-\alpha)| < 0.1$, also, we have assumed $\sin\alpha_2 \leq 0.1$ and $\sin\alpha_3 \leq 0.1$.

We identify h to be the 125 GeV Higgs boson discovered at the LHC and restrict the parameters in the following range :

$$\begin{aligned}
&1 < \tan\beta < 5, \quad \cos(\beta-\alpha) \in [-0.1, 0.1], \quad v_1 = 450\ \text{GeV},\\
&M_{H^0} \in [1, 100]\ \text{GeV}, \quad M_{s_1} \in [150, 450]\ \text{GeV}, \quad M_{s_2} \in [10, 100]\ \text{GeV},\\
&M_{H^\pm} \in [100, 300]\ \text{GeV}, \quad M_{A^0} \in [100, 300]\ \text{GeV}, \quad M_{A_2} \in [100, 300]\ \text{GeV},\\
&\sin\alpha_{2,3} \in [-0.1, 0.1], \quad \sin\theta \in [-0.1, 0.1], \quad \sin\theta_{2,3} \in [-0.1, 0.1], \quad \sin\gamma \in [-0.1, 0.1].
\end{aligned} \tag{4.71}$$

For the above range of masses, the scale $\Lambda \sim (300 - 600)$ GeV for $c = -1$. Note that $\tan\beta > 1$ allows only the scenario $M_h > M_{H^0}$ otherwise λ_{H_2} will pick up a very large value. One can have the scenario $M_h < M_{H^0}$ when $\tan\beta < 1$, however, these choices will lead to the large values of λ_{H_1}, and at the same time top-Yukawa $y_t >> 1$.

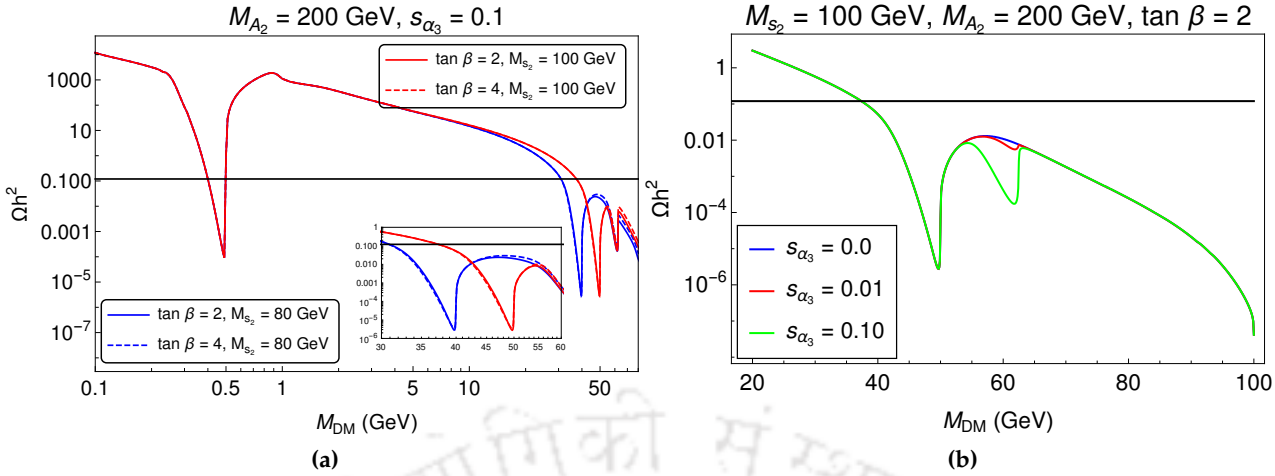

Figure 4.17: (a) The variation of relic abundance with the dark matter mass for different values of tan β and the mass M_{s_2}. In the inset we have zoomed into the annihilation peaks of the DM for $30 < M_{DM}(\text{GeV}) < 60$. The black solid line denotes the Planck observed relic of DM. (b) Same as in Fig. 4.17a for different values of sine of the mixing angle α_3.

DM Phenomenology

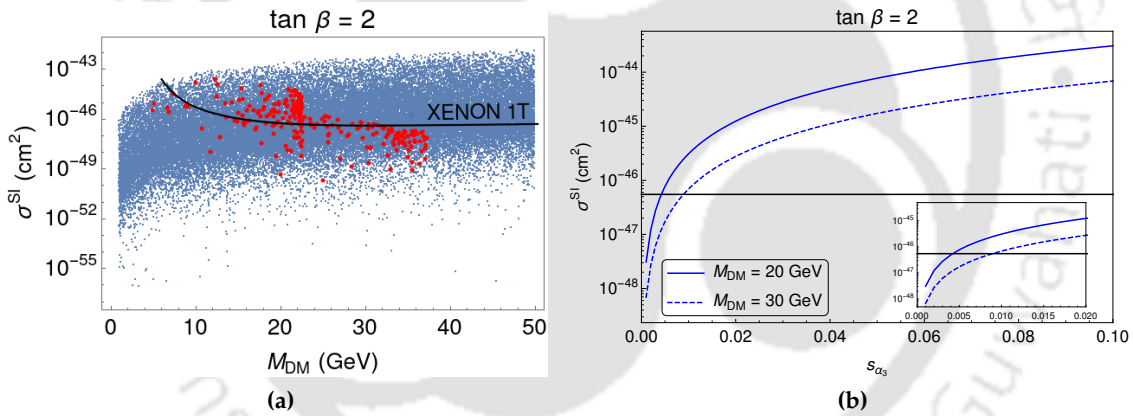

Figure 4.18: (a) The bounds on M_{DM} from relic and the allowed limit on DM direct detection cross section (σ^{SI}). (b) The variation of σ^{SI} with s_{α_3} for different allowed values of M_{DM}.

In this case, at the leading order, the contributions to the relic abundance and the direct detection cross-section will come from similar type of annihilation diagrams, as shown in Fig. D.1. Hence the true relic abundance is expected to be satisfied only around the resonances of the different scalar and vector mediators. There will be no coannihilations in this case. Apart from $M_{Z'}$ and $g_{Z'}$, the other model parameters which will have a dominant role in DM searches are given by M_{s_2}, s_{α_3} and $Y_{22}^{\varphi} \approx \frac{\sqrt{2}M_{N_2}}{v_2}$. The other parameters which will have a subdominant role are given by M_{s_1}, M_{A_2}, $\tan\beta$ and s_{α_2}. Therefore, we have fixed their values at $M_{s_1} = 400$ GeV, $M_{A_2} = 200$ GeV and $s_{\alpha_2} = 0.1$, respectively. In Fig. 4.17a, we have shown the variation of the dark matter relic abundance with DM mass for two different values of tan β. The nature of the curve is similar to the one observed in our toy model 1 (see Fig. 4.7a). When the DM mass is in the sub-GeV range, the $Z^{'}$ mediated annihilation will be dominant similar to the previous case. As expected,

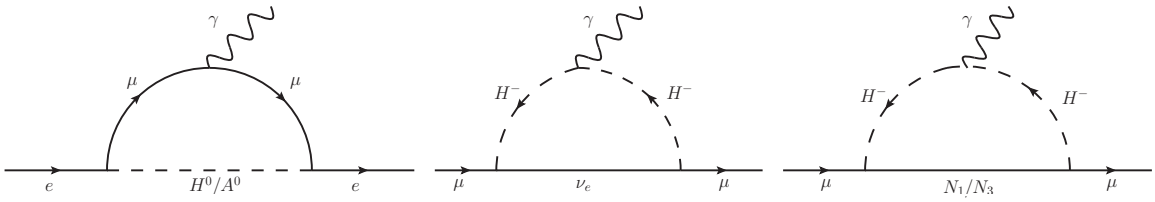

Figure 4.19: The diagrams which will contribute to muon and electron magnetic moments.

the current bound on relic density will be satisfied at the DM masses close to the value $M_{Z'}/2$, and at a value $M_{DM} < M_{s_2}/2$. There are different peaks for $M_{DM} > M_{s_2}/2$ which correspond to the different resonance annihilation of the DM through the Higgs portal. In all the resonances for $M_{DM} > M_{s_2}/2$, the relic is much below the present observed abundance. The allowed values of DM mass are mostly limited in the sub-GeV to less than 50 GeV mass. Note that the relic is almost insensitive to the value of $\tan\beta$. Also, as shown in Fig. 4.17b the sine of mixing angle α_3 does not have an impact on the allowed regions of M_{DM}. Although, we have chosen very small values of s_{α_3}, the situation will not change even for larger values of s_{α_3}.

In Fig. 4.18a, we have shown the regions of M_{DM} allowed by relic density bound and the current experimental limit on the DM direct detection cross section σ^{SI} from XENON 1T. To generate this plot we consider $\tan\beta = 2$, and the values of the other relevant parameters are the following: $0 < s_{\alpha_3} < 0.01$, and $10 \leq M_{s_2} \leq 100$ GeV. All the other relatively less relevant parameters are fixed at the values as mentioned above. The maximum value of M_{DM} allowed by the data on the relic and σ^{SI} is ~ 40 GeV. Note from Fig. 4.18b that the current limit on σ^{SI} put stringent bound on s_{α_3}. For example, for $M_{DM} \approx 30$ GeV the allowed value of s_{α_3} can not be larger than 0.01. Here, we have shown the plot for $\tan\beta = 2$; however, as shown above, the results will be similar for other allowed values of $\tan\beta$. Like in the case of toy model-I, the contributions to spin-dependent direct detection cross sections are negligibly small in this model as well.

Electron Anomalous Magnetic Moment and LFV

Magnetic Moments :- In this model, apart from the contribution from a $U(1)_X$ gauge particle as has been discussed in sub-section 4.3.2, the contributions to the muon and electron magnetic moment will come from the respective diagrams shown in Fig. 4.19. The contributions from these diagrams from left to the right, respectively, are summarised in the following equations:

$$\Delta a_e^{(H)} = \frac{m_e^2}{8\pi^2 M_H^2}\frac{|Y_{12}^\ell|^2}{12}, \quad \text{with } H \equiv (H^0, A^0), \tag{4.72}$$

$$\Delta a_\mu^{\nu} = -\frac{m_\mu^2}{8\pi^2 M_{H^\pm}^2}\frac{|Y_{32}^\ell|^2}{12}, \tag{4.73}$$

$$\Delta a_\mu^{N} = -\frac{m_\mu^2 |R_2|^2}{8\pi^2 M_{H^\pm}^2}\int_0^1 dx \frac{x^2(1-x)}{x + (1-x)\frac{M_N^2}{M_{H^\pm}^2}}. \tag{4.74}$$

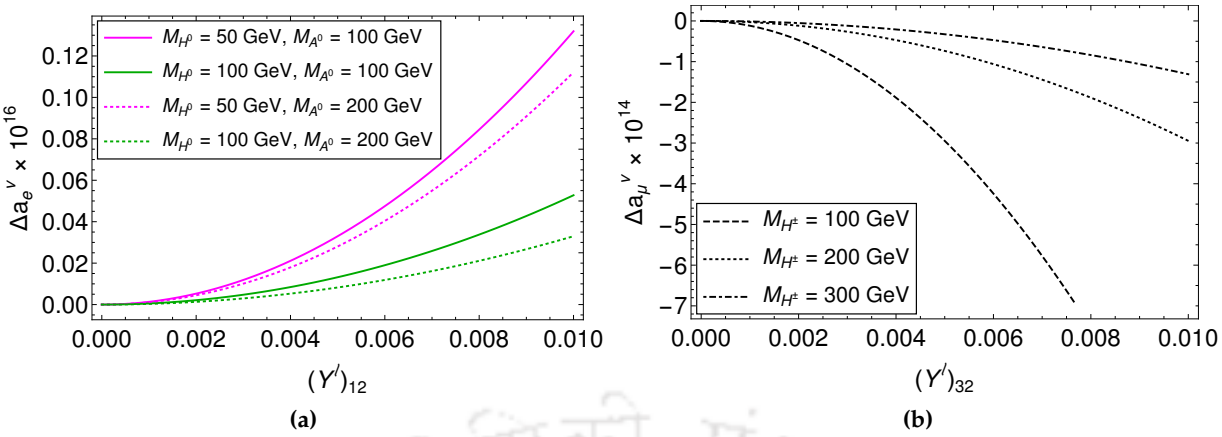

Figure 4.20: (a) Variation of Δa_e^{ν} with the relevant Yukawa coupling Y_{12}^{ℓ} for different values of M_{H^0} and M_{A^0}. (b) Dependencies of Δa_μ^{ν} with Y_{32}^{ℓ}.

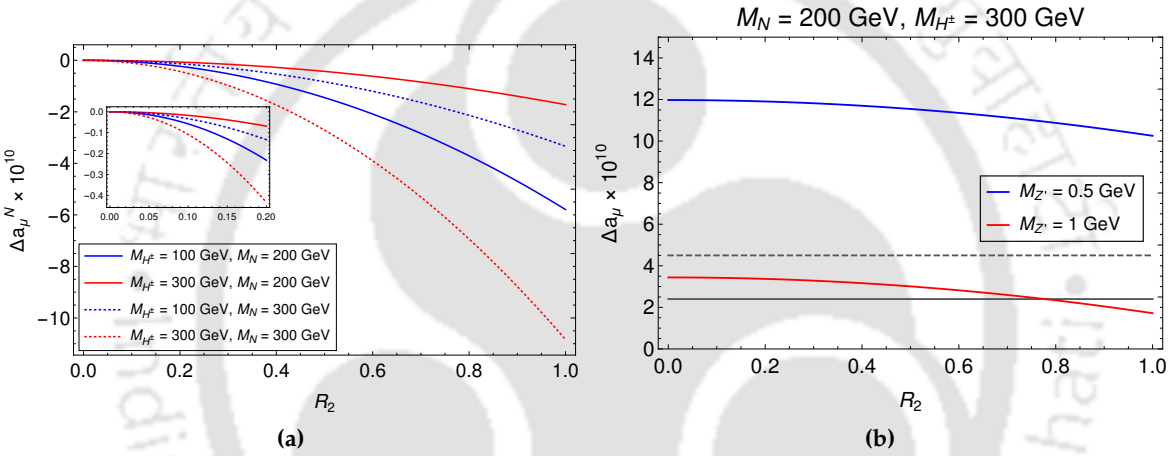

Figure 4.21: (a) The variation of Δa_μ with $R_2 \equiv \sqrt{\left(Y_{21}^{\nu\,2} + Y_{23}^{\nu\,2}\right)}$ for different values of $M_{N_1} = M_{N_3} = M_N$ and M_{H^+}. (b) The total contributions in Δa_μ from the diagrams in Fig. 4.19 and 4.3. The grey horizontal line is the allowed 3-σ lower limit [12], while the dashed grey line represents the 3-σ lower limit of a very recent estimate [14].

Here, we have defined $|R_2|^2 \equiv \left((Y_{21}^{\nu})^2 + (Y_{23}^{\nu})^2\right)$ in the same way as we defined R_1, R_3 in the previous toy model. To do so, we have assumed the same masses for N_1 and N_3. Note that the contributions in $\Delta a_e^{(H)}$ is sensitive to the Yukawa coupling $|Y_{12}^{\ell}|$, and the contributions in Δa_μ are coming from the diagrams with ν_τ and N_1/N_3 in the loop, respectively.

The variations of Δa_e with $|Y_{12}^{\ell}|$ for different values of M_{H^0} and M_{A^0} are shown in Fig. 4.20a. Note that the contribution to Δa_e is highly suppressed and the values like $Y_{12}^{\ell} \gtrsim 0.01$ are allowed. As can be seen from Fig. 4.20b, the contribution to Δa_μ from the diagram with ν_τ in the loop is highly suppressed. In Fig. 4.21, we have shown the variation of Δa^μ with $|R_2|$ for different values of M_{H^0} and M_N. Note that the contributions in Δa_μ from the diagram with right-handed neutrinos are significant and have negative values. We have already shown earlier that the contribution from the diagram with X with a mass $M_X \approx 0.5$ GeV can accommodate the current discrepancy in Δa_μ. The large negative contribution from diagrams with N_1 or N_3 (in the loop) will reduce the value of Δa_μ obtained from a diagram with X. However, note that, for lower values of R_2 i.e. $R_2 \lesssim 0.5$,

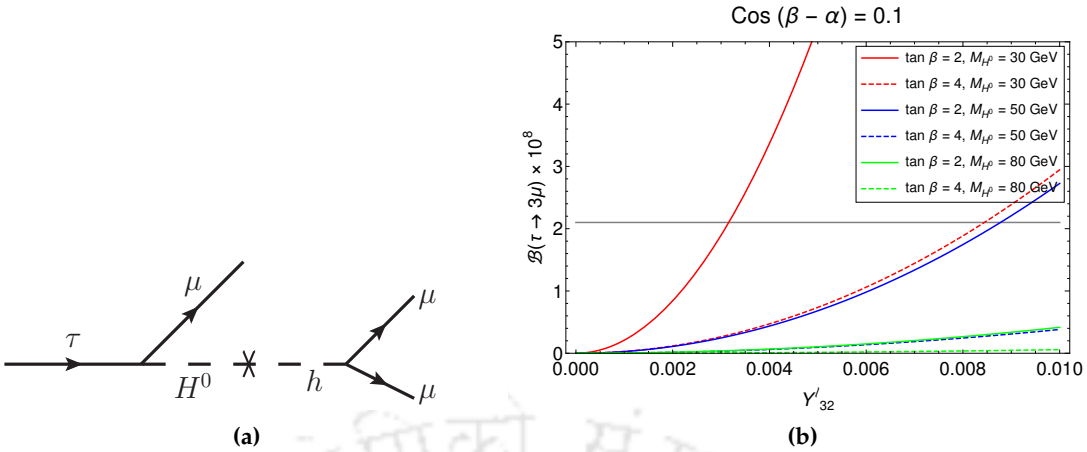

Figure 4.22: (a) Higgs mediated diagram contributing to $\tau \to 3\mu$ process. (b) Variation of $\mathcal{B}_\tau$ with the coupling Y^ℓ_{32} for different values of tanβ and M_{H^0}. The constraint $\cos(\beta - \alpha) = 0.1$ has been used while calculating the branching fraction. The gray line denotes the experimental upper bound on the branching fraction.

the effects are not that significant. Therefore, to explain Δa_μ we can restrict R_2 to a low value. In Fig. 4.21b, we have shown the variation of the total contribution to Δa_μ with R_2 for the ultimate choices of the other relevant parameters.

Lepton Flavour Violation :- In our second model, there won't be any contribution to the processes like $\tau \to \mu\gamma$, $\mu \to e\gamma$ or $\tau \to e\gamma$. However, from Eqn. (4.57), one can see that the charge lepton mass matrix is not diagonal and is given by

$$M_\ell = \begin{pmatrix} \frac{v}{\sqrt{2}}Y^\ell_{11} & \frac{u}{\sqrt{2}}Y^\ell_{12} & \frac{v}{\sqrt{2}}Y^\ell_{13} \\ 0 & \frac{v}{\sqrt{2}}Y^\ell_{22} & 0 \\ \frac{v}{\sqrt{2}}Y^\ell_{31} & \frac{u}{\sqrt{2}}Y^\ell_{32} & \frac{v}{\sqrt{2}}Y^\ell_{33} \end{pmatrix}. \tag{4.75}$$

Due to the presence of off-diagonal terms in the charged lepton mass matrix, we have a contribution to the lepton flavour violating decay $\tau \to 3\mu$ as shown in Fig. 4.22a. Although the contribution is mixing suppressed, the stringent limit on the branching fraction will put a direct constraint on the Yukawa coupling Y^ℓ_{32} since the process occurs at tree level. The upper bound on the branching fraction from the Belle Collaboration [274] is

$$\mathcal{B}_\tau < 2.1 \times 10^{-8} \tag{4.76}$$

at 90% CL. The amplitude for the process can be written in the form

$$\mathcal{M}_\tau = g^s_{LL}(\bar{\mu}_L \mu_R)(\bar{\mu}_R \tau_L) \tag{4.77}$$

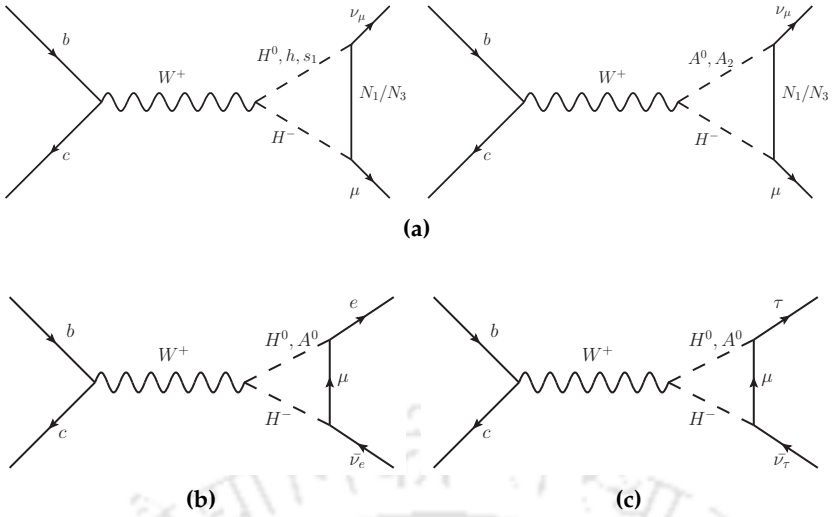

Figure 4.23: Diagrams contributing to $b \to c\ell\bar{\nu}_\ell$ decays ($\ell = e, \mu, \tau$).

where

$$g^s_{LL} = \left(\frac{Y^{\ell\,*}_{32} m_\mu s_\alpha}{v M^2_{H^0}}\right) \tag{4.78}$$

and the branching fraction is given by[275]

$$\mathcal{B}_\tau = \left(\frac{T_\tau m^5_\tau |g^s_{LL}|^2}{128 \times 48\pi^3}\right) \int_0^1 dx \int_0^1 d(\cos\theta) \left[3x^2 - 2x^3 + x^2\cos\theta - 2x^3\cos\theta\right] \tag{4.79}$$

where T_τ is the lifetime of the τ lepton, $x = 2E_{\bar{\mu}}/m_\tau$ is the reduced energy of the antimuon, and θ is angle between the polarization of the τ and the momentum of the antimuon.

In Fig. 4.22b, we show the variation of the branching fraction of $\tau \to 3\mu$ with Y^ℓ_{32} for three different values of M_{H^0}, and in each of these cases, we have chosen two different values of $\tan\beta$. It is evident from the plot that experimental upper limit on $\mathcal{B}(\tau \to 3\mu)$ restricts the allowed regions of Y^ℓ_{32} and M_{H^0}, and the preferable choice is $Y^\ell_{32} \lesssim 0.005$ for $M_{H^0} \gtrsim 50$ GeV. The decay width is also sensitive to the value of $\tan\beta$. Therefore, for all practical purposes it is convenient to set Y^ℓ_{32} to a very small value, say 0.001, in order to evade this strong bound.

Additional contribution to $b \to c\ell\bar{\nu}_\ell$

In this case, the diagrams that will contribute to $b \to c\ell\bar{\nu}_\ell$ (with $\ell = e, \mu$ and τ) decays are given in Figs. 4.23. The diagrams in Fig. 4.23a will contribute to $b \to c\mu\bar{\nu}_\mu$ decays, whereas those in Figs. 4.23b and 4.23c will contribute to $b \to ce\bar{\nu}_e$ and $b \to c\tau\bar{\nu}_\tau$ decays respectively. The resulting Wilson coefficient contributing to $b \to c\mu\bar{\nu}_\mu$ can be written as:

$$\mathcal{C}^{(H)}_{V_1} = \frac{Y^{\nu\,2}_{2j}}{32\pi^2} g_{HH^-W^+} \int_0^1 dx \int_0^{1-x} \ln \Delta^j_{WHH}, \quad \text{with } H \equiv (H^0, h, s_1, A^0, A_2), \tag{4.80}$$

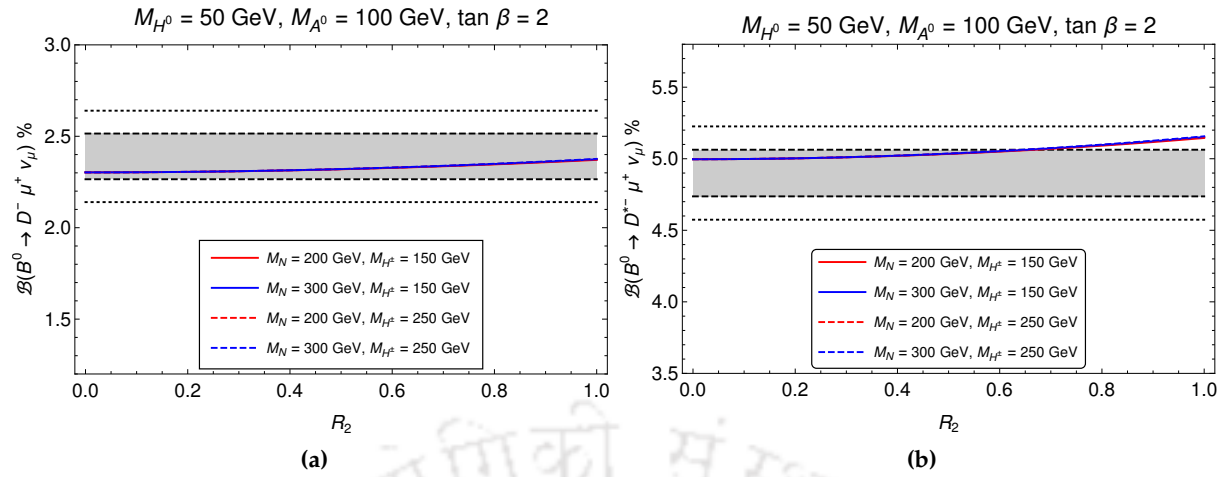

Figure 4.24: Variation of the branching fraction of $\bar{B} \to D\mu\bar{\nu}_\mu$ (Fig. 4.24a) and $\bar{B} \to D^*\mu\bar{\nu}_\mu$ (Fig. 4.24b) with R_2 for two different values of M_N and $M_{H^\pm}$ each. The other relevant parameters are kept fixed as shown in the plot labels. In both the plots, the gray shaded band is the measured branching fraction of the B-decays in their 1σ CL respectively while the dotted lines denote the 2σ allowed band.

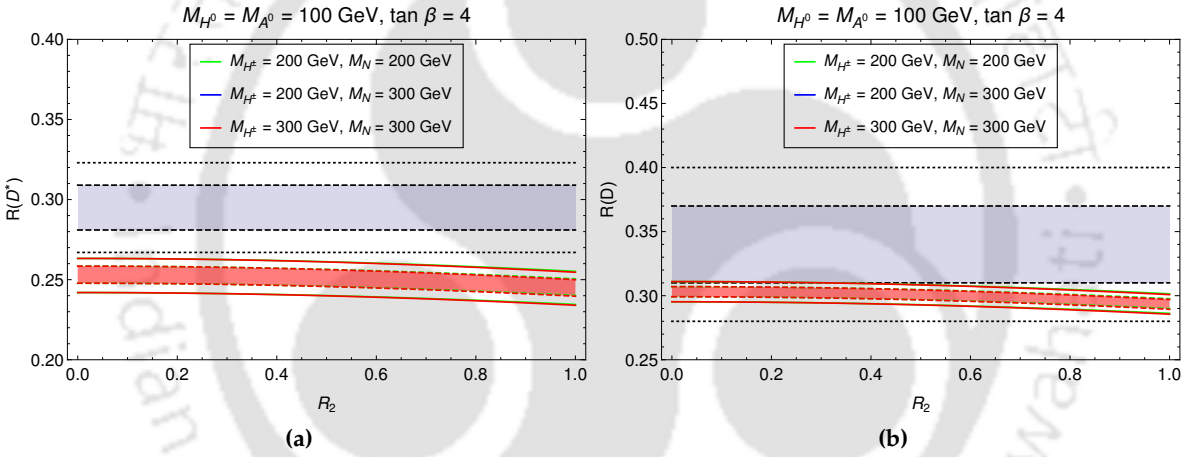

Figure 4.25: Variation of R_{D^*} (left) and R_D (right) with R_2 for different values of M_N and $M_{H^\pm}$. The shaded gray region is the experimental 1σ allowed region while the dotted lines denote the same in the 2σ CI. The shaded and unshaded colored bands (red,blue,green) signify the theoretical uncertainty in the 1σ and 2σ CI respectively.

where the coupling $g_{HH^-W^+}$ between the charged Higgs, W-boson and the different neutral scalars are given by :

$$
\begin{aligned}
g_{H^0H^-W^+} &= \frac{g}{2}(c_\gamma \mathcal{R}_{\alpha_{44}} + s_\gamma \mathcal{R}_{\alpha_{14}}), \qquad & g_{hH^-W^+} &= \frac{g}{2}(c_\gamma \mathcal{R}_{\alpha_{41}} + s_\gamma \mathcal{R}_{\alpha_{11}}), \\
g_{s_1H^-W^+} &= \frac{g}{2}(c_\gamma \mathcal{R}_{\alpha_{42}} + s_\gamma \mathcal{R}_{\alpha_{12}}), \qquad & g_{A^0H^-W^+} &= \frac{g}{2}(c_\gamma \mathcal{R}_{\theta_{44}} + s_\gamma \mathcal{R}_{\theta_{14}}), \\
g_{A_2H^-W^+} &= \frac{g}{2}(c_\gamma \mathcal{R}_{\theta_{43}} + s_\gamma \mathcal{R}_{\theta_{13}}),
\end{aligned}
\tag{4.81}
$$

where, $\mathcal{R}_{\alpha_{ij}}$ is the (ij) element of the rotation matrix given that diagonalises the CP even mass matrix given in Appendix B.2, and similarly for $\mathcal{R}_{\theta_{ij}}$. The factor Δ^j_{WHH} is given in Eqn. (4.36). However, it is evident from the Lagrangian that the dominant contributions would come from the diagrams containing H^0 and A^0 in the loop since their coupling with the neutrinos are not mixing

suppressed unlike the other Higgses.

The contributions to $b \to ce\bar{\nu}_e$ and $b \to c\tau\bar{\nu}_\tau$ from the diagrams as mentioned above are negligibly small. The contributions come from the second term of the Yukawa Lagrangian in Eqn. (4.57). The Wilson coefficients in these cases are sensitive to the off-diagonal Yukawas of the charged lepton mass mixing matrix. Also, we have already obtained a direct bound on the coupling Y^{ℓ}_{32} from the branching fraction of $\tau \to 3\mu$ in the previous section and fixed it to 0.001. For such a small Yukawa, the resulting WC will have a value of order $\mathcal{O}(10^{-9})$ which is negligibly small and hence it can safely be neglected. Note that even if we choose $Y^{\ell}_{32} \approx 0.01$, the contributions to the WC will be of order $\mathcal{O}(10^{-7})$. Similar conclusion holds for the electron final state. Therefore, we will only focus on the contribution to the muon channel.

If we assume, for simplicity, the masses of N_1 and N_3 are equal, then the Wilson coefficient will be proportional to the parameter R_2 which we have already defined in the previous subsection. We can then constrain the parameter space of R_2 and $M_N \equiv M_{N_1} = M_{N_3}$ from the data on R_D, R_{D^*} and $\bar{B} \to D^{(*)}\mu\bar{\nu}_\mu$. In Fig. 4.24, we show the variation of the branching fractions of $\bar{B} \to D^{(*)}\mu\bar{\nu}_\mu$ with R_2 for two different values of M_N and $M_{H^\pm}$ each, keeping the masses of the neutral scalars H^0, A^0 fixed. Also we keep $\tan\beta$ fixed at 2 and choose α such that $\cos(\beta-\alpha) = 0.1$. We see that even for a large ($\sim \mathcal{O}(1)$) R_2, the branching fraction of $\bar{B} \to D^{(*)}\mu\bar{\nu}_\mu$ remains within the 2σ experimental range. Also, we have noted that the change in the branching fraction with the mass of the charged scalar or the heavy neutrino is insignificant (the legends overlap in the figure). We have also studied the impact on R_{D^*} and R_D, and the results are shown in Figs. 4.25a and 4.25b, respectively. Note that it is hard to explain R_{D^*} even if we take both the theory and the measured errors within their 2σ confidence interval (CI)[6]. However, we can conveniently explain the observation in R_D even if we consider the data and theory at their 1σ CI. Also, even though large values of R_2 is allowed by the branching fractions to the muon mode, the data on $R_{D^{(*)}}$ restricts the value of R_2 to $\lesssim 0.5$ for the entire range of RHN or charged scalar mass.

Neutrino Mass Generation

In this case the minimal seesaw mechanism will help us give rise to the neutrino mass. From the Yukawa interactions in Eqn. (4.57), one can obtain the Dirac neutrino mass matrix M_D and the Majorana mass matrix M_R to be :

$$M_D = \begin{pmatrix} \frac{v}{\sqrt{2}}Y^{\nu}_{11} & 0 & \frac{v}{\sqrt{2}}Y^{\nu}_{13} \\ \frac{u}{\sqrt{2}}Y^{\nu}_{21} & 0 & \frac{u}{\sqrt{2}}Y^{\nu}_{23} \\ \frac{v}{\sqrt{2}}Y^{\nu}_{31} & 0 & \frac{v}{\sqrt{2}}Y^{\nu}_{33} \end{pmatrix}, \quad M_R = \begin{pmatrix} \frac{v_1}{\sqrt{2}}Y^{\varphi}_{11} & 0 & \frac{v_1}{\sqrt{2}}Y^{\varphi}_{13} \\ 0 & \frac{v_2}{\sqrt{2}}Y^{\varphi}_{22} & 0 \\ \frac{v_1}{\sqrt{2}}Y^{\varphi}_{31} & 0 & \frac{v_1}{\sqrt{2}}Y^{\varphi}_{33} \end{pmatrix}. \tag{4.82}$$

[6]It was discussed in refs. [96, 276] that at the moment, the predictions of R_{D^*} depend too much on the experimental results on $B \to D^*\mu\nu_\mu$ and $B \to D^*e\nu_e$ decay, and with the changes in the data the predictions are changing. For a prediction independent of any experimental inputs, we have to wait till the inputs from the lattice at non-zero recoil angle of the outgoing meson are available.

Thus the light active neutrino masses can be obtained from the seesaw formula given by:

$$m_\nu = -\left(M_D^T M_R^{-1} M_D\right). \tag{4.83}$$

By using the structure of M_D, M_R in the type I seesaw [46, 48, 50, 277] formula for light neutrino masses mentioned above, we find a general structure of light neutrino mass matrix without any textures unlike that found in toy model I. However, the light neutrino mass matrix has rank 2 predicting the lightest neutrino mass to be vanishing. While neutrino oscillation experiments can not constrain such a scenario, other experiments like neutrinoless double beta decay which is sensitive to absolute neutrino mass scale can shed more light on such scenario in future.

4.6 Possible Collider Signatures

4.6.1 Higgs Invisible decays

In any NP model it is quite an exciting prospect to look into the non-standard or undetected decays of the SM Higgs as a complementary search for BSM particles. The toy models that we discussed above constitute of a dark matter particle that couple to the SM Higgs boson through its mixing with singlet scalars. Also, there is a viable parameter space in both the models where the dark matter mass is lighter than the Higgs. Under such a scenario, it would be a useful exercise to study the model contribution to Higgs invisible decay and use the available data on it to further constrain the model parameters. All the relevant diagrams contributing to the Higgs invisible decay are shown in Fig. 4.26. From the figure it is almost clear that the dominating invisible decay of Higgs would be to the DM N_2 for $M_{N_2} < M_h/2$ and the decay to 4ν via gauge bosons would in general be suppressed compared to this tree level decay. However, since the new gauge boson in our model, Z', is light (sub-GeV), the contribution mediated by Z' could also be quite significant. The third decay, involving one heavy boson Z and a light Z', is in general suppressed by the very small value of the gauge mixing parameter ϵ ($\sim 10^{-4}$) that we considered. Hence, one can safely neglect the contribution from this decay mode. Therefore we will only consider the first two decay modes in our calculation.

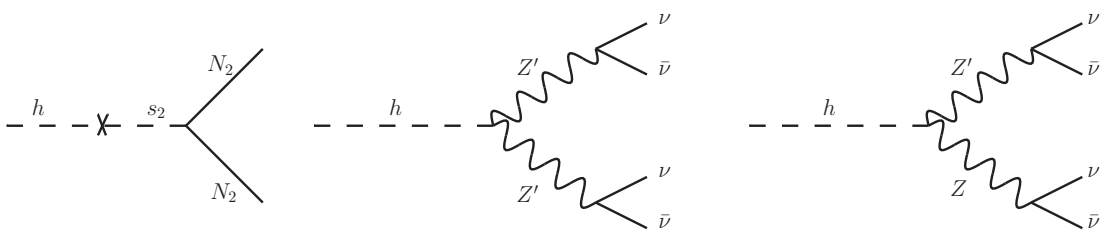

Figure 4.26: Invisible Higgs decay channels.

Both ATLAS and CMS have looked into such invisibly decaying Higgs mainly through its inclusive production in the vector boson fusion mode, as well as in the associated production of a

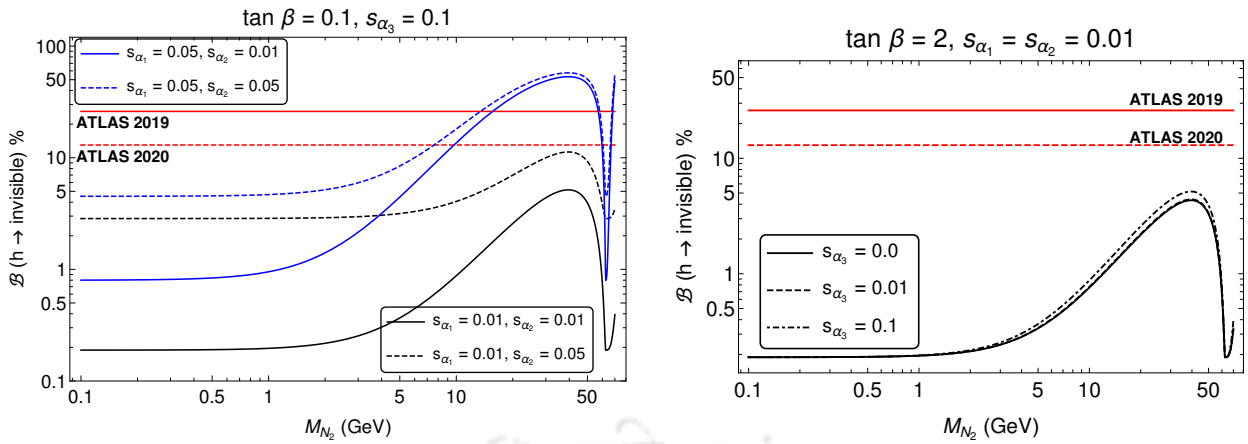

Figure 4.27: Higgs invisible branching fraction as a function of M_{N_2} for two different values of s_{α_1} and s_{α_2} each is shown. The red solid line is the upper bound from ATLAS 2019 [15] while the red dashed line is the upper bound from their recent announcement in April 2020[16].

Higgs with a Z boson. The constraint on the Higgs invisible decay branching fraction from the ATLAS experiment at LHC is [15]

$$\mathcal{B}(h \to \text{Invisible}) = \frac{\Gamma(h \to \text{Invisible})}{\Gamma(h \to SM) + \Gamma(h \to \text{Invisible})} \leq 26\% \tag{4.84}$$

while the recent ATLAS announcement [16] puts a more stringent constraint at 13%. The Higgs decay to SM particles is known to be around 4 MeV. In the following two subsections, we will discuss the impact of this upper limit on the model parameters, in particular the mixing angles.

Toy Model 1

The invisible decay width of Higgs to dark matter is given by :

$$\Gamma(h \to N_2 N_2) = \frac{1}{8\pi}\frac{M_{N_2}^2}{v_2^2} M_h \left(1 - \frac{4M_{N_2}^2}{M_h^2}\right)^{3/2} (s_{\alpha_2} + c_{\alpha_2}^2 s_{\alpha_1} s_{\alpha_3})^2. \tag{4.85}$$

On the other hand, the decay of Higgs to SM neutrinos via XX, or equivalently via $Z'Z'$ is given by :

$$\Gamma(h \to Z'Z' \to 4\nu_\ell) = \frac{1}{8\pi}\frac{g_{hZ'Z'}^2}{M_h}\left(1 - \frac{4M_{Z'}^2}{M_h^2}\right)^{1/2}\left(3 + \frac{M_h^4}{4M_{Z'}^4} - \frac{M_h^2}{M_{Z'}^2}\right) \times \sum_\ell [\mathcal{B}(Z' \to 2\nu_\ell)]^2 \tag{4.86}$$

where $g_{hZ'Z'} = 8g_X^2(c_{\alpha_2}s_{\alpha_1}v_1 + 4s_{\alpha_2}v_2)$ is the effective coupling of SM Higgs with Z' via mixing with the singlet scalars. For our model, $\sum_\ell [\mathcal{B}(Z' \to 2\nu_\ell)]^2 \approx 0.14$ for $M_{Z'} = 1$ GeV and $g_{Z'} = 10^{-3}$. Therefore, the total invisible decay width of Higgs is given by the sum of the decay widths as mentioned above. In Fig. 4.27, we have shown the variation of the Higgs invisible decay with the mass of dark matter for different values of the mixing angles. Note that only small mixing like $s_{\alpha_2} = 0.01$, $s_{\alpha_1} = 0.01$ are allowed by the current limit for the entire mass range of N_2. However, s_{α_3} could be as large as 0.1.

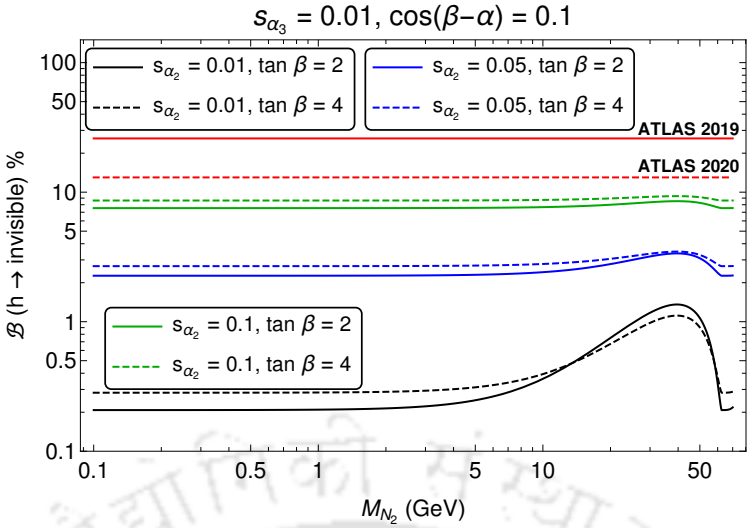

Figure 4.28: The variation of Higgs invisible branching fraction with the DM mass for different values of the other relevant parameters in toy model 2. The red solid and dashed lines have a similar description as given in Fig. 4.27.

Toy Model 2

In our second model, the contribution to the Higgs invisible decay width is given by

$$\Gamma(h \to N_2 N_2) = \frac{1}{8\pi}\frac{M_{N_2}^2}{v_2^2} M_h \left(1 - \frac{4M_{N_2}^2}{M_h^2}\right)^{3/2} \mathcal{R}_{31}^2. \tag{4.87}$$

Also, the decay of Higgs to SM neutrinos via $Z'Z'$ is given by :

$$\Gamma(h \to Z'Z' \to 4\nu_\ell) = \frac{1}{8\pi}\frac{g_{hZ'Z'}^2}{M_h}\left(1 - \frac{4M_{Z'}^2}{M_h^2}\right)^{1/2}\left(3 + \frac{M_h^4}{4M_{Z'}^4} - \frac{M_h^2}{M_{Z'}^2}\right) \times \sum_\ell [\mathcal{B}(Z' \to 2\nu_\ell)]^2 \tag{4.88}$$

where $g_{hZ'Z'} = 8g_X^2(\mathcal{R}_{12}v_1 + 4\mathcal{R}_{13}v_2)$ is the effective coupling of SM Higgs with Z' via mixing with the singlet scalars. Again, the sum of squares of branching fraction, $\sum_\ell [\mathcal{B}(Z' \to 2\nu_\ell)]^2 \approx 0.14$ for $M_{Z'} = 1$ GeV as mentioned before. In Fig. 4.28, we have shown the dependencies of the $\mathcal{B}(h \to$ invisible$)$ with the DM mass and other relevant parameters in toy model 2, like sine of the mixing angles and $\tan\beta$. Note that our chosen benchmark values like $s_{\alpha_2} = 0.01$, $s_{\alpha_3} = 0.01$ and $\tan\beta = 2$ or 4 are allowed by the current bound on $\mathcal{B}(h \to$ invisible$)$.

4.6.2 LFV decays of Higgs

It is evident from the Yukawa interactions in eqs. (4.15) and (4.57) that there exists lepton flavour violating decays of the Higgs (h) for both the Toy models. However, there are notable differences between the allowed LFV channels in the two models. The $U(1)_X$ charge assignments of the charged leptons are such that in both the models we will get the $h \to \tau e$ decay, for example, see Fig. 4.29a. However, only Toy Model II contributes to LFV $h \to \mu\tau$ and $h \to \mu e$ decays via the mixing of the h with the H^0 as shown in the Fig. 4.29b.

So far no excess have been observed in these channels at the LHC searches and the most recent

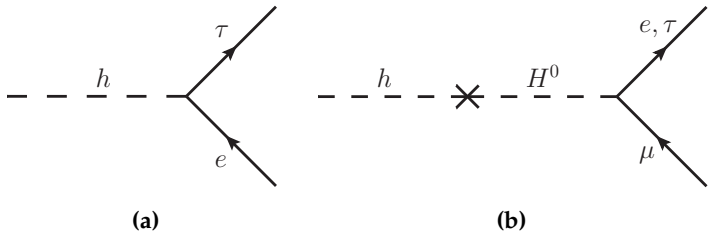

Figure 4.29: Lepton Flavour Violating decays of Higgs boson.

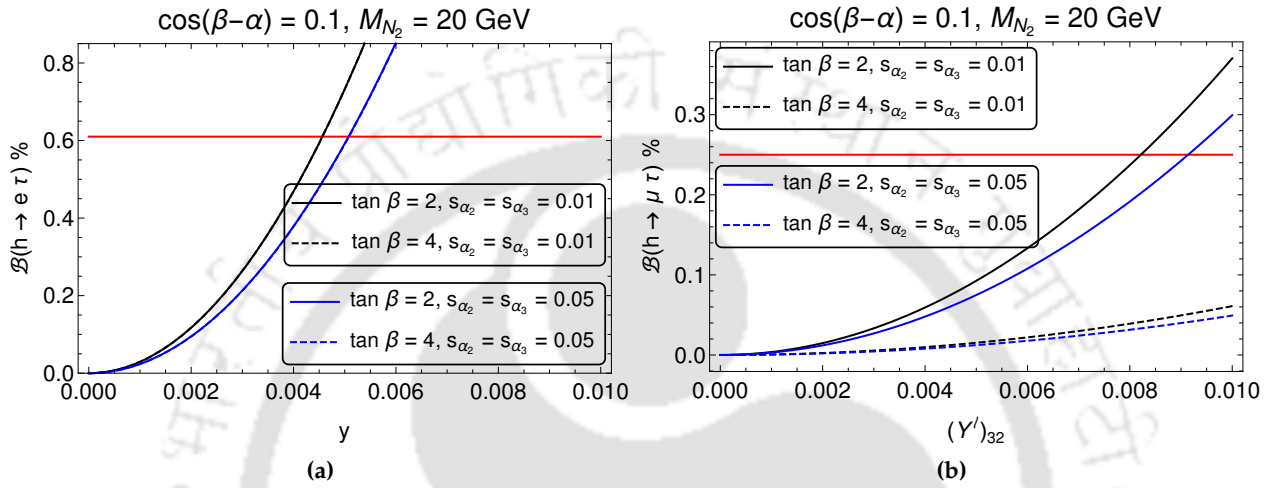

Figure 4.30: (a)Variation of $\mathcal{B}(h \to e\tau)$ with off-diagonal Yukawa coupling y for two different values of tan β and other mixing angles. The red line denotes the upper limit on the branching ratio. (b) Similar variation for $\mathcal{B}(h \to \mu\tau)$ is shown.

upper limits on the lepton flavour violating branching fractions of the Higgs boson by CMS [278] reads

$$\begin{aligned} \mathcal{B}(h \to e\tau) &< 0.61\%, \\ \mathcal{B}(h \to \mu\tau) &< 0.25\%. \end{aligned} \tag{4.89}$$

These limits will be helpful to constrain the lepton flavour violating Higgs couplings Y^{ℓ}_{ij} where $(i, j = 1, 3)$ & $i \neq j$. The general expression for the branching fraction for the LFV Higgs decay is given by

$$\begin{aligned} \mathcal{B}(h \to \ell_i \ell_j) &= \left(\frac{|y|^2}{16\pi M_h \Gamma_h^{\text{tot}}}\right)\left[\left(1-\left(\frac{m_{\ell_i}+m_{\ell_j}}{M_h}\right)^2\right)\left(1-\left(\frac{m_{\ell_i}-m_{\ell_j}}{M_h}\right)^2\right)\right]^{1/2}(M_h^2 - m_{\ell_i}^2 - m_{\ell_j}^2) \\ &\approx \left(\frac{|y|^2 M_h}{16\pi\Gamma_h^{\text{tot}}}\right), \quad \text{for} \quad m_{\ell_i}, m_{\ell_j} << M_h. \end{aligned} \tag{4.90}$$

Here, $\Gamma_h^{\text{tot}} = \Gamma(h \to SM) + \Gamma(h \to \text{Invisible})$ and y denotes the effective LFV coupling. In most of the allowed parameter spaces, we can expect $\Gamma(h \to \text{Invisible}) << \Gamma(h \to SM)$; however, there are regions where it might be relevant to consider. In both the models, for $h \to \tau e$ decays the effective LFV coupling is given by $y \equiv \sqrt{{Y^{\ell}_{13}}^2 + {Y^{\ell}_{31}}^2}$. As mentioned earlier, there won't be any contribution to $h \to \mu\tau$ or $h \to \mu e$ decays in Toy Model I. In Toy Model II, the expression for the

braching fraction for $h \to \mu\tau$ decay is given by

$$\mathcal{B}(h \to \mu\tau) = \left(\frac{s_\alpha^2 |Y_{32}^\ell|^2}{2}\right)\left(\frac{M_h}{16\pi\Gamma_h^{\rm tot}}\right), \tag{4.91}$$

which in the limit $\alpha \to 0$, gives us the corresponding expression for $h \to e\tau$ decay. We will obtain the expression for $\mathcal{B}(h \to \mu e)$ after replacing Y_{32}^ℓ by Y_{12}^ℓ in Eqn. (4.91).

In Fig. 4.30a we have shown the variation of $\mathcal{B}(h \to e\tau)$ with the effective coupling y. Since the contribution will be similar for both the models, we have not shown it separately for the two. It can be clearly understood from the plot that the coupling cannot be larger than ~ 0.005 irrespective of the value of $\tan\beta$ or other angles. There is very little dependence on s_{α_2} or s_{α_3} which is coming from the contributions in $\Gamma(h \to \text{Invisible})$ (see Eqn. (4.85)) in the denominator. For illustrative purpose, we have shown the variation for $M_{N_2} = 20$ GeV; however, we have checked that the variation does not change significantly on changing the DM mass.

In Fig. 4.30b we show a similar variation of the branching ratio to the $\mu\tau$ mode with Y_{32}^ℓ for two different values of tan β and other mixing angles. As mentioned earlier, this decay mode is specific for Toy Model II only. Since this process is mixing induced, both $\tan\beta$ and Y_{32}^ℓ are tightly constrained from the data. As expected, the branching fraction is sensitive to both the mixing parameters β and α. Note that for $\tan\beta = 2$, the allowed values of Y_{32}^ℓ is $Y_{32}^\ell < 0.01$. However, for $\tan\beta > 2$, more higher values of the Yukawa coupling are allowed. In general, higher values of the $\tan\beta$ prefers higher values of the Yukawa coupling. This is expected since the constraint $|\cos(\beta - \alpha)| = 0.1$ implies smaller sin α for large tan β. Once again the conclusions are not affected significantly by the DM mass. Also, we have noted that for values like $\tan\beta = 2$ and $s_{\alpha_2} = s_{\alpha_3} = 0.01$, the branching fraction $\mathcal{B}(h \to \mu e) \leq 0.4\%$ for $Y_{12}^\ell \leq 0.01$.

$\ell^+\ell^- + \not{E}_T$	4ℓ
$pp \to Z \to Z\ s_2 \to \ell^+\ell^-\not{E}_T$ (Toy Model-I and II)	$pp \to \ell^+\ell^-\gamma \to 4\ell$
$pp \to Z \to Z'\ s_2 \to \ell^+\ell^-\not{E}_T$ (Toy Model-I and II)	$pp \to \ell^+\ell^- Z' \to 4\ell$
$pp \to h \to h\ s_2 \to \ell^+\ell^-\not{E}_T$ (Toy Model-I and II)	$pp \to Z'Z' \to 4\ell$
$pp \to H^+H^- \to \mu^+\mu^-\not{E}_T$ (Only in Toy Model-I)	

Table 4.5: Collider signatures resulting in dilepton and 4-lepton final states for both Toy Models.

Sl.No.	Benchmark point (BP)	$\sigma(pp \to H^+H^- \to \mu^+\mu^-\not{E}_T)$ (fb)
(A)	$M_{H^\pm} = 500$ GeV, $M_{N_2} = 20$ GeV, $Y_{22} = 0.1$	2.45
(B)	$M_{H^\pm} = 500$ GeV, $M_{N_2} = 40$ GeV, $Y_{22} = 0.1$	2.39
(C)	$M_{H^\pm} = 500$ GeV, $M_{N_2} = 20$ GeV, $Y_{22} = 0.2$	39.2
(D)	$M_{H^\pm} = 800$ GeV, $M_{N_2} = 20$ GeV, $Y_{22} = 0.1$	0.58

Table 4.6: Production cross-section of the dimuon $+\not{E}_T$ final state generated from intermediate inert charged Higgses. This production is exclusively for Toy model I.

Sl.No.	Benchmark point (BP)	$\sigma^{2\ell+\not{E}_T}$ (fb)		$\sigma^{4\ell}$ (fb)	
		Toy I	Toy II	Toy I	Toy II
1.	$M_{N_2} = 20$ GeV, $M_{Z'} = 1$ GeV	0.10	0.074	25.54	25.54
2.	$M_{N_2} = 40$ GeV, $M_{Z'} = 1$ GeV	0.07	0.066		
3.	$M_{N_2} = 20$ GeV, $M_{Z'} = 0.5$ GeV	0.10	0.074	25.57	25.57
4.	$M_{N_2} = 40$ GeV, $M_{Z'} = 0.5$ GeV	0.07	0.065		

Table 4.7: Production cross-section of the dilepton $+\not{E}_T$ ($\sigma^{2\ell+\not{E}_T}$) and 4ℓ ($\sigma^{4\ell}$) final states for some specific benchmark points of the two toy models. The intermediate channels that lead to such final states are listed in Table. 4.5. Please note that the cross-section for the dilepton $+\not{E}_T$ channel for Toy model I quoted here excludes the contribution from the charged Higgs mediated diagram (which we have separately shown in Table. 4.6).

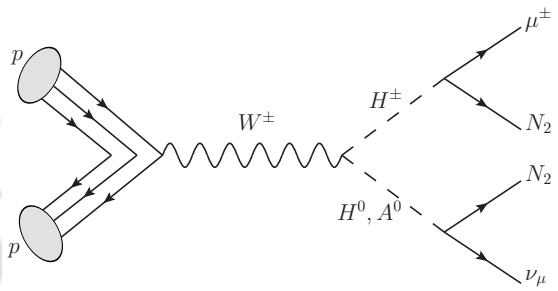

Figure 4.31: Feynman diagram for the production of $\mu^{\pm} + \not{E}_T$ final state at LHC (Toy Model I).

4.6.3 Other Possible Signatures

In this subsection, we would like to briefly discuss some other possible collider signatures of our Toy models at the LHC, in addition to the specific ones mentioned above. Here, we will only mention a few exciting channels for the search at the LHC; a detailed analysis is beyond the scope of this study. It is quite evident that the most notable collider signals would be the multi-lepton final states with or without an associated missing energy ($\not{E}_T$). More importantly, the dilepton (2ℓ) + $\not{E}_T$ channel which can be probed with excellent precision in the high luminosity colliders in the near future, has the potential to discriminate the two Toy models. A few of the dominating production channels are mentioned in Table 4.5. Note that the search for 4ℓ final states will not be a unique test of our toy models. This is because, in all the cases, the primary decay channels are via the production of Z' which is very common in NP models with an additional $U(1)_X$ gauge bosons. The details of the collider searches for such an extension with a sub-GeV $M_{Z'}$ can be seen from [243]. However, the search of $(2\ell + \not{E}_T)$ could be helpful to probe Toy model I since the process is also mediated by the production and decay of the new scalars. In Table 4.5, we have mentioned only the dominating production channels. We have noted that for the allowed values of the model parameters, as discussed earlier, the production cross-section $\sigma^{2\ell+\not{E}_T}$ in Toy Model-I is much larger than that in Toy Model-II. This is due to the presence of an additional channel $pp \to H^+H^- \to \mu^+\mu^-\not{E}_T$ in Toy Model-I. The corresponding production cross-section of this specific channel for some benchmark scenarios are given in Table 4.6. Here, the events are generated in `MADGRAPH` [205] at $\sqrt{s} = 14$ TeV. Depending on the charged Higgs mass and associated coupling Y_{22}, the cross-section can be quite large. For the rest of three channels as mentioned

Sl.No.	Benchmark point (BP)	$\sigma(\mu^\pm + \not{E}_T)$ (fb)
1.	$M_{H^\pm} = 500$ GeV, $M_{H^0} = 200$ GeV, $\lambda_5 = 0.01$, $M_{N_2} = 20$ GeV, $Y_{22} = 0.1$	0.0044
2.	$M_{H^\pm} = 500$ GeV, $M_{H^0} = 200$ GeV, $\lambda_5 = 0.01$, $M_{N_2} = 40$ GeV, $Y_{22} = 0.1$	0.0041
3.	$M_{H^\pm} = 500$ GeV, $M_{H^0} = 200$ GeV, $\lambda_5 = 0.01$, $M_{N_2} = 20$ GeV, $Y_{22} = 0.2$	0.071
4.	$M_{H^\pm} = 500$ GeV, $M_{H^0} = 200$ GeV, $\lambda_5 = 0.01$, $M_{N_2} = 20$ GeV, $Y_{22} = 0.5$	2.77
5.	$M_{H^\pm} = 200$ GeV, $M_{H^0} = 200$ GeV, $\lambda_5 = 0.01$, $M_{N_2} = 20$ GeV, $Y_{22} = 0.2$	0.263

Table 4.8: Production cross-section of the monomuon $+\not{E}_T$ final state in Toy Model I.

No.	Benchmark Point	$\sigma(\tau^+\mu^-\mu^-e^+) + \sigma(\tau^-\mu^+\mu^+e^-)$ (in fb)	$\sigma(\tau\tau\mu e)$ (fb)
1.	$M_{H^0} = 50$ GeV, $M_{A^0} = 100$ GeV, $Y^\ell_{12} = Y^\ell_{32} = 0.005$	1.106	0.026
2.	$M_{H^0} = 100$ GeV, $M_{A^0} = 100$ GeV, $Y^\ell_{12} = Y^\ell_{32} = 0.005$	0.008	1.85×10^{-4}

Table 4.9: Possible signature of Toy Model II with the corresponding production cross-sections.

in Table 4.5, the estimated production cross-sections for a few benchmark scenarios are given in Table 4.7. As one can see, the production cross-sections are very small, which is expected since the diagrams mentioned here are mostly mixing induced which we have assumed to be small. Note that the cross-sections are insensitive to the mass of Z'. We have checked that in both the toy models, among these three channels the dominating contribution will come from $pp \to Z \to Z\, s_2 \to \ell^+\ell^- \not{E}_T$. Therefore, this channel will not be helpful to discriminate the signatures of Toy Model-I from that of Toy Model-II. However, as one can see that $\sigma(pp \to H^+H^- \to \mu^+\mu^-\not{E}_T)$ is much larger than the production cross-sections for the rest of three channels, therefore, at the colliders a dedicated search for $\mu^+\mu^- + \not{E}_T$ signature could be helpful to probe Toy Model-I. Please note than in order to obtain long-lived charged scalars whose decay length $(c\tau) \gtrsim 0.1$ mm, we need Yukawa coupling of the order of $\sim (10^{-6} - 10^{-5})$. This will give very low production cross-section of the final state and therefore techniques like displaced muon and kink vertex will not be applicable. So we do not discuss it further.

Another interesting collider signature could be the production of $(\mu^\pm + \not{E}_T)$ which is an exclusive feature of Toy Model I and can be a smoking gun signal. It can be observed at a pp collider like the LHC where the intermediate particles leading to such a final state are the inert charged Higgs $(H^\pm)$ and inert neutral scalars (H^0, A^0) as shown in Fig. 4.31. The readers may recall that the inert Higgs couples to muon along with the dark matter. Due to electroweak interaction, it is possible to have sizeable production of H^+-H^0 which then decay to give a mono-muon plus missing energy final state. There are no other contributing diagrams to this muon specific signal. The other mono-lepton channels (say the mono-electon for example) will be kinematically suppressed due to the associated heavy neutrinos in the final state. The mono-muon signal is cleaner than the mono-jet searches and therefore it is possible to tag the muon. The major background is the $W(\ell\nu)$ process but one can expect a clean signal away from the W-boson mass window. The other minor backgrounds include $t, t\bar{t}, Z/\gamma*(\ell\ell), \gamma +$ jets and VV (where V stands for the SM vector bosons W, Z). As can be seen from Table. 4.8, for a few suitable benchmark values of the scalar and DM masses and coupling Y_{22}, it is possible to obtain a few femtobarns of production cross-section. In

Toy Model-II, the $U(1)_X$ charge of H_2 forbids its coupling with muon and N_2 simultaneously, instead it couples with the other RHNs (N_1, N_3). Also the scalars are in general lighter than N_1, N_3. Therefore, once again, the $\mu^\pm + \not{E}_T$ production at LHC will be kinematically suppressed. The probable collider signatures of Toy Model-II will be the productions of $\tau^+\mu^-\mu^-e^+$, $\tau^-\mu^+\mu^+e^-$ and $\tau\tau\mu e$ events at the LHC via the production and decay of H^0H^0. This is possible only in Toy Model-II since in this model, H^0 takes part in LFV interactions, which is not allowed in Toy Model-I. In a few benchmark scenarios, the corresponding production cross-sections are given in Table 4.9. As expected, the cross-sections are highly sensitive to the mass of H^0. Note that for the above mentioned four-lepton final states the SM background will be highly suppressed. Therefore, a dedicated search of these four lepton states with specific flavour and charge could be useful to test our Toy Model-II.

4.7 Summary

We have extended the SM by an Abelian $U(1)_X$ gauge group which results in a massive gauge boson (X) that couples only to leptons and has a small kinetic mixing with the SM Z boson. We have considered only the low masses of X ($M_X \lesssim 1$ GeV). In this kind of extension, we will get new contributions to flavour changing processes like $b \to s\ell^+\ell^-$ decays, and the new contribution will be in ΔC_9^ℓ which is the WC of the operator $\mathcal{O}_9$. Here, $\mathcal{O}_9$ is a left-handed quark current operator with vector muon/electron coupling. Also, in this model, the contributions to such flavour changing processes will be in both the electron and muon final states. At the same time, we will get new contributions in anomalous magnetic moment of the muon. We use the present data on R_K, R_{K^*}, the ratio of branching fraction $\mathcal{B}(B^0 \to K^{*0}\chi(\mu^+\mu^-))/\mathcal{B}(B^0 \to K^{*0}\mu^+\mu^-)$, $\mathcal{B}(B \to K^{(*)}e^+e^-)$, and muon anomalous magnetic moment to constrain $U(1)_X$ charges of the SM leptons. Also, the values ΔC_9^μ and ΔC_9^e which are obtained from the analysis are consistent with the global fit results of the data in $b \to s\ell^+\ell^-$ decays including various angular observables. Additionally, we consider all upper bounds from different experimental data on such light Abelian gauge boson mass and its couplings.

Now charging the SM fermion under a generic $U(1)_X$ symmetry makes the theory anomalous. To get an anomaly-free renormalisable model, we have incorporated additional chiral fermions into the model. In order to fit our requirements with a minimal particle content, we have considered a scenario where the three generation of leptons having vector type $U(1)_X$ interactions have corresponding charges $(n_1, n_2, n_3) = (-1, 2, -1)$ respectively. Such a choice is consistent with the data and also ensures anomaly cancellations after adding one right-handed neutrino per fermion generation having equal, and opposite $U(1)_X$ charges as that of SM lepton in that generation. Also, we have added additional singlet and doublet Higgs fields to get the desired mass spectrum. To prevent a direct coupling of the RHNs with the lepton doublets via SM Higgs, we impose a discrete $\mathcal{Z}_2$ symmetry on the particles in two different ways which lead to two distinct models and phenomenology. This kind of symmetry restrictions will provide a natural candidate for DM in our extended models. At the same time, the chosen particle content of the models can also generate

light neutrino masses, in agreement with neutrino oscillation data.

We are able to successfully study the DM phenomenology which is almost similar for the two Toy models but they have different neutrino mass generation mechanisms. The scalar content is very rich with an additional scalar doublet and two scalar singlets apart from the usual SM Higgs doublet. However, the second scalar doublet has very distinct features and plays different roles in each of the two Toy models. The low gauge boson X mass allows us to evade stringent constraints from LHC, while facing tight constraints from other low energy experiments. We ensure that our analysis is consistent with the LEP II bounds on $U(1)_X$ gauge boson mass and coupling and the bounds from other light boson search experiments. Few preliminary results have also been shown and discussed.

The two toy models lead to phenomenological implications that can be tested at the collider experiments. The promising channels are the 4-lepton final states, dilepton (2ℓ) + $\not{E}_T$ etc. Also, in the low energy experiments the potential signatures may come from the FCNC processes, like $b \to s(d) + invisible$, $s \to d + invisible$, $c \to u + invisible$ which will lead to rare decays of $B_q/K/D$ mesons to a relatively lighter meson final state with invisible particles. Also, both the models will contribute to LFV $h \to \tau e$ decays.

We have discussed some distinct features of both the models which could be helpful to discriminate the signatures of the two models at different experiments. At the LHC, the production of $\mu^{\pm} + \not{E}_T$ and lepton-specific $\mu^+\mu^- + \not{E}_T$ events could be the possible signatures of Toy Model-I which is not possible to get in Toy Model-II. On the other hand, the search for the specific multi-leptonic states like $\tau^+\mu^-\mu^-e^+$, $\tau^-\mu^+\mu^+e^-$ and $\tau\tau\mu e$ could be useful to identify the potential signatures of Toy Model-II. In the context of Higgs LFV, Toy Model-II contributes to $h \to \tau\mu$ and $h \to \mu e$ decays while Toy Model-I does not. Similarly, there are a few examples of the potential observables in the low energy sector: Toy Model-I contributes significantly to the semileptonic or purely leptonic decays $B_q/K/D$ mesons via the following quark level transitions: $b \to c(u)\tau\bar{\nu}_\tau$, $s \to u\tau\bar{\nu}_\tau$, $c \to s\tau\bar{\nu}_\tau$. However, Toy Model-II does not have significant contributions to these decays with τ in the final states. In Toy Model-II, we do not have any contribution in $\tau \to e\gamma$, $\tau \to \mu\gamma$ and $\mu \to e\gamma$ LFV decays; however, this model contributes to $\tau \to 3\mu$ decay. On the other hand, Toy Model-I contributes only in $\tau \to e\gamma$, not in all the other LFV decays as considered above. More precise data from future experiments will be able to discriminate between such toy models while confirming or ruling out some part of the available parameter space.

Chapter 5

Constraining New Physics with Possible Dark Matter Signatures from a Global CKM Fit

5.1 Introduction

The simplest way to devise a dark matter model is by considering a scalar, fermionic or vector field obeying the SM gauge symmetries whose stability can be ensured by an additional discrete $\mathcal{Z}_2$ symmetry under which the DM is odd but all other SM particles are even. However, in order to annihilate into SM particles and give rise to the correct relic abundance, there has to be a mediator between the dark and the visible sectors. The interactions of the mediator with the visible sector must include a non-zero vertex with the SM quark fields among others such that, the DM can scatter off a fixed target nuclei and be detected from any hint of nuclear recoil. However, such interactions might also impact important flavour physics observables which most of the dark matter analyses do not take into consideration. In this chapter, we are going to investigate the constraints on the dark matter parameter space from flavour data in the context of a simple dark matter model.

5.2 Model : Fermion Dark Matter with Scalar Mediator

For an illustration of our main objective, here we consider an extension of the SM by a singlet Dirac fermion dark matter χ and a real singlet scalar S. The DM decay is stabilized by imposing a discrete $\mathcal{Z}_2$ symmetry under which $\chi \to -\chi$ while all other particles remain even under the transformation. The most general renormalizable Lagrangian for such a model can be written as

$$\mathcal{L} = \mathcal{L}_{SM} + \frac{1}{2}\bar{\chi}(i\partial\!\!\!/ - m_\chi)\chi - \frac{1}{2}(\partial_\mu S)^2 - \left[\bar{\chi}(C'_s + iC'_p\gamma_5)\chi + \bar{\psi}(C_s + iC_p\gamma_5)\psi\right] S - V(H,S) \tag{5.1}$$

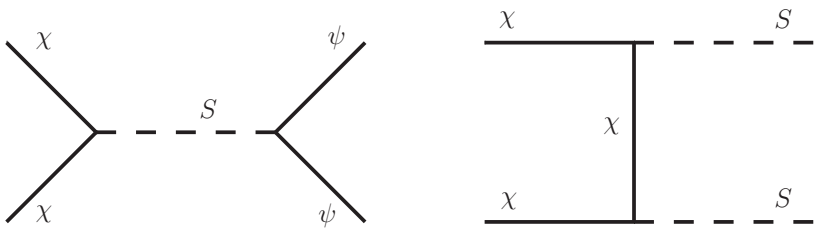

Figure 5.1: Annihilation channels for the spin-0 mediated fermionic dark matter model under consideraion.

where, H denotes the SM Higgs doublet and ψ denotes SM fermions. The scalar potential $V(H,S)$ can be of the form

$$V(H,S) = \mu_H^2 H^\dagger H + \frac{1}{2}\lambda_H (H^\dagger H)^2 + \mu_1^3 S + \frac{\mu_S^2}{2} S^2 + \frac{\mu_3}{3!} S^3 + \frac{\lambda_S}{4!} S^4 + \lambda_1 (H^\dagger H) S + \frac{\lambda_2}{2} (H^\dagger H) S^2. \quad (5.2)$$

We are mostly interested in the DM phenomenology and not in the exact details of the origin of the scalar sector. Hence for simplicity we decouple the two Higgses by considering zero mixing and obtain the mass eigenstates as $m_h^2 = \lambda_H^2 v_H^2 = (125)^2$ GeV^2 with $v_H = 246$ GeV and $M_S^2 = \mu_S^2$ GeV^2. This also helps us evade stringent constraints coming from Higgs portal DM searches and collider constraints due to $h \to invisible$ decays. For studies based on such models in the literature, see [279–284]. Also, in our study, we mostly focus on effective DM interaction with SM quarks i.e $\psi \equiv q$. There are plenty of analyses on such leptophobic DM models in the perspective of LHC and indirect detection searches [282–287].

Following the Lagrangian given in Eqn. (5.1), it is evident that the dominant channel for DM annihilation will be the s-channel transition $\bar{\chi}\chi \to \bar{\psi}\psi$ shown by the Feynman diagram in the LHS of Fig. 5.1. There can also be a t-channel annihilation $\bar{\chi}\chi \to SS$ as shown in Fig. 5.1 but for heavy scalars, that contribution will be much suppressed. The thermally averaged dark matter annihilation cross-section $< \sigma v >$ is usually expressed as a partial-wave expansion in powers of the square of the relative velocity between the annihilating particles as given in Eqn. (2.10). The dominant contribution to the s-channel DM annihilation rate for pure scalar interaction mediation is velocity suppressed due to the absence of s-wave terms. However, in presence of the pseudoscalar coupling C_p, there is an enhancement in the annihilation cross-section due to the presence of an unsuppressed s-wave [41]. Also, there will be contributions in direct detection cross section. The advantage of non-zero pseudoscalar interaction is that the WIMP-nucleon scattering cross-sections from such operators are spin dependent and velocity suppressed. This kind of pseudoscalar interactions helps to evade stringent bounds from present direct detection (DD) bound from the experimental searches. The phenomenology of such pseudoscalar mediators have been extensively studied in [283, 288–291]. While the pseudoscalar operators help weaken the direct detection scattering cross-section with a momentum suppression, they also amplify the chances of probing the WIMP at indirect detection experiments through initial/final state radiation or bremsstrahlung processes [292–297]. The only way to obtain a spin-independent direct detection cross-section is to have a non-zero scalar-scalar effective interaction i.e $C_s, C_s' \neq 0$.

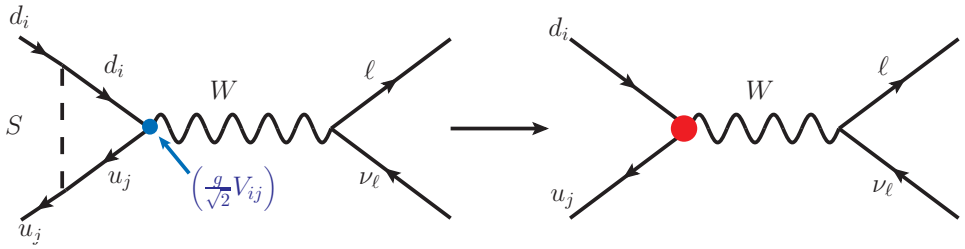

Figure 5.2: Loop correction to the $d_i \to u_j W$ vertex in the presence of a real scalar S. The vertex modification will have direct impact on the vertex CKM factor V_{ij}.

5.3 Contributions in $d_i \to u_j \ell \nu_\ell$ decays

In the previous section, we define a Lagrangian (Eqn. (5.1)) which contains interactions of SM fermions with the scalar S:

$$\mathcal{L}^f_{int} = \bar{\psi}(C_s + iC_p\gamma_5)\psi S. \tag{5.3}$$

In this analysis, we have considered only the quarks and assumed universal coupling for all the quarks. Note that this kind of interaction will affect the SM charged current vertex $\bar{d}_j\gamma^\mu(1-\gamma_5)u_i W_\mu$ at one loop. There will be new contributions in the semileptonic or purely leptonic decay rates $\Gamma_{(d_j\to u_i\ell\nu_\ell)}$ $(\ell = leptons)$ due to this type of correction. The representative diagram is shown in Fig. 5.2, wherein these decays receive vertex corrections from the heavy scalar exchanges in the loop. The Cabbibo-Kobyashi-Masakawa (CKM) element V_{ij} appear as a vertex factor of the charged current interactions in the SM.

The most general effective Hamiltonian for the $d_i \to u_j \ell\nu$ processes in a similar fashion as written for the $b \to c\ell\nu$ Hamiltonian in Eqn. (2.8) :

$$\mathcal{H}^{d_i\to u_j}_{\text{eff}} = \frac{4G_F}{\sqrt{2}}V_{ij}\left[(\delta_{\ell\ell} + C^\ell_{V_1})\mathcal{O}^\ell_{V_1} + C^\ell_{V_2}\mathcal{O}^\ell_{V_2} + C^\ell_{S_1}\mathcal{O}^\ell_{S_1} + C^\ell_{S_2}\mathcal{O}^\ell_{S_2} + C^\ell_T\mathcal{O}^\ell_T\right] \tag{5.4}$$

where C^ℓ_X $(X = V_1, V_2, S_1, S_2, T)$ are the Wilson coefficients (WCs) corresponding to the operator basis

$$\begin{aligned}
\mathcal{O}^\ell_{V_1} &= (\bar{u}_{jL}\gamma^\mu d_{iL})(\bar{\ell}_L\gamma_\mu\nu_L),\\
\mathcal{O}^\ell_{V_2} &= (\bar{u}_{jR}\gamma^\mu d_{iR})(\bar{\ell}_L\gamma_\mu\nu_L),\\
\mathcal{O}^\ell_{S_1} &= (\bar{u}_{jL}d_{iR})(\bar{\ell}_R\nu_L),\\
\mathcal{O}^\ell_{S_2} &= (\bar{u}_{jR}d_{iL})(\bar{\ell}_R\nu_L),\\
\mathcal{O}^\ell_T &= (\bar{u}_{jR}\sigma^{\mu\nu}d_{iL})(\bar{\ell}_R\sigma_{\mu\nu}\nu_L).
\end{aligned} \tag{5.5}$$

There are no lepton flavour violating vertices in the Lagrangian under consideration (5.1). Hence, for all practical purposes, we can remove the suffix ℓ in the operator basis and write $C^\ell_X \equiv C_X$. Note that in the SM, at the tree level, the contribution is obtained only from $\mathcal{O}_{V_1}$. Along with $\mathcal{O}_{V_1}$, the rest of the operators alone or in combinations may appear in different NP scenarios. Therefore, the WC C_X incorporates the NP effects in these decays, and in the SM, $C_X = 0$.

In the SM, the $d_i \to u_j W$ vertex has a $V-A$ structure i.e $\gamma^\mu(1-\gamma_5)$. As will be shown in the next subsection, the corrections due to NP have a direct impact on the vertex factors, which in this case are the CKM elements $V_{ij}\frac{g}{\sqrt{2}}$. The semileptonic and purely leptonic decays rates are directly proportional to the vertex factors. The detailed mathematical expressions of the decay rate distributions of the exclusive semileptonic $P \to M^{(*)}\ell\nu_\ell$ and purely leptonic $P \to \ell\nu_\ell$ decays can be seen from ref. [98] where P and M are the pseudoscalar mesons, and M^* is a vector meson. Here, we would like to mention that most of the CKM elements, like $|V_{ud}|$, $|V_{cd}|$, $|V_{us}|$, $|V_{cs}|$, $|V_{ub}|$, $|V_{cb}|$, are extracted from the semileptonic and purely leptonic (few cases) $d_i \to u_j \ell \nu_\ell$ decays with $\ell = \mu$, or e. The underline assumption is that these decays with the light leptons will be less sensitive to any NP effects. The vertex correction shown in Fig. 5.2 may introduce additional operators (other than $V-A$ type) due to operator mixing. The measured decay rates, along with some other inputs from lattice (decay constants and form factors), are the useful probe of the CKM elements $|V_{ij}|$. In the presence of new four-fermi operators defined in Eqn. (5.4), the decay rates will be modified. If only the vertex factor is modified, then the extracted values of the $|V_{ij}|$ (with) can be directly used to constrain the new couplings. Otherwise, we need to fit the decay rates to constrain the new couplings. In the following subsections, we will discuss it in detail.

Also, it is important to mention that all these CKM elements are extracted with reasonably good precision. For example $|V_{ud}|$ and $|V_{cs}|$ are known with an error $\approx .01\%$ while $|V_{us}|$ and $|V_{cd}|$ are known with an accuracy of 0.1%. The $|V_{ub}|$ and $|V_{cb}|$ are relatively less precisely known. Therefore, it is natural to expect tight constraints on the new couplings C_s and C_p from an analysis of the CKM observables, purely leptonic and exclusive semileptonic decay rates, respectively. Note that $|V_{ub}|$ and $|V_{cb}|$ are also extracted from semileptonic inclusive decays. To constrain the new couplings, we did not consider the inputs from inclusive decays. Constraining the NP from inclusive decays requires a separate dedicated analysis. However, we do not expect much of an improvement since the CKM elements are much more precise than $|V_{ub}|$ and $|V_{cb}|$.

5.3.1 Effective vertex

As mentioned earlier, in the SM the coupling strength for the $d_i \to u_j W$ charged current interation is given by $\frac{igV_{ij}}{\sqrt{2}}$ and the interaction is of the type $(V-A)$. However, the one-loop correction of this charged current vertex due to the interaction given in Eqn. (5.3) introduces one new $(V+A)$ type interaction in addition to the original $(V-A)$ type interaction. The corresponding Feynman diagram can be seen from Fig. 5.2, and the effective charged current interaction can be written as:

$$\begin{aligned}\mathcal{L}^{eff}_{d_i\to u_j W} &= \frac{igV_{ij}}{2\sqrt{2}}\left[C_L \bar{u}_j \gamma_\mu(1-\gamma_5)d_i + C_R \bar{u}_j \gamma_\mu(1+\gamma_5)d_i\right] W^\mu \\ &= \frac{igV_{ij}}{2\sqrt{2}}\left[C_L\mathcal{O}_L + C_R\mathcal{O}_R\right] W^\mu. \end{aligned} \tag{5.6}$$

Here, the effects of NP coming from the loop corrections are introduced in the coefficients C_L and C_R, respectively. Hence, we can say that at the tree level (pure SM) $C_L = 1$ and $C_R = 0$.

We have done the calculation in a unitary gauge using dimensional regularization. The loop

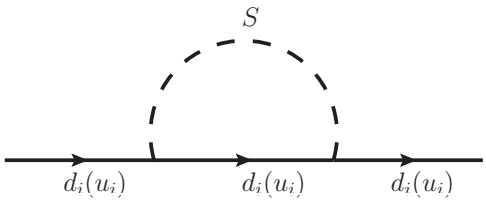

Figure 5.3: Quark self energy corrections in the presence of the new interaction given in Eqn. (5.3).

factor C_L does not receive any $\frac{1}{\epsilon}$ pole, however C_R had a pole

$$pole_{C_R} = \frac{C_s^2 + C_p^2}{16\pi^2}\left(-\frac{1}{2\epsilon}\right), \tag{5.7}$$

which can be removed by introducing appropriate counter terms. The counter term can be obtained from the wave function renormalization which we have calculated from the quark self-energy correction diagram given in Fig. 5.3, from this diagram we have obtained a pole relevant for wave function renormalization as given below:

$$pole_{SE} = \frac{C_s^2 + C_p^2}{16\pi^2}\left(\frac{1}{2\epsilon}\right)\not{p}. \tag{5.8}$$

Here, p is the incoming momentum of the quark under consideration. Hence, we can define the wave function renomalization constant for the left and right handed quark field as:

$$\delta Z_{ii}^L = \delta Z_{ii}^R = \frac{C_s^2 + C_p^2}{16\pi^2}\frac{1}{2\epsilon}. \tag{5.9}$$

Note that from the vertex corrections, the divergence piece appears in C_R, not in C_L, and at the tree level $C_R = 0$. Therefore, only the wave function renormalization would not be sufficient to cancel the divergence. Also, the counter term related to $\mathbf{O}_L$ needs to be absorbed since C_L at loop level does not have any divergences. We need to introduce the counterterms due to operator renormalization or equivalently by the renormalization of the coupling constants. Following operator renormalization, in general, one can write the matrix elements of an unrenormalized operator $\mathcal{O}_m^{(0)}$ in terms of the renormalized one as

$$\langle \mathcal{O}_m^{(0)} \rangle = \sqrt{Z_{u_i} Z_{d_j}}\, Z_{mn} \langle \mathcal{O}_n \rangle. \tag{5.10}$$

In the other method, one can define the respective interaction Hamiltonian as

$$\begin{aligned} \mathcal{H} = C_m^{(0)} \mathcal{O}_m^{(0)} &= (Z_{mn}^c C_n)\sqrt{Z_{u_i} Z_{d_j}}\,\mathcal{O}_n \\ &= C_m \mathcal{O}_m + (Z_{mn}^c \sqrt{Z_{u_i} Z_{d_j}} - \delta_{mn}) C_n \mathcal{O}_m. \end{aligned} \tag{5.11}$$

Both the methods are equivalent with

$$Z_{nm}^{-1} = Z_{mn}^c.$$

.

In our analysis, to obtain the renormalized vertex (Eqn. (5.6)) we define the counter term following Eqn. (5.11). The required wave function renormalization constant are obtained from Eqn. (5.9). To absorb the remaining divergences, the required renormalization constants for the couplings C_L and C_R are given by

$$\delta Z^c_{LL} = -\frac{C_s^2 + C_p^2}{16\pi^2}\frac{1}{2\epsilon}, \text{ and } \delta Z^c_{RL} = -\frac{C_s^2 + C_p^2}{16\pi^2}\frac{1}{4\epsilon}. \tag{5.12}$$

Note that here, we have written $Z = 1 + \delta Z$. At the tree level $C_R = 0$, hence we do not need Z_{RR} and Z_{LR}. However, in principle Z_{RL} should be equal to Z_{LR}[1].

Using the renormalized vertex, after integrating out the W field from the diagram of Fig. 5.2 we obtain the following effective Hamiltonian

$$\mathcal{H}_{\text{eff}}^{d_i \to u_j} = \frac{4G_F}{\sqrt{2}} V_{ij} \left[(1 + C_{V_1})\mathcal{O}_{V_1} + C_{V_2}\mathcal{O}_{V_2}\right], \tag{5.13}$$

where the operators are defined in Eqn. (5.6), the WCs C_{V_1} and C_{V_2} will be obtained from C_L and C_R, respectively which are the following

$$C_{V_1}^{q_i \to q_j} \equiv C_{V_1}^{q_i q_j} = \left(\frac{4 m_i m_j C_s^2}{16\pi^2}\right) C_0 \tag{5.14}$$

and

$$C_{V_2}^{q_i \to q_j} \equiv C_{V_2}^{q_i q_j} = \frac{C_T}{16\pi^2}\int_0^1 dx \int_0^{1-x} dz \left(\frac{1}{2} + ln\, \Delta\right), \tag{5.15}$$

with

$$C_0 = \int_0^1 dx \int_0^{1-x} dz \left(\frac{1+x}{\Delta}\right) \tag{5.16}$$

and $C_T = (C_s^2 + C_p^2)$. Here, $\Delta = xM_S^2 + (1-x)(1-x-z)m_i^2 + (1-x)z m_j^2 + z(1-x-z)q^2$, m_i, m_j are the masses of quarks u_i, d_j. Here q^2 is the energy carried by the W-boson propagator and for meson decays of the form : $P \to M^{(*)}\ell\nu_\ell$, and q^2 can range from m_ℓ^2 to $(m_P - m_{M^{(*)}})^2$. Numerically, the value of the NP WC is quite insensitive to the value of q^2 in this range.

The important point to note here is the fact that the contribution to the left-handed (LH) quark current vector operator $\mathcal{O}_{V_1}$ is proportional to the product of the external quark masses. Hence, for light quarks, such as u, d, s etc, the loop contribution is zero in the massless quark limit. Even for heavier quark transitions, for example, $b \to c\ell\nu$, C_{V_1} is quite suppressed as compared to C_{V_2} for heavy scalar mediator masses (even when $C_s = 1$). The contribution in C_{V_2} increases with the increase of scalar mass. Therefore, for numerical analysis one can practically set $C_{V_1} \approx 0$.

We want to point out that, in the SM we can have similar vertex corrections with the scalar S replaced by the SM Higgs or by a Z boson in Fig. 5.2. We can parametrize such correction as $\delta C_{V_1}^{SM}$ which represent a small shift from $C_{V_1}^{SM} = 1$. For SM Higgs, there won't be any contribution in

[1] We have checked that the one-loop correction to $(\mathcal{O}_R)_{1-loop}$ introduces the same divergence piece in C_L as given in Eqn. (5.7) for C_R at the present case.

C_{V_2} and the contribution in $\delta C_{V_1}^{SM}$ is $\lesssim 10^{-8}$. Also, for SM Z-boson, the contribution to both in $\delta C_{V_1}^{SM}$ and C_{V_2} are negligibly small as compared to the new contribution in C_{V_2}. We have dropped any such contribution from our analysis; they have a negligible impact on our findings.

5.3.2 Contributions in the decays: semileptonic and leptonic

Using the effective Hamiltonian given in Eqn. (5.13), the differential decay rate for the $P \to M\ell\nu_\ell$ is written as [158].

$$\frac{d\Gamma(P \to M\ell\nu_\ell)}{dq^2} = \frac{G_F^2|V_{ij}|^2}{\pi^3 m_P^3} q^2 \sqrt{\lambda_M(q^2)} \left(1 - \frac{m_\ell^2}{q^2}\right) |1 + C_{V_1} + C_{V_2}|^2 \left\{ \left(1 + \frac{m_\ell^2}{2q^2}\right) {H_{V,0}^s}^2 + \frac{3}{2}\frac{m_\ell^2}{q^2} {H_{V,t}^s}^2 \right\}, \tag{5.17}$$

while that for $P \to M^*\ell\nu_\ell$

$$\begin{aligned}\frac{d\Gamma(P \to M^*\ell\nu_\ell)}{dq^2} = \frac{G_F^2|V_{ij}|^2}{\pi^3 m_P^3} q^2 \sqrt{\lambda_{M^*}(q^2)} \left(1 - \frac{m_\ell^2}{q^2}\right) \times \Bigg\{ \\ (|1 + C_{V_1}|^2 + |C_{V_2}|^2) \left[\left(1 + \frac{m_\ell^2}{2q^2}\right) (H_{V,+}^2 + H_{V,-}^2 + H_{V,0}^2) + \frac{3}{2}\frac{m_\ell^2}{q^2} H_{V,t}^2 \right] \\ - 2\mathcal{R}e[(1 + C_{V_1})C_{V_2}^*] \left[\left(1 + \frac{m_\ell^2}{2q^2}\right) (H_{V,0}^2 + 2H_{V,+}\, H_{V,-}) + \frac{3}{2}\frac{m_\ell^2}{q^2} H_{V,t}^2 \right] \Bigg\},\end{aligned} \tag{5.18}$$

The helicity amplitudes are written in terms of the QCD form factors as given below

$$H_{V,0}^s(q^2) = \sqrt{\frac{\lambda_M(q^2)}{q^2}} f_+(q^2)\,, \tag{5.19a}$$

$$H_{V,t}^s(q^2) = \frac{m_P^2 - m_M^2}{\sqrt{q^2}} f_0(q^2). \tag{5.19b}$$

and

$$H_{V,\pm}(q^2) = (m_P + m_{M^*}) A_1(q^2) \mp \frac{\sqrt{\lambda_{M^*}(q^2)}}{m_P + m_{M^*}} V(q^2)\,, \tag{5.20a}$$

$$H_{V,0}(q^2) = \frac{m_P + m_{M^*}}{2m_{M^*}\sqrt{q^2}} \left[-(m_P^2 - {m_{M^*}}^2 - q^2) A_1(q^2) + \frac{\lambda_{M^*}(q^2)}{(m_P + m_{M^*})^2} A_2(q^2) \right], \tag{5.20b}$$

$$H_{V,t}(q^2) = -\sqrt{\frac{\lambda_{M^*}(q^2)}{q^2}} A_0(q^2)\,, \tag{5.20c}$$

(5.20d)

respectively. The branching fraction for $P \to \ell\nu_\ell$ corresponding to the same Hamiltonian is:

$$\mathcal{B}(P \to \ell\nu_\ell) = \frac{\tau_P}{8\pi} m_P m_\ell f_P^2 G_f^2 \left(1 - \frac{m_\ell^2}{m_P^2}\right) |V_{ij}(1 + C_{V_1} - C_{V_2})|^2\,. \tag{5.21}$$

From the above decay rate distributions, we can see that the new contributions in $P \to M\ell\nu_\ell$

and $P \to \ell\nu_\ell$ decays will modify only the vertex from $|V_{ij}| \to |V'_{ij}| = |V_{ij}(1 + C_{V_1} \pm C_{V_2})|$, respectively. However, in $P \to M^*\ell\nu_\ell$ transitions the new contributions will modify the q^2 distribution. Therefore, the CKM elements $|V'_{ij}|$ extracted from purely leptonic or $P \to M\ell\nu_\ell$ decays, can be directly used to constrain the new parameters along with the Wolfenstein parameters: A, λ, ρ and η with which we need to parametrize $|V_{ij}|$. Note that $|V_{cb}|$ is extracted from both $B \to D\ell\nu_\ell$ and $B \to D^*\ell\nu_\ell$ decays. Hence, to extract the Wolfenstein parameters along with the new parameters from $B \to D^*\ell\nu_\ell$ decays, we need to redo the fit to the experimental data. We will discuss the detail in the next section.

5.4 Numerical Analysis and Results

5.4.1 $B \to D^*\ell\nu$ Observables

As pointed out in the previous section, for the NP scenario under consideration we need to fit the decay rate distributions of $B \to D^*\ell\nu_\ell$ decays to extract the CKM parameters along with the new physics parameters. The methodology of this fit will be similar to the one given in refs. [96, 276] with a very recent updated results from Fermilab Lattice Collaboration [298]. For the first time, they have provided the $B \to D^*$ form factors at non-zero recoils. They provide a set of synthetic data based on the Boyd-Grinstein-Lebed (BGL) parametrization [299] of the form factors truncated at $N = 2$ at three w values, $\{1.03, 1.10, 1.17\}$, along with their correlations. We have used these data points in our analysis. Like before, we have utilized the untagged dataset for the four-fold decay distribution of $B \to D^*\ell\nu$ by the Belle collaboration [300]. Also, we have used $B \to D^*$ form factors at $q^2 = 0$ from the QCD Light-Cone Sum Rules (LCSR) [301]. Additionaly, the Fermilab/MILC lattice input, $h_{A_1}(1) = 0.906(13)$ [302], allow us to efficiently constrain the form factor parameter a_0^f and hence, $|V_{cb}|$.

The four form factors relevant for $B \to D^*\ell\nu_\ell$ decay are $\mathcal{F}_i = \{f(z), g(z), \mathcal{F}_1(z), \mathcal{F}_2(z)\}$. In the BGL method of parametrization, these form factors can be expressed as a series expansion in z as

$$\mathcal{F}_i(z) = \frac{1}{P_i(z)\phi_i(z)} \sum_{j=0}^{N} a_j^{\mathcal{F}_i} z^j, \tag{5.22}$$

where z is related to the recoil angle w as

$$z = \frac{\sqrt{w+1} - \sqrt{2}}{\sqrt{w+1} + \sqrt{2}}. \tag{5.23}$$

The recoil angle is related to the momentum transfer q^2 as $q^2 = m_B^2 + m_{D^*}^2 - 2m_B m_{D^*} w$. The functions $P_i(z)$, called the Blaschke factors, are given by

$$P_i(z) = \prod_p \frac{z - z_p}{1 - z z_p}, \tag{5.24}$$

Dataset	Fit Quality		Parameter	Fit Result
	χ^2/dof	p-Value		
Belle [300] + $h_{A_1}(1)$ [302] + LCSR [301] + Lattice [298]	52.82/45	19.75%	$\lvert V_{cb}\rvert$	$38.69(79)\times 10^{-3}$
			a_0^f	0.0123(1)
			a_1^f	0.0222(96)
			a_2^f	−0.522(196)
			a_0^g	0.0318(10)
			a_1^g	−0.133(63)
			a_2^g	−0.62(146)
			$a_1^{\mathcal{F}_1}$	0.0021(15)
			$a_0^{\mathcal{F}_2}$	0.0515(12)
			$a_1^{\mathcal{F}_2}$	−0.149(59)
			$a_2^{\mathcal{F}_2}$	0.987(932)

Table 5.1: Fit result for the frequentist analysis of the mentioned $B \to D^*\ell\bar{\nu}_\ell$ dataset for the SM scenario.

which are used to eliminate the poles at $z = z_p$ where,

$$z_p = \frac{\sqrt{(m_B + m_{D^*})^2 - m_P^2} - \sqrt{4m_B m_{D^*}}}{\sqrt{(m_B + m_{D^*})^2 - m_P^2} + \sqrt{4m_B m_{D^*}}}. \tag{5.25}$$

Here m_P denotes the pole masses and can be looked up in [303]. The outer functions $\phi_i(z)$ are chosen to be

$$\begin{aligned}
\phi_f &= \frac{4r}{m_B^2}\sqrt{\frac{n_I}{6\pi\chi_{1^+}^T(0)}}\frac{(1+z)(1-z)^{3/2}}{\left[(1+r)(1-z)+2\sqrt{r}(1+z)\right]^4},\\
\phi_g &= 16r^2\sqrt{\frac{n_I}{3\pi\tilde{\chi}_{1^-}^T(0)}}\frac{(1+z)^2(1-z)^{-1/2}}{\left[(1+r)(1-z)+2\sqrt{r}(1+z)\right]^4},\\
\phi_{\mathcal{F}_1} &= \frac{4r}{m_B^3}\sqrt{\frac{n_I}{6\pi\chi_{1^+}^T(0)}}\frac{(1+z)(1-z)^{5/2}}{\left[(1+r)(1-z)+2\sqrt{r}(1+z)\right]^5},\\
\phi_{\mathcal{F}_2} &= 8\sqrt{2}r^2\sqrt{\frac{n_I}{\pi\tilde{\chi}_{1^+}^L(0)}}\frac{(1+z)^2(1-z)^{-1/2}}{\left[(1+r)(1-z)+2\sqrt{r}(1+z)\right]^4}
\end{aligned} \tag{5.26}$$

where $r = m_{D^*}/m_B$ and the other inputs can be found in [303]. Therefore, for $N = 2$, there are twelve coefficients, $a_j^{\mathcal{F}_i}$ for the four form factors. These coefficients satisfy the following weak unitarity constraints :

$$\sum_{j=0}^{N}(a_j^g)^2 < 1, \quad \sum_{j=0}^{N}(a_j^f)^2 + (a_j^{\mathcal{F}_1})^2 < 1, \quad \sum_{j=0}^{N}(a_j^{\mathcal{F}_2})^2 < 1. \tag{5.27}$$

	A	λ	$\bar{\rho}$	$\bar{\eta}$	Fit Quality	
					χ^2/dof	p-Value
CKMFitter'19	$0.8235^{+0.0056}_{-0.0145}$	$0.224837^{+0.000251}_{-0.000060}$	$0.1569^{+0.0102}_{-0.0061}$	$0.3499^{+0.0079}_{-0.0065}$	-	-
Our Result	0.8205 ± 0.0075	0.22462 ± 0.00031	0.1607 ± 0.0093	0.3558 ± 0.0088	34.18/23	6.26%
Updated 2021 Results	0.8178 ± 0.0070	0.22498 ± 0.00029	0.1734 ± 0.0092	0.374 ± 0.011	37.25/25	8.37%

Table 5.2: Comparison of the best fit estimates of the Wolfenstein parameters by the CKMFitter group and our group from the global CKM fit in the SM framework. The two results are consistent with each other within 1σ limit of the errors. We also provide the χ^2/dof and the goodness of fit for our fit results. The last row contains the best parameter estimates of the global scenario with the most updated inputs.

Further, there are two kinematical constraints on the form factors, one each at zero and maximum recoil :

$$\mathcal{F}_1(1) = m_B(1-r)f(1), \tag{5.28}$$

$$\mathcal{F}_2(w_{max}) = \frac{1+r}{m_B^2(1+w_{max})(1-r)r}\mathcal{F}_1(w_{max}). \tag{5.29}$$

We consider these constraints in our analysis to remove two of the BGL coefficients from the theory. In the limit of massless leptons, the decay distribution becomes insensitive to the form factor $\mathcal{F}_2$. Hence, only 8 independent form factor coefficients are required to be fit the theory to the data. For the numerical analysis presented here we perform a maximum likelihood estimation of the parameters using Optex, a Mathematica based package. The fit results are given in table 5.1, the value of $|V_{cb}|$ is very much consistent with the one obtained in [298]. In the following section we will utilize this value of $|V_{cb}|$ for a global CKM fit without NP.

5.4.2 CKM Fit

As we have mentioned in the previous section, the new physics contributions to semileptonic ($P \to M\ell\nu_\ell$) and leptonic decays will impact the vertex factor, which is proportional to the square of the magnitude of the corresponding CKM element. Hence, we need to extract the parameters related to NP alongside the other Wolfenstein parameters. This means that we need to do a dedicated fit to all these parameters using the machinery used by the CKMFitter group to fit only the CKM parameters.

To validate the code, we recreate the Summer'19 SM fit performed by the CKMFitter group using the same set of inputs and observables as mentioned in [304]. The details of the theoretical expressions for the observables can be found in [98, 202, 305, 306]. We report our fit results in Table. 5.2 in comparison to the CKMFitter 2019 results. They are consistent with each other within 1σ confidence interval (CI). We have further used some most recent updates of the CKM observables as listed in Table. 5.3 and redo the fit in this "*Updated 2021*" scenario. This is the most updated global fit results after CKMFitter 2019. The other relevant inputs are given in Table. 5.4. Note that the fit results of all the four parameters are consistent with 2019 results within 1σ CI, however,

Observable	Value	Reference
$\lvert V_{ud}\rvert$ (nucl)	0.97420 ± 0.00021	[75]
$\lvert V_{us}\rvert f_+^{K\to\pi}(0)$	0.2165 ± 0.0004	[76]
$\lvert V_{cd}\rvert_{\nu N}$	0.30 ± 0.011	[1]
$\lvert V_{cs}\rvert_{W\to c\bar{s}}$	$0.94^{+0.32}_{-0.26} \pm 0.13$	[1]
$\lvert V_{ub}\rvert_{excl}$	$(3.91 \pm 0.13) \times 10^{-3}$	[94, 95]
$\lvert V_{ub}\rvert_{incl}$	$(4.10^{+0.09}_{-0.22} \pm 0.15) \times 10^{-3}$	[307]
$\lvert V_{cb}\rvert_{B\to D}$	$(40.84 \pm 1.15) \times 10^{-3}$	[276]
$\lvert V_{cb}\rvert_{B\to D^*}$	$(38.69 \pm 0.79) \times 10^{-3}$	this work
$\lvert V_{cb}\rvert_{incl}$	$(42.16 \pm 0.50) \times 10^{-3}$	[308]
$\mathcal{B}(\Lambda_p \to p\mu^-\bar{\nu}_\mu)_{q^2>15}/\mathcal{B}(\Lambda_p \to \Lambda_c\mu^-\bar{\nu}_\mu)_{q^2>7}$	$(0.947 \pm 0.081) \times 10^{-2}$	[309]
$\mathcal{B}(B^- \to \tau^-\bar{\nu}_\tau)$	$(1.09 \pm 0.24) \times 10^{-4}$	[98]
$\mathcal{B}(D_s^- \to \mu^-\bar{\nu}_\mu)$	$(5.51 \pm 0.16) \times 10^{-3}$	[98]
$\mathcal{B}(D_s^- \to \tau^-\bar{\nu}_\tau)$	$(5.52 \pm 0.24) \times 10^{-2}$	[98]
$\mathcal{B}(D^- \to \mu^-\bar{\nu}_\mu)$	$(3.77 \pm 0.18) \times 10^{-4}$	[98]
$\mathcal{B}(D^- \to \tau^-\bar{\nu}_\tau)$	$(1.20 \pm 0.27) \times 10^{-3}$	[98]
$\mathcal{B}(K^- \to e^-\bar{\nu}_e)$	$(1.582 \pm 0.007) \times 10^{-5}$	[1]
$\mathcal{B}(K^- \to \mu^-\bar{\nu}_\mu)$	0.6356 ± 0.0011	[1]
$\mathcal{B}(\tau^- \to K^-\bar{\nu}_\tau)$	$(0.6986 \pm 0.0085) \times 10^{-2}$	[98]
$\mathcal{B}(K^- \to \mu^-\bar{\nu}_\mu)/\mathcal{B}(\pi^- \to \mu^-\bar{\nu}_\mu)$	1.3367 ± 0.0029	[1]
$\mathcal{B}(\tau^- \to K^-\bar{\nu}_\tau)/\mathcal{B}(\tau^- \to \pi^-\bar{\nu}_\tau)$	$(6.438 \pm 0.094) \times 10^{-2}$	[98]
$\mathcal{B}(B_s \to \mu^+\mu^-)$	$(2.9 \pm 0.7 \pm 0.2) \times 10^{-9}$	[100]
$\lvert V_{cd}\rvert f_+^{D\to\pi}(0)$	0.1426 ± 0.0018	[98]
$\lvert V_{cs}\rvert f_+^{D\to K}(0)$	0.7180 ± 0.0033	[98]
$\lvert\varepsilon_K\rvert$	$(2.228 \pm 0.011) \times 10^{-3}$	[1]
Δm_d	$(0.5065 \pm 0.0019)\ \text{ps}^{-1}$	[98]
Δm_s	$(17.757 \pm 0.021)\ \text{ps}^{-1}$	[98]
$\sin 2\beta$	0.71 ± 0.09	[98]
ϕ_s	-0.055 ± 0.021	[98]
α	$(85.2^{+4.8}_{-4.3})^\circ$	[98]
γ	$(67 \pm 4)^\circ$	[104]

Table 5.3: List of observables used for the CKM fit (*Updated 2021*) in the SM framework. For the NP analysis we have not used the inclusive measurements of $\lvert V_{ub}\rvert$ and $\lvert V_{cb}\rvert$. All other inputs have been considered.

Input Parameters	Value	Reference
$f_+^{K\to\pi}(0)$	0.9706(27)	$N_f = 2+1+1$ [77]
$f_{K^\pm}/f_{\pi^\pm}$	1.1932(19)	$N_f = 2+1+1$[77]
f_K	155.7 ± 0.13	$N_f = 2+1+1$ [77]
$f_+^{DK}(0)$	0.747(19)	$N_f = 2+1+1$ [77]
$f_+^{D\pi}(0)$	0.666(29)	$N_f = 2+1$ [77]
f_{B_s}	230.3(1.3) MeV	$N_f = 2+1+1$ [77]
f_{B_s}/f_B	1.209(0.005)	$N_f = 2+1+1$ [77]
B_K	0.7625(97)	$N_f = 2+1$ [77]
f_{D_s}	249.9(5) MeV	$N_f = 2+1+1$ [77]
f_{D_s}/f_D	1.1783(16)	$N_f = 2+1+1$ [77]
$\zeta(\Lambda_p \to p\mu^-\bar{\nu}_\mu)_{q^2>15}/\zeta(\Lambda_p \to \Lambda_c\mu^-\bar{\nu}_\mu)_{q^2>7}$	$1.471 \pm 0.096 \pm 0.290$	[2]
B_{B_s}	$1.327 \pm 0.016 \pm 0.030$	[77]
B_{B_s}/B_{B_d}	$1.007 \pm 0.013 \pm 0.014$	$N_f = 2$ [77]
$\bar{m}_c(m_c)$	$1.2982 \pm 0.0013 \pm 0.0120$ GeV	[2]
$\bar{m}_t(m_t)$	$(165.26 \pm 0.11 \pm 0.30$ GeV	[2]
η_{tt}	$0.402 \pm 0 \pm 0.007$	[2]
η_{ut}	$0.55 \pm 0 \pm 0.024$	[2]
$\eta_B(\bar{M}S)$	$0.5510 \pm 0 \pm 0.0022$	[2]

Table 5.4: List of aditional inputs for the CKM fit.

the fit values $\bar{\rho}$ and $\bar{\eta}$ are slightly higher than earlier. The best fit points for $\bar{\rho}$ is increased by 8% while that for $\bar{\eta}$ is about 5%. Primarily, these shifts are due to changes in the inputs of α, γ and $\sin 2\beta$ which have been updated from the previous 2019 inputs. Fig. 5.4 shows the single parameter profile-likelihoods for the global CKM fit with the most updated inputs and observables. This is the most updated best fit estimates of the CKM parameters.

5.4.3 CKM Fit including new physics

As mentioned earlier, due to the presence of the WC corresponding to the $V+A$ operator $\mathcal{O}_{V_2}$, the decay distribution of $P \to M^*\ell\nu_\ell$ decays will be modified unlike the alteration of the vertex CKM factor in case of the other $P \to M\ell\nu_\ell$ and $P \to \ell\nu_\ell$ decays. Hence, in order to perform the fit for the NP scenarios, we consider both the CKM observables listed in Table. 5.3 as well as the list of $B \to D^*\ell\bar{\nu}_\ell$ data mentioned in the previous subsection. Also, as mentioned earlier, we do not consider the inclusive determinations of $|V_{ub}|$ and $|V_{cb}|$ for the NP fit. The fit results are reported in Table. 5.6.

At first, we have presented the fit results of the analysis of $B \to D^*\ell\bar{\nu}_\ell$ alone in Table. 5.5. We are fitting $C_T = C_s^2 + C_p^2$ along with $|V_{cb}|$ and the BGL coefficients for three different masses M_S of the new scalar. In all three cases, the fitted values of the BGL coefficients are identical; hence we have presented in only one case. Note that because of the new contribution in the decay rate distribution, there is a small shift ($\approx 1.5\%$) in the best fit values of $|V_{cb}|$. However, the fitted values

Mass (TeV)	Fit Quality		Parameter	Fit Result
	χ^2/dof	p-Value		
0.5	53.21/44	16.09%	C_T	$0.107(401)$
			$\lvert V_{cb}\rvert$	$39.30(85) \times 10^{-3}$
			a_0^f	$0.0123(1)$
			a_1^f	$0.0228(96)$
			a_2^f	$-0.520(199)$
			a_0^g	$0.0316(10)$
			a_1^g	$-0.140(66)$
			a_2^g	$-0.40(159)$
			$a_1^{\mathcal{F}_1}$	$0.0020(17)$
			$a_0^{\mathcal{F}_2}$	$0.0513(13)$
			$a_1^{\mathcal{F}_2}$	$-0.149(60)$
			$a_2^{\mathcal{F}_2}$	$0.987(940)$
1.0	53.21/44	16.09%	C_T	$0.096(359)$
			$\lvert V_{cb}\rvert$	$39.30(79) \times 10^{-3}$
1.5	53.21/44	16.09%	C_T	$0.090(339)$
			$\lvert V_{cb}\rvert$	$39.30(85) \times 10^{-3}$

Table 5.5: Fit result for the frequentist analysis for different NP scenario with the same $B \to D^* \ell \bar{\nu}_\ell$ dataset as Table. 5.1.

Case		χ^2/dof	p-Value (%)	Fit Result				
				C_T	A	λ	$\bar{\rho}$	$\bar{\eta}$
No NP		87.2	6.9	–	0.79974 ± 0.00769	0.224982 ± 0.000293	0.17668 ± 0.00970	0.38651 ± 0.01186
NP	0.5 TeV	87.0	6.0	-0.090 ± 0.203	0.79952 ± 0.00770	0.224980 ± 0.000293	0.17723 ± 0.00979	0.38747 ± 0.01210
	1.0 TeV	85.9	7.0	-0.018 ± 0.016	0.79974 ± 0.00769	0.224975 ± 0.000293	0.17679 ± 0.00970	0.38673 ± 0.01187
	1.5 TeV	85.8	7.1	-0.0009 ± 0.0008	0.79979 ± 0.00769	0.224975 ± 0.000293	0.17667 ± 0.00970	0.38653 ± 0.01186

Table 5.6: Fit Results for the Wolfenstein parameters and C_T with and without NP. For the NP analyses, we have shown the results for three benchmark values of the mediator mass, $M_S = (0.5, 1.0, 1.5)$ TeV.

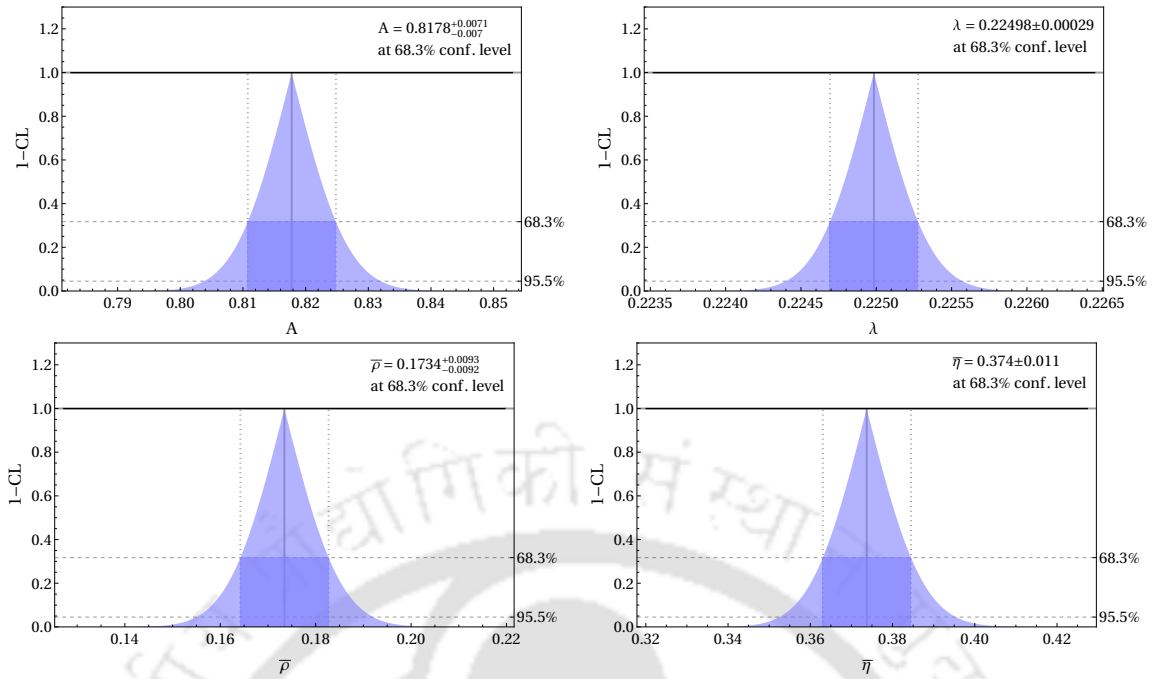

Figure 5.4: 1D profile-likelihoods for the CKM Wolfenstein parameters $A, \lambda, \bar{\rho}, \bar{\eta}$ for the global CKM 2021 Standard Model fit. The best fit estimates at 68.3% confidence level are mentioned in each case.

are consistent within 1-σ CI with the one obtained without any NP (Table. 5.1). As expected, we have obtained a zero consistent solution for C_T. However at the present level of precision, a relatively large value like $C_T \approx 0.5$ is allowed by the data.

In a second fit, we have included the data on $B \to D^* \ell \bar{\nu}_\ell$ alongside all the other data used in the CKM fit. The presence of a new contribution in $P \to M\ell\nu_\ell$ and $P \to \ell\nu_\ell$ decays modifies the CKM element to $|V'_{ij}| = |V_{ij}(1 \pm C_{V_2})|$ (with $C_{V_1} = 0$). In such cases, the measured values of the elements should be considered $|V'_{ij}|$ while $|V_{ij}|$ will be parametrized in terms of A, λ, $\bar{\rho}$ and $\bar{\eta}$. Here, in the expansion of V_{ij} we have considered terms up to order λ^8. The fit results are presented in Table. 5.6. We have analyzed the available data for three different values of M_S. Note that in the presence of NP, λ remains practically unchanged while the changes in A and $\bar{\rho}$ are in the fourth decimal places and that for $\bar{\eta}$ is at the third decimal place. For all the three values of M_S the allowed ranges of C_T is consistent with zero. For a value of M_S around 500 *GeV* C_T could be as large as ± 0.2 (at 1-σ CI). The negative values of C_T could be accomodated by introducing phases in C_s and C_p, for example, by the following replacements: $C_s \to e^{i\pi/2} C_s = iC_s$ and $C_p \to e^{i\pi/2} C_p = iC_p$[2]. The important point to note here is that for a relatively higher value of M_S ($\gtrsim 1.5$ TeV), the allowed range of C_T is becoming close to zero and $|C_T| \lesssim 0.0017$. This indicates that a very high value of M_S will be discared by the data under consideration.

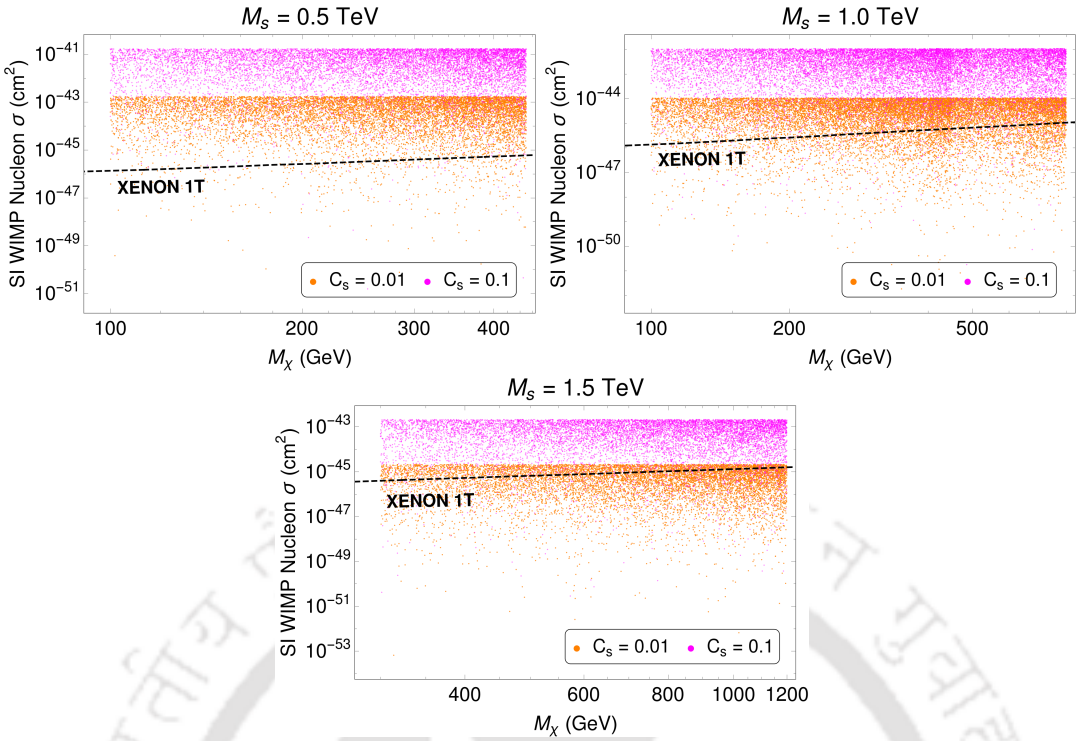

Figure 5.5: The spin independent scattering cross-section is plotted against the dark matter mass for the three values of M_S and two values of C_s. Also C_s' has been varied in the range $[0.0, 0.5]$. The black dashed line is the upper limit on the cross-section from the XENON-1T experiment [18].

5.4.4 DM phenomenology

We point out the main results of the DM phenomenology in this section. In order to generate the parameter space we work in the basis of C_s and C_T. Hence, for a fixed value of C_s, the allowed values of C_p can be inferred from the best fit estimates of C_T as tabulated in 5.6. For simplicity, we only consider the positive allowed solutions for C_T in the 2σ range of the best fit estimate for the DM analysis. Since the CKM data has already put significant bounds on the above couplings, the DM vertex factors C_s', C_p' might have very less freedom from the relic and DD data.

For non-zero values of the scalar couplings C_s, C_s', the spin-independent direct detection (SIDD) bounds will play a crucial role in constraining their upper limits. In order to estimate the allowed ranges of these scalar portal couplings, we plot the direct detection cross-section as a function of DM mass for $M_S = 0.5, 1.0$ and 1.5 TeV respectively as shown in Fig. 5.5. To check the DD bound on the scalar couplings, for each value of M_S, we plot the SIDD for two specific values of C_s, as shown in the plot legends, while varying the other relevant coupling C_s' in $[0.0, 0.5]$. The coupling C_p' has no role to play in the SI cross section and so, without loss of generality, we set it to zero while scanning the parameter space, while C_p is varied within the allowed range of C_T for a fixed heavy scalar mass. From the three plots shown in Fig. 5.5, we find that $C_s = 0.1$ can be easily ruled out by the SIDD upper bound constraint (shown in black dashed line) for $M_S < 1(\text{TeV})$. It will be safe to consider $C_s = 0.01$ in all three cases, although the parameter space is still quite restricted

[2]In principle, one can consider C_s and C_p to be complex with the respective phases as unknowns which can be constrained from the data on mixing. We did not explore that possibility which we will keep for a future work. Also, it is to be noted that our NP scenario have negligible impacts on $K - \bar{K}$ or $B_q - \bar{B}_q$ (q =d,s) mixing.

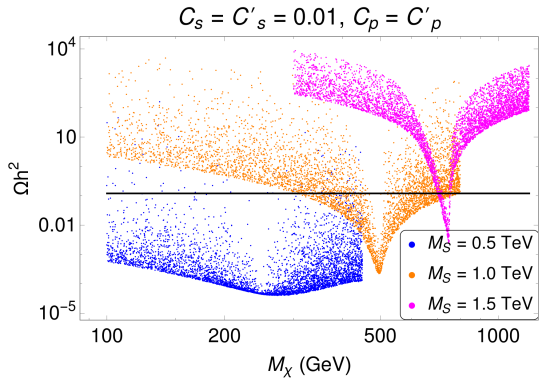

Figure 5.6: Here we plot the relic abundance as a function of the DM mass for the three values of M_S, as denoted by the blue, orange and magenta points, when C_p is varied in its allowed range and C'_p is taken to be same as C_p. See text for more details.

for $M_S = 0.5$ TeV. Since the SIDD cross-section also increases with increasing values of C'_s, very large values will not be allowed from the data. As a conservative estimate, we fix both C_s and C'_s at a value 0.01 for the subsequent plots.

Once the bound on the scalar couplings is obtained, it is easier to check for the allowed regions of the pseudoscalar coupling from the relic data. In Fig. 5.6, we show the variation of the relic abundance with the DM mass for $M_S = 0.5, 1.0$ and 1.5 TeV, in blue, orange and magenta points respectively, for the scenario $C_p = C'_p = \sqrt{C_T - C_s^2}$. Therefore the scan ranges for the different mediator masses are :

$$C_p \in [0, 0.55], \text{ for } \mathrm{M_s} = 0.5 \text{ TeV} \tag{5.30}$$

$$C_p \in [0, 0.10], \text{ for } \mathrm{M_s} = 1.0 \text{ TeV} \tag{5.31}$$

$$C_p \in [0, 0.02], \text{ for } \mathrm{M_s} = 1.5 \text{ TeV} \tag{5.32}$$

The black solid line signifies the Planck allowed present day relic abundance of DM. From the scans, we find that the correct relic is satisfied for a wide range of DM masses much away from resonance region for lower values of M_S. As we increase the mass, the parameter space gets confined to the resonance region only.

We have also investigated the case : $C_p \neq C'_p$. We find out the allowed parameter space which satisfy the relic and DD bounds. For three different masses, the correlation between C'_p and M_χ are shown in Fig. 5.7 with scattered red points. To generate these plots, we vary C'_p within the range $[0, 0.5]$ and C_p is constrained by the bound of C_T (Eqn. 5.32) while we fix C_s and C'_s to a low value as discussed above. With the increasing values of M_S, to explain the bounds, we need relatively larger values of C'_p since C_p is much more restricted in such cases (from flavour data). For $M_S = 0.5$ TeV, only low values of C'_p is favoured as can be seen from Fig. 5.8. In all the cases, we obtain solutions in a large range of DM masses.

We also explore the case $C_s = C_p$, with $C_s = 0.001$ for $M_S = 0.5$ TeV and $C_s = 0.01$ for $M_S = 1$ and 1.5 TeV. The results are shown in Fig. 5.7 with scattered blue points. Like before, we vary C'_p in the range $[0, 0.5]$. Note that in this particular case, it will be hard to satisfy the relic and DD

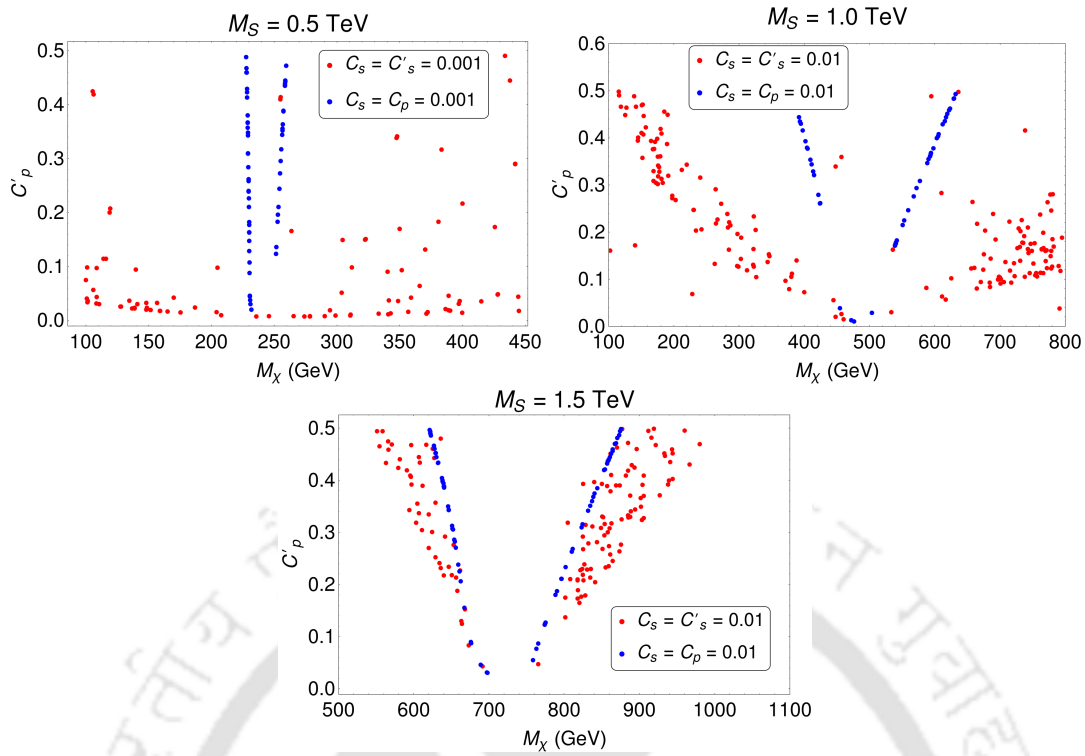

Figure 5.7: In the above plots we scan the parameter space of C'_p and M_χ for the different choices of the other couplings as shown by the point legends. Both the blue and red points satisfy the constraints from relic and DD bounds.

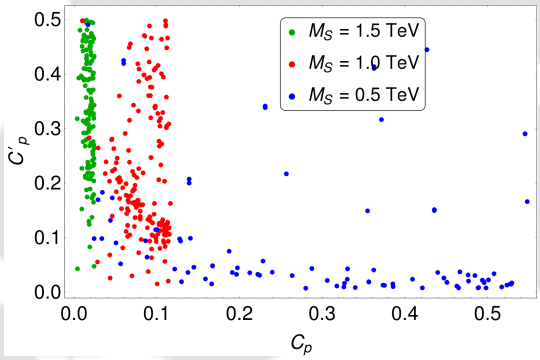

Figure 5.8: The plot shows the correlations between C_p and C'_p for the relic and DD satisfied parameter space for three different values of M_S.

bounds with $C'_p = C'_s$. For all the three masses, we find that the parameter space shrinks to the resonance region irrespective of the value of C'_p when both C_s and C_p are fixed to very low values.

5.5 Summary

In this chapter we have considered a simple fermionic dark matter scenario whose interactions with the SM is mediated by a heavy neutral scalar. There is no symmetry to forbid the interactions of the SM quarks to this new scalar. Hence, it will contribute to the charged current vertices of $\bar{d}_i u_j W$ at one loop level. The modifications to the $P \to M$ and $P \to M^*$ transitions due to the new interactions are quite contrasting. In case of the leptonic $P \to \ell\nu_\ell$ and semileptonic $P \to M$ decays, the vertex factors will be altered while in case of the $P \to M^*$ semileptonic decays,

the q^2 decay distribution itself is modified. As a recent developement, lattice results on the form factors of the $B \to D^* \ell \nu_\ell$ decay at non-zero recoil are now available. Therefore we update the SM prediction of the CKM element $|V_{cb}|$ before incorporating the new physics effects. We obtain $|V_{cb}| = 38.69(79) \times 10^{-3}$ at 68% CL.

With this new update and all other available CKM measurements, we perform a global fit in presence of the new physics effects for some fixed values of the mediator mass. From this fit, we are only able to constrain the combination C_T and not the individual couplings C_s, C_p. We show that for high values of M_S, the coupling gets very severely constrained from the data. From the dark matter SIDD constraints, we are able to restrict the scalar couplings C_s and C_s' to very small values $\sim \mathcal{O}(0.01)$. This automatically translates to a bound on the parameter C_p from out fit results on C_T. However, since the pseudoscalar couplings have velocity suppressed contribution to the spin-dependent DD cross-section, there remains some freedom in C_p'.

Chapter 6

Summary and Outlook

We understand that dark matter exists in copious amounts in our Universe, which the SM of particle physics fails to address. Therefore, it is essential to introduce new degrees of freedom in the particle content that will not only solve the dark matter problem, but also provide a solution to other pertaining questions in particle physics. As discussed in the literature, there are multiple ways of tackling this issue from a model builder's point of view. Since we do not know the exact properties of the dark matter, one can formulate dark matter models with scalars, fermions or even vector bosons. In this thesis, for example, we consider scenarios with scalar and fermionic dark matter. Due to the null results from direct detection dark matter searches, we also do not have any idea about the probable mass of DM particles. Hence, physicists have explored dark matter masses spanning a range from $\sim 10^{-13}$ GeV$/c^2$ (eg., axion dark matter) to as large as $\sim 10^{19}$ GeV$/c^2$ (for primordial black holes as DM candidates). In general, the WIMP like scenarios have been predominantly studied due to its easy accessibility in present experimental probes (both direct and collider searches). However, new physics models that introduce a dark matter candidate at the weak scale, can often have contributions to certain low energy flavour physics observables due to the interactions of the DM with SM particles. This opens up a whole new possibility of finding indirect signatures of dark matter physics in flavour experiments complementary to the more conventional probes of dark matter.

From the quark flavour physics perspective, we are currently in the precision era where scientists are constantly trying to make more and more precise measurements with large statistics. There has also been tremendous progress in the theoretical understanding of hadronic parameters such as form factors, decay constants, bag factors etc. from lattice simulations. Therefore this wealth of accurate and statistically significant flavour data help us to disentangle the NP contributions to observables from the SM ones, thereby putting stringent constraint on new physics models. There is a plethora of various dark matter models in literature, most of which do not take into account such low energy flavour constraints in their analyses. In this thesis, we have highlighted how flavour physics data can have significant influence on the parameter space of single component WIMP-like dark matter models.

Interestingly, while some decays restrict the parameter space of new models, some decay modes

also give us probable hints of new physics. For example, the LFUV observables $R_{K^{(*)}}$, corresponding to the semileptonic FCNC decay $b \to s\ell^+\ell^-$, deviates significantly from its SM prediction. It could be exceedingly possible that such deviations could arise due to family non-universal interactions of WIMPs with the SM fermions. In the thesis, we have not only constructed a model with lepton family dependent couplings in order to resolve the discrepancies, but also shown how the degree of non-universality is related to triangle anomaly cancellation requirements of gauged $U(1)$ models. In the process, we also achieved a natural gateway to small neutrino masses and unconventional collider signals in some cases which can be pursued by experimentalists to validate our proposals. Although the flavour anomalies are not strong enough to conclude the presence of newer degrees of freedom, there is a hope that this anomaly would not be easily washed out in the near future since it has been there for a very long time. More data from Belle-II, the future upgrade of Belle, could shed light on the fate of the LFUV ratios. We have also made specific predictions to few exclusive and inclusive B-decays to invisible final states which could be useful to provide missing links to the study of both neutrinos as well as dark matter. Therefore it is important to put significant effort on these modes from both experimental and theoretical point of view.

In the last part of the thesis we have explicitly shown the bounds on general scalar and pseudoscalar couplings of a heavy spin-0 mediators of DM interactions from CKM measurements. During the process, we have also been able to produce state of the art results on the global Unitarity Triangle fit in the SM as well as the above new physics scheme. The study could be well extended to spin-1 mediators as well which would allow us to restrict the vector and axial-vector couplings to the dark sector in a similar fashion as done for the spin-0 case.

In the thesis, we mostly pay attention to the single component WIMP type DM scenarios. However, there is no reason to believe that the total abundance of dark matter in the Universe is made up of only one type of species. There are several BSM proposals that succesfully address the dark matter problem using multipartite scenarios. Such models are especially motivated from the absence of observable signals at direct detection experiments. Once again, phenomenologists have overlooked the flavour constraints while performing their analysis. Therefore the studies presented in this thesis could be well extended to the multi-component dark matter models as well.

Flavour physics has played an essential/indirect role in many discoveries in particle physics. We have reached a precision era and can measure a lot of observables with an accuracy of 1%. In the long run, more precise measurements are expected from Belle-II and LHCb in the near future. Progress from the theory is in place and more expected. Keeping in mind the difficulties in collider searches, the first hint of new degrees of freedom may come from flavour data. Also, such a wealth of precise data will be beneficial to constrain the parameter spaces of a variety of NP models.

Appendix A

Renormalization Group (RG) Analysis

In this section we provide the one loop and two loop RG evolution equations for the SM and NP Yukawa and gauge couplings for the models discussed in Chapter. 3.

The RG equations can be in general written as :

$$\frac{d\lambda}{d\mu} \equiv \beta_\lambda = \beta_\lambda^I + \beta_\lambda^{II} \tag{A.1}$$

where λ is any arbitrary coupling, μ is the energy scale and $\beta^{I(II)}$ is the one(two)-loop beta function.

A.1 One-Loop RG Requations

In this section we present the one-loop RG evolution equations for the gauge, quartic and Yukawa couplings.

The evolution of the gauge couplings are given by :

$$(4\pi)^2\beta_{g_s}^I = -6g_s^3, \quad (4\pi)^2\beta_g^I = -3g^3, \quad (4\pi)^2\beta_{g_1}^I = +\frac{35}{3}g_1^3 \tag{A.2}$$

where, g_s, g and g_1 are the SU(3), SU(2) and U(1) gauge couplings respectively.

The RG equations for the quartic couplings are given by :

$$\begin{aligned}
(4\pi)^2\beta_{\lambda_1}^I &= -24Y_t^2Y_b^2 - 12Y_b^4 - 12Y_t^4 + 4\lambda_3^2 + 2\lambda_4^2 + 2\lambda_5^2 + 12\lambda_1^2 + 4\lambda_3\lambda_4 - 3\lambda_1 g_1^2 \\
&\quad - 9\lambda_1 g^2 + \frac{3g_1^4}{4} + \frac{9g^4}{4} + \frac{3}{2}g^2g_1^2 - 4Y_\tau^4 + 4\lambda_1 Y_\tau^2, \\
(4\pi)^2\beta_{\lambda_2}^I &= -12\lambda_b^2 + 2\lambda_4^2 + 2\lambda_5^2 - 4\lambda_\mu^4 - 4\lambda_\tau^4 - 8\lambda_\mu^2\lambda_\tau^2 + 12\lambda_2^2 + 4\lambda_3^2 + 4\lambda_3\lambda_4 + 4\lambda_2\lambda_\mu^2 \\
&\quad + 4\lambda_2\lambda_\tau^2 + \frac{3g_1^4}{4} + \frac{9g^4}{4} + \frac{3}{2}g^2g_1^2 - 3\lambda_2 g_1^2 - 9\lambda_2 g^2 + 12\lambda_2\lambda_b^2, \\
(4\pi)^2\beta_{\lambda_3}^I &= +4\lambda_3^2 + 2\lambda_4^2 + 2\lambda_5^2 + 2\lambda_1\lambda_4 + 2\lambda_2\lambda_4 + 6\lambda_1\lambda_3 + 6\lambda_2\lambda_3 + \frac{3g_1^4}{4} + \frac{9g^4}{4} - \frac{3}{2}g^2g_1^2 \\
&\quad - 9\lambda_3 g^2 - 3\lambda_3 g_1^2 + 2\lambda_3 Y_\tau^2 + 2\lambda_3\lambda_\mu^2 + 2\lambda_3\lambda_\tau^2 + 6\lambda_3 Y_b^2 + 6\lambda_3 Y_t^2 + 6\lambda_3\lambda_b^2,
\end{aligned} \tag{A.3}$$

$$
\begin{aligned}
(4\pi)^2\beta^I_{\lambda_5} =& + 2\lambda_1\lambda_5 + 2\lambda_2\lambda_5 + 8\lambda_3\lambda_5 + 12\lambda_3\lambda_5 - 9\lambda_5 g^2 - 3\lambda_5 g_1^2 + 2\lambda_5 Y_\tau^2 + 2\lambda_5\lambda_\mu^2 \\
&+ 2\lambda_5\lambda_\tau^2 + 6\lambda_5 Y_b^2 + 6\lambda_5 Y_t^2 + 6\lambda_5\lambda_b^2, \\
(4\pi)^2\beta^I_{\lambda_{45}} =& - 12\lambda_b^2 Y_b^2 - 12\lambda_b^2 Y_t^2 + 4\lambda_4^2 + 8\lambda_5^2 - 4\lambda_\mu^2 Y_\tau^2 - 4\lambda_\tau^2 Y_\tau^2 + 2\lambda_1\lambda_4 + 2\lambda_1\lambda_5 - 9\lambda_4 g^2 \\
&- 3\lambda_4 g_1^2 - 9\lambda_5 g^2 - 3\lambda_5 g_1^2 + 2\lambda_2\lambda_4 + 2\lambda_2\lambda_5 + 2\lambda_4 Y_\tau^2 + 2\lambda_4\lambda_\mu^2 + 2\lambda_4\lambda_\tau^2 + 2\lambda_5 Y_\tau^2 \\
&+ 2\lambda_5\lambda_\mu^2 + 2\lambda_5\lambda_\tau^2 + 3g_1^2 g^2 + 6\lambda_4 Y_t^2 + 6\lambda_4 Y_b^2 + 6\lambda_4\lambda_b^2 + 6\lambda_5 Y_t^2 + 6\lambda_5 Y_b^2 + 6\lambda_5\lambda_b^2 \\
&+ 8\lambda_3\lambda_4 + 8\lambda_3\lambda_5 + 12\lambda_4\lambda_5.
\end{aligned}
$$

where $\lambda_{45} = \lambda_4 + \lambda_5$.

The RG equations for the Yukawa couplings are given by :

$$
\begin{aligned}
(4\pi)^2\beta^I_{Y_t} =& Y_t\left(\frac{1}{2}\lambda_b^2 + \frac{9}{2}Y_b^2 + \frac{9}{2}Y_t^2 + Y_\tau^2 - 8g_s^2 - \frac{9}{4}g^2 - \frac{5}{12}g_1^2\right), \\
(4\pi)^2\beta^I_{Y_b} =& Y_b\left(\frac{1}{2}\lambda_b^2 + \frac{9}{2}Y_b^2 + \frac{9}{2}Y_t^2 + Y_\tau^2 - 8g_s^2 - \frac{9}{4}g^2 - \frac{17}{12}g_1^2\right), \\
(4\pi)^2\beta^I_{Y_\tau} =& Y_\tau\left(\frac{1}{2}\lambda_\mu^2 + \frac{1}{2}\lambda_\tau^2 + 3Y_b^2 + 3Y_t^2 + \frac{5}{2}Y_\tau^2 - \frac{9}{4}g^2 - \frac{15}{4}g_1^2\right), \\
(4\pi)^2\beta^I_{\lambda_b} =& \lambda_b\left(\frac{9}{2}\lambda_b^2 + \frac{1}{2}Y_b^2 + \frac{1}{2}Y_t^2 + \lambda_\mu^2 + \lambda_\tau^2 - 8g_s^2 - \frac{9}{4}g^2 - \frac{5}{12}g_1^2\right), \\
(4\pi)^2\beta^I_{\lambda_\mu} =& \lambda_\mu\left(\frac{5}{2}\lambda_\mu^2 + \frac{5}{2}\lambda_\tau^2 + 3\lambda_b^2 + \frac{1}{2}Y_\tau^2 - \frac{9}{4}g^2 - \frac{15}{4}g_1^2\right), \\
(4\pi)^2\beta^I_{\lambda_\tau} =& \lambda_\tau\left(\frac{5}{2}\lambda_\mu^2 + \frac{5}{2}\lambda_\tau^2 + 3\lambda_b^2 + \frac{1}{2}Y_\tau^2 - \frac{9}{4}g^2 - \frac{15}{4}g_1^2\right).
\end{aligned}
\tag{A.4}
$$

A.2 Two Loop RG Equations

The two loop RG equations for the SM gauge couplings are given by:

$$
\begin{aligned}
\beta^{II}_{g_s} &= \frac{g_s^3}{(4\pi)^4}\left(-7g_s^2 - 2Y_b^2 - 2Y_t^2 + \frac{13}{6}g_1^2 + \frac{9}{2}g^2 - 2\lambda_b^2\right), \\
\beta^{II}_{g} &= \frac{g^3}{(4\pi)^4}\left(8g^2 + 2g_1^2 + 12g_s^2 - \frac{3}{2}Y_b^2 - \frac{3}{2}Y_t^2 - \frac{3}{2}\lambda_b^2 - \frac{1}{2}Y_\tau^2 - \frac{1}{2}\lambda_\mu^2 - \frac{1}{2}\lambda_\tau^2\right), \\
\beta^{II}_{g_1} &= \frac{g_1^3}{(4\pi)^4}\left(\frac{214}{9}g_1^2 + 6g^2 + \frac{52}{3}g_s^2 - \frac{17}{6}Y_b^2 - \frac{5}{6}Y_t^2 - \frac{5}{2}Y_\tau^2 - \frac{5}{2}\lambda_\mu^2 - \frac{5}{2}\lambda_\tau^2 - \frac{5}{6}\lambda_b^2\right).
\end{aligned}
\tag{A.5}
$$

The two loop RG equations for the SM Yukawa couplings are given by :

$$
\begin{aligned}
\beta^{II}_{Y_t} = \frac{Y_t}{(4\pi)^4}\Bigg(& - 12Y_t^4 - 12Y_b^4 - 24Y_b^2Y_t^2 - \frac{5}{2}Y_b^2\lambda_b^2 - \frac{5}{2}Y_t^2\lambda_b^2 - \frac{5}{2}\lambda_b^4 + \lambda_3^2 + \lambda_4^2 + \lambda_3\lambda_4 + \frac{3}{2}\lambda_1^2 \\
& + \frac{3}{2}\lambda_5^2 - 6\lambda_1 Y_b^2 - 6\lambda_1 Y_t^2 - 4\lambda_4\lambda_b^2 - 2\lambda_3\lambda_b^2 + 16g_s^2Y_b^2 + 16g_s^2Y_t^2 - \frac{304}{3}g_s^4 - \frac{47}{72}g_1^4 \\
& - \frac{21}{4}g^4 - \frac{9}{4}Y_\tau^2Y_b^2 - \frac{9}{4}Y_\tau^2Y_t^2 - \frac{9}{4}Y_\tau^4 - \frac{3}{4}\lambda_\mu^2\lambda_b^2 - \frac{3}{4}\lambda_\tau^2\lambda_b^2 - \frac{3}{4}Y_\tau^2\lambda_\mu^2 - \frac{3}{4}Y_\tau^2\lambda_\tau^2 \\
& + \frac{16}{3}g_s^2\lambda_b^2 + \frac{29}{16}g_1^2Y_b^2 + \frac{33}{16}g^2\lambda_b^2 + \frac{135}{16}g^2Y_b^2 + \frac{135}{16}g^2Y_t^2 + \frac{187}{48}g_1^2Y_t^2 + \frac{247}{144}g_1^2\lambda_b^2 \\
& + 9g^2g_s^2 + 20g_s^2Y_b^2 + 20g_s^2Y_t^2 - \frac{9}{4}g_1^2g^2 + \frac{15}{8}g^2Y_\tau^2 + \frac{25}{8}g_1^2Y_\tau^2 + \frac{25}{24}g_1^2Y_t^2 + \frac{31}{9}g_1^2g_s^2 \\
& + \frac{45}{8}g^2Y_b^2 + \frac{45}{8}g^2Y_t^2 + \frac{85}{24}g_1^2Y_b^2\Bigg),
\end{aligned}
$$

$$\beta^{II}_{Y_b} = \frac{Y_b}{(4\pi)^4}\Bigg(- 12Y_b^4 - 12Y_t^4 - 24Y_b^2Y_t^2 - \frac{5}{2}\lambda_b^2Y_b^2 - \frac{5}{2}\lambda_b^2Y_t^2 - \frac{5}{2}\lambda_b^4 + \lambda_3^2 + \lambda_4^2 + \lambda_3\lambda_4 + \frac{3}{2}\lambda_1^2 + \frac{3}{2}\lambda_5^2$$
$$- 6\lambda_1Y_b^2 - 6\lambda_1Y_t^2 - 4\lambda_4\lambda_b^2 - 2\lambda_3\lambda_b^2 + 16g_s^2Y_b^2 + 16g_s^2Y_t^2 - \frac{304}{3}g_s^4 - \frac{41}{144}g_1^2\lambda_b^2 - \frac{21}{4}g^4$$
$$- \frac{9}{4}Y_\tau^2Y_b^2 - \frac{9}{4}Y_\tau^2Y_t^2 - \frac{9}{4}Y_\tau^4 - \frac{3}{4}\lambda_\mu^2\lambda_b^2 - \frac{3}{4}\lambda_\tau^2\lambda_b^2 - \frac{3}{4}\lambda_\mu^2Y_\tau^2 - \frac{3}{4}\lambda_\tau^2Y_\tau^2 + \frac{16}{3}g_s^2\lambda_b^2 + \frac{33}{16}g^2\lambda_b^2$$
$$+ \frac{35}{48}g_1^2Y_t^2 + \frac{135}{16}g^2Y_b^2 + \frac{135}{16}g^2Y_t^2 + \frac{223}{48}g_1^2Y_b^2 + 9g^2g_s^2 + 20g_s^2Y_b^2 + 20g_s^2Y_t^2 + \frac{77}{8}g_1^4$$
$$- \frac{3}{4}g_1^2g^2 + \frac{15}{8}g^2Y_\tau^2 + \frac{19}{9}g_1^2g_s^2 + \frac{25}{8}g_1^2Y_\tau^2 + \frac{25}{24}g_1^2Y_t^2 + \frac{45}{8}g^2Y_b^2 + \frac{45}{8}g^2Y_t^2 + \frac{85}{24}g_1^2Y_b^2\Bigg),$$

$$\beta^{II}_{Y_\tau} = \frac{Y_\tau}{(4\pi)^4}\Bigg(- \frac{3}{4}Y_\tau^4 - \lambda_\mu^2Y_\tau^2 - \lambda_\tau^2Y_\tau^2 - 2\lambda_\mu^2\lambda_\tau^2 - \lambda_\mu^4 - \lambda_\tau^4 + \lambda_3^2 + \lambda_4^2 + \lambda_3\lambda_4 + \frac{3}{2}\lambda_1^2 + \frac{3}{2}\lambda_5^2 - 6\lambda_1Y_\tau^2 - 4\lambda_4\lambda_\mu^2$$
$$- 4\lambda_4\lambda_\tau^2 - 2\lambda_3\lambda_\mu^2 - 2\lambda_3\lambda_\tau^2 - \frac{27}{2}Y_t^2Y_b^2 - \frac{27}{4}Y_b^2Y_\tau^2 - \frac{27}{4}Y_t^2Y_\tau^2 - \frac{27}{4}Y_t^4 - \frac{27}{4}Y_b^4\frac{21}{4}g^4 - \frac{9}{4}\lambda_b^2Y_b^2$$
$$- \frac{9}{4}\lambda_b^2Y_t^2 + \frac{33}{16}g^2\lambda_\mu^2 + \frac{33}{16}g^2\lambda_\tau^2 + \frac{103}{16}g_1^2\lambda_\mu^2 + \frac{103}{16}g_1^2\lambda_\tau^2 + \frac{129}{16}g_1^2Y_\tau^2 + \frac{135}{16}g^2Y_\tau^2 + \frac{791}{24}g_1^4$$
$$+ 20g_s^2Y_b^2 + 20g_s^2Y_t^2 + \frac{9}{4}g_1^2g^2 + \frac{15}{8}g^2Y_\tau^2 + \frac{25}{8}g_1^2Y_\tau^2 + \frac{25}{24}g_1^2Y_t^2 + \frac{45}{8}g^2Y_b^2 + \frac{45}{8}g^2Y_t^2 + \frac{85}{24}g_1^2Y_b^2\Bigg). \tag{A.6}$$

Appendix B

Orthogonal Rotation Matrices

Here, we supply the most general forms of real orthogonal rotation matrices of dimensions 3 and 4. These matrices have been extensively used in Chapter. 4 and useful for the discussions related to the mixings of scalar fields.

B.1 3×3 Rotation Matrix

A 3×3 orthogonal rotation matrix can be defined as

$$\mathcal{O} = \begin{pmatrix} c_{\alpha_{12}} c_{\alpha_{13}} & s_{\alpha_{12}} c_{\alpha_{13}} & s_{\alpha_{13}} \\ -s_{\alpha_{12}} c_{\alpha_{23}} - c_{\alpha_{12}} s_{\alpha_{23}} s_{\alpha_{13}} & c_{\alpha_{12}} c_{\alpha_{23}} - s_{\alpha_{12}} s_{\alpha_{23}} s_{\alpha_{13}} & s_{\alpha_{23}} c_{\alpha_{13}} \\ s_{\alpha_{12}} s_{\alpha_{23}} - c_{\alpha_{12}} c_{\alpha_{23}} s_{\alpha_{13}} & -c_{\alpha_{12}} s_{\alpha_{23}} - s_{\alpha_{12}} c_{\alpha_{23}} s_{\alpha_{13}} & c_{\alpha_{23}} c_{\alpha_{13}} \end{pmatrix} \tag{B.1}$$

where $c_{\alpha_{ij}} \equiv \cos \alpha_{ij}$ and $s_{\alpha_{ij}} \equiv \sin \alpha_{ij}$.

B.2 4×4 Rotation Matrix

The components of a general 4×4 real orthogonal matrix without phase are given by :

$$\begin{aligned} \mathcal{R}_{11} &= c_{12} c_{13} c_{14}, \\ \mathcal{R}_{12} &= c_{13} c_{14} s_{12}, \\ \mathcal{R}_{13} &= c_{14} s_{13}, \\ \mathcal{R}_{14} &= s_{14}, \\ \mathcal{R}_{21} &= -c_{23} c_{24} s_{12} - c_{12} c_{24} s_{13} s_{23} - c_{12} c_{13} s_{14} s_{24}, \\ \mathcal{R}_{22} &= c_{12} c_{23} c_{24} - c_{24} s_{12} s_{13} s_{23} - c_{13} s_{12} s_{14} s_{24}, \\ \mathcal{R}_{23} &= c_{13} c_{24} s_{23} - s_{13} s_{14} s_{24}, \\ \mathcal{R}_{24} &= c_{14} s_{24}, \end{aligned} \tag{B.2}$$

$$\mathcal{R}_{31} = -c_{12}c_{23}c_{34}s_{13} + c_{34}s_{12}s_{23} - c_{12}c_{13}c_{24}s_{14}s_{34} + c_{23}s_{12}s_{24}s_{34} + c_{12}s_{13}s_{23}s_{24}s_{34},$$

$$\mathcal{R}_{32} = -c_{12}c_{34}s_{23} + s_{12}(-c_{13}c_{24}s_{14} + s_{13}s_{23}s_{24})s_{34} - c_{23}(c_{34}s_{12}s_{13} + c_{14}s_{24}s_{34}),$$

$$\mathcal{R}_{33} = c_{13}c_{23}c_{34} - c_{24}s_{13}s_{14}s_{34} - c_{13}s_{23}s_{24}s_{34},$$

$$\mathcal{R}_{34} = c_{14}c_{24}s_{34},$$

$$\mathcal{R}_{41} = -c_{12}c_{13}c_{24}c_{34}s_{14} + c_{12}s_{13}(c_{34}s_{23}s_{24} + c_{23}s_{34}) + s_{12}(c_{23}c_{34}s_{24} - s_{23}s_{34}),$$

$$\mathcal{R}_{42} = -c_{13}c_{24}c_{34}s_{12}s_{14} + s_{12}s_{13}(c_{34}s_{23}s_{24} + c_{23}s_{34}) + c_{12}(-c_{23}c_{34}s_{24} + s_{23}s_{34}),$$

$$\mathcal{R}_{43} = -c_{24}c_{34}s_{13}s_{14} - c_{13}(c_{34}s_{23}s_{24} + c_{23}s_{34}),$$

$$\mathcal{R}_{44} = c_{14}c_{24}c_{34}.$$

where $s_{ij} \equiv \sin \alpha_{ij}$ and $c_{ij} \equiv \cos \alpha_{ij}$.

Appendix C

Useful Coupling Constants

In this section, we summarize the useful coupling constants appearing in the Toy models discussed in Chapter. 4 in terms of the parameters of interest such as the physical masses, vacuum expectation values and mixing angles.

C.1 Coupling Constants : Toy Model I

The coupling constants relevant for Toy Model I are

$$
\begin{aligned}
\lambda_1 &= \frac{c_{\alpha_2}^2(c_{\alpha_1}^2 M_h^2 + M_{s_1}^2 s_{\alpha_1}^2) + M_{s_2}^2 s_{\alpha_2}^2}{v^2}, \\
\lambda_3 &= \frac{2(\lambda_L v^2 + M_{H^\pm}^2 - M_{H^0}^2)}{v^2}, \\
\lambda_4 &= \left(\frac{M_{H^0}^2 + M_{A^0}^2 - 2M_{H^\pm}^2}{v^2}\right) \\
\lambda_5 &= \left(\frac{M_{H^0}^2 - M_{A^0}^2}{v^2}\right), \\
\lambda_6 &= \frac{1}{v_1^2}\left(c_{\alpha_2}^2 M_{s_2}^2 s_{\alpha_3}^2 + M_h^2(c_{\alpha_3}\, s_{\alpha_1} + c_{\alpha_1}\, s_{\alpha_2}\, s_{\alpha_3})^2 + M_{s_1}^2(c_{\alpha_1}\, c_{\alpha_3} - c_{\alpha_1}\, s_{\alpha_2}\, s_{\alpha_3})^2\right), \\
\lambda_7 &= \frac{1}{v_2^2}\Bigg(c_{\alpha_3}^2(c_{\alpha_2}^2 M_{s_2}^2 + (c_{\alpha_1}^2 M_h^2 + M_{s_1}^2 s_{\alpha_1}^2)s_{\alpha_2}^2) + (c_{\alpha_1}^2 M_{s_1}^2 + M_h^2 s_{\alpha_1}^2)s_{\alpha_3}^2 \\
&\quad + 2c_{\alpha_1}\, c_{\alpha_3}(-M_h^2 + M_{s_1}^2)s_{\alpha_1}\, s_{\alpha_2}\, s_{\alpha_3}\Bigg) - \frac{M_{A_2}^2 s_\gamma^2 v_1^2}{4v_2^4}, \\
\lambda_8 &= \frac{1}{v_1 v_2}\Bigg(c_{\alpha_1}^2\, c_{\alpha_3}(-M_{s_1}^2 + M_h^2 s_{\alpha_2}^2)s_{\alpha_3} + c_{\alpha_3}(c_{\alpha_2}^2 M_{s_2}^2 + s_{\alpha_1}^2(-M_h^2 + M_{s_1}^2 s_{\alpha_2}^2))s_{\alpha_3} \\
&\quad + c_{\alpha_1}\, s_{\alpha_1}\, s_{\alpha_2}(M_h^2 - M_{s_1}^2)(c_{\alpha_3}^2 - s_{\alpha_3}^2)\Bigg) + \frac{M_{A_2}^2 s_\gamma^2}{2v_2^2}, \\
\lambda_{\varphi_1} &= \frac{1}{v_1 v}\left(c_{\alpha_1}\, c_{\alpha_2}\, c_{\alpha_3}\, s_{\alpha_1}(-M_h^2 + M_{s_1}^2) + c_{\alpha_2}\, s_{\alpha_2}\, s_{\alpha_3}(-c_{\alpha_1}^2 M_h^2 + M_{s_2}^2 + s_{\alpha_1}^2 M_{s_1}^2)\right), \\
\lambda_{\varphi_2} &= \frac{1}{v_2 v}\left(c_{\alpha_2}\, c_{\alpha_3}\, s_{\alpha_2}(-c_{\alpha_1}^2 M_h^2 + M_{s_2}^2 - s_{\alpha_1}^2 M_{s_1}^2) + c_{\alpha_1}\, c_{\alpha_2}\, s_{\alpha_1}\, s_{\alpha_3}(M_h^2 - M_{s_1}^2)\right), \\
\delta &= -\left(\frac{M_{A_2}^2 s_\gamma^2}{2\sqrt{2}v_2}\right).
\end{aligned}
\tag{C.1}
$$

C.2 Coupling Constants : Toy Model II

The couplings relevant for Toy Model II are given by :

$$
\begin{aligned}
\lambda_{H_1} &= \frac{c_\alpha^2(c_{\alpha_3}^2(c_{\alpha_2}^2 M_h^2 + M_{s_1}^2 s_{\alpha_2}^2) + M_{s_2}^2 s_{\alpha_3}^2) + M_{H^0}^2 s_\alpha^2}{v^2},\\
\lambda_{H_2} &= \frac{(s_{\alpha_2}^2(c_{\alpha_3}^2(c_{\alpha_2}^2 M_h^2 + M_{s_1}^2 s_{\alpha_2}^2) + M_{s_2}^2 s_{\alpha_3}^2) + M_{H^0}^2 c_\alpha^2)\tan^2\beta}{v^2},\\
\lambda_{\varphi_1} &= -\frac{(c_\theta^2 M_{A_2}^2 s_{\theta_3}^2 + M_{A^0}^2 s_\theta^2)v^2}{4v_1^4} + \frac{c_{\alpha_2}^2 M_{s_1}^2 + M_h^2 s_{\alpha_2}^2}{v_1^2},\\
\lambda_{\varphi_2} &= -\frac{3(c_\theta^2 M_{A_2}^2 s_{\theta_3}^2 + M_{A^0}^2 s_\theta^2)v^2}{16v_2^4} + \frac{c_{\alpha_3}^2 M_{s_2}^2 + (M_h^2 c_{\alpha_2}^2 + M_{s_1}^2 s_{\alpha_2}^2)s_{\alpha_3}^2}{v_2^2},\\
\delta &= \frac{(M_{A^0}^2 s_\theta^2 + c_\theta^2 M_{A_2}^2 s_{\theta_3}^2)v^2}{8\sqrt{2}v_1^2 v_2},\\
\lambda &= -\frac{(M_{A^0}^2 s_\theta^2 + c_\theta^2 M_{A_2}^2 s_{\theta_3}^2)\tan^2\beta}{v^2 v_1 v_2},\\
\lambda_1 &= \frac{\tan\beta(c_\alpha s_\alpha(M_{H^0}^2 - c_{\alpha_3}^2(c_{\alpha_2}^2 M_h^2 + M_{s_1}^2 s_{\alpha_2}^2) - M_{s_2}^2 s_{\alpha_3}^2) + 2M_{H^\pm}^2 s_\gamma^2 \tan\beta)}{v^2},\\
\lambda_2 &= \frac{(-2M_{H^\pm}^2 s_\gamma^2 + M_{A^0}^2 s_\theta^2 + c_\theta^2 M_{A_2}^2 s_{\theta_3}^2)\tan^2\beta}{v^2},\\
\lambda_3 &= \frac{(M_{A^0}^2 s_\theta^2 + c_\theta^2 M_{A_2}^2 s_{\theta_3}^2)v^2 + 8c_{\alpha_2}(M_h^2 - M_{s_1}^2)s_{\alpha_2}s_{\alpha_3}v_1 v_2}{8v_1^2 v_2^2},\\
\lambda_4 &= \frac{(M_{A^0}^2 s_\theta^2 + c_\theta^2 M_{A_2}^2 s_{\theta_3}^2)v + 2c_\alpha c_{\alpha_2} c_{\alpha_3}(-M_h^2 + M_{s_1}^2)s_{\alpha_2}v_1}{2vv_1^2},\\
\lambda_5 &= \frac{(M_{A^0}^2 s_\theta^2 + c_\theta^2 M_{A_2}^2 s_{\theta_3}^2)v - 2c_\alpha c_{\alpha_3}(c_{\alpha_2}^2 M_h^2 - M_{s_2}^2 + M_{s_1}^2)s_{\alpha_3}v_2}{2vv_2^2},\\
\lambda_6 &= \frac{\tan\beta(M_{A^0}^2 s_\theta^2 + c_\theta^2 M_{A_2}^2 s_{\theta_3}^2)v\,\tan\beta + 2c_{\alpha_2}c_{\alpha_3}(M_h^2 - M_{s_1}^2)s_\alpha s_{\alpha_2}v_1)}{2vv_1^2},\\
\lambda_7 &= \frac{\tan\beta(M_{A^0}^2 s_\theta^2 + c_\theta^2 M_{A_2}^2 s_{\theta_3}^2)v\,\tan\beta + 2c_{\alpha_3}s_\alpha(c_{\alpha_2}^2 M_h^2 - M_{s_1}^2 + M_{s_2}^2 s_{\alpha_2}^2)s_{\alpha_3}v_2)}{2vv_2^2}.
\end{aligned}
\tag{C.2}
$$

Appendix D

Dark Matter Annihilation Diagrams

In this section we point out the leading and sub-leading annihilation channels of the DM scenario described in Chapter. 4.

D.1 Leading Annihilation Diagrams

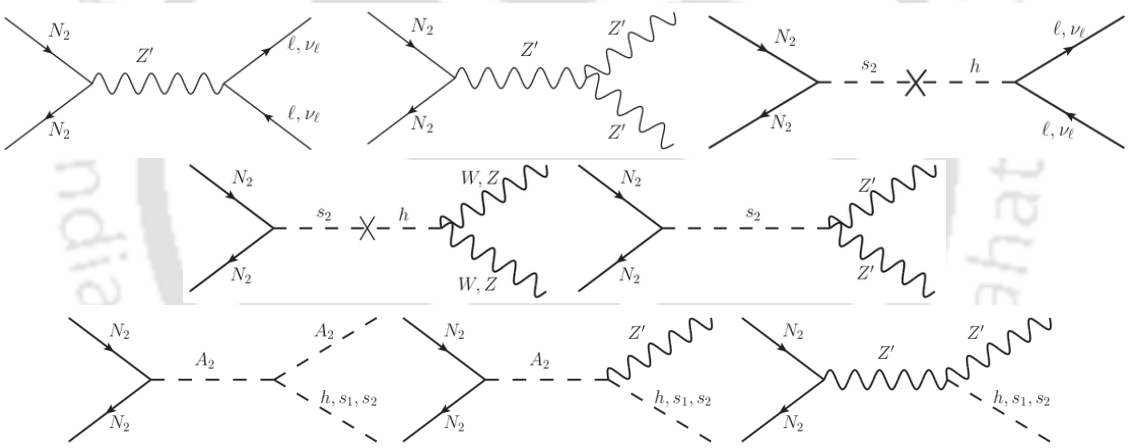

Figure D.1: The diagrams giving leading contributions to the relic abundance.

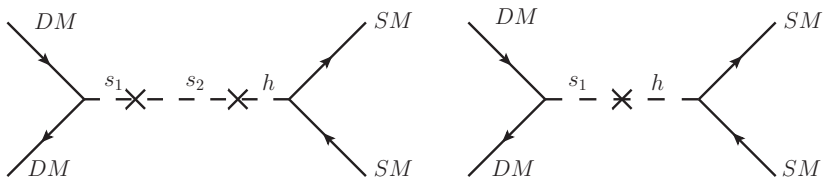

Figure D.2: Dark matter annihilation diagrams in the modified setup scenario of Toy Model-I as discussed in section. 4.5.

D.2 Subleading Annihilation Diagrams

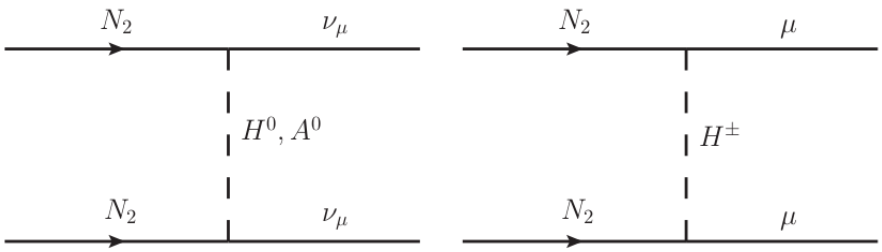

Figure D.3: Subleading contributions to the relic.

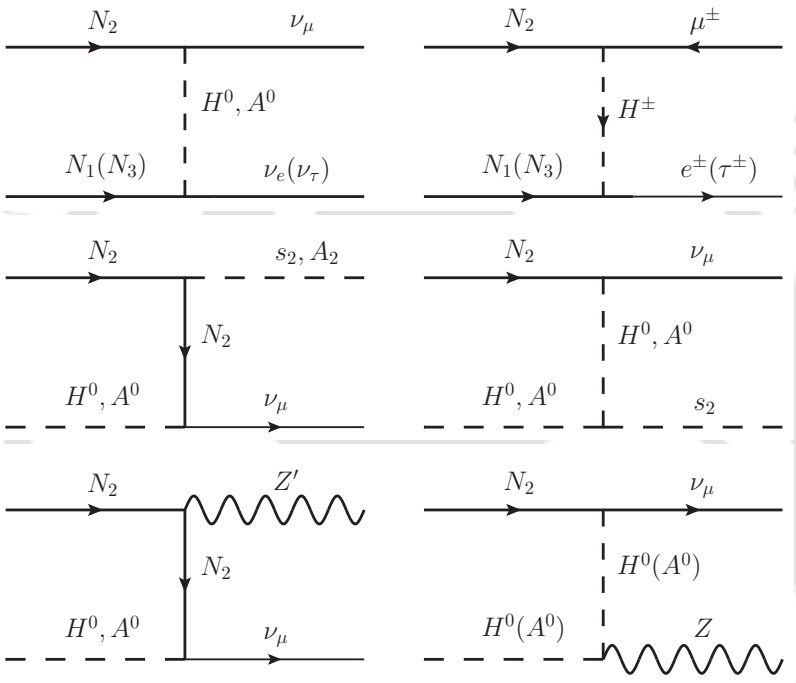

Figure D.4: Subleading Co-annihilation diagrams.

Bibliography

[1] Particle Data Group collaboration, P. Zyla et al., *Review of Particle Physics*, *PTEP* **2020** (2020) 083C01.

[2] CKMfitter Group collaboration, "CKMfitter global fit results as of Summer 19." http://ckmfitter.in2p3.fr/www/results/plots_summer19/num/ckmEval_results_summer19.pdf.

[3] ATLAS collaboration, G. Aad et al., *Observation of a new particle in the search for the Standard Model Higgs boson with the ATLAS detector at the LHC*, *Phys. Lett. B* **716** (2012) 1–29, [1207.7214].

[4] CMS collaboration, S. Chatrchyan et al., *Observation of a New Boson at a Mass of 125 GeV with the CMS Experiment at the LHC*, *Phys. Lett. B* **716** (2012) 30–61, [1207.7235].

[5] https://ef.engr.utk.edu/hyperphysics/hbase/Astro/darmat.html.

[6] M. Schumann, *Direct Detection of WIMP Dark Matter: Concepts and Status*, *J. Phys. G* **46** (2019) 103003, [1903.03026].

[7] I. Esteban, M. C. Gonzalez-Garcia, M. Maltoni, T. Schwetz and A. Zhou, *The fate of hints: updated global analysis of three-flavor neutrino oscillations*, *JHEP* **09** (2020) 178, [2007.14792].

[8] "Nufit collaboration." http://www.nu-fit.org/.

[9] G. Gelmini and P. Gondolo, *DM Production Mechanisms*, 1009.3690.

[10] S. Giagu, *WIMP Dark Matter Searches With the ATLAS Detector at the LHC*, *Front. in Phys.* **7** (2019) 75.

[11] J. Cooley, *Overview of Non-Liquid Noble Direct Detection Dark Matter Experiments*, *Phys. Dark Univ.* **4** (2014) 92–97, [1410.4960].

[12] Particle Data Group collaboration, M. Tanabashi et al., *Review of Particle Physics*, *Phys. Rev. D* **98** (2018) 030001.

[13] H. F. A. Group, "Updates of Semileptonic Results for Spring 2019." https://hflav-eos.web.cern.ch/hflav-eos/semi/spring19/main.shtml, 2019.

[14] T. Aoyama et al., *The anomalous magnetic moment of the muon in the Standard Model*, 2006.04822.

[15] ATLAS collaboration, M. Aaboud et al., *Combination of searches for invisible Higgs boson decays with the ATLAS experiment*, *Phys. Rev. Lett.* **122** (2019) 231801, [1904.05105].

[16] ATLAS collaboration, *Search for invisible Higgs boson decays with vector boson fusion signatures with the ATLAS detector using an integrated luminosity of 139 fb^{-1}*, .

[17] Planck collaboration, N. Aghanim et al., *Planck 2018 results. I. Overview and the cosmological legacy of Planck*, *Astron. Astrophys.* **641** (2020) A1, [1807.06205].

[18] XENON collaboration, E. Aprile et al., *Dark Matter Search Results from a One Ton-Year Exposure of XENON1T*, *Phys. Rev. Lett.* **121** (2018) 111302, [1805.12562].

[19] A. Salam and J. C. Ward, *Weak and electromagnetic interactions*, *Nuovo Cim.* **11** (1959) 568–577.

[20] S. L. Glashow, *Partial Symmetries of Weak Interactions*, *Nucl. Phys.* **22** (1961) 579–588.

[21] J. Goldstone, A. Salam and S. Weinberg, *Broken Symmetries*, *Phys. Rev.* **127** (1962) 965–970.

[22] S. Weinberg, *A Model of Leptons*, *Phys. Rev. Lett.* **19** (1967) 1264–1266.

[23] F. Englert and R. Brout, *Broken Symmetry and the Mass of Gauge Vector Mesons*, *Phys. Rev. Lett.* **13** (1964) 321–323.

[24] P. W. Higgs, *Broken Symmetries and the Masses of Gauge Bosons*, *Phys. Rev. Lett.* **13** (1964) 508–509.

[25] G. S. Guralnik, C. R. Hagen and T. W. B. Kibble, *Global Conservation Laws and Massless Particles*, *Phys. Rev. Lett.* **13** (1964) 585–587.

[26] N. Cabibbo, *Unitary symmetry and leptonic decays*, *Phys. Rev. Lett.* **10** (Jun, 1963) 531–533.

[27] M. Kobayashi and T. Maskawa, *CP-Violation in the Renormalizable Theory of Weak Interaction*, *Progress of Theoretical Physics* **49** (02, 1973) 652–657, [https://academic.oup.com/ptp/article-pdf/49/2/652/5257692/49-2-652.pdf].

[28] L. Wolfenstein, *Parametrization of the Kobayashi-Maskawa Matrix*, *Phys. Rev. Lett.* **51** (1983) 1945.

[29] J. D. Bjorken and S. L. Glashow, *Elementary Particles and SU(4)*, *Phys. Lett.* **11** (1964) 255–257.

[30] S. L. Glashow, J. Iliopoulos and L. Maiani, *Weak Interactions with Lepton-Hadron Symmetry*, *Phys. Rev. D* **2** (1970) 1285–1292.

[31] J. H. Christenson, J. W. Cronin, V. L. Fitch and R. Turlay, *Evidence for the 2π Decay of the K_2^0 Meson*, *Phys. Rev. Lett.* **13** (1964) 138–140.

[32] SLAC-SP-017 collaboration, J. E. Augustin et al., *Discovery of a Narrow Resonance in e^+e^- Annihilation*, *Phys. Rev. Lett.* **33** (1974) 1406–1408.

[33] E598 collaboration, J. J. Aubert et al., *Experimental Observation of a Heavy Particle J*, *Phys. Rev. Lett.* **33** (1974) 1404–1406.

[34] F. Zwicky, *Die Rotverschiebung von extragalaktischen Nebeln*, *Helv. Phys. Acta* **6** (1933) 110–127.

[35] V. C. Rubin and W. K. Ford, Jr., *Rotation of the Andromeda Nebula from a Spectroscopic Survey of Emission Regions*, *Astrophys. J.* **159** (1970) 379–403.

[36] C. L. Bennett, A. Banday, K. M. Gorski, G. Hinshaw, P. Jackson, P. Keegstra et al., *Four year COBE DMR cosmic microwave background observations: Maps and basic results*, *Astrophys. J. Lett.* **464** (1996) L1–L4, [astro-ph/9601067].

[37] WMAP collaboration, G. Hinshaw et al., *Nine-Year Wilkinson Microwave Anisotropy Probe (WMAP) Observations: Cosmological Parameter Results*, *Astrophys. J. Suppl.* **208** (2013) 19, [1212.5226].

[38] G. Bertone, D. Hooper and J. Silk, *Particle dark matter: Evidence, candidates and constraints*, *Phys. Rept.* **405** (2005) 279–390, [hep-ph/0404175].

[39] M. Taoso, G. Bertone and A. Masiero, *Dark Matter Candidates: A Ten-Point Test*, *JCAP* **03** (2008) 022, [0711.4996].

[40] F. Tanedo, "Defense Against the Dark Arts : Notes on dark matter and particle physics." https://www.physics.uci.edu/ tanedo/files/notes/DMNotes.pdf.

[41] G. Arcadi, M. Dutra, P. Ghosh, M. Lindner, Y. Mambrini, M. Pierre et al., *The waning of the WIMP? A review of models, searches, and constraints*, *Eur. Phys. J. C* **78** (2018) 203, [1703.07364].

[42] R. J. Scherrer and M. S. Turner, *On the Relic, Cosmic Abundance of Stable Weakly Interacting Massive Particles*, *Phys. Rev. D* **33** (1986) 1585.

[43] G. Steigman and M. S. Turner, *Cosmological Constraints on the Properties of Weakly Interacting Massive Particles*, *Nucl. Phys. B* **253** (1985) 375–386.

[44] R. Davis, D. S. Harmer and K. C. Hoffman, *Search for neutrinos from the sun*, *Phys. Rev. Lett.* **20** (May, 1968) 1205–1209.

[45] Super-Kamiokande collaboration, Y. Fukuda et al., *Evidence for oscillation of atmospheric neutrinos*, *Phys. Rev. Lett.* **81** (1998) 1562–1567, [hep-ex/9807003].

[46] P. Minkowski, *$\mu \to e\gamma$ at a Rate of One Out of 10^9 Muon Decays?*, *Phys. Lett. B* **67** (1977) 421–428.

[47] M. Gell-Mann, P. Ramond and R. Slansky, *Complex Spinors and Unified Theories*, *Conf. Proc. C* **790927** (1979) 315–321, [1306.4669].

[48] R. N. Mohapatra and G. Senjanovic, *Neutrino Mass and Spontaneous Parity Nonconservation*, *Phys. Rev. Lett.* **44** (1980) 912.

[49] M. Magg and C. Wetterich, *Neutrino Mass Problem and Gauge Hierarchy*, *Phys. Lett. B* **94** (1980) 61–64.

[50] J. Schechter and J. W. F. Valle, *Neutrino Masses in SU(2) x U(1) Theories*, *Phys. Rev. D* **22** (1980) 2227.

[51] R. N. Mohapatra and G. Senjanovic, *Neutrino Masses and Mixings in Gauge Models with Spontaneous Parity Violation*, *Phys. Rev. D* **23** (1981) 165.

[52] R. Foot, H. Lew, X. G. He and G. C. Joshi, *Seesaw Neutrino Masses Induced by a Triplet of Leptons*, *Z. Phys. C* **44** (1989) 441.

[53] E. Ma, *Pathways to naturally small neutrino masses*, *Phys. Rev. Lett.* **81** (1998) 1171–1174, [hep-ph/9805219].

[54] D. Wyler and L. Wolfenstein, *Massless Neutrinos in Left-Right Symmetric Models*, *Nucl. Phys. B* **218** (1983) 205–214.

[55] G. C. Branco, W. Grimus and L. Lavoura, *The Seesaw Mechanism in the Presence of a Conserved Lepton Number*, *Nucl. Phys. B* **312** (1989) 492–508.

[56] M. B. Gavela, T. Hambye, D. Hernandez and P. Hernandez, *Minimal Flavour Seesaw Models*, *JHEP* **09** (2009) 038, [0906.1461].

[57] J. Barry, W. Rodejohann and H. Zhang, *Light Sterile Neutrinos: Models and Phenomenology*, *JHEP* **07** (2011) 091, [1105.3911].

[58] H. Zhang, *Light Sterile Neutrino in the Minimal Extended Seesaw*, *Phys. Lett. B* **714** (2012) 262–266, [1110.6838].

[59] T. P. Cheng and L.-F. Li, *Neutrino Masses, Mixings and Oscillations in SU(2) x U(1) Models of Electroweak Interactions*, *Phys. Rev. D* **22** (1980) 2860.

[60] D. Chang and R. N. Mohapatra, *Small and Calculable Dirac Neutrino Mass*, *Phys. Rev. Lett.* **58** (1987) 1600.

[61] E. Ma, *Verifiable radiative seesaw mechanism of neutrino mass and dark matter*, *Phys. Rev. D* **73** (2006) 077301, [hep-ph/0601225].

[62] P. S. B. Dev and A. Pilaftsis, *Minimal Radiative Neutrino Mass Mechanism for Inverse Seesaw Models*, *Phys. Rev. D* **86** (2012) 113001, [1209.4051].

[63] Y. Zhang, X. Ji and R. N. Mohapatra, *A Naturally Light Sterile neutrino in an Asymmetric Dark Matter Model*, *JHEP* **10** (2013) 104, [1307.6178].

[64] S. Pascoli, *Neutrino physics*, *CERN Yellow Rep. School Proc.* **6** (2019) 213–259.

[65] R. J. Cooke, M. Pettini and C. C. Steidel, *One Percent Determination of the Primordial Deuterium Abundance*, *Astrophys. J.* **855** (2018) 102, [1710.11129].

[66] Planck collaboration, N. Aghanim et al., *Planck 2018 results. VI. Cosmological parameters*, 1807.06209.

[67] A. D. Sakharov, *Violation of CP Invariance, C asymmetry, and baryon asymmetry of the universe*, *Pisma Zh. Eksp. Teor. Fiz.* **5** (1967) 32–35.

[68] J. M. Cline, *Baryogenesis*, in *Les Houches Summer School - Session 86: Particle Physics and Cosmology: The Fabric of Spacetime*, 9, 2006. hep-ph/0609145.

[69] G. Isidori, G. Ridolfi and A. Strumia, *On the metastability of the standard model vacuum*, *Nucl. Phys. B* **609** (2001) 387–409, [hep-ph/0104016].

[70] G. Degrassi, S. Di Vita, J. Elias-Miro, J. R. Espinosa, G. F. Giudice, G. Isidori et al., *Higgs mass and vacuum stability in the Standard Model at NNLO*, *JHEP* **08** (2012) 098, [1205.6497].

[71] S. Alekhin, A. Djouadi and S. Moch, *The top quark and Higgs boson masses and the stability of the electroweak vacuum*, *Phys. Lett. B* **716** (2012) 214–219, [1207.0980].

[72] A. Hebecker and J. Hisano, *Grand Unified Theories*, *PDG Review* (2020) .

[73] MuLan collaboration, V. Tishchenko et al., *Detailed Report of the MuLan Measurement of the Positive Muon Lifetime and Determination of the Fermi Constant*, *Phys. Rev. D* **87** (2013) 052003, [1211.0960].

[74] J. Hardy and I. Towner, *$|V_{ud}|$ from nuclear β decays* , in *Proceedings of 9th International Workshop on the CKM Unitarity Triangle — PoS(CKM2016)*, vol. 291, p. 028, 2017. DOI.

[75] J. Hardy and I. Towner, *Nuclear Beta Decays and CKM Unitarity*, in *13th Conference on the Intersections of Particle and Nuclear Physics*, 6, 2018. 1807.01146.

[76] M. Moulson, *Experimental determination of V_{us} from kaon decays*, in *Proceedings of 9th International Workshop on the CKM Unitarity Triangle — PoS(CKM2016)*, vol. 291, p. 033, 2017. DOI.

[77] Flavour Lattice Averaging Group collaboration, S. Aoki et al., *FLAG Review 2019: Flavour Lattice Averaging Group (FLAG)*, *Eur. Phys. J. C* **80** (2020) 113, [1902.08191].

[78] B. Belfatto, R. Beradze and Z. Berezhiani, *The CKM unitarity problem: A trace of new physics at the TeV scale?*, *Eur. Phys. J. C* **80** (2020) 149, [1906.02714].

[79] Y. Grossman, E. Passemar and S. Schacht, *On the Statistical Treatment of the Cabibbo Angle Anomaly*, *JHEP* **07** (2020) 068, [1911.07821].

[80] A. M. Coutinho, A. Crivellin and C. A. Manzari, *Global Fit to Modified Neutrino Couplings and the Cabibbo-Angle Anomaly*, *Phys. Rev. Lett.* **125** (2020) 071802, [1912.08823].

[81] M. Kirk, *Cabibbo anomaly versus electroweak precision tests: An exploration of extensions of the Standard Model*, *Phys. Rev. D* **103** (2021) 035004, [2008.03261].

[82] A. Crivellin, F. Kirk, C. A. Manzari and M. Montull, *Global Electroweak Fit and Vector-Like Leptons in Light of the Cabibbo Angle Anomaly*, *JHEP* **12** (2020) 166, [2008.01113].

[83] B. Capdevila, A. Crivellin, C. A. Manzari and M. Montull, *Explaining $b \to s\ell^+\ell^-$ and the Cabibbo angle anomaly with a vector triplet*, *Phys. Rev. D* **103** (2021) 015032, [2005.13542].

[84] G. C. Branco, J. T. Penedo, P. M. F. Pereira, M. N. Rebelo and J. I. Silva-Marcos, *Addressing the CKM unitarity problem with a vector-like up quark*, *JHEP* **07** (2021) 099, [2103.13409].

[85] D. Marzocca and S. Trifinopoulos, *Minimal Explanation of Flavor Anomalies: B-Meson Decays, Muon Magnetic Moment, and the Cabibbo Angle*, *Phys. Rev. Lett.* **127** (2021) 061803, [2104.05730].

[86] A. K. Alok, A. Dighe, S. Gangal and J. Kumar, *A natural resolution for the Cabibbo angle anomaly and $R_{K^{(*)}}$*, 2108.05614.

[87] Belle collaboration, L. Widhalm et al., *Measurement of $D^0 \to \pi\ell\nu(K\ell\nu)$ Form Factors and Absolute Branching Fractions*, *Phys. Rev. Lett.* **97** (2006) 061804, [hep-ex/0604049].

[88] BaBar collaboration, J. P. Lees et al., *Measurement of the $D^0 \to \pi^- e^+ \nu_e$ differential decay branching fraction as a function of q^2 and study of form factor parameterizations*, *Phys. Rev. D* **91** (2015) 052022, [1412.5502].

[89] BESIII collaboration, M. Ablikim et al., *Study of Dynamics of $D^0 \to K^- e^+ \nu_e$ and $D^0 \to \pi^- e^+ \nu_e$ Decays*, *Phys. Rev. D* **92** (2015) 072012, [1508.07560].

[90] BESIII collaboration, M. Ablikim et al., *Study of decay dynamics and CP asymmetry in $D^+ \to K_L^0 e^+ \nu_e$ decay*, *Phys. Rev. D* **92** (2015) 112008, [1510.00308].

[91] BESIII collaboration, M. Ablikim et al., *Analysis of $D^+ \to \bar{K}^0 e^+ \nu_e$ and $D^+ \to \pi^0 e^+ \nu_e$ semileptonic decays*, *Phys. Rev. D* **96** (2017) 012002, [1703.09084].

[92] Belle collaboration, L. Cao et al., *Measurements of partial branching fractions of inclusive $B \to X_u \ell \nu_\ell$ decays with hadronic tagging*, *Phys. Rev. D* **104** (2021) 012008, [2102.00020].

[93] T. Mannel and P. Urquijo, *Semileptonic B-Hadron Decays, Determination of V_{cb} and V_{ub}*, *PDG Review* (2020) .

[94] A. Biswas, S. Nandi, S. K. Patra and I. Ray, *A closer look at the extraction of $|V_{ub}|$ from $B \to \pi\ell\nu$*, *JHEP* **07** (2021) 082, [2103.01809].

[95] A. Biswas and S. Nandi, *A closer look at observables from exclusive semileptonic $B \to (\pi, \rho)\ell\nu_\ell$ decays*, 2105.01732.

[96] S. Jaiswal, S. Nandi and S. K. Patra, *Updates on extraction of $|V_{cb}|$ and SM prediction of R(D*) in $B \to D^*\ell\nu_\ell$ decays*, *JHEP* **06** (2020) 165, [2002.05726].

[97] LHCb collaboration, R. Aaij et al., *Determination of the quark coupling strength $|V_{ub}|$ using baryonic decays*, *Nature Phys.* **11** (2015) 743–747, [1504.01568].

[98] HFLAV collaboration, Y. S. Amhis et al., *Averages of b-hadron, c-hadron, and τ-lepton properties as of 2018*, *Eur. Phys. J.* **C81** (2021) 226, [1909.12524].

[99] F. Archilli, "Rare penguin decays at LHCb."

[100] CMS collaboration, A. M. Sirunyan et al., *Measurement of properties of $B_s^0 \to \mu^+\mu^-$ decays and search for $B^0 \to \mu^+\mu^-$ with the CMS experiment*, *JHEP* **04** (2020) 188, [1910.12127].

[101] C. Bobeth, M. Gorbahn, T. Hermann, M. Misiak, E. Stamou and M. Steinhauser, *$B_{s,d} \to l^+l^-$ in the Standard Model with Reduced Theoretical Uncertainty*, *Phys. Rev. Lett.* **112** (2014) 101801, [1311.0903].

[102] M. Beneke, C. Bobeth and R. Szafron, *Power-enhanced leading-logarithmic QED corrections to $B_q \to \mu^+\mu^-$*, *JHEP* **10** (2019) 232, [1908.07011].

[103] H. F. A. Group, "Results on Time-Dependent CP Violation and Measurements Related to the Angles of the Unitarity Triangle: Winter conferences (Moriond, etc.) and PDG 2021." https://hflav-eos.web.cern.ch/hflav-eos/triangle/latest/.

[104] LHCb collaboration, *Updated LHCb combination of the CKM angle γ*, .

[105] R. N. Mohapatra et al., *Theory of neutrinos: A White paper*, *Rept. Prog. Phys.* **70** (2007) 1757–1867, [hep-ph/0510213].

[106] LHCb collaboration, R. Aaij et al., *Search for Lepton-Flavor Violating Decays $B^+ \to K^+\mu^\pm e^\mp$*, *Phys. Rev. Lett.* **123** (2019) 241802, [1909.01010].

[107] LHCb collaboration, R. Aaij et al., *Search for the lepton-flavor violating decays $B_s^0 \to e^\pm\mu^\mp$ and $B^0 \to e^\pm\mu^\mp$*, *Phys. Rev. Lett.* **111** (2013) 141801, [1307.4889].

[108] LHCb collaboration, R. Aaij et al., *Search for the lepton-flavour violating decays $B^0_{(s)} \to e^\pm\mu^\mp$*, *JHEP* **03** (2018) 078, [1710.04111].

[109] LHCb collaboration, R. Aaij et al., *Search for the lepton-flavour-violating decays $B_s^0 \to \tau^\pm\mu^\mp$ and $B^0 \to \tau^\pm\mu^\mp$*, *Phys. Rev. Lett.* **123** (2019) 211801, [1905.06614].

[110] G. Hiller and F. Kruger, *More model-independent analysis of $b \to s$ processes*, *Phys. Rev. D* **69** (2004) 074020, [hep-ph/0310219].

[111] C. Bobeth, G. Hiller and G. Piranishvili, *Angular distributions of $\bar{B} \to \bar{K}\ell^+\ell^-$ decays*, *JHEP* **12** (2007) 040, [0709.4174].

[112] M. Bordone, G. Isidori and A. Pattori, *On the Standard Model predictions for R_K and R_{K^*}*, *Eur. Phys. J. C* **76** (2016) 440, [1605.07633].

[113] LHCb collaboration, R. Aaij et al., *Test of lepton universality in beauty-quark decays*, 2103.11769.

[114] LHCb collaboration, R. Aaij et al., *Test of lepton universality with $B^0 \to K^{*0}\ell^+\ell^-$ decays*, *JHEP* **08** (2017) 055, [1705.05802].

[115] Belle collaboration, A. Abdesselam et al., *Test of lepton flavor universality in $B \to K^*\ell^+\ell^-$ decays at Belle*, *Phys. Rev. Lett.* **126** (2021) 161801, [1904.02440].

[116] S. Bhattacharya, A. Biswas, S. Nandi and S. K. Patra, *Exhaustive model selection in $b \to s\ell\ell$ decays: Pitting cross-validation against the Akaike information criterion*, *Phys. Rev. D* **101** (2020) 055025, [1908.04835].

[117] A. Biswas, S. Nandi, I. Ray and S. K. Patra, *New physics in $b \to s\ell\ell$ decays with complex Wilson coefficients*, 2004.14687.

[118] L.-S. Geng, B. Grinstein, S. Jäger, S.-Y. Li, J. Martin Camalich and R.-X. Shi, *Implications of new evidence for lepton-universality violation in $b \to s\ell^+\ell^-$ decays*, 2103.12738.

[119] W. Altmannshofer and P. Stangl, *New Physics in Rare B Decays after Moriond 2021*, 2103.13370.

[120] M. Algueró, B. Capdevila, S. Descotes-Genon, J. Matias and M. Novoa-Brunet, ***$b \to s\ell\ell$*** *global fits after Moriond 2021 results*, in *55th Rencontres de Moriond on Electroweak Interactions and Unified Theories*, 4, 2021. 2104.08921.

[121] S. Bhattacharya, S. Nandi and S. Kumar Patra, *$b \to c\tau\nu_\tau$ Decays: a catalogue to compare, constrain, and correlate new physics effects*, *Eur. Phys. J. C* **79** (2019) 268, [1805.08222].

[122] C. Murgui, A. Peñuelas, M. Jung and A. Pich, *Global fit to $b \to c\tau\nu$ transitions*, *JHEP* **09** (2019) 103, [1904.09311].

[123] S. Kumbhakar, A. K. Alok, D. Kumar and S. U. Sankar, *A global fit to $b \to c\tau\bar{\nu}$ anomalies after Moriond 2019*, *PoS* **EPS-HEP2019** (2020) 272, [1909.02840].

[124] S. Bhattacharya, S. Nandi, S. K. Patra and S. Sahoo, *'Deep' Dive into $b \to c$ Anomalies: Standardized and Future-proof Model Selection Using Self-normalizing Neural Networks*, 2008.04316.

[125] P. A. M. Dirac, *The Quantum theory of electron. 2.*, *Proc. Roy. Soc. Lond. A* **118** (1928) 351.

[126] A. Keshavarzi, K. S. Khaw and T. Yoshioka, *Muon $g-2$: current status*, 2106.06723.

[127] Muon g-2 collaboration, G. W. Bennett et al., *Final Report of the Muon E821 Anomalous Magnetic Moment Measurement at BNL*, *Phys. Rev. D* **73** (2006) 072003, [hep-ex/0602035].

[128] Muon g-2 collaboration, B. Abi et al., *Measurement of the Positive Muon Anomalous Magnetic Moment to 0.46 ppm*, *Phys. Rev. Lett.* **126** (2021) 141801, [2104.03281].

[129] A. V. Manohar, *Effective field theories*, *Lect. Notes Phys.* **479** (1997) 311–362, [hep-ph/9606222].

[130] K. G. Wilson and W. Zimmermann, *Operator product expansions and composite field operators in the general framework of quantum field theory*, *Commun. Math. Phys.* **24** (1972) 87–106.

[131] J. C. Collins, *Renormalization: An Introduction to Renormalization, The Renormalization Group, and the Operator Product Expansion*, vol. 26 of *Cambridge Monographs on Mathematical Physics*. Cambridge University Press, Cambridge, 1986, 10.1017/CBO9780511622656.

[132] Y. Nambu, *The Confinement of Quarks*, *Sci. Am.* **235N5** (1976) 48–70.

[133] V. A. Khoze and M. A. Shifman, *Heavy quarks*, *Phys. Usp.* **26** (1983) 387–424.

[134] I. I. Y. Bigi, N. G. Uraltsev and A. I. Vainshtein, *Nonperturbative corrections to inclusive beauty and charm decays: QCD versus phenomenological models*, *Phys. Lett. B* **293** (1992) 430–436, [hep-ph/9207214].

[135] A. Khodjamirian, G. Stoll and D. Wyler, *Calculation of long distance effects in exclusive weak radiative decays of B meson*, *Phys. Lett. B* **358** (1995) 129–138, [hep-ph/9506242].

[136] T. Feldmann, *Short and long distance QCD effects in B meson decays*, *AIP Conf. Proc.* **717** (2004) 533–542, [nucl-th/0310008].

[137] C. Bobeth, M. Chrzaszcz, D. van Dyk and J. Virto, *Long-distance effects in $B \to K^* \ell\ell$ from analyticity*, *Eur. Phys. J. C* **78** (2018) 451, [1707.07305].

[138] T. Huber, T. Hurth, J. Jenkins, E. Lunghi, Q. Qin and K. K. Vos, *Long distance effects in inclusive rare B decays and phenomenology of $\bar{B} \to X_d \ell^+ \ell^-$*, *JHEP* **10** (2019) 228, [1908.07507].

[139] I. Montvay and G. Munster, *Quantum fields on a lattice*. Cambridge Monographs on Mathematical Physics. Cambridge University Press, 3, 1997, 10.1017/CBO9780511470783.

[140] C. Davies, *Precision lattice QCD calculations and predictions of fundamental physics in heavy quark systems*, *Journal of Physics: Conference Series* **46** (sep, 2006) 107–121.

[141] C. Gattringer and C. B. Lang, *Quantum chromodynamics on the lattice*, vol. 788. Springer, Berlin, 2010, 10.1007/978-3-642-01850-3.

[142] E. de Rafael, *An Introduction to sum rules in QCD: Course*, in *Les Houches Summer School in Theoretical Physics, Session 68: Probing the Standard Model of Particle Interactions*, 7, 1997. hep-ph/9802448.

[143] P. Colangelo and A. Khodjamirian, *QCD sum rules, a modern perspective*, hep-ph/0010175.

[144] E. Witten, *Baryons in the 1/n Expansion*, *Nucl. Phys. B* **160** (1979) 57–115.

[145] T. D. Cohen, *Chiral and large-Nc limits of quantum chromodynamics and models of the baryon*, *Rev. Mod. Phys.* **68** (1996) 599–608.

[146] E. E. Jenkins, *Large N(c) baryons*, *Ann. Rev. Nucl. Part. Sci.* **48** (1998) 81–119, [hep-ph/9803349].

[147] H. Georgi, *Heavy quark effective field theory*, in *Theoretical Advanced Study Institute in Elementary Particle Physics (TASI 91): Perspectives in the Standard Model*, 8, 1991.

[148] A. G. Grozin, *Introduction to the heavy quark effective theory. part 1*, hep-ph/9908366.

[149] M. Neubert, *Heavy quark symmetry*, *Phys. Rept.* **245** (1994) 259–396, [hep-ph/9306320].

[150] T. Mannel, *Review of heavy quark effective theory*, *Frascati Phys. Ser.* **7** (1997) 107–129, [hep-ph/9611411].

[151] A. J. Buras and M. Munz, *Effective Hamiltonian for $B \to X(s)e^+e^-$ beyond leading logarithms in the NDR and HV schemes*, *Phys. Rev. D* **52** (1995) 186–195, [hep-ph/9501281].

[152] W. Altmannshofer, P. Ball, A. Bharucha, A. J. Buras, D. M. Straub and M. Wick, *Symmetries and Asymmetries of $B \to K^*\mu^+\mu^-$ Decays in the Standard Model and Beyond*, *JHEP* **01** (2009) 019, [0811.1214].

[153] D. Becirevic, N. Kosnik, F. Mescia and E. Schneider, *Complementarity of the constraints on New Physics from $B_s \to \mu^+\mu^-$ and from $B \to Kl^+l^-$ decays*, *Phys. Rev. D* **86** (2012) 034034, [1205.5811].

[154] G. Hiller and M. Schmaltz, *R_K and future $b \to s\ell\ell$ physics beyond the standard model opportunities*, *Phys. Rev. D* **90** (2014) 054014, [1408.1627].

[155] R. Alonso, B. Grinstein and J. Martin Camalich, *$SU(2) \times U(1)$ gauge invariance and the shape of new physics in rare B decays*, *Phys. Rev. Lett.* **113** (2014) 241802, [1407.7044].

[156] L.-S. Geng, B. Grinstein, S. Jäger, J. Martin Camalich, X.-L. Ren and R.-X. Shi, *Towards the discovery of new physics with lepton-universality ratios of $b \to s\ell\ell$ decays*, *Phys. Rev. D* **96** (2017) 093006, [1704.05446].

[157] J. Aebischer, W. Altmannshofer, D. Guadagnoli, M. Reboud, P. Stangl and D. M. Straub, *B-decay discrepancies after Moriond 2019*, *Eur. Phys. J. C* **80** (2020) 252, [1903.10434].

[158] Y. Sakaki, M. Tanaka, A. Tayduganov and R. Watanabe, *Testing leptoquark models in* $\bar{B} \to D^{(*)}\tau\bar{\nu}$, *Phys. Rev. D* **88** (2013) 094012, [1309.0301].

[159] D. Bečirević, M. Fedele, I. Nišandžić and A. Tayduganov, *Lepton Flavor Universality tests through angular observables of* $\overline{B} \to D^{(*)}\ell\overline{\nu}$ *decay modes*, 1907.02257.

[160] E. W. Kolb and M. S. Turner, *The Early Universe*, vol. 69. 1990.

[161] G. Jungman, M. Kamionkowski and K. Griest, *Supersymmetric dark matter*, *Phys. Rept.* **267** (1996) 195–373, [hep-ph/9506380].

[162] P. Gondolo and G. Gelmini, *Cosmic abundances of stable particles: Improved analysis*, *Nucl. Phys. B* **360** (1991) 145–179.

[163] K. Griest and D. Seckel, *Three exceptions in the calculation of relic abundances*, *Phys. Rev. D* **43** (1991) 3191–3203.

[164] M. W. Goodman and E. Witten, *Detectability of Certain Dark Matter Candidates*, *Phys. Rev. D* **31** (1985) 3059.

[165] D. G. Cerdeno and A. M. Green, *Direct detection of WIMPs*, 1002.1912.

[166] LUX collaboration, D. S. Akerib et al., *Results from a search for dark matter in the complete LUX exposure*, *Phys. Rev. Lett.* **118** (2017) 021303, [1608.07648].

[167] XENON collaboration. https://science.purdue.edu/xenon1t/?cat=3.

[168] DARWIN collaboration, J. Aalbers et al., *DARWIN: towards the ultimate dark matter detector*, *JCAP* **11** (2016) 017, [1606.07001].

[169] PandaX-II collaboration, C. Fu et al., *Spin-Dependent Weakly-Interacting-Massive-Particle–Nucleon Cross Section Limits from First Data of PandaX-II Experiment*, *Phys. Rev. Lett.* **118** (2017) 071301, [1611.06553].

[170] LUX collaboration, D. S. Akerib et al., *Results on the Spin-Dependent Scattering of Weakly Interacting Massive Particles on Nucleons from the Run 3 Data of the LUX Experiment*, *Phys. Rev. Lett.* **116** (2016) 161302, [1602.03489].

[171] G. Cowan, *Statistical data analysis*. 1998.

[172] L. Lista, *Practical Statistics for Particle Physicists*, in *2016 European School of High-Energy Physics*, 9, 2016. 1609.04150. DOI.

[173] D. Borah, L. Mukherjee and S. Nandi, *Low scale U(1)$_X$ gauge symmetry as an origin of dark matter, neutrino mass and flavour anomalies*, *JHEP* **12** (2020) 052, [2007.13778].

[174] J. Kawamura, S. Okawa and Y. Omura, *Interplay between the* $b \to s\ell\ell$ *anomalies and dark matter physics*, *Phys. Rev. D* **96** (2017) 075041, [1706.04344].

[175] D. Aristizabal Sierra, F. Staub and A. Vicente, *Shedding light on the $b \to s$ anomalies with a dark sector*, *Phys. Rev. D* **92** (2015) 015001, [1503.06077].

[176] S. Baek, *Dark matter contribution to $b \to s\mu^+\mu^-$ anomaly in local $U(1)_{L_\mu - L_\tau}$ model*, *Phys. Lett. B* **781** (2018) 376–382, [1707.04573].

[177] J. M. Cline, *B decay anomalies and dark matter from vectorlike confinement*, *Phys. Rev. D* **97** (2018) 015013, [1710.02140].

[178] J. M. Cline and J. M. Cornell, *$R(K^{(*)})$ from dark matter exchange*, *Phys. Lett. B* **782** (2018) 232–237, [1711.10770].

[179] N. G. Deshpande and E. Ma, *Pattern of Symmetry Breaking with Two Higgs Doublets*, *Phys. Rev. D* **18** (1978) 2574.

[180] R. Barbieri, L. J. Hall and V. S. Rychkov, *Improved naturalness with a heavy Higgs: An Alternative road to LHC physics*, *Phys. Rev. D* **74** (2006) 015007, [hep-ph/0603188].

[181] M. Cirelli, N. Fornengo and A. Strumia, *Minimal dark matter*, *Nucl. Phys. B* **753** (2006) 178–194, [hep-ph/0512090].

[182] L. Lopez Honorez, E. Nezri, J. F. Oliver and M. H. G. Tytgat, *The Inert Doublet Model: An Archetype for Dark Matter*, *JCAP* **02** (2007) 028, [hep-ph/0612275].

[183] L. Lopez Honorez and C. E. Yaguna, *The inert doublet model of dark matter revisited*, *JHEP* **09** (2010) 046, [1003.3125].

[184] L. Lopez Honorez and C. E. Yaguna, *A new viable region of the inert doublet model*, *JCAP* **01** (2011) 002, [1011.1411].

[185] A. Arhrib, Y.-L. S. Tsai, Q. Yuan and T.-C. Yuan, *An Updated Analysis of Inert Higgs Doublet Model in light of the Recent Results from LUX, PLANCK, AMS-02 and LHC*, *JCAP* **06** (2014) 030, [1310.0358].

[186] A. Dasgupta and D. Borah, *Scalar Dark Matter with Type II Seesaw*, *Nucl. Phys. B* **889** (2014) 637–649, [1404.5261].

[187] D. Borah, S. Sadhukhan and S. Sahoo, *Lepton Portal Limit of Inert Higgs Doublet Dark Matter with Radiative Neutrino Mass*, *Phys. Lett. B* **771** (2017) 624–632, [1703.08674].

[188] D. Borah and A. Gupta, *New viable region of an inert Higgs doublet dark matter model with scotogenic extension*, *Phys. Rev. D* **96** (2017) 115012, [1706.05034].

[189] XENON collaboration, E. Aprile et al., *First Dark Matter Search Results from the XENON1T Experiment*, *Phys. Rev. Lett.* **119** (2017) 181301, [1705.06655].

[190] CMS collaboration, V. Khachatryan et al., *Search for new physics in final states with two opposite-sign, same-flavor leptons, jets, and missing transverse momentum in pp collisions at sqrt(s) = 13 TeV*, JHEP **12** (2016) 013, [1607.00915].

[191] ATLAS collaboration, M. Aaboud et al., *Search for supersymmetry in final states with missing transverse momentum and multiple b-jets in proton-proton collisions at $\sqrt{s} = 13$ TeV with the ATLAS detector*, JHEP **06** (2018) 107, [1711.01901].

[192] M. Gustafsson, S. Rydbeck, L. Lopez-Honorez and E. Lundstrom, *Status of the Inert Doublet Model and the Role of multileptons at the LHC*, Phys. Rev. D **86** (2012) 075019, [1206.6316].

[193] P. Poulose, S. Sahoo and K. Sridhar, *Exploring the Inert Doublet Model through the dijet plus missing transverse energy channel at the LHC*, Phys. Lett. B **765** (2017) 300–306, [1604.03045].

[194] A. Datta, N. Ganguly, N. Khan and S. Rakshit, *Exploring collider signatures of the inert Higgs doublet model*, Phys. Rev. D **95** (2017) 015017, [1610.00648].

[195] E. Lundstrom, M. Gustafsson and J. Edsjo, *The Inert Doublet Model and LEP II Limits*, Phys. Rev. D **79** (2009) 035013, [0810.3924].

[196] J. P. Leveille, *The Second Order Weak Correction to (G-2) of the Muon in Arbitrary Gauge Models*, Nucl. Phys. B **137** (1978) 63–76.

[197] G. Bhattacharyya, K. B. Chatterjee and S. Nandi, *Correlated enhancements in D(s) —> l nu, (g-2) of muon, and lepton flavor violating tau decays with two R-parity violating couplings*, Nucl. Phys. B **831** (2010) 344–357, [0911.3811].

[198] M. Lindner, M. Platscher and F. S. Queiroz, *A Call for New Physics : The Muon Anomalous Magnetic Moment and Lepton Flavor Violation*, Phys. Rept. **731** (2018) 1–82, [1610.06587].

[199] A. Lenz and U. Nierste, *Theoretical update of $B_s - \bar{B}_s$ mixing*, JHEP **06** (2007) 072, [hep-ph/0612167].

[200] L. F. Abbott, P. Sikivie and M. B. Wise, *Constraints on Charged Higgs Couplings*, Phys. Rev. D **21** (1980) 1393.

[201] J. Charles, S. Descotes-Genon, Z. Ligeti, S. Monteil, M. Papucci and K. Trabelsi, *Future sensitivity to new physics in B_d, B_s, and K mixings*, Phys. Rev. D **89** (2014) 033016, [1309.2293].

[202] J. Charles et al., *Current status of the Standard Model CKM fit and constraints on $\Delta F = 2$ New Physics*, Phys. Rev. D **91** (2015) 073007, [1501.05013].

[203] L3 collaboration, P. Achard et al., *Search for heavy neutral and charged leptons in e^+e^- annihilation at LEP*, Phys. Lett. B **517** (2001) 75–85, [hep-ex/0107015].

[204] A. Alloul, N. D. Christensen, C. Degrande, C. Duhr and B. Fuks, *FeynRules 2.0 - A complete toolbox for tree-level phenomenology*, Comput. Phys. Commun. **185** (2014) 2250–2300, [1310.1921].

[205] J. Alwall, R. Frederix, S. Frixione, V. Hirschi, F. Maltoni, O. Mattelaer et al., *The automated computation of tree-level and next-to-leading order differential cross sections, and their matching to parton shower simulations*, *JHEP* **07** (2014) 079, [1405.0301].

[206] T. Sjostrand, S. Mrenna and P. Z. Skands, *PYTHIA 6.4 Physics and Manual*, *JHEP* **05** (2006) 026, [hep-ph/0603175].

[207] H1 and for the ZEUS collaboration, R. Placakyte, *Parton Distribution Functions*, in *31st International Symposium on Physics In Collision*, 11, 2011. 1111.5452.

[208] CMS collaboration, A. M. Sirunyan et al., *Search for natural and split supersymmetry in proton-proton collisions at $\sqrt{s} = 13$ TeV in final states with jets and missing transverse momentum*, *JHEP* **05** (2018) 025, [1802.02110].

[209] F. Lyonnet and I. Schienbein, *PyR@TE 2: A Python tool for computing RGEs at two-loop*, *Comput. Phys. Commun.* **213** (2017) 181–196, [1608.07274].

[210] N. Chakrabarty, D. K. Ghosh, B. Mukhopadhyaya and I. Saha, *Dark matter, neutrino masses and high scale validity of an inert Higgs doublet model*, *Phys. Rev. D* **92** (2015) 015002, [1501.03700].

[211] S. Bißmann, G. Hiller, C. Hormigos-Feliu and D. F. Litim, *Multi-lepton signatures of vector-like leptons with flavor*, *Eur. Phys. J. C* **81** (2021) 101, [2011.12964].

[212] A. Crivellin, G. D'Ambrosio and J. Heeck, *Explaining $h \to \mu^{\pm}\tau^{\mp}$, $B \to K^*\mu^+\mu^-$ and $B \to K\mu^+\mu^-/B \to Ke^+e^-$ in a two-Higgs-doublet model with gauged $L_\mu - L_\tau$*, *Phys. Rev. Lett.* **114** (2015) 151801, [1501.00993].

[213] A. Crivellin, G. D'Ambrosio and J. Heeck, *Addressing the LHC flavor anomalies with horizontal gauge symmetries*, *Phys. Rev.* **D91** (2015) 075006, [1503.03477].

[214] W. Altmannshofer, C.-Y. Chen, P. S. Bhupal Dev and A. Soni, *Lepton flavor violating Z' explanation of the muon anomalous magnetic moment*, *Phys. Lett.* **B762** (2016) 389–398, [1607.06832].

[215] W. Altmannshofer, S. Gori, S. Profumo and F. S. Queiroz, *Explaining dark matter and B decay anomalies with an $L_\mu - L_\tau$ model*, *JHEP* **12** (2016) 106, [1609.04026].

[216] D. Bhatia, S. Chakraborty and A. Dighe, *Neutrino mixing and R_K anomaly in U(1)$_X$ models: a bottom-up approach*, *JHEP* **03** (2017) 117, [1701.05825].

[217] P. Ballett, M. Hostert, S. Pascoli, Y. F. Perez-Gonzalez, Z. Tabrizi and R. Zukanovich Funchal, *Z's in neutrino scattering at DUNE*, *Phys. Rev.* **D100** (2019) 055012, [1902.08579].

[218] Z.-L. Han, R. Ding, S.-J. Lin and B. Zhu, *Gauged $U(1)_{L_\mu - L_\tau}$ Scotogenic Model in light of $R_{K^{(*)}}$ Anomaly and AMS-02 Positron Excess*, 1908.07192.

[219] P. Langacker, *The Physics of Heavy Z' Gauge Bosons*, *Rev. Mod. Phys.* **81** (2009) 1199–1228, [0801.1345].

[220] A. Datta, J. Liao and D. Marfatia, *A light Z' for the R_K puzzle and nonstandard neutrino interactions*, *Phys. Lett. B* **768** (2017) 265–269, [1702.01099].

[221] F. Sala and D. M. Straub, *A New Light Particle in B Decays?*, *Phys. Lett.* **B774** (2017) 205–209, [1704.06188].

[222] F. C. Correia and S. Fajfer, *Light mediators in anomaly free U (1)$_X$ models. Part I. Theoretical framework*, *JHEP* **10** (2019) 278, [1905.03867].

[223] F. C. Correia and S. Fajfer, *Light mediators in anomaly free U (1)$_X$ models. Part II. Constraints on dark gauge bosons*, *JHEP* **10** (2019) 279, [1905.03872].

[224] L. Darmé, M. Fedele, K. Kowalska and E. M. Sessolo, *Flavour anomalies from a split dark sector*, *JHEP* **08** (2020) 148, [2002.11150].

[225] A. Davidson, *$B - L$ as the fourth color within an $\mathrm{SU}(2)_L \times \mathrm{U}(1)_R \times \mathrm{U}(1)$ model*, *Phys. Rev. D* **20** (1979) 776.

[226] R. N. Mohapatra and R. E. Marshak, *Local b-l symmetry of electroweak interactions, majorana neutrinos, and neutron oscillations*, *Phys. Rev. Lett.* **44** (May, 1980) 1316–1319.

[227] D. Borah and R. Adhikari, *Abelian Gauge Extension of Standard Model: Dark Matter and Radiative Neutrino Mass*, *Phys. Rev. D* **85** (2012) 095002, [1202.2718].

[228] R. Adhikari, D. Borah and E. Ma, *New U(1) Gauge Model of Radiative Lepton Masses with Sterile Neutrino and Dark Matter*, *Phys. Lett. B* **755** (2016) 414–417, [1512.05491].

[229] D. Nanda and D. Borah, *Common origin of neutrino mass and dark matter from anomaly cancellation requirements of a $U(1)_{B-L}$ model*, *Phys. Rev. D* **96** (2017) 115014, [1709.08417].

[230] D. Borah, D. Nanda, N. Narendra and N. Sahu, *Right-handed neutrino dark matter with radiative neutrino mass in gauged $B - L$ model*, *Nucl. Phys. B* **950** (2020) 114841, [1810.12920].

[231] B. Barman, D. Borah, P. Ghosh and A. K. Saha, *Flavoured gauge extension of singlet-doublet fermionic dark matter: neutrino mass, high scale validity and collider signatures*, *JHEP* **10** (2019) 275, [1907.10071].

[232] A. Biswas, D. Borah and D. Nanda, *Type III seesaw for neutrino masses in U(1)$_{B-L}$ model with multi-component dark matter*, *JHEP* **12** (2019) 109, [1908.04308].

[233] D. Nanda and D. Borah, *Connecting Light Dirac Neutrinos to a Multi-component Dark Matter Scenario in Gauged $B - L$ Model*, *Eur. Phys. J. C* **80** (2020) 557, [1911.04703].

[234] A. Biswas and A. Shaw, *Reconciling dark matter, $R_{K^{(*)}}$ anomalies and $(g-2)_\mu$ in an $L_\mu - L_\tau$ scenario*, *JHEP* **05** (2019) 165, [1903.08745].

[235] J. A. Dror, R. Lasenby and M. Pospelov, *New constraints on light vectors coupled to anomalous currents*, *Phys. Rev. Lett.* **119** (2017) 141803, [1705.06726].

[236] J. A. Dror, R. Lasenby and M. Pospelov, *Dark forces coupled to nonconserved currents*, *Phys. Rev. D* **96** (2017) 075036, [1707.01503].

[237] P. Ilten, Y. Soreq, M. Williams and W. Xue, *Serendipity in dark photon searches*, *JHEP* **06** (2018) 004, [1801.04847].

[238] Y. Jho, Y. Kwon, S. C. Park and P.-Y. Tseng, *Search for muon-philic new light gauge boson at Belle II*, *JHEP* **10** (2019) 168, [1904.13053].

[239] M. Bauer, P. Foldenauer and J. Jaeckel, *Hunting All the Hidden Photons*, *JHEP* **18** (2020) 094, [1803.05466].

[240] BaBar collaboration, J. Lees et al., *Search for a muonic dark force at BABAR*, *Phys. Rev. D* **94** (2016) 011102, [1606.03501].

[241] M. Lindner, F. S. Queiroz, W. Rodejohann and X.-J. Xu, *Neutrino-electron scattering: general constraints on Z' and dark photon models*, *JHEP* **05** (2018) 098, [1803.00060].

[242] M. Carena, A. Daleo, B. A. Dobrescu and T. M. P. Tait, *Z' gauge bosons at the Tevatron*, *Phys. Rev.* **D70** (2004) 093009, [hep-ph/0408098].

[243] F. F. Deppisch, S. Kulkarni and W. Liu, *Searching for a light Z' through Higgs production at the LHC*, *Phys. Rev. D* **100** (2019) 115023, [1908.11741].

[244] LHCb collaboration, R. Aaij et al., *Search for hidden-sector bosons in $B^0 \to K^{*0}\mu^+\mu^-$ decays*, *Phys. Rev. Lett.* **115** (2015) 161802, [1508.04094].

[245] LHCb collaboration, R. Aaij et al., *Differential branching fraction and angular analysis of the decay $B^0 \to K^{*0}\mu^+\mu^-$*, *JHEP* **08** (2013) 131, [1304.6325].

[246] R. H. Parker, C. Yu, W. Zhong, B. Estey and H. Müller, *Measurement of the fine-structure constant as a test of the standard model*, *Science* **360** (Apr, 2018) 191–195.

[247] T. Hurth, F. Mahmoudi and S. Neshatpour, *On the new LHCb angular analysis of $B \to K^*\mu^+\mu^-$: Hadronic effects or New Physics?*, 2006.04213.

[248] A. J. Buras, J. Girrbach-Noe, C. Niehoff and D. M. Straub, *$B \to K^{(*)}\nu\overline{\nu}$ decays in the Standard Model and beyond*, *JHEP* **02** (2015) 184, [1409.4557].

[249] Z. Calcuttawala, A. Kundu, S. Nandi and S. K. Patra, *Optimal observable analysis for the decay $b \to s$ plus missing energy*, *Eur. Phys. J. C* **77** (2017) 650, [1702.06679].

[250] M. Drewes et al., *A White Paper on keV Sterile Neutrino Dark Matter*, *JCAP* **01** (2017) 025, [1602.04816].

[251] L. Basso, S. Moretti and G. M. Pruna, *A Renormalisation Group Equation Study of the Scalar Sector of the Minimal B-L Extension of the Standard Model*, *Phys. Rev.* **D82** (2010) 055018, [1004.3039].

[252] T. Robens and T. Stefaniak, *Status of the Higgs Singlet Extension of the Standard Model after LHC Run 1*, *Eur. Phys. J.* **C75** (2015) 104, [1501.02234].

[253] F. Bojarski, G. Chalons, D. Lopez-Val and T. Robens, *Heavy to light Higgs boson decays at NLO in the Singlet Extension of the Standard Model*, *JHEP* **02** (2016) 147, [1511.08120].

[254] G. Belanger, B. Dumont, A. Goudelis, B. Herrmann, S. Kraml and D. Sengupta, *Dilepton constraints in the Inert Doublet Model from Run 1 of the LHC*, *Phys. Rev.* **D91** (2015) 115011, [1503.07367].

[255] G. Belanger, F. Boudjema, A. Pukhov and A. Semenov, *micrOMEGAs_3: A program for calculating dark matter observables*, *Comput. Phys. Commun.* **185** (2014) 960–985, [1305.0237].

[256] D. Mahanta and D. Borah, *Fermion dark matter with N_2 leptogenesis in minimal scotogenic model*, *JCAP* **11** (2019) 021, [1906.03577].

[257] XENON collaboration, E. Aprile et al., *Dark Matter Search Results from a One Ton-Year Exposure of XENON1T*, *Phys. Rev. Lett.* **121** (2018) 111302, [1805.12562].

[258] Belle collaboration, R. Glattauer et al., *Measurement of the decay $B \to D\ell\nu_\ell$ in fully reconstructed events and determination of the Cabibbo-Kobayashi-Maskawa matrix element $|V_{cb}|$*, *Phys. Rev. D* **93** (2016) 032006, [1510.03657].

[259] Belle collaboration, E. Waheed et al., *Measurement of the CKM matrix element $|V_{cb}|$ from $B^0 \to D^{*-}\ell^+\nu_\ell$ at Belle*, *Phys. Rev. D* **100** (2019) 052007, [1809.03290].

[260] R. Alonso, B. Grinstein and J. Martin Camalich, *Lifetime of B_c^- Constrains Explanations for Anomalies in $B \to D^{(*)}\tau\nu$*, *Phys. Rev. Lett.* **118** (2017) 081802, [1611.06676].

[261] ATLAS collaboration, G. Aad et al., *Test of the universality of τ and μ lepton couplings in W-boson decays from $t\bar{t}$ events with the ATLAS detector*, 2007.14040.

[262] L. Lavoura, *General formulae for f(1) $\to$ f(2) gamma*, *Eur. Phys. J. C* **29** (2003) 191–195, [hep-ph/0302221].

[263] P. F. de Salas, D. V. Forero, C. A. Ternes, M. Tortola and J. W. F. Valle, *Status of neutrino oscillations 2018: 3σ hint for normal mass ordering and improved CP sensitivity*, *Phys. Lett.* **B782** (2018) 633–640, [1708.01186].

[264] I. Esteban, M. C. Gonzalez-Garcia, A. Hernandez-Cabezudo, M. Maltoni and T. Schwetz, *Global analysis of three-flavour neutrino oscillations: synergies and tensions in the determination of θ_{23}, δ_{CP}, and the mass ordering*, *JHEP* **01** (2019) 106, [1811.05487].

[265] J. A. Casas and A. Ibarra, *Oscillating neutrinos and $\mu \to e, \gamma$*, *Nucl. Phys.* **B618** (2001) 171–204, [hep-ph/0103065].

[266] T. Toma and A. Vicente, *Lepton Flavor Violation in the Scotogenic Model*, *JHEP* **01** (2014) 160, [1312.2840].

[267] KATRIN collaboration, M. Aker et al., *Improved Upper Limit on the Neutrino Mass from a Direct Kinematic Method by KATRIN*, *Phys. Rev. Lett.* **123** (2019) 221802, [1909.06048].

[268] H. Borgohain and D. Borah, *Revisiting Majorana Neutrino Textures in the Light of Dark LMA*, 2004.05622.

[269] C.-Y. Chen, M. Freid and M. Sher, *Next-to-minimal two Higgs doublet model*, *Phys. Rev. D* **89** (2014) 075009, [1312.3949].

[270] A. Drozd, B. Grzadkowski, J. F. Gunion and Y. Jiang, *Extending two-Higgs-doublet models by a singlet scalar field - the Case for Dark Matter*, *JHEP* **11** (2014) 105, [1408.2106].

[271] M. Muhlleitner, M. O. P. Sampaio, R. Santos and J. Wittbrodt, *The N2HDM under Theoretical and Experimental Scrutiny*, *JHEP* **03** (2017) 094, [1612.01309].

[272] S. von Buddenbrock, A. S. Cornell, E. D. Iarilala, M. Kumar, B. Mellado, X. Ruan et al., *Constraints on a 2HDM with a singlet scalar and implications in the search for heavy bosons at the LHC*, *J. Phys. G* **46** (2019) 115001, [1809.06344].

[273] A. Arhrib, R. Benbrik, M. El Kacimi, L. Rahili and S. Semlali, *Extended Higgs sector of 2HDM with real singlet facing LHC data*, *Eur. Phys. J. C* **80** (2020) 13, [1811.12431].

[274] K. Hayasaka et al., *Search for Lepton Flavor Violating Tau Decays into Three Leptons with 719 Million Produced Tau+Tau- Pairs*, *Phys. Lett. B* **687** (2010) 139–143, [1001.3221].

[275] Z. Calcuttawala, A. Kundu, S. Nandi and S. K. Patra, *New physics with the lepton flavor violating decay $\tau \to 3\mu$*, *Physical Review D* **97** (May, 2018) .

[276] S. Jaiswal, S. Nandi and S. K. Patra, *Extraction of $|V_{cb}|$ from $B \to D^{(*)}\ell\nu_\ell$ and the Standard Model predictions of $R(D^{(*)})$*, *JHEP* **12** (2017) 060, [1707.09977].

[277] M. Gell-Mann, P. Ramond and R. Slansky, *Complex Spinors and Unified Theories*, *Conf. Proc.* **C790927** (1979) 315–321, [1306.4669].

[278] CMS collaboration, A. M. Sirunyan et al., *Search for lepton flavour violating decays of the Higgs boson to $\mu\tau$ and $e\tau$ in proton-proton collisions at $\sqrt{s} = 13$ TeV*, *JHEP* **06** (2018) 001, [1712.07173].

[279] D. Schmeier, *Effective Models for Dark Matter at the International Linear Collider*, other thesis, 8, 2013.

[280] A. Greljo, J. Julio, J. F. Kamenik, C. Smith and J. Zupan, *Constraining Higgs mediated dark matter interactions*, *JHEP* **11** (2013) 190, [1309.3561].

[281] S. Matsumoto, Y.-L. S. Tsai and P.-Y. Tseng, *Light Fermionic WIMP Dark Matter with Light Scalar Mediator*, *JHEP* **07** (2019) 050, [1811.03292].

[282] T. Li, *Simplified dark matter models in the light of AMS-02 antiproton data*, *JHEP* **04** (2017) 112, [1612.09501].

[283] T. Li, *Revisiting the direct detection of dark matter in simplified models*, *Phys. Lett. B* **782** (2018) 497–502, [1804.02120].

[284] E. Morgante, *Simplified Dark Matter Models*, *Adv. High Energy Phys.* **2018** (2018) 5012043, [1804.01245].

[285] C. Arina, E. Del Nobile and P. Panci, *Dark Matter with Pseudoscalar-Mediated Interactions Explains the DAMA Signal and the Galactic Center Excess*, *Phys. Rev. Lett.* **114** (2015) 011301, [1406.5542].

[286] J. Abdallah et al., *Simplified Models for Dark Matter Searches at the LHC*, *Phys. Dark Univ.* **9-10** (2015) 8–23, [1506.03116].

[287] C. Arina et al., *A comprehensive approach to dark matter studies: exploration of simplified top-philic models*, *JHEP* **11** (2016) 111, [1605.09242].

[288] M. J. Dolan, F. Kahlhoefer, C. McCabe and K. Schmidt-Hoberg, *A taste of dark matter: Flavour constraints on pseudoscalar mediators*, *JHEP* **03** (2015) 171, [1412.5174].

[289] J. M. No, *Looking through the pseudoscalar portal into dark matter: Novel mono-Higgs and mono-Z signatures at the LHC*, *Phys. Rev. D* **93** (2016) 031701, [1509.01110].

[290] G. Arcadi, M. Lindner, F. S. Queiroz, W. Rodejohann and S. Vogl, *Pseudoscalar Mediators: A WIMP model at the Neutrino Floor*, *JCAP* **03** (2018) 042, [1711.02110].

[291] N. F. Bell, G. Busoni and I. W. Sanderson, *Loop Effects in Direct Detection*, *JCAP* **08** (2018) 017, [1803.01574].

[292] R. Flores, K. A. Olive and S. Rudaz, *Radiative Processes in Lsp Annihilation*, *Phys. Lett. B* **232** (1989) 377–382.

[293] N. F. Bell, J. B. Dent, A. J. Galea, T. D. Jacques, L. M. Krauss and T. J. Weiler, *W/Z Bremsstrahlung as the Dominant Annihilation Channel for Dark Matter, Revisited*, *Phys. Lett. B* **706** (2011) 6–12, [1104.3823].

[294] N. F. Bell, J. B. Dent, T. D. Jacques and T. J. Weiler, *Dark Matter Annihilation Signatures from Electroweak Bremsstrahlung*, *Phys. Rev. D* **84** (2011) 103517, [1101.3357].

[295] N. F. Bell, Y. Cai, J. B. Dent, R. K. Leane and T. J. Weiler, *Enhancing Dark Matter Annihilation Rates with Dark Bremsstrahlung*, *Phys. Rev. D* **96** (2017) 023011, [1705.01105].

[296] J. Kumar, J. Liao and D. Marfatia, *Dark matter annihilation with s-channel internal Higgsstrahlung*, *Phys. Lett. B* **759** (2016) 277–281, [1605.00611].

[297] S. J. Clark, J. B. Dent, B. Dutta and L. E. Strigari, *Indirect detection of the partial p wave via the s wave in the annihilation cross section of dark matter*, *Phys. Rev. D* **99** (2019) 083003, [1901.01454].

[298] Fermilab Lattice, MILC collaboration, A. Bazavov et al., *Semileptonic form factors for $B \to D^* \ell\nu$ at nonzero recoil from 2 + 1-flavor lattice QCD*, 2105.14019.

[299] C. G. Boyd, B. Grinstein and R. F. Lebed, *Precision corrections to dispersive bounds on form-factors*, *Phys. Rev. D* **56** (1997) 6895–6911, [hep-ph/9705252].

[300] Belle collaboration, E. Waheed et al., *Measurement of the CKM matrix element $|V_{cb}|$ from $B^0 \to D^{*-} \ell^+ \nu_\ell$ at Belle*, *Phys. Rev. D* **100** (2019) 052007, [1809.03290].

[301] N. Gubernari, A. Kokulu and D. van Dyk, *$B \to P$ and $B \to V$ Form Factors from B-Meson Light-Cone Sum Rules beyond Leading Twist*, *JHEP* **01** (2019) 150, [1811.00983].

[302] Fermilab Lattice, MILC collaboration, J. A. Bailey et al., *Update of $|V_{cb}|$ from the $\bar{B} \to D^* \ell \bar{\nu}$ form factor at zero recoil with three-flavor lattice QCD*, *Phys. Rev. D* **89** (2014) 114504, [1403.0635].

[303] D. Bigi, P. Gambino and S. Schacht, *$R(D^*)$, $|V_{cb}|$, and the Heavy Quark Symmetry relations between form factors*, *JHEP* **11** (2017) 061, [1707.09509].

[304] CKMFitter Group collaboration. .

[305] J. Charles et al., *Predictions of selected flavour observables within the Standard Model*, *Phys. Rev. D* **84** (2011) 033005, [1106.4041].

[306] CKMFitter Group collaboration, J. Charles, A. Hocker, H. Lacker, S. Laplace, F. R. Le Diberder, J. Malcles et al., *CP violation and the CKM matrix: Assessing the impact of the asymmetric B factories*, *Eur. Phys. J. C* **41** (2005) 1–131, [hep-ph/0406184].

[307] B. Capdevila, P. Gambino and S. Nandi, *Perturbative corrections to power suppressed effects in $\bar{B} \to X_u \ell\nu$*, *JHEP* **04** (2021) 137, [2102.03343].

[308] M. Bordone, B. Capdevila and P. Gambino, *Three loop calculations and inclusive V_{cb}*, 2107.00604.

[309] LHCb collaboration, R. Aaij et al., *Determination of the quark coupling strength $|V_{ub}|$ using baryonic decays*, *Nature Phys.* **11** (2015) 743–747, [1504.01568].